The Dissertation Committee for Jonathan Florez
certifies that this is the approved version of the following dissertation:

Exploring the Interplay Between Star Formation and Active Galactic Nuclei and the Role of Environment in Galaxy Evolution

Committee:

Shardha Jogee, Supervisor

Steven L. Finkelstein

Michael Boylan-Kolchin

Volker Bromm

Neal J. Evans

Christopher Conselice

Exploring the Interplay Between Star Formation and Active Galactic Nuclei and the Role of Environment in Galaxy Evolution

by

Jonathan Florez

Dissertation

Presented to the Faculty of the Graduate School of

The University of Texas at Austin

in Partial Fulfillment

of the Requirements

for the Degree of

Doctor of Philosophy

The University of Texas at Austin

August 2021

This thesis is dedicated to my partner, Michelle, who has been a constant source of support and encouragement throughout the challenges of both life and graduate school. I am incredibly grateful to have you in my life. This thesis is also dedicated to my parents, who have been extremely supportive of my studies and all other pursuits in life.

Acknowledgments

Many people have contributed to the work presented throughout this thesis that deserve to acknowledged. First and foremost, I thank my advisor, Shardha Jogee, for critical commentary and suggestions for Chapters 1, 3, 4, and 5 of this thesis. I also thank Shardha for providing so much guidance and support during my time in graduate school. I thank my former advisor, Andreas Berlind, for providing critical feedback and commentary for Chapter 2 of this thesis. I also thank Sheila Kannappan, David Stark, Katie Eckert, Amanda Moffett, Romeel Davé, Sofía Cora, Rainer Weinberger, Lars Hernquist, Steve Finkelstein, Stephanie LaMassa, Meg Urry, Tonima Ananna, and all my other collaborators who have contributed to the work presented here.

Jonathan Florez

The University of Texas at Austin

August 2021

Exploring the Interplay Between Star Formation and Active Galactic Nuclei and the Role of Environment in Galaxy Evolution

Publication No. _____

Jonathan Florez, Ph.D.
The University of Texas at Austin, 2021

Supervisor: Shardha Jogee

One of the central goals of extragalactic astronomy is to understand how galaxies grow their stellar mass and central black holes, the connection between star formation and active galactic nuclei (AGN), and the impact of environment on this growth. In this thesis, I utilize multiwavelength surveys that are both deep and wide, advanced computational codes that model the spectral energy distributions of galaxies with and without AGN, as well as state-of-the-art simulations of galaxy evolution in order to explore how galaxy properties are impacted by their surround-

ing environment and AGN activity. These studies explore galaxies over a redshift range of $0.015 < z < 0.023$ (lookback time of ~ 0.2 to ~ 0.3 Gyr), and over a redshift range of $0.5 < z < 3.0$ (lookback time of ~ 5 to ~ 12 Gyr). The large-area surveys used here provide some of the largest and most statistically robust samples to-date of rare massive galaxies (with stellar mass $M_* > 10^{11}\ M_\odot$) and extremely luminous AGN (with X-ray luminosity $L_X > 10^{44}$ erg s^{-1}) out to $z \sim 3$, thereby limiting the effects of cosmic variance and Poisson statistics. I analyze the observed stellar masses and star formation rates of galaxies as a function of environment and AGN activity, compare the empirical results to theoretical models of galaxy evolution, and discuss the implications of such comparisons. This work will provide significant guidance and constraints to the future development of theoretical models of galaxy growth.

In Chapter 2 (Florez et al. 2021, ApJ, 906, 97) I measure the environmental dependence, where environment is defined by the distance to the third nearest neighbor, of multiple galaxy properties inside the Environmental COntext (ECO) catalog. I focus primarily on void galaxies at redshifts $z = 0.015 - 0.023$, which I define as the 10% of galaxies having the lowest local density. I compare the properties of void and non-void galaxies: baryonic mass, color, fractional stellar mass growth rate (FSMGR), morphology, and gas-to-stellar-mass ratio. The void galaxies typically have lower baryonic masses than galaxies in denser environments, and they display the properties expected of a lower mass population: they have more late-types, are bluer, have higher FSMGR, and are more gas rich. I also control for baryonic mass and investigate the extent to which void galaxies are different at fixed mass. I find that void galaxies are bluer, more gas-rich, and more star forming at fixed mass than non-void galaxies, which is a possible signature of galaxy assembly bias and other environmental processes. Furthermore, I show that these trends persist even at fixed mass and morphology, and I find that voids host a distinct

population of early-types that are bluer and more star-forming than the typical red and quenched early-types. In addition to these empirical observational results, I also present theoretical results from mock catalogs with built-in galaxy assembly bias. I show that a simple matching of galaxy properties to (sub)halo properties, such as mass and age, can recover the observed environmental trends in the local galaxy population.

In Chapter 3 (Florez et al. 2020, MNRAS, 497, 3273) I investigate the relation between AGN and star formation activity at $0.5 < z < 3$ by analyzing 898 galaxies with high X-ray luminosity AGN ($L_X > 10^{44}$ erg s^{-1}) and a large comparison sample of $\sim 320,000$ galaxies without such AGN. My samples are selected from a large (11.8 deg^2) area in Stripe 82 that has multi-wavelength (X-ray to far-IR) data. The enormous comoving volume (~ 0.3 Gpc^3) at $0.5 < z < 3$ minimizes the effects of cosmic variance and captures a large number of massive galaxies ($\sim 30,000$ galaxies with $M_* > 10^{11}$ $M_\odot$) and high X-ray luminosity AGN. While it is typical for studies of galaxy evolution to discard AGN host galaxies, I fit the SED of galaxies with and without high X-ray luminosity AGN with Code Investigating GALaxy Emission (CIGALE) and include AGN emission templates. I find that without this inclusion, stellar masses and star formation rates in AGN host galaxies can be overestimated, on average, by factors of up to ~ 5 and ~ 10, respectively. The average star formation rate of galaxies with X-ray luminous AGN is higher by a factor of ~ 3 to 10 compared to galaxies without X-ray luminous AGN at fixed stellar mass and redshift, suggesting that high star formation rates and high AGN X-ray luminosities may be fueled by common mechanisms. The vast majority ($> 95\%$) of galaxies with X-ray luminous AGN at $z = 0.5 - 3$ do not show quenched star formation: this suggests that if AGN feedback quenches star formation, the associated quenching process takes a significant time to act and the quenched phase sets in after the highly luminous phases of AGN activity.

In numerical simulations and theoretical models of galaxy evolution, AGN and star formation activity are closely linked and AGN feedback is invoked to regulate galaxy growth. However, few empirical tests exist on how well the models and simulations implement the growth and interplay between AGN and star formation. To address this issue, in Chapter 4 (Florez et al. submitted) I compare the hydrodynamical simulations IllustrisTNG and SIMBA, and the semi-analytical model SAG to the empirical results on AGN and star formation at cosmic noon reported in Chapter 3. The main results of my comparisons are: (i) SAG and IllustrisTNG both qualitatively reproduce the empirical result that galaxies with high X-ray luminosity AGN have higher mean star formation rates, at a given stellar mass, than galaxies without such AGN. SAG, however, strongly over-produces the number density of high X-ray luminosity AGN by a factor of 10 to 100, while IllustrisTNG shows a lack of high X-ray luminosity AGN at high stellar mass ($M* > 10^{11}\ M_{\odot}$) at $z \sim 2$. (ii) In SIMBA, the mean star formation rate of galaxies with high X-ray luminosity AGN is lower than the star formation rate of galaxies without such AGN. Contrary to the data, many high X-ray luminosity AGN in SIMBA have quenched star formation, suggesting that AGN feedback, or other feedback modes in galaxies with such AGN, might be too efficient in SIMBA. I discuss the implications of these results for our understanding of the evolution of galaxies and the growth of their stellar masses and black holes across cosmic time.

Table of Contents

Acknowledgments . . . . . **v**

Abstract . . . . . **vi**

List of Tables . . . . . **xv**

List of Figures . . . . . **xvii**

Chapter 1 Introduction **1**

1.1 Interplay Between AGN and Star Formation in Galaxy Evolution . . 1

1.1.1 Growth of Galaxies and Black Holes 1

1.1.2 Practical Challenges of Studying Highly Luminous AGN . . . 4

1.1.3 The AGN-Star Formation Connection 6

1.1.4 AGN Feedback in Observations and Theory 7

1.2 Role of Environment in Galaxy Evolution 9

1.3 Thesis Overview 12

1.3.1 Selection of Galaxies with and without High X-ray Luminosity AGN 13

1.3.2 SED Fitting: Methods and Testing Reliability of Output . . 14

1.3.3 Detailed Comparisons to Theoretical Models of Galaxy Evolution 15

1.3.4 Environmental Metrics 16

Chapter 2 Void Galaxies Follow a Distinct Evolutionary Path in the Environmental Context Catalog 18

2.1 Introduction 18

2.2 Data and Methods 22

2.2.1 ECO/RESOLVE 22

2.2.2 Photometric Data & Morphologies 23

2.2.3 Baryonic Properties of ECO Galaxies 24

2.2.4 Environment Metrics 25

2.3 Results 32

2.3.1 Observed Properties of Void Galaxies 32

2.3.2 Are Void Galaxies Different at Fixed Mass? 36

2.3.3 Are Void Galaxies Different at Fixed Morphology? 44

2.4 Comparison with Theory: Testing Assembly Bias 47

2.4.1 Conditional Abundance Matching 47

2.4.2 Mock Catalog Construction 50

2.4.3 Results 52

2.5 Discussion 53

2.5.1 Comparison with Previous Results 53

2.5.2 E/S0s as Merger Remnants in Voids 54

2.6 Summary 55

Chapter 3 Exploring AGN and Star Formation Activity of Massive Galaxies at Cosmic Noon 58

3.1 Introduction 58

3.2 Data & Sample Selection 63

3.2.1 NEWFIRM K-band Selected Catalog 63

3.2.2 Stripe 82X 64
3.2.3 VICS82 and WISE Supplemental Data 65
3.2.4 Sample Selection 66
3.3 SED Fitting 75
3.3.1 Impact of AGN Emission on SED Fit and Derived Physical Properties 81
3.4 Derived Stellar Mass and SFR of Sample Galaxies 83
3.4.1 Distribution of Stellar Masses 85
3.4.2 Distribution of Star Formation Rates 88
3.4.3 Testing CIGALE SFRs Against Previously Published Empirical SFRs 92
3.4.4 Testing CIGALE SFRs Against SFRs from Mock SEDs . . . 93
3.5 Results 96
3.5.1 SFR as a Function of Stellar Mass and Redshift 96
3.5.2 Properties and Fraction of Galaxies with Quenched Star Formation 101
3.6 Discussion 106
3.7 Summary 109

Chapter 4 AGN and Star Formation at Cosmic Noon: Comparison of Data to Theoretical Models 112
4.1 Introduction 112
4.2 Overview of Empirical Results and Data Analysis in Paper 1 116
4.2.1 Photometric Catalogs 117
4.2.2 Sample Selection 118
4.2.3 SED Fitting 120
4.2.4 Estimate of Stellar Mass and SFR Completeness Limits . . . 121
4.3 Updates to the Sample Selection 122

4.4 Demographics of high X-ray luminosity AGN 125
4.5 Theoretical Models and Numerical Simulations 127
4.5.1 IllustrisTNG 129
4.5.2 SIMBA 131
4.5.3 SAG 132
4.5.4 Obtaining an X-ray Luminosity from the BHAR 133
4.6 Comparison of Empirical Results to Theoretical Models 135
4.6.1 The X-ray Luminosity Function 137
4.6.2 High X-ray Luminosity AGN on the SFR-Stellar Mass Plane 139
4.7 Discussion 144
4.8 Summary 149

Chapter 5 Summary and Future Work 154
5.1 Key Results 155
5.1.1 How do Galaxies Evolve in Low Density and Void-like Environments? 155
5.1.2 What is the Relation Between AGN Activity and Star Formation in Massive Galaxies at Cosmic Noon? 156
5.1.3 What Can We Infer about AGN Feedback? 158
5.1.4 How Well Do Theoretical Models Reproduce Observed Properties of Galaxies with and without High X-ray Luminosity AGN? 159
5.2 Future Work 163
5.2.1 Searching for Signatures of Mergers in Massive Galaxies with and without X-ray Luminous AGN 163
5.2.2 AGN Growth and Feedback 167
5.2.3 Environmental Studies 170
5.2.4 Advancements in SED Fitting 172

5.2.5 Improving Numerical Simulations and Theoretical Models of AGN Growth and Feedback 174

Appendices 176

Appendix A Appendix to Chapter 3 177

A.1 Assessing the Impact of WISE Data on the Analysis 177

Appendix B Appendix to Chapter 4 182

B.1 Applying the L12 Bolometric Correction to Theoretical Models . . . 182

B.2 Calculating Bolometric Luminosity with a Dependence on Eddington Ratio 184

Bibliography 189

List of Tables

2.1 Test statistic and p-values of the Anderson-Darling (AD) k-sample test performed between the void and non-void galaxy property distributions shown in Figure 2.6. Results are shown for both the ECO and RESOLVE-A semester samples. 35

2.2 Test statistic and p-values of the AD k-sample test performed between the void and mass-matched non-void galaxy property distributions shown in Figure 2.6. Results are shown for both the ECO and RESOLVE-A semester samples. 39

2.3 Number of satellites vs. centrals in the ECO baryonic-mass and stellar-mass complete void and non-void galaxy samples. 40

2.4 Number of late-type and early-type galaxies in the ECO void and non-void galaxy samples. 45

3.1 (1) The sample S0-DECam-NEWFIRM-IRAC contains galaxies which have a detection in the u, g, r, i, z bands, S/N > 5 in the K-band, and S/N > 2 in the two IRAC bands, and overlap with the Stripe 82X survey (see flowchart in Figure 3.1 for an illustration of how samples are selected). (2) The sample S1-Lum-AGN contains a subset of galaxies in S0-DECam-NEWFIRM-IRAC that have an X-ray luminous AGN. The total number of galaxies in the sample, as well as the number of galaxies with X-ray luminosities above the completeness limit ($L_X > L_{X,\mathrm{lim}}$) and stellar masses above the 95% stellar mass completeness limit ($M_* > M_{*,95\%\mathrm{lim}}$) are shown. (3) The sample S1-Lum-AGN-WISE contains the much smaller subset of galaxies in S1-Lum-AGN that have matching WISE photometry. (4) The sample S2-No-Lum-AGN contains the subset of galaxies in S0-DECam-NEWFIRM-IRAC that do not contain an X-ray luminous AGN. (5) The sample S2-No-Lum-AGN-WISE contains the smaller subset of sources in S2-No-Lum-AGN that also have WISE photometry. 73

4.1 (1) The sample S0-DECam-NEWFIRM-IRAC contains galaxies which have a detection in the u, g, r, i, z bands, S/N > 5 in the K-band, and S/N > 2 in the two IRAC bands, and overlap with the Stripe 82X survey. (2) The sample S1-Lum-AGN contains a subset of galaxies in S0-DECam-NEWFIRM-IRAC that have a high X-ray luminosity AGN. The total number of galaxies in the sample, as well as the number of galaxies with X-ray luminosities above the completeness limit ($L_X > L_{X,\mathrm{lim}}$) and stellar masses above the 95% stellar mass completeness limit ($M_* > M_{*,95\%\mathrm{lim}}$) are shown. (3) The sample S2-No-Lum-AGN contains the subset of galaxies in S0-DECam-NEWFIRM-IRAC that do not contain an high X-ray luminosity AGN. 119

List of Figures

2.1 The true baryonic mass for ECO galaxies with gas mass detections (x-axis) vs. the predicted baryonic mass derived from the PGF technique (y-axis). Void galaxies are shown as yellow stars while the rest of the sample is shown as blue circles. Also shown is the line-of-best fit, from a least squares regression, for void galaxies (red, dashed) and for all galaxies (black, solid). The line of best fit is only measured for galaxies with a baryonic mass above the completeness limit ($M_b > 10^{9.3} M_\odot$) 25

2.2 The ECO sample in 5 ° thick Dec slices increasing from the top left panel, in Cartesian coordinates. The top 10 percent most statistically significant voids identified by the ZOBOV algorithm are shown here, with each non-gray color representing a different void. All other galaxies are shown as gray points. It is clear that many galaxies that are classified as belonging to voids are actually in high density regions. 26

2.3 Voronoi densities (y-axis) vs. third nearest neighbor densities (x-axis) of the ECO galaxy sample. The cut for void galaxies (indicated by the dashed lines) was arbitrarily chosen to categorize $\sim 10\%$ of galaxies with the lowest densities as void galaxies by both methods. 28

2.4 Similar to Figure 2.2, the ECO sample is shown here in 5 ° thick Dec slices increasing from the top left panel. All void galaxies found by the Nth nearest neighbor algorithm are shown in blue, while non-void galaxies are shown as gray points. 29

2.5 Normalized histogram of the baryonic mass distribution of galaxies in ECO for void galaxies (blue) and non-void galaxies (red) above the completeness limit with Poisson errors. 33

2.6 This figure shows normalized histograms of color, FSMGR, and $M_{\rm gas}/M_*$ for void (blue) and non-void galaxies (red) in the RESOLVE-A semester (top) and ECO at $Dec. > 5^{\circ}$ (bottom). The green line represents a sample of non-void galaxies with a baryonic mass distribution that matches that of the void galaxy sample. In the top panels, values of $M_{\rm gas}$ come primarily from observations whereas in the bottom panels values of $M_{\rm gas}$ come from a combination of observed and predicted gas masses (see Section 2.3). All the data shown here is complete in baryonic mass above $M_b = 10^{9.3} M_{\odot}$. 34

2.7 Left: For $(u-r)^e$ (top panels), $\log(FSMGR)$ (middle panels), and $\log(M_{\rm gas}/M_*)$ (bottom panels), we show the mean of each property in eight bins of baryonic mass for void galaxies (blue) and non-void galaxies (red) in intervals of $\Delta \log M_b = 0.2$. We show this for all void and non-void galaxies (solid) and for void and non-void galaxy group centrals (dot-dashed). Each data point is placed in the middle of the mass bin and error bars show 1σ uncertainties derived from a bootstrap resampling inside each bin. The p-value of the $T_{n,3}$ test statistic is shown in each panel for all void and non-void galaxies and for void and non-void galaxy centrals (see text). Right: Similar to left panels, but galaxy properties are measured inside seven bins of stellar mass with $\Delta \log M_* = 0.2$. For clarity, we only show the data for all void and non-void galaxies in this plot (i.e., we do not make distinctions between satellites and centrals). We also show the p-value of the $T_{n,3}$ test statistic between void and non-void galaxies in each panel. 37

2.8 $(u-r)^e$ color distributions of void galaxies (blue) and non-void galaxies (red) in eight bins of baryonic mass. The mass bins are the same eight as in Figure 2.7. The number of void galaxies inside each mass bin is also shown on each panel, as well as the p-value of the AD test statistic between void and non-void galaxies. 42

2.9 Gas-to-stellar mass ratio distribution of void galaxies (blue) and non-void galaxies (red) in the same eight bins of baryonic mass as in Figure 2.8. As in Figure 2.8, we show the p-value of the AD test statistic in each panel. 43

2.10 Similar to Figure 2.7, we show the mean of $(u-r)^e$, $\log(FSMGR)$, and $\log(M_{\rm gas}/M_*)$ for void (blue) and non-void (red) galaxy late-types (dashed) and early-types (solid) inside six bins of baryonic mass. We also show, as in Figure 2.7, the p-value of the $T_{n,3}$ test statistic performed between void and non-void galaxies at fixed morphology in each panel. 44

2.11 Similar to 2.7 and 2.10, we show the mean of different observed galaxy properties at fixed baryonic mass in ECO for void (blue circles) and non-void (red circles) galaxies, as well as our results for three mock catalogs (solid, dashed, and dot-dashed lines) that vary by the amount of scatter assigned to the relation between color and the 100 Myr accretion rate of the (sub)halo. Blue lines correspond to the mock void galaxies and red lines correspond to mock non-void galaxies. Model 1 (dot-dashed) assumes no relation between color and the 100 Myr accretion rate. Model 2 (dashed) assigns a correlation coefficient of -0.6 to the relation between color and the 100 Myr accretion rate. Model 3 (solid) assumes a monotonic relation between $u-r$ and the 100 Myr accretion rate of the halo, so no scatter is included in the color assignment of this model. 48

3.1 Flowchart that demonstrates how our samples are selected. We start with the DECam-NEWFIRM-IRAC catalog and create a sample of sources that fit our selection criteria, which we refer to as S0-DECam-NEWFIRM-IRAC (see Sections 3.2.1 and 3.2.4). We then crossmatch S0-DECam-NEWFIRM-IRAC with the Stripe 82X catalog via the MLE method and create samples with and without an X-ray match, which we refer to as S1-Lum-AGN (see Section 3.2.4) and S2-No-Lum-AGN (see Section 3.2.4), respectively. We then search for WISE detections in both S1-Lum-AGN and S2-No-Lum-AGN and create two more samples, which we refer to as S1-Lum-AGN-WISE and S2-No-Lum-AGN-WISE. The reader can refer to Table 3.2.4 for number of objects in each sample complete in X-ray luminosity and stellar mass. We note that although we have 932 sources with X-ray luminous AGN in sample S1-Lum-AGN, only 898 of these are have a good SED fit with a reduced χ^2 of less than 5. We therefore only analyze these 898 sources in S1-Lum-AGN for this work. 67

3.2 The full (0.5-10 keV) X-ray luminosity function of all XMM AO13 sources that fall in SHELA (black), those that have a reliable counterpart in the DECam-NEWFIRM-IRAC catalog through crossmatching with the MLE method (red), matched sources with a WISE-3 detection (dark blue) and matched sources with a WISE-4 detection (light blue) in four different bins of redshift. The luminosity function here is computed using the $V_{\rm max}$ method (see Section 2.4.1). The dashed line in each panel indicates the 80% X-ray luminosity completeness limit, computed from the 80% flux limit at the upper edge of each redshift bin. 69

3.3 This figure compares model SED fits for a galaxy, whose redshift and Stripe 82X ID is displayed in each panel, with a type II X-ray luminous AGN in our samples S1-Lum-AGN (top two panels, with data coverage out to 4.5 μm and S1-Lum-AGN-WISE (bottom two panels with data coverage out to 22 μm) for SED fits that do not include AGN emission (left) and include AGN emission (right). The final model SED fit (solid black line) with AGN emission (right) is made up of the attenuated stellar emission (blue; which is inferred from the unattenuated stellar emission (magenta)), the dust emission from dust heated by massive stars from recent SF (red), the combined AGN emission (purple) from the accretion disk (particularly important at UV+optical wavelengths) and the dusty torus (particularly important at the $3-1000$ μm wavelength range). The best-fit model SED without AGN emission (left) clearly cannot provide a good fit to the observed fluxes at wavelengths past 1 μm, therefore, the AGN emission templates are needed in order to constrain all emission above 1 μm. While WISE data at 12 and 22 μm can provide important constraints on the SED at longer wavelengths, a comparison of the top and bottom right panels of Figure 3.3 shows that for the galaxy fitted here, the IRAC 3.6 and 4.5 μm photometry alone, without any WISE photometry, can provide important constraints on the SED fits with AGN emission templates. 76

3.4 Left: Stellar mass and SFR estimates for our sample of galaxies with X-ray luminous AGN (S1-Lum-AGN) when AGN emission is included in the SED fit (x-axis) versus when AGN emission is not included (y-axis). Points are colored according to their fractional AGN contamination ($f_{\rm AGN}$), defined as the fraction of light in the $8-1000$ μm wavelength range that is contributed by the AGN. Right: Difference in log stellar mass and SFR as a function of the fractional AGN contamination. Also shown is the median (red circles) log difference of stellar mass and SFR with and without the AGN emission in the SED fit in four bins of $f_{\rm AGN}$ with the median absolute deviation shown as error bars. Note that for $f_{\rm AGN} > 0.4$ stellar masses and star formation rates (SFRs) can be overestimated on average, by a factor of up to ~ 5 and ~ 10, respectively, if AGN emission templates are not included in the SED fit. 77

3.5 Galaxy stellar mass function (SMF) for our samples of galaxies with (S1-Lum-AGN, black) and without (S2-No-Lum-AGN, red) X-ray luminous AGN at four different redshift ranges. All galaxies with X-ray luminous AGN (S1-Lum-AGN) are complete in X-ray luminosity at their respective redshift bin; we show the X-ray completeness limit in each panel. The dashed vertical line indicates the stellar mass completeness of the sample of galaxies without X-ray luminous AGN (S2-No-Lum-AGN) at each bin. The error bars at each stellar mass bin are Poisson errors. The SMF is calculated using the $1/V_{\rm max}$ correction described in Section 3.2.4 for the X-ray luminosity function. We find that the SMF of galaxies with X-ray luminous AGN is much lower than the SMF of galaxies without X-ray luminous AGN by $\sim$ 2 orders of magnitude at $M_* > 10^{11}$ $M_\odot$ and by $\sim$ 3 orders of magnitude at $M_* < 10^{11}$ $M_\odot$. 84

3.6 The observed galaxy SMF of our sample of galaxies without X-ray luminous AGN (S2-No-Lum-AGN, red) in four redshift bins with observed literature values at the corresponding redshifts plotted from Muzzin et al. (2013) at $z = 0.5 - 2.5$ (blue, stars), Ilbert et al. (2013) at $z = 0.5 - 2.5$ (orange, triangles), and Kawinwanichakij et al. (2020) at $z \sim 0.75$ and $z \sim 1.25$ (purple, squares). As in Figure 3.5 for our sample, the red dashed line represents the stellar completeness limit of our sample, error bars represent Poisson errors, and the SMF is calculated using the $1/V_{\rm max}$ method. We end the last redshift bin here at $z = 2.5$, instead of $z = 3.0$, for comparison purposes. We find good agreement with other observed SMFs at all redshifts for galaxies with $\log(M_*/M_\odot) > 11$ and at all stellar masses above our completeness limit for all redshift ranges except $z = 1.5 - 2.0$ (see text). 86

3.7 We plot the normalized histograms of the log of the measured SFR for our sample of galaxies with (S1-Lum-AGN, black) and without (S2-No-Lum-AGN, red) X-ray luminous AGN across four different redshift bins. The measured SFR refers to the intrinsic dust-corrected SFR derived from the SFH produced by SED fitting with CIGALE of the observed photometry from the UV to the IRAC 4.5 μm band. Note that galaxies with X-ray luminous AGN have a distribution of intrinsic SFRs skewed towards higher values than galaxies without X-ray luminous AGN. We also plot as dotted lines our estimated 5σ completeness limit for the observed dust-extincted FUV-based SFR, which is estimated from the 5σ detection limit in the u-band and g-band filters, which most closely trace the rest-frame 1500 Å luminosity at $z = 0.5 - 1.5$ and $z = 1.5 - 3.0$, respectively. See text in section 4.2 for details. 89

3.8 SFRs from CANDELS (y-axis) compared to SFRs derived from CIGALE using CFHT (u, g, r, i, z), NEWFIRM (K-band), and IRAC (3.6 and 4.5 μm) photometry for a sample of 38 galaxies with X-ray luminous AGN having $L_X > 10^{43}$ erg s^{-1}. Also shown is the one-to-one line (dashed, black). 93

3.9 Comparison of SFRs from the mock galaxies (x-axis) versus SFRs obtained from the SED fit with CIGALE to the mock galaxy fluxes (y-axis). We do not include WISE photometry in this test in order to resemble the fits we are doing with our S1-Lum-AGN sample. Also shown is the one-to-one line and the mean of the log(SFR) (magenta circles) with the standard deviation represented by the error bars. All points are color-coded by their density on the x (mock SFR) and y (fit SFR) plane, where density is calculated by counting number of neighbors around each data point inside a circular aperture. We find relatively good agreement between the true SFRs of the mock galaxies and the CIGALE-derived SFRs above $\sim 1\ M_{\odot}\mathrm{yr}^{-1}$. At the low end of the true SFRs, some mock galaxies have high CIGALE-derived SFRs, however, only 2% of the mock galaxies have true SFRs that differ from their CIGALE-derived SFR by a factor of 10 or more and only 10% of mock galaxies have true SFRs that differ from the CIGALE-derived SFRs by a factor of 4 or more. 94

3.10 SFR vs. stellar mass for our sample of galaxies with (S1-Lum-AGN, black stars) and without (S2-No-Lum-AGN, colored points) X-ray luminous AGN in four different redshift bins. The S2-No-Lum-AGN galaxies are color-coded by their density on the stellar mass-SFR plane (see text). The dashed vertical line on each panel shows the stellar mass completeness limit in that bin (see Section 3.4.1). The X-ray completeness limit for S1-Lum-AGN is shown in each redshift bin in log units of ergs per second. Also shown are the mean SFR of S2-No-Lum-AGN as a function of stellar mass (red circles), which we refer to as the main sequence, the line that falls 1 dex below the main sequence (dotted magenta) and the line where the specific SFR is $10^{-11}\mathrm{yr}^{-1}$ (blue dashed). It is striking that galaxies with X-ray luminous AGN have higher mean SFRs than galaxies without X-ray luminous AGN at a given stellar mass (see also Figure 3.11). Note also that very few galaxies with X-ray luminous AGN have quenched SF if we use the common definition of quenched galaxies as having a specific SFR $< 10^{-11}\mathrm{yr}^{-1}$. 97

3.11 The mean SFRs for our sample of galaxies with (S1-Lum-AGN, black circles) and without (S2-No-Lum-AGN, red circles, same as those shown in Figure 3.10) X-ray luminous AGN as a function of stellar mass across four redshift bins. We show the total number (N1 and N2) of galaxies in each sample above the stellar mass completeness limit (shown here as vertical dashed lines), as well as the number of galaxies with X-ray luminous AGN in each stellar mass bin above the X-ray luminosity completeness limit. Error bars are 1σ values from a bootstrap analysis. The mean SFRs of galaxies with X-ray luminous AGN are higher by a factor of 3 to 10 than those of galaxies without X-ray luminous AGN at a given stellar mass. 98

3.12 This figure shows the quenched fraction as a function of stellar mass in four different bins of redshift spanning $z = 0.5 - 3$ using two definitions of quiescence, whereby quenched galaxies are defined as having a sSFR $< 10^{-11}\mathrm{yr}^{-1}$ (left panels) or as having a SFR at least 1 dex below the main sequence at a given stellar mass (right panels). In all panels, we plot the fraction of galaxies that are quenched among the sample of galaxies with (S1-Lum-AGN; black circles) and without (S2-No-Lum-AGN; red circles) X-ray luminous AGN. The small dashed red lines in each panel represent the quenched fraction of S2-No-Lum-AGN in all the redshift ranges for easy visualization of the evolution of the quenched fraction with redshift. Poison errors are shown on this plot as error bars. The quenched fractions based on the two definitions of quiescence are roughly consistent at $z < 1.5$, but differ significantly at higher redshifts ($z = 1.5 - 3$) where the quenched fraction based on sSFR is lower by a factor of $\sim 2 - 3$ at $z = 1.5 - 2$ and by a factor of $\sim 5 - 10$ at $z = 2 - 3$ for galaxies with $M_* > 10^{11}\ M_\odot$. The quenched fractions are a strong function of stellar mass in each redshift bin and generally increase with stellar mass, except possibly at the very highest stellar masses. 102

4.1 We compare the hard (2-10 keV) XLF of our sample of high X-ray luminosity AGN (S1-Lum-AGN, blue), which is based on XMM AO13 sources that have a reliable counterpart in our NEWFIRM K_S-selected catalog, to the XLF from all sources in XMM AO13 (red), and to the XLF from published studies Miyaji et al. (2015) (black, solid), Buchner et al. (2015) (red, shaded), and Hopkins et al. (2007) (gray, solid). The vertical dashed line in each panel indicates the 95% X-ray luminosity completeness limit, computed from the 95% flux limit at the upper edge of each redshift bin. The error bars computed for our sample are Poisson errors, and we calculate the XLF using the $1/V_{\rm max}$ method. We find relatively good agreement between our XLF values and those from the literature, especially at luminosities greater than $L_X = 10^{44.5}$ erg s^{-1}. 128

4.2 The hard (2-10 keV) X-ray luminosity function of our crossmatched sample (blue, same from Figure 4.1) and the full matched and unmatched XMM AO13 sample that falls in our survey footprint (red, same from Figure 4.1) compared to the XLF measured for SAG (orange), IllustrisTNG (green) and SIMBA (magenta) in three different redshift bins. All error bars shown are Poisson errors. Each row corresponds to a different bolometric correction that was used to obtain the X-ray luminosity from the bolometric luminosity in the simulations. Row 1 uses the bolometric correction from L12, and row 2 uses the bolometric correction from H07. Regardless of the bolometric correction used, SAG appears to over-predict the number density of galaxies with high X-ray luminosity AGN, relative to the observed sample, at all redshifts and X-ray luminosities. The XLF of IllustrisTNG appears to agree relatively well with the observed XLF, especially when assuming the bolometric correction from H07. The XLF for SIMBA appears to show that SIMBA over-predicts the number density of galaxies, regardless of bolometric correction used, though not to the extent that SAG does. 136

4.3 The stellar mass-SFR relation for galaxies with (black, stars) and without (colored) high X-ray luminosity AGN for our observed sample (first row), for SAG (second row), for IllustrisTNG (third row), and for SIMBA (fourth row) in three different redshift bins. The galaxies without high X-ray luminosity AGN are color-coded by their density on the mass-SFR plane. The dashed vertical line shows the observed stellar mass completeness limit at each redshift range. Also shown in each panel is the mean SFR, at fixed stellar mass, for the sample of galaxies without high X-ray luminosity AGN (red circles), which we refer to as the main sequence, and the line that falls 1 dex below the main sequence (dotted magenta). We used the H07 bolometric correction to obtain X-ray luminosities in the models for this figure. Compared to the data, SAG strongly over-produces the number density of AGN of high X-ray luminosity in all three redshift bins, as is seen in Figure 4.2, while IllustrisTNG shows a lack of high X-ray luminosity AGN at high stellar masses ($M_* > 10^{11}\ M_\odot$) at $z \sim 2$. However, both SAG and IllustrisTNG qualitatively reproduce the empirical results that galaxies with high X-ray luminosity AGN have higher mean SFR than galaxies without such AGN at a given stellar mass (see Figure 4.4). Contrary to the data, in SIMBA the majority of galaxies with high X-ray luminosity AGN appear to have quenched SF. 141

4.4 Row 1: The mean SFR as a function of stellar mass for the sample of galaxies with (black circles) and without (red circles, same as Figure 4.3) high X-ray luminosity AGN. Rows 2-4: Similar to first row, but for SAG (row 2), IllustrisTNG (row 3), and SIMBA (row 4). As in Figure 4.3, the BC of H07 was used to obtain hard X-ray luminosities in the models shown here. In qualitative agreement with the data, SAG and IllustrisTNG show enhanced SFR in galaxies with high X-ray luminosity AGN compared to galaxies without such AGN, except at the highest stellar masses in IllustrisTNG. Contrary to the data, galaxies with high X-ray luminosity AGN in SIMBA have a mean SFR, at a given stellar mass, that is lower than the mean SFR of galaxies without such AGN. 142

5.1 From the bottom panels of Figure 14 in Springel et al. (2005), this figure shows the time evolution of the total black hole accretion rate (bottom) and the star formation rate (top) of two galaxies during a merger. The red dots correspond to different phases of the merger. The first red dot corresponds to the phase of the merger just after the first passage of the two discs. The second red dot corresponds to the phase of the merger when the galaxies are coalescing, at which point the star formation and black hole accretion rates peak. Finally, the third red dot corresponds to the phase of the merger just after the galaxies have fully merged. Given the results reported in Chapter 3 showing that high X-ray luminosity AGN are frequently found in galaxies with high star formation rates, it is not unreasonable to think that galaxies with high X-ray luminosity AGN are likely experiencing a merger with another galaxy and are in the phase of the merger represented by the second red dot in this figure, where black hole accretion and star formation activity peak. It would be possible to further test this scenario in observations with deep X-ray data by analyzing if AGN with lower black hole accretion rates, and therefore lower X-ray luminosities, tend to exist in galaxies with low, average, or high star formation rates. 165

5.2 Four example SEDs for galaxies with high X-ray luminosity AGN at $z = 1.5 - 2$. These SEDs were generated by CIGALE and visually inspected for a potential JWST proposal. The different components of the SED shown here correspond to the attenuated (blue) and unattenuated (magenta) stellar emission, the dust emission due to star formation (red), the AGN emission (purple, dashed), and the total sum of these different components that produce the model spectrum (black). The blue circles show the photometric fluxes with error bars. The AGN to stellar light ratio appears to be lowest at wavelengths of $\sim 1 - 3$ μm, while AGN emission appears to largely dominate the SED outside of these wavelengths. If one wished to therefore study the stellar components of such galaxies, it would appear particularly useful to focus on obtaining observations of these galaxies at near to mid-infrared wavelengths. 168

A.1 Similar to Figure 3.4 but for sources in S1-Lum-AGN-WISE, that is, galaxies with X-ray luminous AGN and WISE photometry available. Left: Stellar mass and SFR estimates for our sample of galaxies with X-ray luminous AGN (S1-Lum-AGN-WISE) when AGN emission is included in the SED fit (x-axis) versus when AGN emission is not included (y-axis). Points are colored according to their fractional AGN contamination ($f_{\rm AGN}$), defined as the fraction of light in the $8-1000$ μm wavelength range that is contributed by the AGN. Right: Difference in log stellar mass and SFR as a function of the fractional AGN contamination. Also shown is the median (red circles) log difference of stellar mass and SFR with and without the AGN emission in the SED fit in four bins of $f_{\rm AGN}$ with the median absolute deviation shown as error bars. We note that the results of this test are qualitatively similar to those shown in Figure 3.4, where WISE photometry is not used in the sample. 179

A.2 Left: The stellar mass estimate of galaxies with (S1-Lum-AGN-WISE, top) and without (S2-No-Lum-AGN, bottom) X-ray luminous AGN. Right: The The SFR estimate of galaxies with (S1-Lum-AGN-WISE, top) and without (S2-No-Lum-AGN, bottom) X-ray luminous AGN. The y-axis on all panels shows the stellar mass (or SFR) value obtained when WISE-3 or WISE-4 photometry is included in the SED fit, while the x-axis shows the value that is obtained when WISE photometry is not included in the SED fit. We find that stellar masses do not vary by more than 0.5 dex when WISE data is excluded from the photometry in either sample. SFRs, on the other hand, can vary by a factor of ~ 1 dex when WISE photometry is not included in the SED fit, however, we find no systematic bias. 180

A.3 The mean SFR of galaxies with (S1-Lum-AGN-WISE) and without (S2-No-Lum-AGN-WISE) X-ray luminous AGN as a function of stellar mass in two different bins of redshift. The dashed vertical line shows the mass completeness limit discussed in Section 3.4.1. Our results here for the two samples with WISE photometry do not change qualitatively from those of Figure 3.11. 181

B.1 The stellar mass-SFR relation for galaxies with (black, stars) and without (colored) high X-ray luminosity AGN for our observed sample (first row), for SAG (second row), for IllustrisTNG (third row), and for SIMBA (fourth row) in three different redshift bins. The galaxies without high X-ray luminosity AGN are color-coded by their density on the mass-SFR plane. The dashed vertical line shows the observed stellar mass completeness limit at each redshift range. Also shown in each panel is the mean SFR, at fixed stellar mass, for the sample of galaxies without high X-ray luminosity AGN (red circles), which we refer to as the main sequence, and the line that falls 1 dex below the main sequence (dotted magenta). We used the L12 bolometric correction to obtain X-ray luminosities in the models for this figure. Both SAG and IllustrisTNG appear to predict that the majority of galaxies with high X-ray luminosity AGN have enhanced SFRs, relative to the main sequence, at $M_* \lesssim 10^{11.5}\ M_\odot$. The majority of galaxies with high X-ray luminosity AGN in SIMBA, however, appear to have quenched SF. These results are consistent with what we found in Figure 4.3 185

B.2 The mean SFR as a function of stellar mass for the sample of galaxies with (black circles) and without (red circles) high X-ray luminosity AGN. As in Figure B.1, the BC of L12 was used to obtain hard X-ray luminosities in the models shown here. SAG and IllustrisTNG appear to show enhanced SFR in galaxies with high X-ray luminosity AGN compared to galaxies without such luminous AGN, except at the highest stellar mass in IllustrisTNG and SAG ($M_* \gtrsim 10^{11.5}\ M_\odot$). SIMBA appears to show that the mean SFR of galaxies with high X-ray luminosity AGN fall below the main sequence, consistent with what we found in Figure 4.4. 186

B.3 Similar to Figure 4.2 which shows the XLF of our observed sample (blue), XMM AO13 (red), and the theoretical models using the L12 BC (top row) and H07 (bottom row) BC. We remind the reader that the dashed vertical line represents the X-ray luminosity completeness limit. Here, we only focus on the SAG model (orange) and show the predicted XLF that arises when we apply two different methods to obtain bolometric luminosity. The SAG XLF with the error bars and circles is the same that is shown in Figure 4.2, where the radiative efficiency ϵ is treated as a constant. The SAG XLF shown by the dashed line is computed by treating the radiative efficiency of the radio accretion mode as a variable that depends on the Eddington ratio (from Fanidakis et al., 2012). The only difference between the two predicted XLFs produced by SAG is seen at the faint end of the XLF in the top panels, where the BC of L12 is applied to get X-ray luminosity. The faint end slope of the SAG XLF predicted by the variable radiative efficiency slightly flattens out relative to the SAG XLF predicted by assuming a constant radiative efficiency. We find that SAG still overproduces high X-ray luminosity AGN and the XLF remains largely unchanged when assuming a variable radiative efficiency to calculate bolometric luminosity. 188

Chapter 1

Introduction

1.1 Interplay Between AGN and Star Formation in Galaxy Evolution

1.1.1 Growth of Galaxies and Black Holes

It is generally accepted that galaxies grow and evolve within the framework of a Λ Cold Dark Matter (ΛCDM; Blumenthal et al., 1984) cosmological model. In the ΛCDM, or standard, model of cosmology, the initial conditions of the early universe give rise to small structures of dark matter that decoupled from the Hubble flow and eventually collapsed to form virialized halos. These halos then go on to merge with other dark matter halos in order to effectively build dark matter halos of increasing size over cosmic time. Galaxies, meanwhile, began to form inside the dark matter halos as baryons accumulated and cooled to form rotating disks of gas. These rotating disks of gas now serve as the building blocks for the large range of galaxy populations we observe today (Steinmetz & Navarro, 2002; Cole et al., 2000). Understanding the mechanisms that drive galaxy growth and evolution is currently a key question in extragalactic astronomy that has serious implications

for theoretical models of galaxy evolution.

Galaxies are generally thought to evolve through a complex variety of mechanisms. Galaxies can grow via mergers and the accretion of gas, which provides fuel for star formation and stellar mass growth. Interactions with the surrounding environment, feedback from star formation and accreting central massive black holes, as well as other internal and external processes can halt, or in some cases accelerate (e.g., Silk, 2013), the growth of galaxies and alter their observed properties. In order to better understand the processes that drive galaxy evolution, it is necessary to study galaxies over a large volume and during a time when galaxies were actively forming large amounts of stars and building their stellar masses and central massive black holes rapidly.

Cosmic noon ($z \sim 1-3$, corresponding to $\sim 2-6$ billion years after the Big Bang) is one of the most important and active epochs of galaxy formation. During this epoch, star formation and black hole accretion in galaxies peaked, protoclusters collapsed into existence (Muldrew et al., 2015; Chiang et al., 2014, 2013), and galaxies underwent significant growth (Madau & Dickinson, 2014). Active galactic nuclei (AGN) activity, which arises directly from the accretion of gas onto a galaxy's central massive black hole, also peaked during this epoch as a result of the rapid growth of black holes. In addition, star forming galaxies began to transition to a population of 'red and dead' galaxies with low star formation rates. Such galaxies dominate the high mass end of the stellar mass function at $z \lesssim 2$ (Kawinwanichakij et al., 2020; Weigel et al., 2016; Eckert et al., 2016; Ilbert et al., 2013; Muzzin et al., 2013) and are frequently found in high density environments, such as clusters (Wagner et al., 2017; Hogg et al., 2004; Balogh et al., 2004; Bernardi et al., 2003). The physical mechanisms responsible for the transition from star forming galaxies to quiescent galaxies are thought to be attributed to a range of internal and external processes, including environmental effects (e.g., mergers, ram pressure stripping,

tidal stripping, etc.), feedback from supernovae (SNe), and feedback from AGN. It is postulated that AGN feedback is capable of heating and/or expelling the gas in a galaxy, if the feedback energy is strong enough, thereby preventing future episodes of star formation and ultimately halting galaxy growth (Hopkins et al., 2006; Di Matteo et al., 2005; Springel et al., 2005) It is currently unclear, however, to what extent AGN feedback contributes to the overall quenching of galaxies at $z \lesssim 2$.

Exploring populations of AGN, especially those that are extremely rare and luminous, can provide important constraints for the improvement and development of theoretical models of galaxy evolution. Many theoretical models and numerical simulations often invoke AGN feedback (Vogelsberger et al., 2020; Pillepich et al., 2019; Davé et al., 2019; Cora et al., 2019, 2018; Nelson et al., 2018; Springel et al., 2018) in order to solve the "overcooling" problem in galaxy formation models, whereby galaxies grow too massive and produce stellar mass functions that do not resemble empirical ones if some form of feedback is not applied to the gas (Naab & Ostriker, 2017; Somerville & Davé, 2015). While AGN feedback is invoked frequently in cosmological simulations, a lack of high spatial and spectral resolution observations of AGN combined with current cosmological simulation resolutions has made it difficult to constrain the physical mechanisms driving black hole growth and the extent to which AGN feedback can heat and/or expel the gas in a galaxy. Cosmological simulations typically cannot resolve galaxies on scales lower than ~ 1 kpc, meaning many assumptions have to be made about how gas gets fed into a black hole and how gas gets heated or ejected by an AGN. Detailed studies of highly luminous AGN are necessary for understanding the role AGN plays in galaxy evolution, and for guiding the physical mechanisms that need to be implemented in theoretical models of galaxy and black hole growth in order to produce better agreement between numerical simulations and observations.

It should be noted that the topic of black hole growth and evolution has

generated great interest over the last couple of years for numerous reasons. Recent "smoking gun" evidence for the existence of black holes was recently provided by the Event Horizon Telescope collaboration in 2019 who captured the image of a shadow cast by a supermassive black hole in M87 (Event Horizon Telescope Collaboration et al., 2019). Other exciting results from Laser Interferometer Gravitational-Wave Observatory (LIGO), for instance, suggest that the merger of a black hole and neutron star are responsible for gravitational waves that were recently detected in 2020 (Abbott et al., 2021). Additionally, the 2021 Nobel Prize in Physics was awarded to Andrea Ghez and Reinhardt Genzel for leading observational work establishing the existence of a supermassive compact object, compatible with being a supermassive black hole, in the center of the Milky Way (e.g., Ghez et al., 2003, 1998; Eckart & Genzel, 1997), as well as to Roger Penrose for theoretical work showing that the general theory of relativity leads to the formation of black holes (Penrose, 1969, 1963). While these results are exciting and captivating, they merely scratch the surface of what we have yet to understand about black hole growth and AGN activity.

1.1.2 Practical Challenges of Studying Highly Luminous AGN

AGN, which had their spectra first characterized in 1943 (Seyfert, 1943) and luminosities later measured in 1963 (Schmidt, 1963), are amongst the most extreme and luminous systems in the Universe. The source of an AGN's bright luminosity is a hot accretion disk made of gas that emits photons at ultraviolet (UV) and optical wavelengths. Many AGN typically have other components that emit powerfully at other wavelengths, such as jets which emit at radio wavelengths (Fabian, 2012; Peterson & Fabian, 2006), dusty tori of gas with temperatures of $T \sim 1,200 - 1,500$ K emitting at mid-infrared wavelengths (Fritz et al., 2006), and coronas of hot gas that reside above supermassive black holes which emit X-rays through inverse Compton scattering of UV and optical accretion disk photons (Haardt & Maraschi, 1991). As

a result, AGN emission can dominate the spectral energy distribution (SED) across a wide range of wavelengths (e.g., X-ray, UV+optical, mid-infrared, radio).

Due to the reasons stated above, studying the star formation activity of galaxies with highly luminous AGN can be rather complicated. The presence of a luminous AGN in a galaxy can make it difficult to disentangle the emission between AGN and star forming processes, especially at UV and optical wavelengths, thereby making it necessary to model the AGN emission when deriving physical properties of galaxies. If one does not properly account for the emission of a luminous AGN when deriving quantities such as the star formation rate or stellar mass of a galaxy, one can overestimate the value of such properties as the UV and optical emission in the SED will attributed to stellar emission and star forming processes rather than AGN activity (see Chapter 3). The most commonly used SED fitting codes in the literature [e.g., EAZY-py (Brammer et al., 2008), MAGPHYS (da Cunha et al., 2008), iSEDfit (Moustakas et al., 2013), GalMc (Acquaviva et al., 2011), FAST (Kriek et al., 2009)] do not account for AGN emission, making them impractical for analyzing the SEDs of galaxies with highly luminous AGN. SED fitting codes that do account for AGN emission [e.g., AGNfitter (Calistro Rivera et al., 2016), SED3FIT (Berta et al., 2013)], on the other hand, will often try to model an AGN component where none may exist, thus making such codes unsuitable for fitting samples of galaxies without highly luminous AGN. For these reasons, many studies of galaxy evolution that explore global trends of star formation explicitly remove or ignore the contribution of galaxies with highly luminous AGN (see Speagle et al., 2014, and references therein). The connection between AGN and star formation, as a consequence, is not so well understood, especially at higher redshifts.

In order to perform a thorough analysis of the highly luminous AGN population, one requires multi-wavelength data that covers a large fraction of the sky. The most luminous AGN in the Universe (with $L_{\rm bol} \gtrsim 10^{47}$ erg s^{-1}) are extremely rare

and have very low number densities. As a result, many small area (< 1 deg^2) legacy fields [e.g., GOODS NICMOS Survey (Conselice et al., 2011), CANDELS (Grogin et al., 2011), COSMOS] that provide rich multi-wavelength data sets, sometimes with photometry in 30 or more filters and spectroscopy for select galaxies, are not ideal for studies of luminous AGN as the small volumes probed by these fields do not yield statistically significant samples of luminous AGN.

In order to study the rare luminous AGN population, one must utilize data from larger field ($\gtrsim$ 10 deg^2) surveys that are capable of mitigating the effects of cosmic variance and capturing a significant population of massive galaxies and highly luminous AGN. Such data sets, however, typically only have photometric data available in ~ 10 or fewer filters and have limited spectroscopic data. Having limited spectroscopic and photometric data inevitably means the analysis will have to rely heavily on SED fitting techniques, validation of SED output results using mock galaxies, and high computing resources in order to manage very large numbers ($\gtrsim 10^5$) of galaxies. Using data from large area surveys, however, is critical for studies of galaxy evolution as the large volume allows one to study galaxies from a wide range of environments as well as mitigate the effects of cosmic variance and Poisson statistics (Moster et al., 2011). More importantly, it allows one to uniformly sample and study extremely rare populations of galaxies, such as galaxies with very high luminosity AGN (with bolometric luminosity $L_{\rm bol} > 10^{47}$ erg s^{-1}) and extremely massive galaxies (with stellar mass $M_* > 5 \times 10^{11}$ $M_\odot$).

1.1.3 The AGN-Star Formation Connection

While it has been postulated that feedback from an AGN is capable of suppressing star formation and galaxy growth, there is observational evidence of AGN and enhanced star formation activity coexisting in galaxies. A so-called AGN-star formation connection has been observed at low redshifts ($z < 0.1$) (Mahoro et al., 2017;

Sanders et al., 1988). Any potential connection between AGN and star formation could be due, in part, to gas fueling both star formation and black hole growth when the angular momentum problem can be overcome (e.g., Jogee, 2006, and references therein), as is the case in mergers (Hopkins et al., 2008). This claimed connection between AGN and star formation, however, is currently a topic of debate as other studies (e.g., Leslie et al., 2016) claim to find AGN activity associated with low rates of star formation at $z < 0.1$.

At higher redshifts, the connection between AGN and star formation is less well-studied. Some studies have claimed that galaxies with high X-ray luminosity AGN have enhanced star formation activity compared to galaxies without high X-ray luminosity AGN and/or that high X-ray luminosity AGN are preferentially found in star-forming galaxies out to $z \sim 2$ (Masoura et al., 2018; Shimizu et al., 2017; Santini et al., 2012; Rosario et al., 2013), while other studies (e.g., Shimizu et al., 2015) have claimed that galaxies with X-ray luminous AGN have decreased star formation rates compared to galaxies without luminous AGN. The work in Chapters 3 and 4 of this thesis sheds light on the relation between AGN and star formation.

1.1.4 AGN Feedback in Observations and Theory

As discussed previously, feedback from an AGN is thought to suppress or reduce star formation and galaxy growth in a variety of ways. Different forms of AGN feedback are postulated to affect the host galaxy and the surrounding gas in different ways. Radiation and winds from the accretion disk near the black hole can heat and/or expel gas on various galactic scales (Hopkins et al., 2016; Roos et al., 2015; Choi et al., 2015; Vogelsberger et al., 2013; Fabian, 2012; Hambrick et al., 2011). Observations of quasars have shown that AGN with typically higher accretion rates ($>$ few percent of the Eddington ratio) are capable of driving molecular and ionised gas outflows with velocities of up to $\sim$ 1000 km s^{-1} or more (Perna et al., 2017;

Liu et al., 2013; Sturm et al., 2011). Radio jets from an AGN, on the other hand, can heat the gas in the intracluster medium (ICM) of clusters of galaxies, therefore preventing the gas from cooling and ultimately preventing future episodes of star formation (Davé et al., 2019; Heckman & Best, 2014; Fabian, 2012; Peterson & Fabian, 2006).

Cosmological simulations often try to model these two forms of AGN feedback (i.e., quasar mode and radio/jet mode). AGN feedback has been modeled in many simulations with varying implementations. Typically, simulations will separate the feedback from the high accretion state, commonly referred to as quasar mode feedback, from the low accretion state feedback, commonly referred to jet or radio mode feedback. How theoretical models distinguish between high and low accretion states also varies from simulation to simulation. Whether AGN feedback imparts thermal or kinetic energy (or some combination of both) on the surrounding gas also depends on the model, as well as the direction in which the feedback is injected. Some simulations treat the AGN feedback as spherical, which makes it highly effective, whereas others explicitly model AGN feedback in the form of bipolar jets that avoid clearing gas near the black hole. While there are many ways to implement AGN feedback, some simulations will try to parametrise black hole growth and AGN feedback based on observations of outflows of molecular and ionised gas (e.g., Perna et al., 2017; Liu et al., 2013; Sturm et al., 2011) as well as observations of radio-loud jets (Fabian, 2012) in galaxies with luminous AGN (Davé et al., 2019). Empirical studies of AGN and star formation activity can guide the implementation of black hole growth and AGN feedback in theoretical models of galaxy evolution by providing important clues on the demographics and distribution of high luminosity AGN, the distribution of high luminosity AGN on the stellar mass-star formation rate plane, and the frequency of high luminosity AGN residing in galaxies with quenched star formation.

1.2 Role of Environment in Galaxy Evolution

It is well established that environment plays an important role in galaxy growth and evolution. Many observational studies over the last several decades have shown that different measures of environment correlate with a multitude of galaxy properties, such as morphology (Norberg et al., 2002; Dressler, 1980; Oemler, 1974), color and luminosity (Hoyle et al., 2012; Hogg et al., 2004; Balogh et al., 2004; Bernardi et al., 2003), star formation rate (Ricciardelli et al., 2014; Rojas et al., 2005), and gas fraction (Meyer et al., 2007), among others. At low redshifts, many 'red and dead' galaxies with low levels of star formation are found in high density environments (Gladders & Yee, 2005), while star-forming galaxies are more commonly found in the field (Dressler, 1980). The differences between galaxies in low and high density environments are often attributed to a combination of nature effects or assembly bias and nurture effects. Within this framework, some of the differences are attributed to galaxies in higher density environments having accelerated evolution due to shorter dynamical and collapse timescales (e.g., accelerated star formation and mass growth) while other differences are assigned to cluster-specific processes that include galaxy-galaxy interactions (e.g., tidal interactions, mergers, harassment), interactions of galaxies with the intra-cluster medium and cluster potential (e.g., ram pressure stripping of cold gas, strangulation, starvation, and virial shock heating) and AGN feedback in the form of radio-loud jets. Such processes are not as prevalent, or present, in lower density environments, thus explaining why star-forming spirals are more likely to be found in the field whereas 'red and dead' ellipticals are more likely to be found in clusters and higher density environments (Dressler, 1980; Oemler, 1974). It should be noted that other physical mechanisms capable of quenching galaxies in the field exist (e.g., strangulation, starvation), however, these mechanisms do not quench star formation as efficiently as some of the aforementioned mechanisms present in high density environments.

At higher redshifts, the relationship between environment and galaxy evolution is less well understood. Some of the trends between galaxy properties and environment found at low redshifts (e.g., decreased star formation activity in higher density environments) appear to extend out to $z \sim 2$ (Etherington et al., 2017; Duivenvoorden et al., 2016; van der Burg et al., 2013). This is currently a topic of debate, however, as other studies find enhanced specific star formation rates in higher density environments at $z \gtrsim 1$ (Elbaz et al., 2007). As a result, few constraints on the role of environment in galaxy evolution exist at higher redshifts.

In order to properly characterize galaxy environment and measure local and large-scale structure, it is necessary to utilize large-area surveys that probe volumes big enough to minimize the effects of cosmic variance and capture a wide range of environments (e.g., clusters, groups, filaments, voids). Spectroscopic redshift surveys are ideal for this purpose as the accurate redshifts are capable of localizing galaxies in 3D, however, such surveys tend to be biased against redder galaxies by selection and suffer from low sampling rates at higher redshifts (e.g., Guzzo et al., 2014). Studies that utilize surveys with highly accurate photometric redshifts, such as COSMOS, are capable of reliably characterizing environment out to higher redshifts (Laigle et al., 2016; Darvish et al., 2015), however, such surveys typically suffer from limited volume, poor Poisson statistics, and cosmic variance due to the small areas (< 2 deg^2) they survey (Moster et al., 2011). For these reasons, studies that extensively analyze trends between galaxy properties and environment have been largely limited to lower redshifts ($z \lesssim 1$). Spectroscopic data from surveys like the Hobby Eberly Telescope Dark Energy Experiment (HETDEX), which targets galaxies across a large volume over a redshift range of $1.9 < z < 3.5$ (Hill et al., 2008), will soon allow for more extensive studies of environment at redshifts around the exciting and dynamic epoch of cosmic noon.

In Chapter 2, I utilize data from a low redshift survey to analyze environ-

mental trends in low-density environments. It is important for our understanding of galaxy evolution to analyze galaxies living in low-density and void-like regions because to they evolve in pristine environments, as opposed to galaxies living in higher density regions which are subject to mergers and other transformative processes. As a result, one can carefully begin to shed light on the balance between nature and nurture in the context of galaxy evolution. Research focused on the galaxy population in low-density regions has revealed that these environments are populated with blue-sequence late-type galaxies (e.g., Bamford et al., 2009; Park et al., 2007; Rojas et al., 2004; Grogin & Geller, 2000, 1999) that are more star-forming and gas-rich than galaxies living in denser environments (e.g., Meyer et al., 2007; Rojas et al., 2005). However, it is currently unclear whether galaxies living in low-density environments are bluer, more star-forming, and more gas-rich at fixed mass and luminosity. Some studies argue that any differences between galaxies in low-density and higher-density environments are simply due to differences between the luminosity and mass distributions found at low versus high density environments (Park et al., 2007; Patiri et al., 2006; Balogh et al., 2004). Other studies, however, argue that void galaxies are intrinsically bluer and more star-forming than galaxies at higher density environments, even at fixed mass or luminosity. My work in Chapter 2 sheds light on this topic by comparing galaxies in low and higher density environments at fixed stellar mass, baryonic mass, and morphology, and by comparing the empirical results to theoretical models of galaxy evolution with built-in assembly bias. These comparisons are critical for guiding the development of future theoretical models of galaxy evolution.

When the HETDEX spectroscopic survey is capable of providing redshifts for a large number of galaxies near cosmic noon, it will be possible to apply the environmental metrics developed in Chapter 2 to galaxies across a large volume at $z = 1.9 - 3.5$. I had previously attempted to apply the environmental metrics de-

veloped in Chapter 2 to data in the SHELA field at higher redshifts $z > 1$, however, the poor quality of photometric redshifts and lack of spectroscopic redshifts made it very difficult to characterize environment. Applying the environment metrics developed in Chapter 2 to the data from the SHELA field will eventually allow one to study the interplay between AGN, star formation activity, and environment at cosmic noon.

1.3 Thesis Overview

In this thesis, I utilize photometric data from various wide-field surveys targeting the Stripe 82 region on the sky in order to explore: (i) The relation between galaxy properties and environment (ii) The connection between AGN and star formation activity in massive galaxies at cosmic noon using one of the largest samples of massive galaxies to-date.

In Chapter 2 I show that galaxies living in low-density environments have, on average, bluer colors, higher star formation rates, and higher gas fractions than galaxies living in higher density environments, with such trends persisting at fixed mass and morphology. I compare these results to models of galaxy evolution with built-in assembly bias and find that matching galaxy properties to sub-halo properties can recover observed environmental trends in the local Universe. In Chapter 3, I show that massive galaxies with high X-ray luminosity AGN have higher star formation rates, on average, than galaxies without such AGN at fixed stellar mass at cosmic noon. I also show that the majority ($> 95\%$) of galaxies with high X-ray luminosity AGN do not have quenched star formation. Lastly, in Chapter 4, I compare the empirical results to theoretical models of galaxy evolution in order to constrain the development of such models. Such comparisons are made possible by advancements made in this thesis, which are discussed below.

1.3.1 Selection of Galaxies with and without High X-ray Luminosity AGN

In order to identify galaxies with and without high X-ray luminosity AGN, I utilize wide and deep multiwavelength photometry obtained over an ~ 11.8 deg^2 region of the Sloan Digital Sky Survey (SDSS) Stripe 82 where the Stripe 82X and *Spitzer*-HETDEX Exploratory Large Area footprints overlap. This includes photometry from Stripe 82X XMM-Newton (X-ray; LaMassa et al., 2016), Dark Energy Camera (DECam *ugriz*; Wold et al., 2019), NEWFIRM (near-infrared; Stevans et al., 2021), and IRAC (mid-infrared; Papovich et al., 2016). This data set offers numerous advantages: (i) The various deep photometric filters spanning UV to mid-infrared wavelengths provide enough wavelength coverage to estimate photometric redshifts, stellar masses, and star formation rates for a large sample of galaxies with and without high X-ray luminosity AGN. (ii) The large area corresponds to a very large comoving volume of ~ 0.3 Gpc^3 at $z = 0.5 - 3.0$ that captures a large number of galaxies with high X-ray luminosity AGN and high stellar mass and makes the uncertainties due to cosmic variance negligible.

The large samples of galaxies yielded by the photometric data sets mentioned above allow for novel studies of rare populations of galaxies. In Chapters 3 and 4 I compute the stellar mass functions, stellar mass-star formation rate relations and quenched fractions of galaxies with and without high X-ray luminosity AGN out to high stellar masses ($M_* \sim 10^{12}$ $M_\odot$), and with robust number statistics above $M_* \sim 10^{11}$ $M_\odot$ relative to other studies of galaxy evolution at similar redshifts. Similarly, the X-ray data we use here allows us to sample the X-ray luminosity function uniformly out to the highest X-ray luminosities ($L_X \sim 10^{45-46}$ erg s^{-1}).

1.3.2 SED Fitting: Methods and Testing Reliability of Output

As stated in Section 1.2, one must carefully account for the emission of AGN activity in the SED fitting of galaxies with high X-ray luminosity AGN. If one does not model the AGN emission of a galaxy with a luminous AGN component during SED fitting, one could easily overestimate the star formation rate or stellar mass of the galaxy as UV, optical, and mid-infrared emission from the AGN is mistakenly attributed to stellar emission and star forming processes. Very few SED fitting codes model AGN emission, and those that do are normally not suited for SED fitting of galaxies without X-ray luminous AGN as they will try to model an AGN component in the SED where none may exist. In this thesis, I use the novel SED fitting code CIGALE (Boquien et al., 2019; Ciesla et al., 2015; Noll et al., 2009) to obtain stellar masses and star formation rates for galaxies with and without high X-ray luminosity AGN. Several studies have used CIGALE to analyze the star forming properties of galaxies with high X-ray luminosity AGN, however, prior to the study we perform in Chapter 3 (Florez et al., 2020), none had used it to self consistently analyze galaxies with and without high X-ray luminosity AGN. Most studies, in fact, normally measure star formation rates and stellar masses for galaxies with and without high X-ray luminosity AGN using different methods or SED fitting procedures (e.g., Masoura et al., 2018; Shimizu et al., 2017, 2015; Santini et al., 2012).

One of the primary advantages of using CIGALE is that it allows the user to optionally include AGN emission templates in the SED fitting procedure. I leveraged this to run the same SED fitting code on a large sample of galaxies with and without high X-ray luminosity AGN and self-consistently obtain stellar masses and star formation rates for both types of galaxies. Since no previous studies had used CIGALE for this purpose, I had to ensure that the derived quantities were reliable by performing numerous tests and consistency checks. First, I compare the CIGALE-derived star formation rates for a group of high X-ray luminosity AGN

selected from the CANDELS field to the star formation rates presented in Yang et al. (2019, 2017). Next, I compare CIGALE-derived star formation rates to the true internal star formation rates for a group of mock galaxy SEDs. Lastly, I compare CIGALE-derived star formation rates and stellar masses to those derived by EAZY-py and find that they are consistent to within a factor of $\sim 3-4$ and a factor of ~ 2, respectively. These consistency checks help determine the robustness and validity of our SED fitting procedure.

1.3.3 Detailed Comparisons to Theoretical Models of Galaxy Evolution

In numerical simulations and theoretical models of galaxy evolution, AGN and star formation activity are closely linked and AGN feedback is invoked to regulate galaxy growth. However, few empirical tests exist on how well the models and simulations implement the growth of black holes and the interplay between AGN and star formation. In Chapter 4 I address this issue by comparing the hydrodynamical simulations IllustrisTNG (Pillepich et al., 2018; Springel et al., 2018; Nelson et al., 2018; Naiman et al., 2018; Marinacci et al., 2018) and SIMBA (Davé et al., 2019), and the semi-analytical model SAG (Cora et al., 2018) to the empirical results on AGN and star formation at cosmic noon reported in Chapter 3. The different theoretical models I analyze in Chapter 4 each have their own benefits and disadvantages. For instance, the hydrodynamical simulations IllustrisTNG and SIMBA each implement detailed physical processes to follow galaxy evolution across cosmic time. While such simulations can give rich detail on the physical quantities present in their simulated galaxies, these models are run on small volumes limited by the effects of cosmic variance and Poisson statistics. In contrast, semi-analytic models (e.g., SAG, SAGE (Croton et al., 2016), and Galacticus (Benson, 2012)) implement prescriptions of galaxy formation on dark matter halo merger trees to populate a

large volume dark-matter-only simulation. Similarly, abundance matching models will match observed galaxy properties to dark matter halos to populate dark-matter-only simulations. These methods are not computationally expensive, however, their implementations of galaxy physics are simplified relative to hydrodynamical simulations.

Chapters 2 and 4 make detailed comparisons of the empirical results obtained in this work with different classes of theoretical models. In Chapter 2, I show that abundance matching models with built-in assembly bias are better at recovering environmental trends than abundance matching models that do not have built-in assembly bias. In Chapter 4 I show how theoretical models of galaxy evolution compare to the empirical results on the AGN and star formation connection at cosmic noon and discuss how such models can be modified to give better agreement with the empirical results, especially in the context of black hole growth and AGN feedback.

1.3.4 Environmental Metrics

The large areas probed by the data sets used in this thesis are ideal for studies of environment. Such large areas correspond to large volumes that yield a wide range of environments, including voids, filaments, groups of varying sizes, and massive clusters of galaxies. In Chapter 2, I utilize the Environmental COntext (ECO) survey, a volume-limited survey complete with spectroscopic redshifts and complete in luminosity at an absolute r-band magnitude brighter than $M_r < -17.33$, to study and analyze galaxies living in low-density and void-like environments. I discuss the method I develop for identifying void galaxies, which is based on a third nearest neighbor metric, and then compare the properties of void and non-void galaxies. I perform numerous comparisons of void and non-void galaxies at fixed stellar mass, at fixed baryonic mass, and at fixed morphology to determine whether void galaxies

have intrinsically different properties than non-void galaxies or if any differences can be attributed due to differences between mass and morphology distributions in low-density and higher-density environments.

In Chapter 2 I also make comparisons of the observational quantities to abundance-matching models with built-in assembly bias. Such comparisons are useful for developing and formulating semi-empirical models of galaxy evolution. I discuss the implications of these results and to what extent environment plays a role in galaxy evolution towards the end of Chapter 2.

Chapter 2

Void Galaxies Follow a Distinct Evolutionary Path in the Environmental Context Catalog

2.1 Introduction

Galaxies that live in low-density and void-like regions are ideal for studies of galaxy evolution due to the pristine environment in which they grow[1]. Mergers and other transformation processes that are common in clusters, such as ram-stripping, are far less present in low-density regions. By studying the galaxies that occupy these void-like regions, one can begin to uncover the careful balance between nature and nurture in the context of galaxy formation.

Cosmological simulations have shown that halos in voids are less massive and that halo structure is largely dependent on environment (Avila-Reese et al., 2005; Wechsler et al., 2006; Jing et al., 2007; Gao & White, 2007; Bett et al.,

[1]The work presented in this chapter was published in the Astrophysical Journal (ApJ) on January 13, 2021 (see Florez et al. 2021, ApJ, 906, 97). As first author, I contributed by writing the paper and performing the full scientific analysis presented therein.

2007). Fakhouri & Ma (2009, 2010) found that the dark matter merger rate has a strong correlation with environmental density; mergers dominate dense regions while diffuse accretion dominates halo growth in voids, thus explaining why voids in the dark matter distribution tend to be occupied by low-mass halos. For a long time, voids in dark matter simulations struggled to reproduce the observed spatial distribution of voids in surveys (Peebles, 2001). Tinker & Conroy (2009), however, were able to demonstrate that void properties are well described in the context of ΛCDM by assuming that the luminosity of galaxies is a function of the host dark matter halo mass and is independent of the large-scale halo environment.

Extensive research has been done on the environmental dependence of galaxy properties in dense regions and clusters. Oemler (1974) and Dressler (1980) were some of the first to show that there exists a morphology-density relation in the distribution of galaxies, especially at higher densities. Over a decade of research has shown that galaxies in high-density regions are much more luminous and redder than those in low-density environments (e.g., Bernardi et al., 2003; Balogh et al., 2004; Hogg et al., 2004). Thanks to the wealth of data that now exist due to the advent of large redshift surveys, it has become possible to study galaxies in lower density environments in great detail. Research focused on the galaxy population in low-density regions has revealed that these environments are populated with blue-sequence late-type galaxies (e.g., Grogin & Geller, 1999, 2000; Rojas et al., 2004; Park et al., 2007; Bamford et al., 2009) that are more star-forming and gas-rich than galaxies living in denser environments (e.g., Rojas et al., 2005; Meyer et al., 2007).

Although the distributions of observable galaxy properties are largely dependent on mass and luminosity, current studies conflict over whether or not these properties depend on environment at fixed mass or luminosity. Balogh et al. (2004) proposed that the star formation of a galaxy is dependent on intrinsic properties, such as luminosity, and is independent of environment. Patiri et al. (2006) found

that the void galaxy property distributions are very similar to non-void galaxies and that there are no strong systematic differences in specific star formation rates between void and non-void galaxies. Similarly, Park et al. (2007) found that variations between galaxy properties with different environments were almost entirely due to differences in the luminosity and morphology distributions. More recent work done by Ricciardelli et al. (2014), however, presents evidence of void galaxies forming stars more efficiently than a control sample of the same stellar mass distribution. They show that larger voids have enhanced star formation activity in the shells surrounding the voids when compared to the smaller voids; however, they interpret this result as possibly being due to differences in dynamical evolution experienced by different sized voids. Additionally, work done by Hoyle et al. (2012) has found that void galaxies are statistically bluer than galaxies of the same magnitude distribution found in higher density environments and that both late and early type galaxies are bluer in voids.

In a ΛCDM universe, it is well established that the clustering of dark matter halos is a strong function of halo mass (e.g. Mo & White, 1996). However, the clustering of halos is also known to depend on other properties like formation history (Gao et al., 2005) and correlated properties like concentration, spin, and measures of local environment (Wechsler et al., 2006; Gao & White, 2007; Mao et al., 2018). Generally, halos that assembled at later times are found to be less clustered than halos of equal mass that assembled at earlier epochs, with the difference in clustering typically being most significant in lower-mass halos. This effect is referred to as "halo assembly bias".

Environment is found to have a particularly strong correlation with the formation time of halos: lower density environments are populated by halos that assembled at later times compared to halos of the same mass living in higher density environments (Fakhouri & Ma, 2009, 2010). However, it remains unclear, what

effect, if any, halo assembly history has on galaxy properties at fixed halo mass; therefore, it is not clear if galaxies also reflect assembly bias, hereafter a phenomena referred to as "galaxy assembly bias". Nevertheless, if the structural properties of halos are correlated with large-scale environment through halo assembly bias, then it seems at least plausible that the correlation that exists between galaxy properties and large-scale environment is also due in part to assembly bias.

Studies that have included galaxy assembly bias have generally concluded that galaxy assembly bias is required in order to explain the observed colors and star formation rates of galaxies in semi-analytic models (Croton et al., 2007) and abundance matching (Zentner et al., 2014; Hearin et al., 2014), although see Zu & Mandelbaum (2018) for a conflicting result. There is even evidence for galaxy assembly bias in cosmological hydrodynamical simulations of galaxy formation where assembly bias is not explicitly modelled (Tonnesen & Cen, 2015).

In this paper we aim to investigate whether void environment plays any role in galaxy formation beyond simply providing different mass and morphology distributions. We use an Nth nearest neighbor method to define our void sample and provide an argument for using this method over Voronoi tessellations when defining a low density sample. We examine the effect of void environment on color, star-formation, gas content, and morphology in observations and we compare to the effect of void environment on color, star-formation, and gas content in a theoretical simulation.

The work is structured as follows. In Section 2 we introduce the data sets, observable properties, and environment metrics that are used for the analysis presented in this work. In Section 3 we present our findings on the properties of galaxies in voids. In Section 4 we compare our results to simulations designed to test assembly bias. Finally in Section 5 we present our conclusions.

2.2 Data and Methods

2.2.1 ECO/RESOLVE

The Environmental COntext (ECO) catalog, a survey of $\sim 13,000$ "local" galaxies with $z \leq 0.023$, is the sample considered for this work (see Moffett et al. (2015) for original survey catalog description and Eckert et al. (2016) for updated catalog photometry and galaxy properties). ECO was constructed to act as a "context survey" for the REsolved Spectroscopy Of a Local VolumE (RESOLVE) survey (Kannappan et al. in prep; Eckert et al., 2015; Stark et al., 2016) in order to calibrate the effects of cosmic variance in large-scale structure. The goal of RESOLVE is to survey and study the stellar mass, baryonic mass, gas-to-stellar mass ratio, star-formation, and dynamical mass of galaxies in a volume-limited census in the local universe by combining photometric and spectroscopic data spanning multiple wavelength regimes.

The ECO region spans a right ascension (RA) range between 130.05 to 237.45 degrees, a declination (DEC) range between -1 and 49.85 degrees, and a line-of-sight velocity range between 2,530 and 7,470 km/s. The region encompassed by ECO on-sky lies where the Updated Zwickly Catalog (UZC; Falco et al. 1999) and Sloan Digital Sky Survey (SDSS; York et al. 2000) redshifts overlap. The ECO region encloses the A-semester of the RESOLVE survey and incorporates redshifts from the RESOLVE, HyperLEDA (Paturel et al., 2003), GAMA (Driver et al., 2011), 2dF (Colless et al., 2001), and 6dF (Jones et al., 2009) surveys. The majority of ECO galaxies are present in SDSS, while $\sim 7\%$ of galaxies are added to the final catalog from other sources. We use a volume-limited sample that is complete in absolute magnitude ($12,698$ galaxies with $M_r < -17.33$) in order to define environment metrics, however, we use a volume-limited sample complete in baryonic mass for our analysis. The ECO galaxy sample is complete in stellar mass at $M_* > 10^{9.1} M_\odot$, having $7,448$ objects with stellar masses above this limit and complete in baryonic mass at $M_b > 10^{9.3} M_\odot$ (Moffett et al., 2015), having $9,526$ objects with baryonic

masses above this limit. We decide to use a baryonic-mass complete sample for this analysis because we are specifically interested in examining how environment affects the baryonic properties of void galaxies. Throughout the analysis we assume $H_0 = 70$ km s^{-1}Mpc^{-1}, and we calculate distances using $D = cz/H_0$.

2.2.2 Photometric Data & Morphologies

For the analysis presented in this paper, we wish to examine properties such as color, gas-to-stellar mass ratio, baryonic & stellar mass, and fractional stellar mass growth rate (FSMGR). Galaxy properties and photometric data are described by Moffett et al. (2015) and Eckert et al. (2016) for the ECO catalog and by Eckert et al. (2015) for the RESOLVE catalog. ECO stellar masses and colors are derived via spectral energy distribution (SED) fitting (see Kannappan et al., 2013, for description of SED fitting procedure). The colors we use here are corrected for internal extinction and have k-corrections implicitly included.

Morphological classifications for ECO are determined from a combination of by-eye classifications and a method that exploits the relation between magnitude and the μ_Δ metric described in Kannappan et al. (2013) which combines the overall surface mass density with a surface mass density contrast. We refer the reader to Moffett et al. (2015) for a full description of how morphologies are derived for all galaxies in ECO.

The FSMGR quantity, described in Kannappan et al. (2013), is a property similar to the specific star formation rate (sSFR) of a galaxy. The FSMGR quantity is defined as FSMGR $\equiv M_{<\mathrm{Gyr}}/M_{>\mathrm{Gyr}}$, where $M_{<\mathrm{Gyr}}$ is the stellar mass of a galaxy that has formed in the previous Gyr, and $M_{>\mathrm{Gyr}}$ is the stellar mass that formed prior to the last Gyr. The sSFR of a galaxy, on the other hand, has the total stellar mass in the denominator meaning its numeric value can never exceed a value of 1, unlike FSMGR which can reach values of up to ~ 10 for highly star forming galaxies.

2.2.3 Baryonic Properties of ECO Galaxies

In ECO, HI data exist for $\sim$ 44% of all galaxies. HI data, and therefore HI gas masses, for ECO galaxies are obtained from the RESOLVE survey (Stark et al., 2016) and the public Arecibo Legacy Fast ALFA (ALFALFA) $\alpha.40$ catalog (Haynes et al., 2011). We consider an HI detection to be robust if it is not confused (i.e., there are no nearby neighbors that could contaminate or confuse the detection) and if it has a signal-to-noise ratio greater than 4. For ECO galaxies lacking robust HI detections, we resort to indirect methods to obtain the gas masses. The gas-to-stellar mass ratio of an ECO galaxy can be determined from a photometric gas fraction (PGF) relation calibrated with the RESOLVE survey (see Eckert et al., 2015, for full description of PGF technique).

The PGF technique takes advantage of the relation between galaxy color and the $M_{\rm HI}/M_*$ gas fraction (Kannappan, 2004). For a galaxy's given color, a probability distribution of gas-to-stellar mass ratios can be made. We use these probability distributions to determine the predicted gas and baryonic masses of galaxies. To derive the predicted HI mass, we implement the $(u-J)$ & b/a color calibration from Eckert et al. (2015) and obtain gas-to-stellar mass ratio distributions for each galaxy. The median of a galaxy's gas-to-stellar mass ratio probability distribution is used to assign a value of $M_{\rm HI}/M_*$ to that galaxy, and the predicted HI mass is then derived from that value using the stellar mass from SED fitting. We multiply all HI gas masses, real or predicted, by a factor of 1.4 to account for Helium. Therefore, all values of gas mass presented in this paper are given by $M_{\rm gas} = 1.4 \times M_{\rm HI}$.

We compute baryonic masses by adding M_* to $M_{\rm gas}$, where $M_{\rm gas}$ is computed from either the PGF technique or HI data depending on the strength of the HI detecion. We can compare a galaxy's predicted baryonic mass to its real baryonic mass if the galaxy has an HI detection either from the RESOLVE or ALFALFA surveys. The RESOLVE HI masses are obtained via 21cm data (Stark et al., 2016),

and the RESOLVE-A region is only 78% complete in HI when counting strong, unconfused detections (i.e. detections that have a signal-to-noise of $SN > 4$ and do not appear contaminated by nearby sources). We show the comparison between real and predicted baryonic masses in Figure 2.1. The error introduced by using a predicted baryonic mass diminishes towards higher masses, as the more massive galaxies are quenched and have baryonic masses that are dominated by the stellar mass. We measure the scatter to be ~ 0.23 dex at lower baryonic masses ($10^{9.3} M_{\odot} < M_{b,\mathrm{real}} < 10^{10.3} M_{\odot}$) and ~ 0.09 at higher baryonic masses ($M_{b,\mathrm{real}} > 10^{10.3} M_{\odot}$).

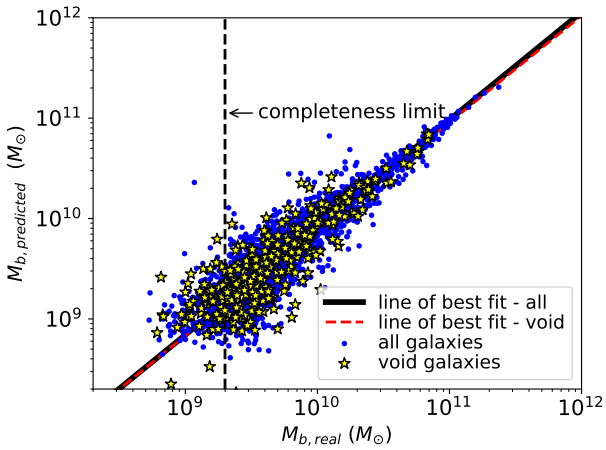

Figure 2.1: The true baryonic mass for ECO galaxies with gas mass detections (x-axis) vs. the predicted baryonic mass derived from the PGF technique (y-axis). Void galaxies are shown as yellow stars while the rest of the sample is shown as blue circles. Also shown is the line-of-best fit, from a least squares regression, for void galaxies (red, dashed) and for all galaxies (black, solid). The line of best fit is only measured for galaxies with a baryonic mass above the completeness limit ($M_b > 10^{9.3} M_{\odot}$)

2.2.4 Environment Metrics

For the analysis described in this paper, we use an Nth nearest neighbor metric to measure the local galaxy density. We adopt $N = 3$ when estimating densities with

the Nth nearest neighbor method. We also performed the analysis using $N = 3, 4, 5,$ and 10, however, there were no major variations in the results of the analysis. In order to achieve robust statistics for our analysis, we assign void status to the 10% of galaxies with lowest local density. We discuss this choice of method for selecting void galaxies in detail below.

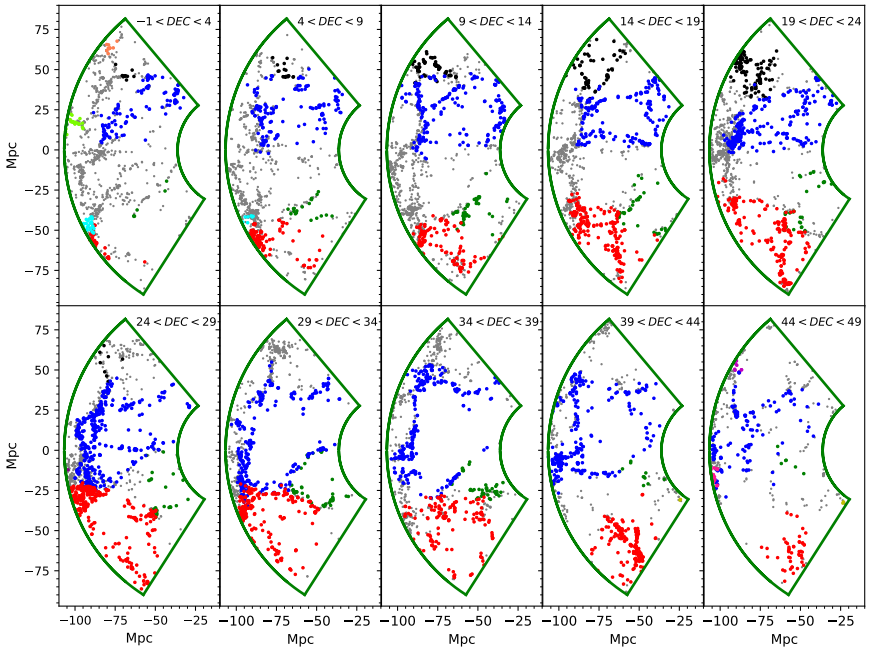

Figure 2.2: The ECO sample in 5° thick Dec slices increasing from the top left panel, in Cartesian coordinates. The top 10 percent most statistically significant voids identified by the ZOBOV algorithm are shown here, with each non-gray color representing a different void. All other galaxies are shown as gray points. It is clear that many galaxies that are classified as belonging to voids are actually in high density regions.

Redshift Distortion Corrections

We implement velocity corrections to the data in order to ensure that our density estimation is less sensitive to finger-of-god effects, such as lower density estimates for galaxies in large groups or cluster galaxies bleeding into voids. First, we run the Berlind et al. (2006) friends-of-friends (FoF) group finder on the ECO data to determine group membership of the galaxies. The choice of FoF linking lengths are motivated by the work done in Eckert et al. (2016) and Duarte & Mamon (2014) who find optimal values of the linking lengths for the study of group-finding and environment. We determine the galaxy type (i.e. central or satellite) for each galaxy in the observation based on the galaxy's r-band absolute magnitude. The central galaxy is, by definition, the brightest galaxy in the galaxy group. We then "collapse" the fingers of god by correcting the velocities of satellite galaxies. The correction process uses real-space and redshift-space versions of mock galaxy catalogs to recover the true radial distribution of galaxies in real space (see Moffett et al., 2015, for complete description of velocity corrections).

We select void galaxy samples with and without finger-of-god corrections and find that 1,044 out of 1,270 galaxies (82%) remain in both void galaxy samples applied to the ECO data. We have performed the analysis of this paper with the void galaxy sample selected from the ECO coordinates that do not have the finger-of-god corrections and find the results remain largely the same. Nonetheless, we keep the finger-of-god corrections in the analysis as this helps prevent cluster and group galaxies from falsely being classified as void galaxies.

Void Classification

In order to designate void status for a given galaxy, we need a way to quantify each galaxy's local density in ECO. We initially experimented with the publicly available void-finding algorithm ZOBOV (Neyrinck, 2008) to find voids, but found that edge

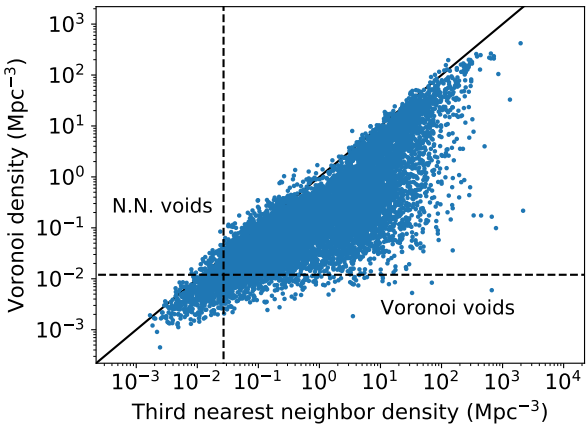

Figure 2.3: Voronoi densities (y-axis) vs. third nearest neighbor densities (x-axis) of the ECO galaxy sample. The cut for void galaxies (indicated by the dashed lines) was arbitrarily chosen to categorize $\sim 10\%$ of galaxies with the lowest densities as void galaxies by both methods.

effects and having a low galaxy density often returned large spurious voids. The ZOBOV algorithm uses Voronoi tessellations to estimate local densities for galaxies and uses those densities to find density depressions in the sample volume. Because ZOBOV is designed to measure a void's shape and size, it includes galaxies living along the void border in its void definition. The problem with galaxies bordering the voids in ZOBOV is that those galaxies also border clusters and filaments, and often have relatively high local densities. We illustrate this in Figure 2.2, which shows void galaxies found by ZOBOV. In order to exclude the void borders from our void definition, we decided to apply a density cut to the galaxies located inside the ZOBOV voids in order to create a better void sample. Since the majority of galaxies with low Voronoi densities also live in ZOBOV voids, the void sample remains essentially the same if one applies a density cut to the Voronoi densities of the entire sample of galaxies instead of just the ZOBOV void galaxies. For comparison purposes, we also estimate densities for galaxies using Nth nearest neighbor distances

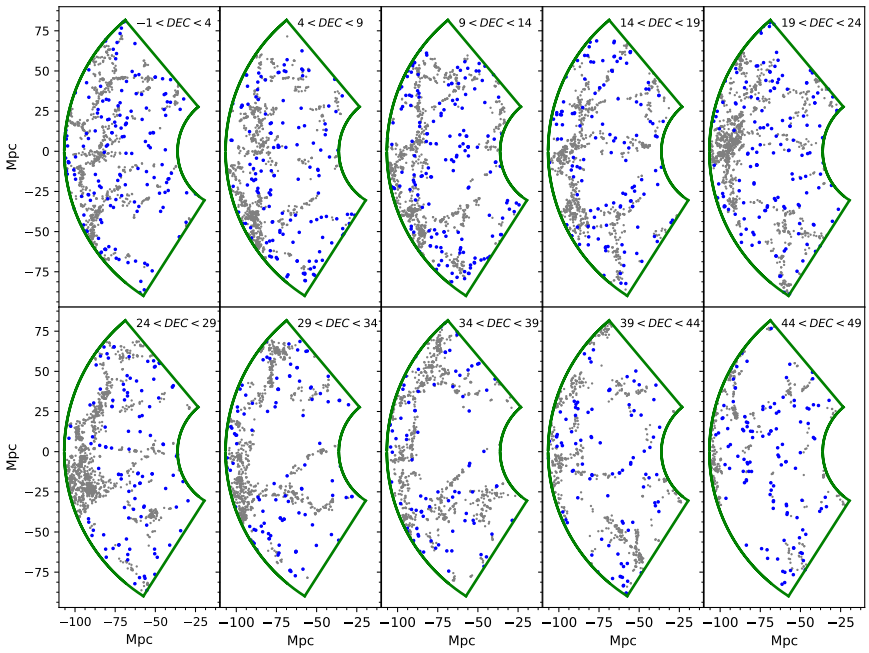

Figure 2.4: Similar to Figure 2.2, the ECO sample is shown here in 5 ° thick Dec slices increasing from the top left panel. All void galaxies found by the Nth nearest neighbor algorithm are shown in blue, while non-void galaxies are shown as gray points.

(adopting N=3) and, in both cases, we define void galaxies as the 10% of galaxies having the lowest density, which yields a statistically significant void sample.

Figure 2.3 directly compares the two methods for estimating density. The comparison reveals that some galaxies can have a low Voronoi density while having a high Nth nearest neighbor density, while the opposite does not hold for galaxies with low Nth nearest neighbor densities. A galaxy can be falsely classified as a void galaxy through the Voronoi tessellation method if that galaxy lives on the border of a cluster or filament because its Voronoi cell will extend into the void, thus having a large volume and a low corresponding density. In contrast, the Nth nearest neighbor density of such a border galaxy will be high. In Figures 2.2 and 2.4, we show void galaxies chosen from both methods. In Figure 2.2, we show void galaxies in the top 10 percent most statistically significant voids identified by ZOBOV. We clarify that this figure includes all galaxies in a given ZOBOV void region, as opposed to the void galaxies chosen by our lowest tenth percentile density cut. Even in the most statistically significant voids, it appears by-eye that many of the ZOBOV void galaxies live in high density regions. This is especially evident in the top right three panels of Figure 2.2. In Figure 2.4 we show the entire void and non-void galaxy sample chosen by our Nth nearest neighbor metric. It is evident in Figure 2.4 that void galaxies chosen via our Nth nearest neighbor method appear to avoid regions of high density, as opposed to void galaxies identified by ZOBOV.

Given these results, we select the Nth nearest neighbor metric (with $N = 3$) to define our void sample. We note that our void definition recovers galaxies that can either be completely isolated or exist in groups of two or three, and a few of the void galaxies even appear to be arranged in thin filamentary-like structures known as tendrils (see Beygu et al., 2013; Alpaslan et al., 2014). Although we choose our void definition based on $N = 3$, the majority ($> 90\%$) of our void galaxies exist in FoF groups of $N = 1$.

The threshold for selecting void galaxies for this analysis is exactly the lowest 10% of galaxies ranked in density, selected from the entire sample of 12,698 ECO galaxies above the luminosity completeness limit ($M_r < -17.33$). This corresponds to a third nearest neighbor density ρ_{void} of less than 0.02 galaxies Mpc^{-3} for the void galaxy sample. The mean third nearest neighbor distance density $\bar{\rho}$ of the entire ECO volume is 0.76 galaxies Mpc^{-3}, meaning the density contrast for the void sample is $\delta < -0.97$, where $\delta = \rho/\bar{\rho} - 1$.

We do not account for edge effects in this study, however, it is important to assess the impact this has on our analysis. To address this, we create a "buffered" subsample of ECO data inside the RA, DEC, and line-of-sight velocity limits listed in Section 2.2.1 for all of ECO and rerun our void finding algorithm. The buffered region we create is the same as that from Moffett et al. (2015), which was specifically designed to mitigate edge effects that arise when computing galaxy environment metrics. The subsample of ECO data we create is 2.4 degrees smaller in RA, leaving a buffer of 1.2 degrees from each edge in RA, 2 degrees smaller in DEC, leaving a buffer of 1 degree from each edge in DEC, and 940 km/s shorter in line-of-sight velocity distances, corresponding to a line-of-sight velocity range of 3,000 to 7,000 km/s. These limits were chosen to ensure that the ECO subsample has a buffer region of at least 1 Mpc in all directions, with an additional allowance of ~ 5.7 Mpc in the line-of-sight velocity distances to compensate for group peculiar velocities that extend up to 400 km/s (Moffett et al., 2015).

The subsample of ECO data we create has a total of 9,359 galaxies complete in absolute magnitude ($M_r < -17.33$) and a total of 936 void galaxies above this limit, corresponding to the lowest 10% of galaxy densities. Of these 936 void galaxies in the buffered subsample of ECO, 877 (93.6%) are in the original (full) ECO sample. We find that the results of this paper do not change when we perform our analysis on the buffered subsample of void galaxies. We therefore decide to keep our original

sample of 1,270 void galaxies, for this analysis.

2.3 Results

In Section 2.3.1 we examine the observable properties of the void sample and compare them to those of the non-void sample. In sections 3.2 & 3.3 we investigate whether the different mass or morphology distributions of the samples drives the differences we see between void and non-void galaxies.

2.3.1 Observed Properties of Void Galaxies

In Figure 2.5 we show the baryonic mass distribution of the void and non-void galaxy sample. The samples have different mass distributions, with void galaxies being less massive on average than non-void galaxies. Our results show that void galaxies rarely have masses greater than $10^{10.6} M_{\odot}$. The void galaxy distribution has an excess in baryonic masses below $10^{9.8} M_{\odot}$ and a deficiency in masses above $\sim 10^{10} M_{\odot}$ when compared to the baryonic mass distribution of all ECO galaxies. While not shown here, we find a similar trend when comparing the stellar mass distributions of the void and non-void galaxy samples.

In Figure 2.6 we examine normalized histograms of void and non-void galaxy properties in ECO and RESOLVE. We show the RESOLVE A semester catalog data in the top panels as it has real HI masses derived from 21cm data and compare that with ECO data in the bottom panels. We impose a cut of $Dec. > 5^{\circ}$ in ECO for this figure only so that the top panels contain and display independent information.

The histograms show that the ECO void galaxies are bluer, more star-forming, and more gas-rich than their non-void counterparts. RESOLVE shows qualitatively similar results, though they are much noisier due to the smaller size of that sample. We perform an Anderson-Darling (AD) k-sample test between the void and non-void galaxy property distributions for each panel shown in Figure 2.6

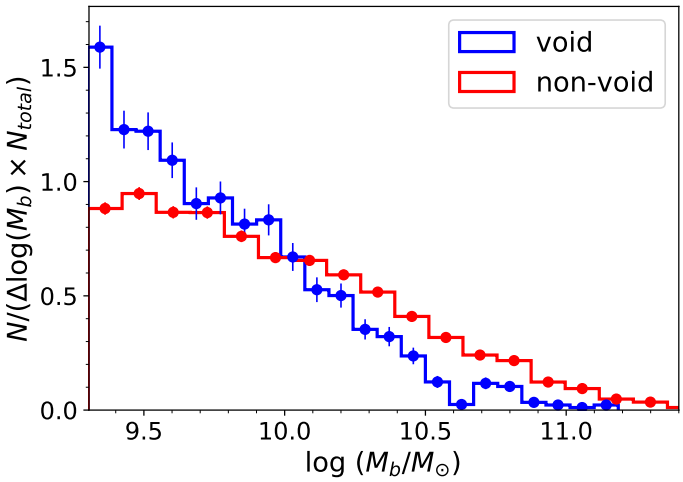

Figure 2.5: Normalized histogram of the baryonic mass distribution of galaxies in ECO for void galaxies (blue) and non-void galaxies (red) above the completeness limit with Poisson errors.

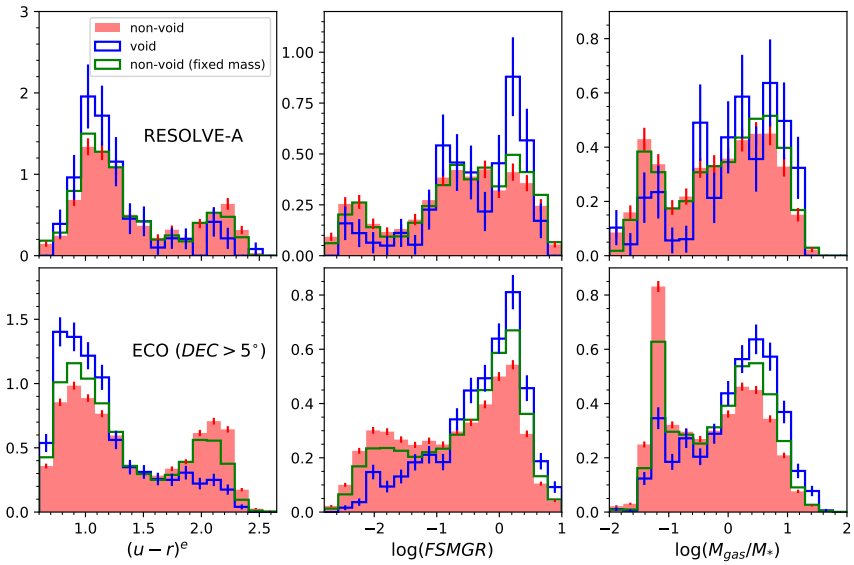

Figure 2.6: This figure shows normalized histograms of color, FSMGR, and $M_{\rm gas}/M_*$ for void (blue) and non-void galaxies (red) in the RESOLVE-A semester (top) and ECO at $Dec. > 5°$ (bottom). The green line represents a sample of non-void galaxies with a baryonic mass distribution that matches that of the void galaxy sample. In the top panels, values of $M_{\rm gas}$ come primarily from observations whereas in the bottom panels values of $M_{\rm gas}$ come from a combination of observed and predicted gas masses (see Section 2.3). All the data shown here is complete in baryonic mass above $M_b = 10^{9.3} M_\odot$.

using the `scipy.stats` package from the SciPy library (Virtanen et al., 2020). We show the results of the test in Table 2.1 and note that p-values are capped at values of 0.001 and 0.25, so p-values above (below) 0.25 (0.001) are only quoted as lower or upper limits. The results of the AD test show that the differences between void and non-void galaxy properties are statistically significant. The two left panels of Figure 2.6 comparing $(u-r)^e$ colors between void and non-void galaxies can be compared to Figure 3 of Hoyle et al. (2012), which shows that void galaxies are statistically bluer than non-void galaxies. These results are not surprising, since void galaxies are less massive and there are well established correlations between mass, color, and gas content, with lower mass galaxies having higher gas fractions (Kannappan, 2004), higher specific star formation rates (Bauer et al., 2005), and bluer colors (Baldry et al., 2004; Dressler, 1980; Hoyle et al., 2012). The interesting question is whether these differences persist at fixed mass.

RESOLVE-A		
galaxy property	AD statistic	p-value
$(u-r)^e$	5.95	0.002
log(FSMGR)	4.15	0.007
$\log(M_{\rm gas}/M_*)$	3.91	0.009
ECO		
galaxy property	AD statistic	p-value
$(u-r)^e$	99.19	≤ 0.001
log(FSMGR)	107.23	≤ 0.001
$\log(M_{\rm gas}/M_*)$	104.58	≤ 0.001

Table 2.1: Test statistic and p-values of the Anderson-Darling (AD) k-sample test performed between the void and non-void galaxy property distributions shown in Figure 2.6. Results are shown for both the ECO and RESOLVE-A semester samples.

2.3.2 Are Void Galaxies Different at Fixed Mass?

We move on to investigate how the properties of void galaxies differ from non-void galaxies when controlling for mass. Referring again to Figure 2.6, we compute histograms for a sample of non-void galaxies that have the same baryonic mass distribution as the void sample. To generate these histograms, we first determine the baryonic mass distributions of the void and non-void samples (shown in Figure 2.5). We then randomly sample from the non-void galaxies with a probability that is proportional to the ratio of the mass distributions in order to build a sample of non-void galaxies with a mass distribution identical to that of the void galaxies. During the random sampling, we check to make sure that a galaxy isn't sampled twice. This process is then repeated 1000 times so that we end up with 1000 samples of non-void galaxies with a void-like mass distribution. The property distributions are all averaged together to generate the green histograms shown in Figure 2.6.

We find that differences between void and non-void galaxies persist when controlling for mass. The void galaxy sample is bluer, more gas-rich, and has higher FSMGR when compared to the mass-matched non-void galaxy sample, despite having the same mass distribution. We note that the difference between the void (blue histograms) and mass-matched non-void (green histograms) galaxy samples is due to environment, while the difference between the mass-matched non-void (green histograms) and unaltered non-void (red histograms) samples is due to baryonic mass. We find that the mass-matched non-void histograms in ECO and RESOLVE-A decrease with respect to the void histograms, in fixed bins, by a factor of ~ 0.2 to 0.5 at bluer colors, higher FSMGRs, and higher gas fractions. The mass-matched non-void histograms increase with respect to the void histograms, in fixed bins, by a factor of $\sim 1-3$ at redder colors, lower FSMGRs and lower gas fractions. As in Section 2.3.1, we perform an AD k-sample test between the void and mass-matched non-void galaxy property distributions for each panel in Figure 2.6 and present the

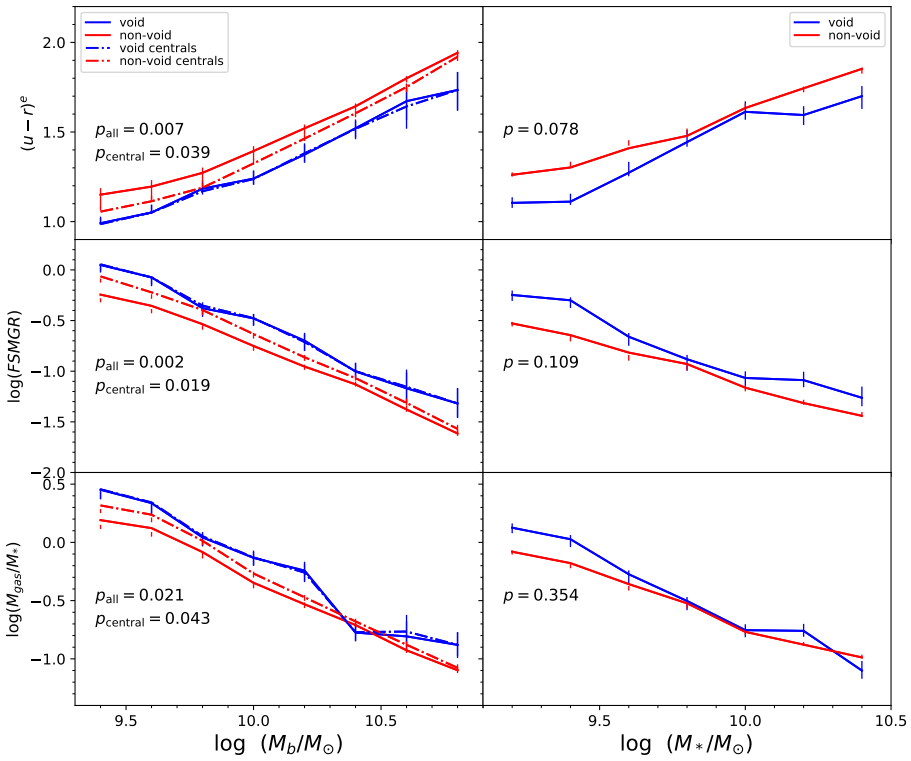

Figure 2.7: Left: For $(u-r)^e$ (top panels), $\log(FSMGR)$ (middle panels), and $\log(M_{\rm gas}/M_*)$ (bottom panels), we show the mean of each property in eight bins of baryonic mass for void galaxies (blue) and non-void galaxies (red) in intervals of $\Delta \log M_b = 0.2$. We show this for all void and non-void galaxies (solid) and for void and non-void galaxy group centrals (dot-dashed). Each data point is placed in the middle of the mass bin and error bars show 1σ uncertainties derived from a bootstrap resampling inside each bin. The p-value of the $T_{n,3}$ test statistic is shown in each panel for all void and non-void galaxies and for void and non-void galaxy centrals (see text). Right: Similar to left panels, but galaxy properties are measured inside seven bins of stellar mass with $\Delta \log M_* = 0.2$. For clarity, we only show the data for all void and non-void galaxies in this plot (i.e., we do not make distinctions between satellites and centrals). We also show the p-value of the $T_{n,3}$ test statistic between void and non-void galaxies in each panel.

results of the tests in Table 2.2. The results of the test show that the quantitative differences between void and non-void galaxy property distributions remain statistically significant in ECO, even when controlling for mass. These differences are less statistically significant in RESOLVE-A, though this could likely be an effect due to the low number of void galaxies (< 100) in RESOLVE-A.

In Figure 2.7 we use an alternative method for controlling the mass distribution of void and non-void galaxies that lets us determine how galaxy properties depend on environment. We bin both samples in stellar and baryonic mass and compare the mean of log(FSMGR), $(u-r)^e$, and $\log(M_{\rm gas}/M_*)$ for void and non-void galaxies in each bin. Error bars are 1σ confidence intervals made from a bootstrap resampling inside each bin. To compute the error from a bootstrap method, we resample (i.e., draw randomly from) the distribution inside each bin of mass x times, where x is the number of objects inside that bin, build a sample from the random draws and compute the mean. We draw objects with replacement so the same object in a given bin can be sampled more than once. We do this 1,000 times and make a distribution of the mean values inside each bin and take the 16th and 84th percentile of this distribution as the error. We find that void galaxies are bluer, more star-forming, and more gas-rich across almost all bins of baryonic mass. We find similar trends when controlling for the stellar mass, across all stellar mass bins.

In order to assess the statistical significance of the comparisons shown in Figure 2.7, we perform a multivariate test for equal distributions based on nearest neighbors. We compute the third nearest neighbor test statistic, $T_{n,3}$, between void and non-void galaxies for the mass ranges shown in Figure 2.7 ($\log(M_b/M_\odot) = 9.3-10.9$ for left panels, $\log(M_*/M_\odot) = 9.1-10.5$ for right panels). We normalize the data, such that each variable has a value between 0 and 1, before computing $T_{n,3}$ and then perform a bootstrap of the $T_{n,3}$ test statistic to obtain a p-value. The p-value of each test is shown in the panels of Figure 2.7.

We find higher p-values ($p > 0.05$) for comparisons between the void and non-void galaxy samples complete in stellar mass, indicating that the differences between the stellar-mass complete samples may not be as statistically significant as the differences between the baryonic-mass complete samples. The difference in sample sizes is important to note, however, as there are 895 total void galaxies being tested in the left panels of Figure 2.7, 857 of which are centrals, while there are 522 total void galaxies being tested in the right panels of Figure 2.7. Similarly, there are 8,288 non-void galaxies and 5,718 non-void galaxy centrals being tested in the left panels of Figure 2.7, while there are 5,821 total non-void galaxies being tested in the right panels of Figure 2.7. We note that these numbers vary from what is listed in Table 2.3 because we do not show the highest mass bins in Figure 2.7 due to very low (< 10) sample sizes for the void galaxies. The difference in sample sizes inevitably leads to higher p-values for the void and non-void galaxy samples being tested in the right panels of Figure 2.7.

RESOLVE-A		
galaxy property	AD statistic	p-value
$(u-r)^e$	3.02	0.019
log(FSMGR)	1.37	0.088
$\log(M_{\rm gas}/M_*)$	0.96	0.13
ECO		
galaxy property	AD statistic	p-value
$(u-r)^e$	43.52	≤ 0.001
log(FSMGR)	46.47	≤ 0.001
$\log(M_{\rm gas}/M_*)$	41.85	≤ 0.001

Table 2.2: Test statistic and p-values of the AD k-sample test performed between the void and mass-matched non-void galaxy property distributions shown in Figure 2.6. Results are shown for both the ECO and RESOLVE-A semester samples.

Part of the differences observed between void and non-void galaxies at fixed mass can be attributed to contributions from satellite galaxies in the non-void pop-

ulations. For this reason, we quantify how much the satellite population contributes to the differences we see between void and non-void galaxies at fixed mass in Figure 2.7. On the left-hand panels in Figure 2.7, we show the mean color, FSMGR, and gas fraction of group centrals for both void and non-void galaxies at fixed baryonic mass. We also compute the $T_{n,3}$ test statistic described above for void and non-void galaxy centrals and show the corresponding p-values in the left panels of Figure 2.7. For reference, we show the number of centrals and satellites in the baryonic and stellar mass complete void and non-void galaxy samples in Table 2.3. The mean of void galaxy group centrals hardly changes, due to the fact that more than 90% of all void galaxies exist inside N= 1 groups. The mean of non-void centrals at fixed baryonic mass, however, appears bluer, more star-forming, and more gas-rich than the mean of all non-void galaxies, especially at lower masses. We note that the p-values of the $T_{n,3}$ test statistic for void and non-void galaxy centrals indicate that the differences between void and non-void galaxies remain statistically significant among the population of centrals. Lower mass non-void galaxies can exist as satellites in large groups and clusters, and those satellites can be expected to have redder colors, lower FSMGRs and gas fractions than galaxies outside of clusters of the same mass as they have been quenched through some of the environmental processes that take place in groups and clusters. Nevertheless, this satellite effect does not explain away all of the differences between void and non-void galaxies. Differences persist even when considering central galaxies alone.

Sample	$\log(M_b/M_\odot) > 9.3$	$\log(M_*/M_\odot) > 9.1$
Void centrals	863	533
Void satellites	38	20
Non-void centrals	5,999	4,622
Non-void satellites	2,626	2,273

Table 2.3: Number of satellites vs. centrals in the ECO baryonic-mass and stellar-mass complete void and non-void galaxy samples.

In order to shed light on why void and non-void galaxies have different properties at fixed mass, we examine some of the property distributions inside each of the baryonic mass bins from Figure 2.7. In Figures 2.8 and 2.9, we examine the color and gas fractions of void and non-void galaxies inside different bins of baryonic mass. We make clear that the samples here are not mass-matched as was done for Figure 2.6, given the narrow range of mass ($\Delta \log(M_b/M_\odot) = 0.2$) in which the void and non-void galaxy properties are being compared for these figures. We perform an AD k-sample test between the void and non-void galaxy population inside each bin of mass in Figures 2.8 and 2.9 and present the p-value in every panel. We remind the reader that the AD p-values are capped below values of 0.001 and above values of 0.25 in `scipy.stats`. Although we report a high (> 0.05) p-value in the panel of Figure 2.8 where $\log(M_b/M_\odot) = 10.5 - 10.7$, and the panels of Figure 2.9 where $\log(M_b/M_\odot) = 9.7 - 9.9$, $10.3 - 10.5$, and $10.5 - 10.7$ we note that sample sizes can affect the reported p-values of these comparisons.

When we investigate the color distribution of void and non-void galaxies inside different bins of baryonic mass (see Figure 2.8), we see that at low masses there appears to be a lack of red sequence galaxies inside of voids. Although a red sequence begins to emerge at higher masses, the voids consistently host a slightly bluer population of galaxies and appear to have a deficit in red sequence galaxies when compared to the non-void population. The number of void galaxies begins to drop significantly past $\log(M_b/M_\odot) > 10.5$, thus reducing the statistical significance of these results, especially at the highest masses. A similar result holds for gas mass fraction (see Figure 2.9), where void galaxies show a significantly weaker gas-poor peak and a correspondingly stronger gas-rich peak than non-void galaxies. We note that the comparison of color for void and non-void galaxies in Figure 2.8 agrees qualitatively with Figure 4 of Hoyle et al. (2012), which shows that void galaxies are bluer than non-void galaxies at fixed magnitude.

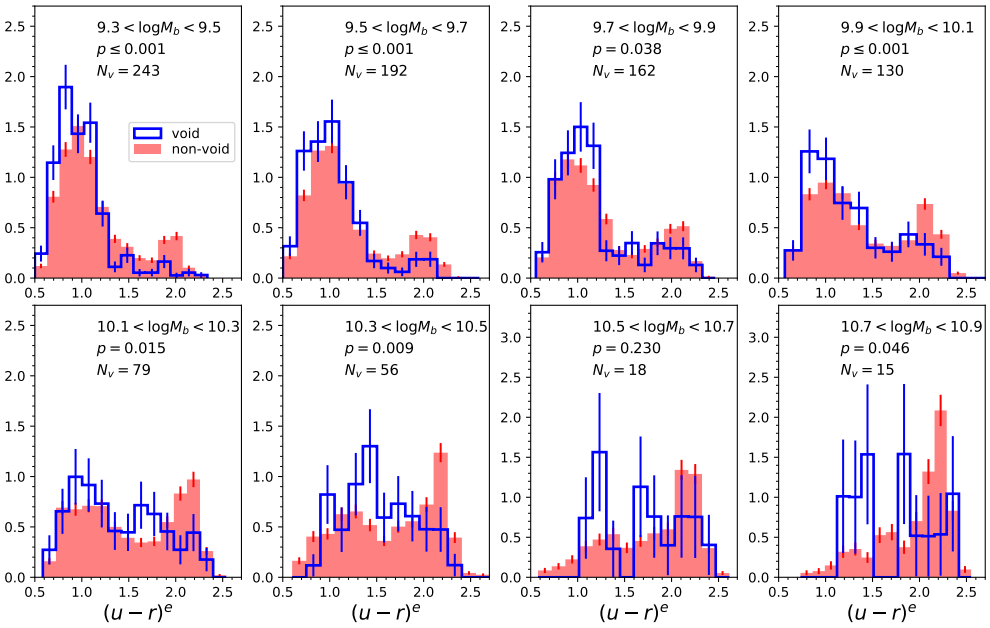

Figure 2.8: $(u-r)^e$ color distributions of void galaxies (blue) and non-void galaxies (red) in eight bins of baryonic mass. The mass bins are the same eight as in Figure 2.7. The number of void galaxies inside each mass bin is also shown on each panel, as well as the p-value of the AD test statistic between void and non-void galaxies.

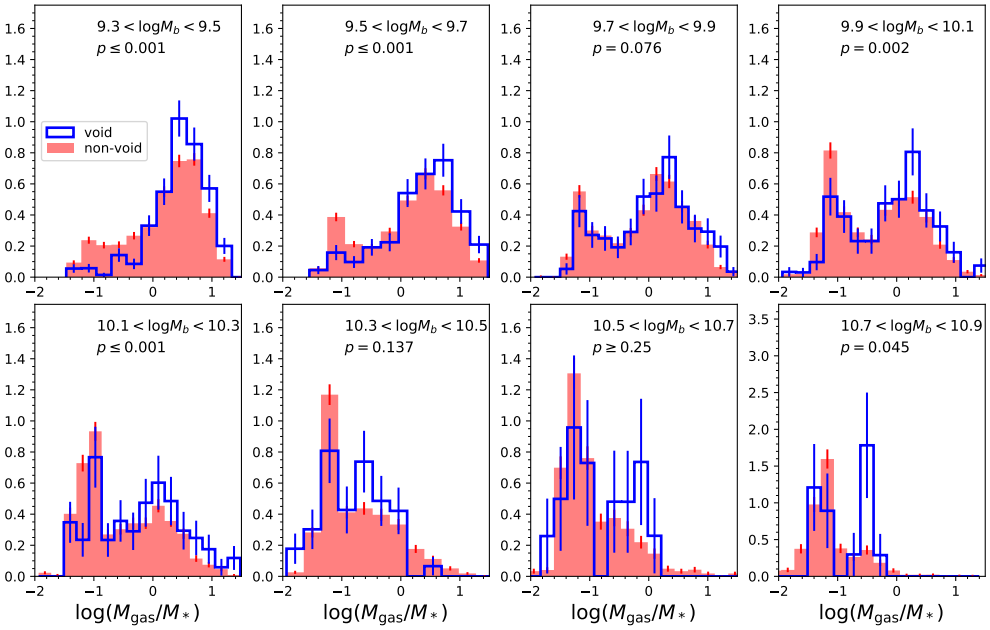

Figure 2.9: Gas-to-stellar mass ratio distribution of void galaxies (blue) and non-void galaxies (red) in the same eight bins of baryonic mass as in Figure 2.8. As in Figure 2.8, we show the p-value of the AD test statistic in each panel.

2.3.3 Are Void Galaxies Different at Fixed Morphology?

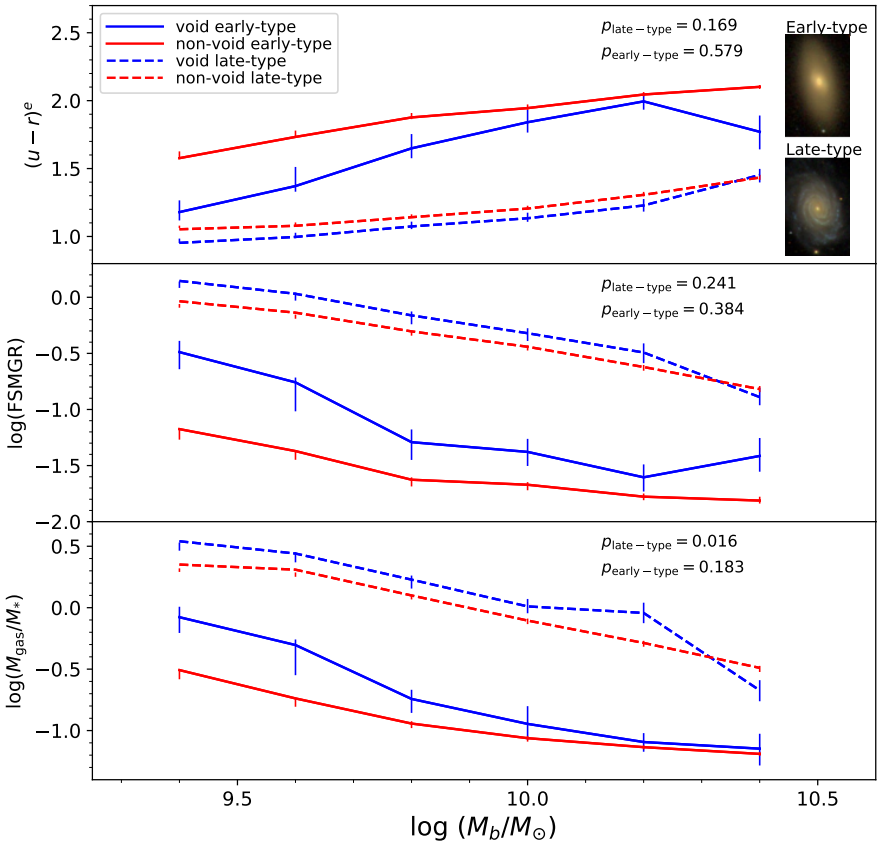

Figure 2.10: Similar to Figure 2.7, we show the mean of $(u-r)^e$, $\log(FSMGR)$, and $\log(M_{\mathrm{gas}}/M_*)$ for void (blue) and non-void (red) galaxy late-types (dashed) and early-types (solid) inside six bins of baryonic mass. We also show, as in Figure 2.7, the p-value of the $T_{n,3}$ test statistic performed between void and non-void galaxies at fixed morphology in each panel.

So far, we have seen that void galaxies are bluer, more star-forming, and more gas-rich than galaxies with higher local densities, and that this is due to more than just the lower mass distribution in voids. In this section we additionally control for morphology in order to determine whether the differences we see between void

and non-void galaxies inside a single bin of baryonic mass can be attributed to differences in the morphological distributions. Because voids tend to be occupied by late-type galaxies with lower masses than higher-density regions, we control for morphology in order to determine if the differences we see in color, FSMGR, and gas fraction can be attributed to the larger number of bluer late-types that exist in low-density regions.

In Table 2.4 we list the number of late types and early types in our void and non-void samples above the baryonic mass completeness limit, as well as the percentage of the total population for each sample. We note that 83% of void galaxies are late-types, whereas 73% of the non-void galaxies are late-types. One might normally expect to find more early-type galaxies inside the non-void environments, however, ECO and RESOLVE are both dominated by dwarf galaxies and late-type fractions are universally higher at low galaxy mass (Conselice, 2006). We remind the reader that ECO and RESOLVE were both designed to explore the low-mass galaxy regime with volume limited samples reaching down to mass limits of $\sim 10^9 M_\odot$. In addition, our non-void definition also includes galaxies in regions of average density explaining why the non-void sample is still dominated by late-types. Nonetheless, since there is a higher fraction of late-type galaxies inside voids than non-voids, it is interesting to control for morphology to determine if the differences we see between the void and non-void galaxies can be attributed to the difference in morphological distributions.

Sample	Total N	% of total
Void Late-types	745	7.9%
Non-void Late-types	6296	66.6%
Void Early-types	148	1.6%
Non-void Early-types	2262	23.9%

Table 2.4: Number of late-type and early-type galaxies in the ECO void and non-void galaxy samples.

In Figure 2.10, we control for both morphology and mass to determine if

the void galaxies are intrinsically different from the non-void galaxies. We find that, even at fixed mass and morphology, void galaxies are different from their non-void counterparts. The late-types appear very similar to each other, but void late-types are still bluer, more gas-rich, and more star forming than non-void late-types. Early-type galaxies, however, show much larger variations in color, FSMGR, and the gas fraction between the void and non-void populations at fixed baryonic mass, suggesting that the properties of early-type galaxies correlate far more with environment than the properties of late-type galaxies.

As described for Figure 2.7, we perform a test for equal distributions using the $T_{n,3}$ statistic for void and non-void galaxy late-types and early-types and report the p-value in each panel of Figure 2.10. We find high p-values ($p > 0.05$) for most of these tests, indicating that these comparisons may not be statistically significant. However, we note again that sample sizes could play a role, especially in the case of early-type galaxies as there are only 148 total void early-type galaxies, and 2,262 non-void early-type galaxies.

Our results show that, although morphology correlates highly with color, star formation, and gas-to-stellar mass ratio, environment still plays a role in the observed properties of galaxies at fixed mass and morphology. We controlled for the mass of late-types and still found discrepancies between these properties, even at higher masses where the error introduced by using a predicted baryonic mass diminishes. The early-type population of void galaxies appears to differ significantly from that of the non-void population at fixed mass. This result is consistent with previous results suggesting that early-types in low-density environments evolve differently from the massive red and dead early-types commonly found in clusters, with low-density environments favoring bluer, lower-mass early-types with recent star formation driven by gas-rich mergers or gas inflows (Kannappan et al., 2009; Stark et al., 2013; Moffett et al., 2015; Lopes et al., 2016).

2.4 Comparison with Theory: Testing Assembly Bias

While we have shown that void and non-void galaxies exhibit differences in color, FSMGR, and gas fractions, even at fixed mass and morphology, we have not discussed how these differences originated. It is currently unclear whether galaxy properties are primarily affected by halo mass, halo mass & age, and/or environment. By comparing our results with simulations, we hope to shed light on the relationship between galaxy properties, halo properties, and environment. In particular, we wish to determine whether our results can be attributed to galaxy assembly bias. We do this by constructing mock galaxy catalogs with built-in assembly bias and we analyze them the same way as we have analyzed the ECO sample.

2.4.1 Conditional Abundance Matching

Conditional abundance matching (CAM; Hearin & Watson, 2013), is an extension of the subhalo abundance matching (SHAM) method (Kravtsov et al., 2004; Vale & Ostriker, 2004; Conroy et al., 2006) for assigning observed galaxy properties to dark matter halo properties. While SHAM only connects a single mass-like galaxy property, like stellar mass, to a single mass-like halo property, like maximum circular velocity, CAM allows for two or more halo properties to influence how galaxy properties are assigned in the SHAM algorithm. For example, CAM has been used to study the dependence of star-formation rate on halo formation history (e.g. Hearin & Watson, 2013; Hearin et al., 2014; Watson et al., 2015; Saito et al., 2016; Paranjape et al., 2015). Here we briefly describe our implementation of CAM.

For our fiducial mocks we assign baryonic mass to (sub)halos based on the value of $V_{\rm peak}$, where $V_{\rm peak}$ is defined as the maximum value that the maximum circular velocity, $V_{\rm max}$, attains during the entire assembly history of the (sub)halo. We define $V_{\rm max} \equiv {\rm Max}\left\{\sqrt{GM(<r)/r}\right\}$, where $M(<r)$ is the mass of the halo enclosed inside some radius r, as the maximum circular velocity of a test particle

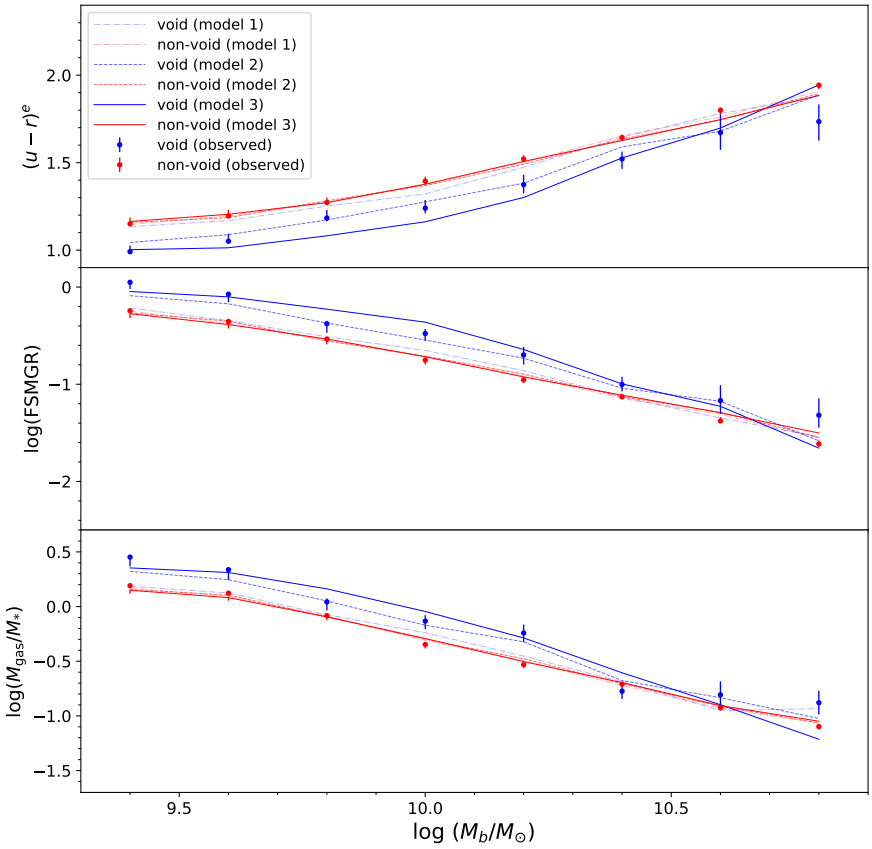

Figure 2.11: Similar to 2.7 and 2.10, we show the mean of different observed galaxy properties at fixed baryonic mass in ECO for void (blue circles) and non-void (red circles) galaxies, as well as our results for three mock catalogs (solid, dashed, and dot-dashed lines) that vary by the amount of scatter assigned to the relation between color and the 100 Myr accretion rate of the (sub)halo. Blue lines correspond to the mock void galaxies and red lines correspond to mock non-void galaxies. Model 1 (dot-dashed) assumes no relation between color and the 100 Myr accretion rate. Model 2 (dashed) assigns a correlation coefficient of -0.6 to the relation between color and the 100 Myr accretion rate. Model 3 (solid) assumes a monotonic relation between $u-r$ and the 100 Myr accretion rate of the halo, so no scatter is included in the color assignment of this model.

orbiting the halo's gravitational potential well. It is well established that using $V_{\rm peak}$ for matching in SHAM based methods results in galaxy clustering statistics in closer agreement with observations compared to other (sub)halo properties (e.g. Reddick et al., 2013; Lehmann et al., 2017), although see Campbell et al. (2018) for some caveats. While the simplest form of SHAM assumes a monotonic relationship between galaxy mass and $V_{\rm peak}$, there is significant evidence for some scatter, $\sim 0.1-0.3$ dex in stellar mass at fixed halo mass (e.g., More et al., 2009; Yang et al., 2009). Given this, we add a constant level of scatter of ~ 0.15 dex at fixed $V_{\rm peak}$ using the deconvolution method of Behroozi et al. (2010) with a publicly available implementation[2].

Once baryonic mass is assigned, in order to assign galaxy color, mock galaxies are probabilistically binned in 0.1 dex bins of baryonic mass using the fuzzy_digitize function in `Halotools` (Hearin et al., 2017). Within each bin, the observed $u-r$ colors of ECO galaxies are used to define a probability distribution: $\mathrm{P_{ECO}}(u-r|M_b)$. If there are N galaxies inside a baryonic mass bin M_b, then the galaxy colors are drawn randomly N times from the distribution $\mathrm{P_{ECO}}(u-r|M_b)$ and the draws are rank-ordered. The (sub)halos inside each bin of baryonic mass are also rank-ordered by an age parameter, the 100 Myr accretion rate (i.e. the mass that the halo has accreted in the previous 100 Myrs). The $u-r$ colors are then assigned to mock galaxies such that redder colors are tied to galaxies that live in (sub)halos with higher values of the 100 Myr accretion rate. The algorithm that assigns colors to mock galaxies also assumes a monotonic relation between $u-r$ and the 100 Myr accretion rate at fixed baryonic mass, so it is necessary to introduce some scatter. We introduce scatter by degrading the rank order correlation following the method described in appendix D in Campbell et al. (2018).

We create eleven mocks with varying levels of scatter between the $u-r$ and

[2]https://bitbucket.org/yymao/abundancematching

100 Myr accretion rate relation. One mock assumes a correlation coefficient of 0.0, meaning that for that mock the $u-r$ color is not tied to the 100 Myr accretion rate. The other ten mocks have correlation coefficients ranging from -0.1 to -1.0, in steps of 0.1, assigned to the relation between $u-r$ color and 100 Myr accretion rate. The mock with a correlation coefficient of -1.0 assumes a monotonic relation between $u-r$ and the 100 Myr accretion rate. By tying galaxy color to a secondary halo property other than mass, we are explicitly building galaxy assembly bias into our mocks. Moreover, the correlation coefficient for this relation encodes the strength of assembly bias, with a value of 0.0 corresponding to no assembly bias and a value of -1.0 corresponding to maximum assembly bias. As we will show, the amount of scatter that works best for this model to match the data adopts a correlation coefficient of $\rho \sim -0.6$ between the $u-r$ and 100 Myr accretion rate parameters (see Fig. 2.11).

Once baryonic mass and $u-r$ color have been assigned to a (sub)halo, we assign other galaxy properties, such as the gas fraction and FSMGR, by identifying an ECO galaxy with similar M_b and $u-r$ as the halo and adopting its other properties. This process results in a mock galaxy distribution that preserves the joint distribution of galaxy properties.

We also experiment with different matching parameters in the models by abundance matching different galaxy properties to $V_{\rm peak}$ and the 100 Myr accretion rate of the dark matter halos, we discuss these results towards the end of this section.

2.4.2 Mock Catalog Construction

We use the Vishnu cosmological N-body simulation that adopts the has a $130h^{-1}$Mpc box size and a dark matter particle mass of $3.215 \times 10^7 h^{-1} M_\odot$ (see Johnson et al. 2019 for a detailed description of the simulation and halo catalogs), to construct our mock catalogs. We populate the simulation using the CAM mock population

framework in `Halotools` (Hearin et al., 2017), as described above. We then extract four independent mock ECO galaxy catalogs from the 130 Mpc/h simulation box. For each mock galaxy catalog, we choose a new location for the observer and we place galaxies in redshift space by using the positions and peculiar velocities of their (sub)halo with respect to the observer. We then make identical geometrical cuts in right ascension, declination, and redshift as those in the ECO sample in redshift space, in order to preserve the same geometry as the ECO sample. We make sure to separate the four mock catalogs from each other by at least 10 Mpc/h, thus making them truly independent.

As a result of this procedure, each of the four mock catalogs has the same geometry, similar number density of galaxies, similar overall clustering, and the same joint distributions of observed properties as the ECO sample. Furthermore, galaxy baryonic mass directly correlates with dark matter halo mass, color directly correlates with halo mass accretion rate at fixed mass, and other observed properties like FSMGR or gas fraction inherit indirect correlations with halo mass and accretion rate through their correlations with baryonic mass and color.

It is worth mentioning here that the size of our simulation box may not be large enough to properly model the formation of large cosmic voids. Nadathur et al. (2017) demonstrate that the "potential fluctuations associated with voids extend over scales of 200-300 Mpc/h." Although we have not shown what impact this consideration could have on our results, we believe it is safe to ignore as our void galaxies are defined by local density rather than large-scale structure. Furthermore, the simulation box is large enough to carve out four independent ECO mock catalogs of densities similar to that of the real ECO catalog, so we believe the simulation box is more than adequate for this type of study.

2.4.3 Results

In Figure 2.11, we show our models with different varying levels of scatter between halo accretion rate and galaxy color at fixed baryonic mass and include the ECO data points from Figure 2.7. We show the results for three models in particular: model 1 which assumes a correlation coefficient of 0.0 to the relation between color and the 100 Myr accretion rate at fixed baryonic mass, model 2 which assumes a correlation coefficient of -0.6 between color and the accretion rate at fixed baryonic mass, and model 3 which assumes a monotonic relation between color and accretion rate (i.e., correlation coefficient is -1.0) at fixed baryonic mass. We find that model 2 matches the data fairly well for both the non-void and void galaxies. Although the mocks are constructed such that the colors of void and non-void galaxies are tied to the halo accretion rate at fixed mass, it is interesting to see in the lower two panels of Figure 2.11 that the observed FSMGR and gas fractions trends at fixed mass also hold up in the mock catalogs, which is attributed to the high correlation that exists between color, FSMGR, and gas fractions. The model with a correlation coefficient of 0.0 represents a simple abundance matching of baryonic mass to $V_{\rm peak}$ and assumes no additional correlation between color and the 100 Myr accretion rate (i.e. no galaxy assembly bias). This model cannot reproduce the observed differences between void and non-void ECO galaxy properties. Galaxy assembly bias is thus required to explain the ECO results, at least in the family of models we consider.

Our resulting mock catalogs also do a fairly good job of matching the data when we abundance match stellar mass to $V_{\rm peak}$ and correlate $M_{\rm gas}/M_*$ to the 100 Myr accretion. When we abundance match FSMGR to the 100 Myr accretion rate, the model matches the data, but only when the correlation is weak. It should not be surprising that the gas fraction and $(u-r)^e$ parameters both work in the model when matched to the 100 Myr accretion rate because the $M_{\rm gas}/M_*$ for this sample is

predicted from color via the PGF technique. The models fail, at all variations with scatter, when we match luminosity to $V_{\rm peak}$ and/or match FSMGR to the 100 Myr accretion rate. While we cannot confirm that the evolution of galaxies is determined solely by assembly bias, as we do not analyze simulations that include the baryonic physics present in different environments, we do show that the void and non-void galaxy trends at fixed mass are recovered in mock catalogs constructed through conditional abundance matching when certain galaxy parameters are abundance matched to the right (sub)halo mass and age parameters.

2.5 Discussion

2.5.1 Comparison with Previous Results

Our results are in general agreement with observational results that have found enhanced specific star formation rates in underdense regions (Rojas et al., 2004; Grogin & Geller, 1999, 2000; Meyer et al., 2007). More recently, Ricciardelli et al. (2014) showed that specific star formation rates are higher in void galaxies, and that this is due to more than just the difference in mass distributions amongst different environments. Our results are also in agreement with those of Hoyle et al. (2012) who find that void galaxies are statistically bluer than non-void galaxies, even at fixed magnitude.

In comparison with theory, Patiri et al. (2006) use a semi-analytic model to study the ratio of blue and red galaxies in void and non-void regions, where the void sample is selected from maximal, non-overlapping spheres with a radius larger than $10\,h^{-1}$ Mpc and devoid of bright of galaxies. The results of their simulation agree with their observed results: the color distribution of galaxies is bimodal in both void and non-void regions, however, the ratio of blue to red galaxies is higher in voids (although this is more pronounced in the simulation than in the observation). They

then control for color and find that the sSFR of void galaxies is similar to that of non-void galaxies in their simulation. They conclude that galaxy properties are not affected by environment at fixed color.

Kreckel et al. (2011) used a hydrodynamical simulation to study the environmental dependence of galaxies in voids. They predicted the trends we observe, but only at faint luminosities. Their void galaxy sample is defined by a large underdense region with a diameter of $\sim 30\,h^{-1}$ Mpc residing at the center of their simulation box. They find that their void galaxies are bluer and more star-forming at fixed luminosity for faint galaxies ($M_r > -16$), but at higher luminosities ($M_r < -18$) they find no difference between the void and non-void galaxies. Although we do not directly control for luminosity, we show at fixed baryonic mass that there is a difference between void and non-void galaxies well above the completeness limit of $M_b = 10^{9.3}$ $M_\odot$, and most of these galaxies have luminosities brighter than $M_r = -18$.

More recent work by Tonnesen & Cen (2015) used a hydrodynamical simulation to analyze stellar and halo mass growth in an overdense and underdense region of a simulation box (on scales of ~ 20 Mpc). Their simulation produced halos with earlier formation times in overdense regions. First, they found that the stellar-to-halo mass ratio depends on large-scale environment and not just halo mass. They also found that the specific star formation of $z = 0$ galaxies is higher in the underdense region of their simulation box when compared to galaxies in the overdense region. Their work suggests that environment, in addition to halo mass, should be considered when assigning stellar masses to halos.

2.5.2 E/S0s as Merger Remnants in Voids

We examine nearest neighbor distances for void galaxies in order to investigate whether there is a merging population of void galaxies that could explain the presence of void early-types. If we consider that possible mergers occur in galaxies that

have a nearest neighbor at < 100 kpc, we find that an extremely small fraction ($< 1\%$) of void galaxies look like candidates for mergers that will later become early-types. Given the larger fraction of void galaxies that are considered early-types, we can interpret this in several ways. One possible explanation could be that the early-types we see do not arise as a consequence of merging or other interactive transformation processes, thus challenging assumptions about how early-types form in the universe.

Observational and theoretical studies of blue early-types do suggest the likelihood, especially in low-density environments, of formation in gas-rich mergers, but gas accretion may also be important (Bekki, 2008; Kannappan et al., 2009; Stark et al., 2013; Verbeke et al., 2014). Another possible explanation for the low number of merger candidates relative to early-types could be that the timescale on which galaxies live in a pre-merger state is far outlived by the lifetime of the post-merger remnant, consistent with a post-merger disk regrowth scenario (Kannappan et al., 2009; Stark et al., 2013; Moffett et al., 2015). Finally, we note that our analysis includes only galaxies brighter than $M_r = -17.33$ and above the baryonic mass completeness limit, so does not rule out current interactions between the void early-type galaxies in our sample and neighboring galaxies whose masses and luminosities fall below our completeness limit.

2.6 Summary

In this work, we have analyzed a sample of void galaxies defined by an Nth nearest neighbor method using the ECO catalog and also consider the RESOLVE-A semester in order to determine the impact of using predicted baryonic masses on the analysis. We examine the color, FSMGR, gas content, and morphology of galaxies in voids and outside of voids. Our results are as follows.

- We find the void galaxies to have a lower baryonic mass distribution than

the non-void galaxies, with an excess of galaxies at $M_b < 10^{9.6} M_\odot$ and a deficit of galaxies at mass above $M_b \sim 10^{10} M_\odot$ with respect to the non-void galaxy baryonic mass distribution. There hardly exist any void galaxies at $M_b > 10^{11} M_\odot$.

- The void galaxies are bluer, more gas-rich, and more star forming than non-void galaxies, although this is partly driven by differences in the mass distributions of the void and non-void samples. When we mass-match the non-void sample to have an identical baryonic mass distribution as the void sample, these differences are approximately cut in half but persist, showing that environment affects galaxy properties even at fixed mass.

- When we study the averaged properties in mass bins, we find that void galaxies are bluer, more gas-rich, and more star forming than non-void galaxies at all masses. Satellite galaxies also contribute to the variations we see in the observed mean quantities between void and non-void galaxies at fixed mass, however, the trends persist (albeit more weakly) when we remove the satellites and only consider central galaxies.

- Controlling for morphology, we find that the galaxies in voids are bluer, more gas-rich, and more star-forming than their non-void counterparts even at fixed mass and morphology. This is true for both early-type and late-type galaxies, though the differences are significantly smaller for late types. Incidentally, we also find that voids host a distinctive population of early-types that are bluer and more gas-rich than the typical quenched red-sequence early-types that exist in clusters, consistent with prior work associating low-mass, gas-rich blue E/S0s with low-density and low halo-mass environments (Kannappan et al., 2009; Moffett et al., 2015).

- When we construct mock catalogs with built-in galaxy assembly bias using

conditional abundance matching, we observe that the color, FSMGR, and $M_{\rm gas}/M_*$ of void and non-void galaxies follow trends similar to those seen in the observed data. We find that the mock catalogs typically match the data to a fair degree when stellar mass or baryonic mass are abundance matched to halo $V_{\rm peak}$ and $(u-r)^e$ or $M_{\rm gas}/M_*$ are abundance matched to the halo mass accretion rate with a modest amount of scatter introduced in the matching. For mock catalogs in which the color or gas fraction is not tied to the age of the (sub)halo, the trends in color, FSMGR, and $M_{\rm gas}/M_*$ for void galaxies are indistinguishable from the non-void galaxies, thus suggesting that galaxy assembly bias is required to explain our observational results.

We have, for the first time, performed an analysis on a void and non-void galaxy population while controlling for both mass and morphology simultaneously. Our results suggest that galaxies living in low-density regions are intrinsically different from the rest of the galaxy population, and that this is due to more than just a difference in mass and morphology distributions.

Chapter 3

Exploring AGN and Star Formation Activity of Massive Galaxies at Cosmic Noon

3.1 Introduction

The epoch of $z \sim 1-3$ (when the universe was only $\sim 2-6$ Gyr old, corresponding to $\sim 15\%$ to 50% of cosmic history) is one of the most important and active epochs of galaxy formation[1]. During this period, star formation (SF) and active galactic nuclei (AGN) activity in galaxies peaked, massive clusters collapsed into existence, and galaxies underwent significant growth. Although SF and AGN activity both peaked during this epoch, it is unclear how the two processes are related. Observations show that the cosmic star formation rate (SFR) density and black hole accretion rate density peak at around $z \sim 2$ and decrease rapidly down to $z \sim 0$ (Dickinson

[1]The work presented in this chapter was published in the Monthly Notices of the Royal Astronomical Society (MNRAS) journal on July 29, 2020 (see Florez et al. 2020, MNRAS, 497, 3273). As first author, I contributed by writing the paper and performing the full scientific analysis presented therein.

et al., 2003; Babić et al., 2007; Hopkins et al., 2007; Wilkins et al., 2008; Jogee et al., 2009; Rigby et al., 2011; Madau & Dickinson, 2014; Delvecchio et al., 2014). Furthermore, it is well known that the central black hole mass of galaxies correlates with the host galaxy bulge mass (Magorrian et al., 1998; McLure & Dunlop, 2002) and bulge velocity dispersion (Ferrarese & Merritt, 2000; Gebhardt et al., 2000; Kormendy & Ho, 2013). These relationships have led to suggestions that the growth of black holes and galaxies may be closely intertwined, but the issue of coevolution is the subject of debate (e.g., Kormendy & Ho, 2013; Jahnke & Macciò, 2011).

AGN activity, which is a direct result of gas accreting onto a host galaxy's central black hole, has often been proposed as a mechanism that can reduce or suppress SF activity, as radiation, winds, and jets expel gas or heat it enough to prevent it from forming stars. Different forms of AGN feedback impact their host galaxies in different ways. AGN feedback from radiation and winds from the accretion disk can heat or expel galactic gas on different physical scales (e.g., Hambrick et al., 2011; Fabian, 2012; Vogelsberger et al., 2013; Choi et al., 2015; Roos et al., 2015; Hopkins et al., 2016; Bieri et al., 2017). Jets from AGNs are thought to play a large role in heating the intracluster medium (ICM) in clusters of galaxies, thus preventing gas from cooling and accreting onto galaxies and ultimately halting future episodes of star formation (e.g., Somerville et al., 2008; Peterson & Fabian, 2006; McNamara & Nulsen, 2007; Cattaneo et al., 2009; Fabian, 2012; Heckman & Best, 2014; Davé et al., 2019). In numerical simulations, some source of heating, such as AGN feedback, is thought to be crucial in solving the "overcooling" problem in galaxy formation, where in absence of feedback, the gas inside dark matter halos cools to form galaxies with mass functions resembling those of the dark matter halos (White & Rees, 1978; Naab & Ostriker, 2017; Somerville & Davé, 2015).

While AGN activity has been linked to a potential suppression of SF as described above, there are phases of galaxy evolution where AGN and SF activity

coexist. A so-called AGN-SF connection has been claimed at $z < 0.1$ (Sanders et al., 1988; Mahoro et al., 2017). This connection, however, is currently a topic of debate as other studies (e.g., Leslie et al., 2016) claim to find AGN activity associated with depressed SF activity at $z < 0.1$. Any potential connection between AGN and SF activity may be due, at least in part, to gas fueling both the circumnuclear SF activity and AGN activity when the angular momentum problem can be overcome (e.g., Jogee, 2006, and references therein), as is the case in gas-rich mergers (Hopkins et al., 2008). At higher redshifts, the AGN-SF connection is less well-studied. Some studies have claimed $1 < z < 3$ galaxies with X-ray luminous AGN, where X-ray emission is measured in the hard band (typically at 2-10 keV) or ultra-hard band (at 14-195 keV), have enhanced SFRs compared to galaxies without X-ray luminous AGN and/or that X-ray luminous AGN are preferentially found in star-forming galaxies out to $z \sim 2$ (Masoura et al., 2018; Santini et al., 2012; Rosario et al., 2013; Shimizu et al., 2017), while other studies (e.g., Shimizu et al., 2015) have claimed that galaxies with X-ray luminous AGN have decreased SFRs compared to galaxies without luminous AGN.

The goal of this work is to explore the general connections, if any, between AGN and SF activity in galaxies at early cosmic times. As outlined above, the relationship between AGN and SF activity might be expected to depend on the evolutionary phase of a galaxy and the AGN activity cycle. It is possible that early-on, X-ray luminous AGN and SF activity coexist when large gas inflows on different physical scales fuel both types of activity. At later times, the AGN feedback phase may start if AGN-driven radiation, winds, and jets eject or heat galactic gas on different scales. Our study aims to explore the relation between AGN and SF activity, and to constrain the relative importance and timescales of these different evolutionary phases.

The processes that regulate SF and AGN activity are important for our un-

derstanding of galaxy evolution as they are intimately tied to the growth of galaxies. Observations have confirmed the existence of massive quenched galaxies up to $z \sim 4$ (Kriek et al., 2006; Baldry et al., 2012; Sherman et al., 2020a; Fang et al., 2018; Muzzin et al., 2013; Stefanon et al., 2013; Glazebrook et al., 2017; Stevans et al., 2021), suggesting that quenching mechanisms can efficiently suppress SF in galaxies at early cosmic times. It is unclear, however, what role (if any) AGN feedback plays in the quenching of massive galaxies. Simulations, such as Illustris (Wellons et al., 2015) and IllustrisTNG (Naiman et al., 2018; Springel et al., 2018; Nelson et al., 2018), largely implement AGN and stellar feedback as the main quenching mechanisms for massive galaxies in their simulations. However, these simulations struggle to produce massive quenched galaxies by $z \sim 3$. We aim to explore the properties of massive, quiescent galaxies with and without X-ray luminous AGN in order to further constrain the processes that quench star formation.

Studying the SF activity of galaxies with X-ray luminous AGN can be rather complicated, as the emission from an AGN can dominate the galaxy spectral energy distribution (SED) at UV, optical, mid-IR, and far-IR wavelengths, thus making it difficult to disentangle the emission between AGN and star forming processes in SED fitting. For this reason, many studies that explore the global stellar mass-SF main sequence of galaxies explicitly remove or ignore the contribution from galaxies with X-ray luminous AGN (Speagle et al., 2014). Although difficult, several studies have attempted to compare the star forming properties of galaxies with X-ray luminous AGN to galaxies without X-ray luminous AGN, with X-ray emission measured in the hard band (at 2-10 keV) (Masoura et al., 2018) and the ultra-hard band (at 14-195 keV) (Shimizu et al., 2017), and find that galaxies with X-ray luminous AGN tend to have enhanced SFRs with respect to galaxies without X-ray luminous AGN. The work presented in this paper will utilize a control sample of galaxies without X-ray luminous AGN that is larger than the control samples presented in

the aforementioned studies and will use the same SED fitting code to measure galaxy properties for galaxies with and without X-ray luminous AGN.

For this study, we create a sample of galaxies with X-ray luminous AGN, where X-ray emission is measured in the full band of Stripe 82X at 0.5-10 keV, and a sample of galaxies without X-ray luminous AGN using the same photometric data and perform SED fits of both samples using Code Investigating GALaxy Emission (CIGALE) (Boquien et al., 2019; Ciesla et al., 2015; Noll et al., 2009) which is capable of disentangling the emission from AGN and star forming processes. This allows us to measure and compare the star forming properties of both samples in the same self-consistent way, unlike many other studies. We select our samples from a very large 11.8 deg^2 field where the Stripe 82X X-ray survey (LaMassa et al., 2016) and the Spitzer-HETDEX Exploratory Large Area (SHELA) IRAC survey overlap Papovich et al. (2016). Our samples have extensive multi-wavelength coverage (e.g., X-ray, UV, optical, near-to-mid-IR, and some far-IR/submillimeter) over the 11.8 deg^2 field, which corresponds to a very large comoving volume of ~ 0.3 Gpc^3 at $z = 0.5 - 3$. Such a large comoving volume minimizes the effects of cosmic variance and captures a large sample of rare massive galaxies ($\sim 30,000$ galaxies with $M_* > 10^{11}$ $M_\odot$) and X-ray luminous AGN (~ 700 objects with $L_X > 10^{44}$ erg s^{-1}), allowing us to provide some of the strongest constraints to-date on the relation between AGN and SF activity at $z \sim 1 - 3$.

This paper is organized as follows. In Section 3.2, we discuss the data we use to select and create our samples of galaxies with and without X-ray luminous AGN. In Section 3.3, we describe the SED fitting method and tests we use to obtain galaxy properties, such as stellar mass and SFR. In Section 3.4, we discuss the stellar mass and SFR distributions of our samples. In Section 3.5.1, we compare the stellar mass-SFR relation of galaxies with and without X-ray luminous AGN. In Section 3.5.2, we present the fraction and properties of quenched galaxies as a function of

mass and redshift. We discuss our findings in Section 3.6 and in Section 3.7 we summarize our results. Throughout this paper we assume $H_0 = 70$ km s^{-1} Mpc^{-1}, $\Omega_M = 0.3$, and $\Omega_\Lambda = 0.7$.

3.2 Data & Sample Selection

The goal of this work is to estimate and compare the star-forming properties of galaxies with and without X-ray luminous AGN at $z = 0.5 - 3$. To accomplish this, we utilize the large-area, multi-wavelength data available in the SHELA/HETDEX footprint, which consists of five photometric data sets: Dark Energy Camera (DECam) u, g, r, i, z (Wold et al., 2019), NEWFIRM K_S (Stevans et al., 2021), *Spitzer*-IRAC 3.6 and 4.5 μm (Papovich et al., 2016), *Herschel*-SPIRE far-IR/submillimeter (HerS, Viero et al., 2014) and Stripe 82X X-ray (LaMassa et al., 2016). We also utilize available J and K_S-band data from the VISTA-CFHT Stripe 82 (VICS82) Near-Infrared Survey (Geach et al., 2017) and mid-IR photometry from the WISE survey (Wright et al., 2010) to supplement this work.

3.2.1 NEWFIRM K-band Selected Catalog

For the analysis presented in this paper, we use photometry from a NEWFIRM K_S-band selected catalog (Stevans et al., 2021) that includes DECam u, g, r, i, z as well as IRAC 3.6 and 4.5 μm photometry spanning an area of 17.5 deg^2 across the SHELA field. The catalog is created using an approach similar to that in Wold et al. (2019) and described in detail in Stevans et al. (2021). In summary, they use Source Extractor (SExtractor; Bertin & Arnouts, 1996) to identify sources in their K_s-band images and report a 5σ depth of ~ 22.4 AB mag inside fixed 2 arcsecond diameter apertures. The K_S-band fluxes that we use for the analysis presented here are the Kron aperture fluxes from SExtractor (e.g., `FLUX_AUTO`). Quality flags in the catalog allow us to exclude objects with saturated, truncated, or corrupted pixels as well

as regions in close proximity to saturated stars from our analysis. The DECam and IRAC magnitudes are derived through forced photometry of NEWFIRM K_S selected sources using the *Tractor* image modeling code (see Lang et al., 2016, for description of code). The *Tractor* code uses the source positions and surface brightness profiles of higher resolution bands to model and derive fluxes for remaining lower resolution bands. This allows the catalog to include individual fluxes for potentially blended sources in IRAC. These deblended DECam and IRAC fluxes are used to create the K_S-selected DECam-NEWFIRM-IRAC catalog that we use for this work.

3.2.2 Stripe 82X

Stripe 82X is an X-ray survey that covers 31.3 deg^2 of the SDSS Stripe 82 Legacy Survey (LaMassa et al., 2013a, 2016; Ananna et al., 2017). The original catalog described in LaMassa et al. (2016) introduced the release of the XMM-Newton Announcement Opportunity 13 ("AO13") data and is combined with archival XMM-*Newton* and *Chandra* X-ray Observatory X-ray data (LaMassa et al., 2013b). We utilize two updated versions of the catalog described in Ananna et al. (2017) (hereafter A17) and LaMassa et al. (2019) (hereafter LM19). The XMM AO13 footprint largely overlaps ($\sim$ 11.8 deg^2 overlap) with the SHELA field, whereas the archival *Chandra* and XMM-*Newton* data footprints hardly overlap with the SHELA field. For this reason, for our analysis we only consider XMM AO13 data from the Stripe 82X catalog, which has a spatial resolution of $\sim$ 6 arcseconds (Strüder et al., 2001).

The A17 Stripe 82X catalog provides multiwavelength counterpart matches to the X-ray sources by crossmatching to the SDSS coadded catalogs of Fliri & Trujillo (2016) and includes IRAC photometry (Papovich et al., 2016; Timlin et al., 2016) in the crossmatching as well. The A17 catalog also provides photometric redshifts for every source in the catalog as well as quality flags that indicate the reliability of the match. A description of how photometric redshifts are obtained for

the sample can be found in A17. The photometric redshifts ($z_{\rm phot}$) when compared to the available spectroscopic redshifts ($z_{\rm spec}$) have a scatter of $|\Delta(z)|/(1+z) \sim 0.06$ where $\Delta(z) = (z_{\rm phot} - z_{\rm spec})$ and a $\sim 14\%$ outlier fraction, where outliers are defined as objects with $|\Delta(z)|/(1+z_{\rm spec}) > 0.15$. We use the A17 catalog to obtain full X-ray fluxes ($0.5-10$ keV), WISE counterpart fluxes, and redshifts for our sample of galaxies with X-ray luminous AGN. We utilize the aforementioned LM19 catalog to add additional spectroscopic redshifts to the sources in XMM AO13, which brings the spectroscopic redshift completeness for our sample of galaxies with X-ray luminous AGN to $\sim 75\%$.

3.2.3 VICS82 and WISE Supplemental Data

A significant portion of the SHELA footprint overlaps with the VICS82 survey (Geach et al., 2017) and the WISE (Wright et al., 2010) mid-IR survey. The DECam-NEWFIRM-IRAC catalog we utilize includes matches to VICS82 $J\&K_S$-band photometry. We make use of the VICS82 $J\&K_S$-band photometry in our analysis in order to better constrain the SED fit at near-IR wavelengths. We crossmatch sources in the DECam-NEWFIRM-IRAC catalog to the AllWISE source catalog Cutri et al. (2013) by considering any objects within 1.5 arcseconds of the NEWFIRM source a match. We utilize the magnitude values from the profile-fitting photometry and only consider sources with S/N > 2 for this work. Due to the lower resolution of WISE photometry ($\sim 6-7$" for WISE-1-3, ~ 12" for WISE-4), we only consider objects a match for this work if the WISE source has no more than one NEWFIRM match within a 5 arcsecond radius, thus avoiding blended sources. In addition, we apply flag quality cuts to make sure none of our WISE sources have image pixels in the measurement aperture that are confused with nearby sources, and/or contaminated by saturated or otherwise unusable pixels. WISE photometry, particularly in the WISE-3 (12 μm) and WISE-4 (22 μm) bands, is particularly useful for constraining

the SED in the mid-IR wavelengths where emission from an AGN can contaminate the emitted light at $3 - 20$ μm and dust emission from SF radiates at $8 - 1000$ μm. As discussed in the following sections and illustrated in Figure 3.1 and Table 3.2.4, we unfortunately find that only a small fraction of our sample has WISE-3 or WISE-4 photometry. Therefore, we mainly use WISE data to determine whether and how our results might change if mid-IR photometry is included (see Appendix).

3.2.4 Sample Selection

In this section we describe how we obtain our samples of galaxies with and without X-ray luminous AGN. We start by selecting all sources in the K_S-selected DECam-NEWFIRM-IRAC catalog that overlap the Stripe 82X AO13 footprint on the sky. From these sources, we create a sample of objects, which we refer to as S0-DECam-NEWFIRM-IRAC, that have a detection in the DECam u, g, r, i, z bands, a signal-to-noise (S/N) > 5 in the NEWFIRM K_S-band, and S/N > 2 in the IRAC 3.6 and 4.5 μm bands. The reader can refer to the flowchart in Figure 3.1 for an illustration of how the samples with and without X-ray luminous AGN are selected from S0-DECam-NEWFIRM-IRAC (described in further detail below).

Galaxies with X-ray Luminous AGN

In order to create a sample of X-ray selected AGN, we crossmatch between XMM AO13 sources from the Stripe 82X catalog and sources in S0-DECam-NEWFIRM-IRAC using the maximum likelihood estimator (MLE) method of Sutherland & Saunders (1992). The MLE method has been widely used to perform crossmatching between X-ray data and multiwavelength counterparts (see Ananna et al., 2017; LaMassa et al., 2016, 2013b; Brusa et al., 2010). We implement the same MLE methodology used in LaMassa et al. (2016). That is, we set our search radius to 7 arcseconds and the background search radius to be between 10 to 45 arcseconds.

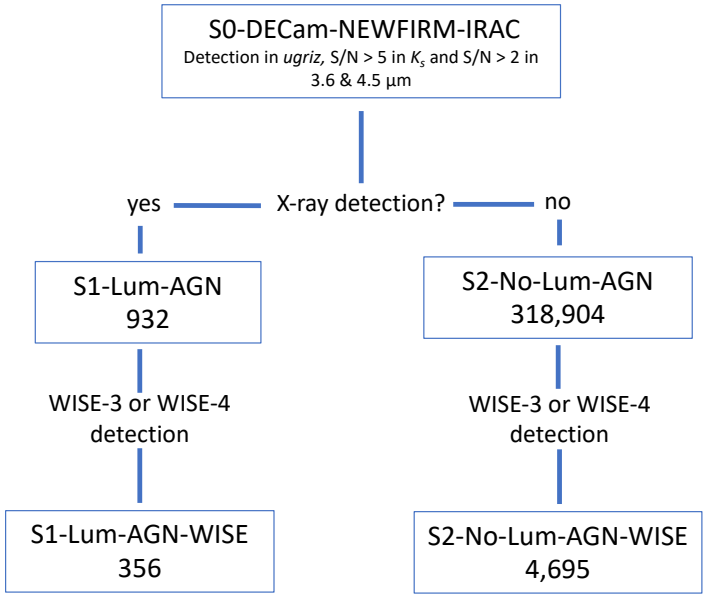

Figure 3.1: Flowchart that demonstrates how our samples are selected. We start with the DECam-NEWFIRM-IRAC catalog and create a sample of sources that fit our selection criteria, which we refer to as S0-DECam-NEWFIRM-IRAC (see Sections 3.2.1 and 3.2.4). We then crossmatch S0-DECam-NEWFIRM-IRAC with the Stripe 82X catalog via the MLE method and create samples with and without an X-ray match, which we refer to as S1-Lum-AGN (see Section 3.2.4) and S2-No-Lum-AGN (see Section 3.2.4), respectively. We then search for WISE detections in both S1-Lum-AGN and S2-No-Lum-AGN and create two more samples, which we refer to as S1-Lum-AGN-WISE and S2-No-Lum-AGN-WISE. The reader can refer to Table 3.2.4 for number of objects in each sample complete in X-ray luminosity and stellar mass. We note that although we have 932 sources with X-ray luminous AGN in sample S1-Lum-AGN, only 898 of these are have a good SED fit with a reduced χ^2 of less than 5. We therefore only analyze these 898 sources in S1-Lum-AGN for this work.

We use X-ray positional error values given in the LaMassa et al. (2016) catalog and assume that the positional errors in the DECam-NEWFIRM-IRAC catalog are negligible compared to those of the X-ray. The only difference in our method to that of LaMassa et al. (2016) is that we consider objects that have a reliability value (R in equation (2) of LaMassa et al. (2016)) greater than 0.5 to be true matches, as any object with $R > 0.5$ is the most likely source inside the search radius to be the true counterpart. We only crossmatch to the K_S-band photometry in the DECam-NEWFIRM-IRAC catalog as we are using a K_S-band selected catalog for the analysis presented here.

Once we find a match between S0-DECam-NEWFIRM-IRAC and XMM AO13, we assign it a photometric or spectroscopic (if available) redshift from A17. We create the sample S1-Lum-AGN from sources in S0-DECam-NEWFIRM-IRAC that have an X-ray match and $z = 0.5 - 3$. From this sample, we search in A17 for any sources that have a WISE detection and include those in our subsample S1-Lum-AGN-WISE. Out of 1,356 unique XMM AO13 X-ray sources that fall in the SHELA footprint at $z = 0.5 - 3$, we find a total of 932 reliable matches in the DECam-NEWFIRM-IRAC catalog. Of these, only 356 sources have a detection in either the WISE-3 or WISE-4 bands.

In Figure 3.2, we show the full (0.5-10 keV) X-ray luminosity function of all sources in XMM AO13, those matched with S0-DECam-NEWFIRM-IRAC, and those that are matched with a WISE-3 or WISE-4 detection. Although we calculate the X-ray luminosity function here to show the effects of requiring photometric completeness and WISE photometry on our sample, we refer the reader to Ananna et al. (2019) for the latest evolving X-ray luminosity function which includes the effects of X-ray absorption and also includes data from multiple surveys in order to overcome the luminosity-redshift correlation in any one flux-limited survey. The X-ray luminosity function here is calculated using the $1/V_{\rm max}$ method described in

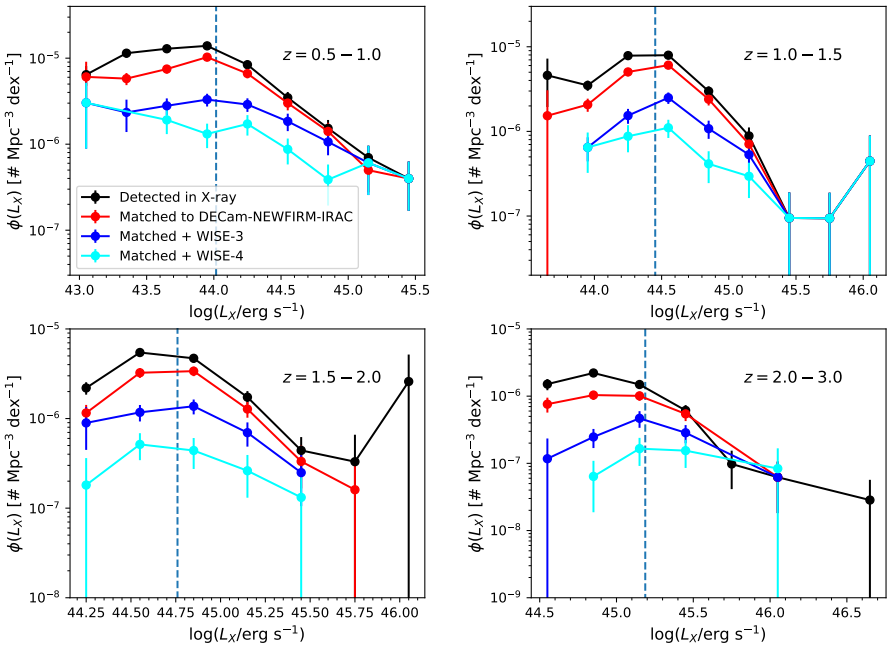

Figure 3.2: The full (0.5-10 keV) X-ray luminosity function of all XMM AO13 sources that fall in SHELA (black), those that have a reliable counterpart in the DECam-NEWFIRM-IRAC catalog through crossmatching with the MLE method (red), matched sources with a WISE-3 detection (dark blue) and matched sources with a WISE-4 detection (light blue) in four different bins of redshift. The luminosity function here is computed using the $V_{\rm max}$ method (see Section 2.4.1). The dashed line in each panel indicates the 80% X-ray luminosity completeness limit, computed from the 80% flux limit at the upper edge of each redshift bin.

Schmidt (1968). In the $1/V_{\rm max}$ method, the luminosity (or mass) function of a sample of galaxies is calculated by dividing the number of galaxies at a given luminosity (or mass) bin by the bin width times the differential comoving volume ΔV_C, where ΔV_C is the difference between the comoving volume ($V_{\rm max}$) at a maximum redshift that a source of given luminosity (or mass) can probe and the comoving volume at the low edge of the redshift bin. This method tries to correct the luminosity (or mass) function for the fact that flux-limited observational surveys increasingly fail to detect faint sources at higher redshifts, and are therefore biased to produce an artificial drop in the number density of faint sources at higher redshifts. We note that the X-ray luminosity function drops by almost an order of magnitude for sources with WISE-3 counterparts above the X-ray completeness limit, and even more for sources with WISE-4 counterparts. This means that requiring a WISE-3 or WISE-4 detection would cause us to incompletely sample the X-ray luminosity function at $z = 0.5 - 3$. Furthermore, as shown in Figure 3.1 and Table 3.2.4, our sample of X-ray luminous AGN (S1-Lum-AGN) would be reduced from 932 to 356 sources if we require WISE detections. Therefore, in order to better sample the X-ray luminosity function and prevent a drastic reduction in sample size, we do not use S1-Lum-AGN-WISE in our main analysis. However, in the Appendix, we perform tests on this sample to verify that the inclusion of WISE mid-IR data would not change the results of this work.

Table 3.2.4 shows the total number of sources ($N_{\rm tot}$) in the full sample based on the DECam-NEWFIRM-IRAC catalog (S0-DECam-NEWFIRM-IRAC), the sample of X-ray luminous AGN (S1-Lum-AGN), and the subset of the latter sample with WISE detections (S1-Lum-AGN-WISE), as well as the number of sources above the X-ray completeness limit and stellar mass completeness limit for each sample. The X-ray luminosity completeness limit we use here is computed from the 80% completeness full flux band limit of XMM AO13 ($F_X = 2.0 \times 10^{-14}$

erg s^{-1} cm^{-2}), estimated from the flux area curves given in LaMassa et al. (2016). We take this flux limit and convert to a luminosity at the high end of each given redshift range to generate an 80% luminosity completeness limit of $L_x = 10^{44.03}$ erg s^{-1} at $z = 0.5 - 1$, $L_x = 10^{44.47}$ erg s^{-1} at $z = 1 - 1.5$, $L_x = 10^{44.78}$ erg s^{-1} at $z = 1.5 - 2$, and $L_x = 10^{45.21}$ erg s^{-1} at $z = 2 - 3$. The source of X-ray emission for all galaxies in this sample should be entirely dominated by the respective AGN component of each galaxy, given that we only analyze sources with $L_X > 10^{44}$ erg s^{-1}. AGN activity is the most likely mechanism in a galaxy capable of producing such high X-ray luminosities (Brandt & Alexander, 2015).

As an additional test, we explore whether our selection of X-ray luminous AGN using the X-ray energy band at 0.5-10 keV might lead us to pick low-luminosity AGN with enhanced SF by comparing our study with other studies that use the more traditional X-ray hard band luminosities, at 2-10 keV, for selecting AGN (LaMassa et al., 2019; Masoura et al., 2018; Brandt & Alexander, 2015; Brandt & Hasinger, 2005). These studies classify sources with hard X-ray band luminosities greater than L(2-10 keV) $\sim 10^{42}$ erg $^{-1}$ as sources hosting X-ray luminous AGN, while galaxies without AGN typically have hard X-ray emission below this threshold and an extremely small number of starburst galaxies may exceed this threshold, but not by much (Lehmer et al., 2008). We compute the rest-frame hard X-ray luminosity for each source as described in LaMassa et al. (2019) and find that all sources in our sample with X-ray full band (0.5-10 keV) luminosities above 10^{44} erg s^{-1} have rest-frame X-ray hard band (2-10 keV) luminosities greater than $10^{43.5}$ erg s^{-1}, which is more than a magnitude greater than the L(2-10 keV) = 10^{42} erg s^{-1} luminosity threshold used in the aforementioned studies. Therefore, we conclude it is unlikely that many of our X-ray luminous AGN are actually low-luminosity AGN with enhanced SF.

It is important to note here that our sample likely contains a large number

of Type I AGN (i.e., AGN whose broad-line region is visible with respect to the observer) and a very small number of Type II AGN (i.e., AGN whose broad-line region is obscured with respect to the observer) as several studies (LaMassa et al., 2016; Burlon et al., 2011) find very few obscured AGN with X-ray luminosities above 10^{44} erg s^{-1}. These obscured sources in Stripe 82X tend to be optically classified as "normal" galaxies but are considered AGN because their X-ray luminosities exceed the 10^{42} erg s^{-1} luminosity threshold, while quasars and broad-line sources can be found at all X-ray luminosities and make up the majority of sources with X-ray luminosities greater than 10^{44} erg s^{-1}. We therefore note that the results of the analysis presented in this paper do not extend to all populations of AGN types, and likely apply mostly to Type I AGN (broad-line sources and quasars). While it is possible that we could also be missing obscured sources in our sample that are intrinsically X-ray luminous AGN, we note that Powell et al. (2020) estimate how many additional X-ray luminous AGN would be added to their high luminosity sample ($L_X > 10^{44.5}$ erg s^{-1}, where L_X is the X-ray full band luminosity at 0.5-10 keV) if they corrected their luminosities for dust obscuration assuming a column density distribution matching that of XMM-XXL AGN (Liu et al., 2016) and found that their sample would only increase by $\lesssim 4\%$. We therefore conclude that our sample of X-ray luminous AGN is unlikely to be missing many luminous AGN due to dust obscuration.

Galaxies without X-ray luminous AGN

We create a sample of galaxies without X-ray luminous AGN, which we refer to as S2-No-Lum-AGN, from sources in S0-DECam-NEWFIRM-IRAC that do not have an X-ray counterpart. We derive photometric redshifts for this sample using the EAZY-py photometric redshift SED fitting code (description of original EAZY code in Brammer et al., 2008) and keep all sources with $z_{\rm phot} = 0.5 - 3$. EAZY-py fits a

Sample	$z = 0.5 - 1.0$	$z = 1.0 - 1.5$	$z = 1.5 - 2.0$	$z = 2.0 - 3.0$
(a)	(b)	(c)	(d)	(e)
(1) S0-DECam-NEWFIRM-IRAC	156,978	91,193	22,753	48,912
(2) S1-Lum-AGN				
i.) Total Number $N_{\rm tot}$	352	273	184	123
ii.) $L_X > L_{X,\rm lim}$	147	136	71	32
iii.) $L_X > L_{X,\rm lim}$ & $M_* > M_{*,95\%\rm lim}$	131	83	30	14
(3) S1-Lum-AGN-WISE				
i.) Total Number $N_{\rm tot}$	133	112	72	39
ii.) $L_X > L_{X,\rm lim}$	75	64	35	19
iii.) $L_X > L_{X,\rm lim}$ & $M_* > M_{*,95\%\rm lim}$	71	37	12	10
(4) S2-No-Lum-AGN				
i.) Total Number $N_{\rm tot}$	156,626	90,920	22,569	48,789
ii.) $M_* > M_{*,95\%\rm lim}$	95,048	42,155	7,991	8,571
(5) S2-No-Lum-AGN-WISE				
i.) Total Number $N_{\rm tot}$	3,487	903	116	189
ii.) $M_* > M_{*,95\%\rm lim}$	3,353	836	98	132

Table 3.1: (1) The sample S0-DECam-NEWFIRM-IRAC contains galaxies which have a detection in the u, g, r, i, z bands, S/N > 5 in the K-band, and S/N > 2 in the two IRAC bands, and overlap with the Stripe 82X survey (see flowchart in Figure 3.1 for an illustration of how samples are selected). (2) The sample S1-Lum-AGN contains a subset of galaxies in S0-DECam-NEWFIRM-IRAC that have an X-ray luminous AGN. The total number of galaxies in the sample, as well as the number of galaxies with X-ray luminosities above the completeness limit ($L_X > L_{X,\rm lim}$) and stellar masses above the 95% stellar mass completeness limit ($M_* > M_{*,95\%\rm lim}$) are shown. (3) The sample S1-Lum-AGN-WISE contains the much smaller subset of galaxies in S1-Lum-AGN that have matching WISE photometry. (4) The sample S2-No-Lum-AGN contains the subset of galaxies in S0-DECam-NEWFIRM-IRAC that do not contain an X-ray luminous AGN. (5) The sample S2-No-Lum-AGN-WISE contains the smaller subset of sources in S2-No-Lum-AGN that also have WISE photometry.

set of Flexible Stellar Population Synthesis (FSPS) templates (Conroy & Wechsler, 2009; Conroy et al., 2009) that span a wide range of galaxy types (e.g., star-forming, quiescent, dusty, etc.) in non-negative linear combination. The photometric redshift, $z_{\rm phot}$, is determined from the combination of templates that have the lowest χ^2 value. To ensure we have a sample of galaxies that are all well fit by the EAZY-py templates, we implement a cut of $\chi^2 < 10$ on the entire sample. Comparison with the available SDSS spectroscopic redshifts reveal a 1σ scatter of $\Delta z/(1+z_{\rm spec}) = 0.037$. Although this comparison is only done for bright, low redshift ($z < 1$) sources, Sherman et al. (2020a) find a 1σ scatter of $\Delta z/(1+z_{\rm spec}) = 0.168$ for a sample of 16 bright $1.5 < z < 3.5$ galaxies with HETDEX spectroscopic redshifts using EAZY-py and the same photometry we use in this work, indicating fair agreement between the EAZY-py redshifts and spectroscopic redshifts. We explore the impact of uncertainty in redshifts on the SFRs of our sample of galaxies without X-ray luminous AGN by shuffling the EAZY-py redshifts by 1σ. For the aforementioned case of $\sigma = 0.037$ (applicable to bright sources with $z < 1$), there is a scatter of $\sim 2-3$ when comparing the reshuffled SFRs to the original SFRs, but the average SFR remains the same. For the case of $1\sigma = 0.168$ (which applies for galaxies at $1.5 < z < 3.0$), we find that after shifting the photometric redshift of our galaxies at $z > 1.5$ by 1σ, the majority ($> 90\%$) of galaxies have reshuffled SFRs within 0.5 dex of the original SFR, while a small percentage ($< 2\%$) have SFRs that shift by more than 1 dex. We therefore conclude that this photometric redshift uncertainty would not change the main results of this paper.

We create a subsample of objects in S2-No-Lum-AGN with a WISE-3 or WISE-4 counterpart, which we refer to as S2-No-Lum-AGN-WISE by crossmatching with the WISE catalog. Similar to what is described for S1-Lum-AGN-WISE in the previous section, we do not include S2-No-Lum-AGN-WISE in our main analysis. Rather, in the Appendix, we perform tests on this sample S2-No-Lum-AGN-WISE

to verify that the inclusion of WISE mid-IR data would not change the results of this work.

Our sample S2-No-Lum-AGN has a total of 318,904 sources. Of these, only 4,695 have a WISE-3 or WISE-4 detection. The number of sources in S2-No-Lum-AGN and S2-No-Lum-AGN-WISE is also shown in Table 3.2.4, along with the number of sources above the stellar mass completeness limit at a given redshift range.

3.3 SED Fitting

In this section we describe the SED fitting process that allows us to derive stellar masses and SFRs for our samples. One challenge that has persisted in the study of AGN host galaxies is determining the impact of AGN emission on the host galaxy's SED and having the ability to accurately decompose the galaxy SED into stellar, dust, and AGN components. An AGN can have a significant effect on the light of the galaxy SED across a wide range of wavelengths, and the magnitude of the effect depends on the strength and phase of the AGN, and the orientation of the AGN with respect to the observer. Another challenge that persists in the study of AGN is due to the wide variety of SED fitting codes. Many SED fitting codes do not include AGN emission templates in their code (e.g., EAZY-py (Brammer et al., 2008), MAGPHYS (da Cunha et al., 2008), iSEDfit (Moustakas et al., 2013), GalMc (Acquaviva et al., 2011), etc.), while others that do include AGN emission (e.g., AGNfitter (Calistro Rivera et al., 2016), SED3FIT (Berta et al., 2013), etc.) will often try to include an AGN component where none may exist, thus making such codes unsuitable for fitting samples of galaxies without X-ray luminous AGN. This creates a further issue: many studies that measure and compare the properties of galaxies with luminous AGN to galaxies without luminous AGN do not estimate the properties of both populations in a self-consistent manner (Shimizu et al., 2015, 2017; Masoura et al., 2018; Santini et al., 2012).

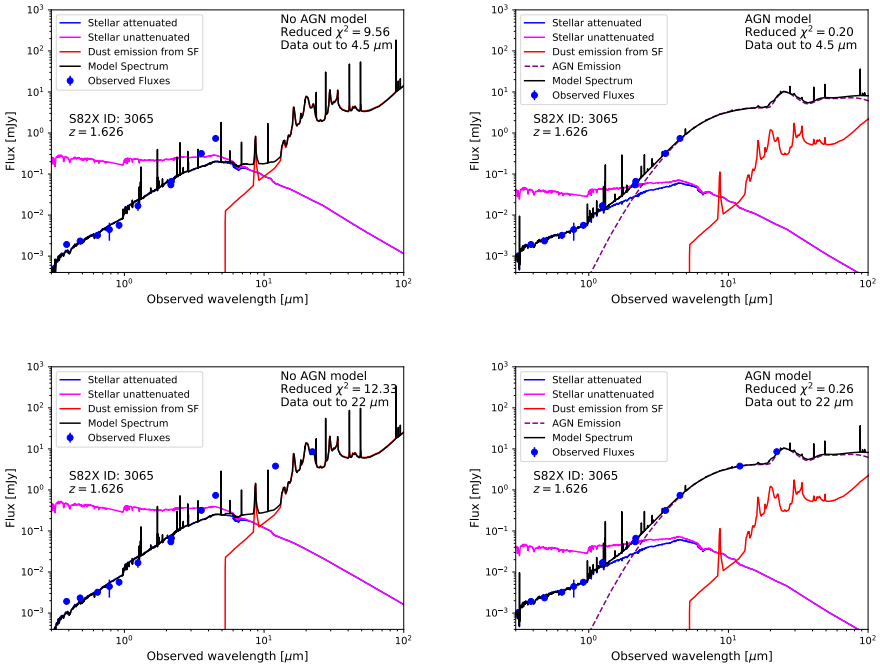

Figure 3.3: This figure compares model SED fits for a galaxy, whose redshift and Stripe 82X ID is displayed in each panel, with a type II X-ray luminous AGN in our samples S1-Lum-AGN (top two panels, with data coverage out to 4.5 μm and S1-Lum-AGN-WISE (bottom two panels with data coverage out to 22 μm) for SED fits that do not include AGN emission (left) and include AGN emission (right). The final model SED fit (solid black line) with AGN emission (right) is made up of the attenuated stellar emission (blue; which is inferred from the unattenuated stellar emission (magenta)), the dust emission from dust heated by massive stars from recent SF (red), the combined AGN emission (purple) from the accretion disk (particularly important at UV+optical wavelengths) and the dusty torus (particularly important at the $3 - 1000$ μm wavelength range). The best-fit model SED without AGN emission (left) clearly cannot provide a good fit to the observed fluxes at wavelengths past 1 μm, therefore, the AGN emission templates are needed in order to constrain all emission above 1 μm. While WISE data at 12 and 22 μm can provide important constraints on the SED at longer wavelengths, a comparison of the top and bottom right panels of Figure 3.3 shows that for the galaxy fitted here, the IRAC 3.6 and 4.5 μm photometry alone, without any WISE photometry, can provide important constraints on the SED fits with AGN emission templates.

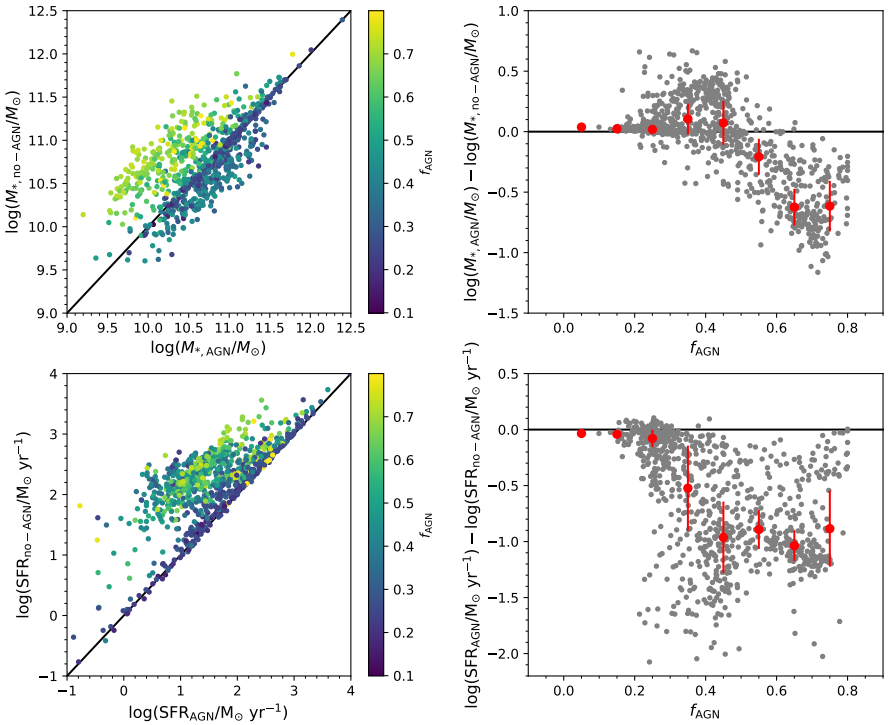

Figure 3.4: Left: Stellar mass and SFR estimates for our sample of galaxies with X-ray luminous AGN (S1-Lum-AGN) when AGN emission is included in the SED fit (x-axis) versus when AGN emission is not included (y-axis). Points are colored according to their fractional AGN contamination (f_{AGN}), defined as the fraction of light in the $8 - 1000$ μm wavelength range that is contributed by the AGN. Right: Difference in log stellar mass and SFR as a function of the fractional AGN contamination. Also shown is the median (red circles) log difference of stellar mass and SFR with and without the AGN emission in the SED fit in four bins of f_{AGN} with the median absolute deviation shown as error bars. Note that for $f_{\mathrm{AGN}} > 0.4$ stellar masses and star formation rates (SFRs) can be overestimated on average, by a factor of up to ~ 5 and ~ 10, respectively, if AGN emission templates are not included in the SED fit.

In order to accurately and consistently estimate properties of galaxies with and without X-ray luminous AGN, we perform SED fitting of both samples using the CIGALE (version 2018.0; Noll et al., 2009; Ciesla et al., 2015) SED fitting code. The CIGALE code offers several advantages over other SED fitting codes. First, CIGALE allows one to optionally include AGN emission templates in the SED fitting. This means one can quantify how the derived galaxy properties are affected by the inclusion or exclusion of AGN emission templates in the fit. More significantly, however, it allows us to derive stellar mass and SFR for galaxies with and without X-ray luminous AGN accurately and consistently using the exact same code.

We fit a total of 9 free parameters to the SED fit for our samples of galaxies with X-ray luminous AGN: 4 parameters for the star formation history (SFH), 1 parameter for the dust attenuation, and 4 parameters for the AGN emission templates. For galaxies without X-ray luminous AGN, we only fit 5 free parameters as we omit fitting the AGN emission templates for these galaxies. In our SED fitting of galaxies with X-ray luminous AGN, we include the AGN emission models of Fritz et al. (2006) for emission from the AGN accretion disk and dusty torus in the fit. For these AGN emission templates, we fit the AGN fraction contamination, $f_{\rm AGN}$, which is the total amount of light emitted at $8 - 1000$ μm that is attributed to the AGN, the orientational angle of the AGN ($\Psi = 0^\circ$ for a type II AGN, $\Psi = 90^\circ$ for a type I AGN), the optical depth at 9.7 μm, and the ratio of the maximum to minimum radii of the dusty torus. For both samples of galaxies with and without X-ray luminous AGN, we include models of dust emission attributed to SF (Dale et al., 2014), and the stellar populations of Bruzual & Charlot (2003). We assume attenuation of the galaxy SED by dust as described in Calzetti et al. (2000), a Chabrier initial mass function (IMF; Chabrier, 2003), and a delayed exponential SFH with a constant burst/quench term described by the following equation:

$$\begin{aligned} &\mathrm{SFR(t)} \propto \mathrm{t} \times \exp\left(-\mathrm{t}/\tau\right), \text{when } \mathrm{t} \leq \mathrm{t_{trunc}} \\ &\mathrm{SFR(t)} \propto \mathrm{r} \times \mathrm{SFR(t = t_{trunc})}, \text{when } \mathrm{t} > \mathrm{t_{trunc}} \end{aligned} \tag{3.1}$$

where r is the constant burst/quench term, defined as the ratio between SFR(t) and SFR(t = $\mathrm{t_{trunc}}$) at $t > t_{\mathrm{trunc}}$, and t_{trunc} is the time at which the SFR experiences an instantaneous increase or decrease given by the burst/quench term r (see Ciesla et al., 2018, 2016, for description of SFH). Previous studies (e.g., Fumagalli et al., 2011; Boselli et al., 2006) have proposed using a delayed SFH which could undergo a strong decrease in SFR. Such an SFH would allow for more flexibility in modeling the recent SFH of quenched galaxies or starbursts (Ciesla et al., 2018, 2016). Ciesla et al. (2017) showed that this SFH provides a good estimate of the SFR on main-sequence galaxies, starbursts, and rapidly quenched systems at all redshifts. The SFRs we report here are the instantaneous SFRs given by this SFH, and thus, are obtained from equation (1) at $t = t_{\mathrm{age}}$, where t_{age} is the presently observed age of the galaxy.

We make note here of the various factors that contribute to the dispersion of estimated SFRs. Work done by Buat et al. (2014) assesses the reliability of estimated SFRs from CIGALE for galaxies at $1 < z < 3$. They report full consistency between the instantaneous SFRs output by CIGALE, assuming different SFHs, to total SFRs estimated by empirical recipes using UV and FIR luminosities, suggesting the choice of SFH in CIGALE does not have a strong impact on the estimated SFR. Additionally, it is important to note that differences in the IMF and metallicity can affect the estimate of SFR. Buat et al. (2014) find that variation in the IMF changes the derived SFRs by a factor of up to ~ 0.17 dex, and variation in metallicity can change the derived SFRs by a factor of up to ~ 0.2. All of these factors are important to consider when estimating and reporting SFRs for a given sample, however, we believe the choice of SFH, IMF, and metallicity for this study

should not have a large impact on our results.

We perform our analysis with the Fritz et al. (2006) smooth dusty torus AGN emission templates because they are by far the most flexible AGN emission models available in CIGALE and cover a large range of parameters. However, we discuss here the implications of selecting the smooth dusty torus models of Fritz et al. (2006) over the clumpy dusty torus models that several other studies have investigated (Mullaney et al., 2011; Meléndez et al., 2014). Observations have provided evidence in favor of both clumpy (Tristram et al., 2007) and smooth (Ibar & Lira, 2007) dusty toroidal distributions which are both often used in modeling the SED of X-ray luminous AGN. Feltre et al. (2012) perform a comparison of both smooth and clumpy dust torus distributions widely used in the literature, comparing the Fritz et al. (2006) models, for a smooth dusty torus, to the Nenkova et al. (2008) models, for a clumpy dusty torus. They find that models with matched parameters between smooth and clumpy distributions do not produce similar SEDs and only a very limited number of random parameter combinations can produce seemingly identical SEDs for both distributions. Interestingly, they find that most of the differences in the SEDs between these two published models are due to different dust chemical composition rather than dust morphology.

In terms of differences caused by dust morphology, Feltre et al. (2012) find that the clumpy AGN emission templates peak at slightly longer wavelengths, tend to have wider IR bumps, and steeper mid-IR slopes than the smooth dust models. It is possible that mean SFRs would be slightly lower when clumpy emission templates are applied as more emission at $8 - 1000$ μm would be attributed to AGN activity, however, this would not be universal as the smooth templates could have wider IR bumps (within a matched parameter space than the clumpy templates).

3.3.1 Impact of AGN Emission on SED Fit and Derived Physical Properties

It is especially important to include AGN emission in the SED fit of galaxies with X-ray luminous AGN as it can have a drastic impact on the derived properties of the host galaxy, such as stellar mass and SFR. In the UV+optical wavelength regime, a large portion of the emitted light of a luminous type I AGN (i.e., an AGN with the broad line region visible to the observer) is attributed to the AGN accretion disk. In the case of type I and possibly type II AGN (i.e., an AGN whose broad line region is obscured with respect to the observer), at rest-frame wavelengths greater than 1μm, the SED of a galaxy with a luminous AGN is impacted by the AGN's dusty torus as the AGN's power-law flux drowns the polycyclic aromatic hydrocarbon (PAH) features in the SED. The CIGALE code includes the AGN emission of the accretion disk, as well as emission from the dusty torus in the SED fit, then carefully removes this emission from the derived SED when estimating the host galaxy properties.

In the top row of Figure 3.3, we show as an example the SED of a galaxy with an X-ray luminous AGN before and after AGN emission is included in the fit for galaxies with data out to 4.5 μm. Note that the AGN emission affects all emission above 1 μm. The bottom row of Figure 3.3 shows the same comparison, but this time also including WISE 12 and 22 μm photometry. While WISE data at 12 and 22 μm can provide important constraints on the SED at long wavelengths, a comparison of the top and bottom right panels of Figure 3.3 shows that in the galaxy fitted here, the IRAC 3.6 and 4.5 μm photometry alone, without any WISE photometry, can provide important constraints on the SED fits with AGN emission templates.

The inclusion of the AGN component can have a strong impact on the derived stellar masses and SFRs as the former will depend on whether the entire SED is dominated by a luminous AGN and the latter will depend on whether the UV and

the near-to-far-IR light is attributed solely to stars and dust associated with SF or to a mix of stars, dust associated with SF, and AGN. When including AGN emission in the model SED fit, the CIGALE code will estimate the fraction ($f_{\rm AGN}$) of light in the $8-1000$ μm wavelength range that is contributed by the AGN. In Figure 3.4, we quantify the effect of not including an AGN component in the SED fitting using our sample of galaxies with X-ray luminous AGN (S1-Lum-AGN), which have data from the UV band out to IRAC 4.5μm, but no WISE data. Galaxies with $f_{\rm AGN} < 0.4$ can have SFRs that are overestimated by a factor of up to 2, on average, and those with $f_{\rm AGN} > 0.4$ can have SFRs overestimated by a factor of up to 10, on average, when AGN emission templates are not included in the SED fitting. In a few cases, the SFR can be overestimated by a factor ~ 100 when AGN emission templates are excluded from the SED fit. For this reason, we emphasize that SED fitting of galaxies with X-ray luminous AGN should require AGN emission templates.

Figure 3.4 also shows the impact on derived stellar masses. For $f_{\rm AGN} > 0.4$, stellar masses can, on average, be overestimated by a factor of up to 5 when AGN emission templates are not included in the SED fit. This happens because without the AGN emission template, all of the of the light emission of the galaxy is assumed to come from stellar sources and dust as opposed to the AGN central engine. For galaxies with $f_{\rm AGN} < 0.4$, stellar masses can be underestimated by a factor of up to 3 if AGN emission templates are not included in the SED fit. The underestimate of stellar masses in some of the galaxies with $f_{\rm AGN} < 0.4$ happens because without the AGN emission templates, the AGN-boosted mid-IR luminosities of these galaxies will be fit by dusty stellar population templates instead of the AGN dusty torus templates. This in turn causes CIGALE to assume that the galaxy SED has a younger, dustier stellar population than it really does, thereby lowering the stellar masses estimates.

As mentioned earlier, the results shown in Figure 3.4 are based on the sample

of galaxies with X-ray luminous AGN (S1-Lum-AGN) that have data from the UV band out to 4.5 μm, but no WISE data at 12 and 22 μm. We made the decision not to limit our analysis to only sources with WISE data as our sample size would be drastically reduced (see Figure 3.1). Instead, we confirmed that not including the WISE data does not change the results in this paper by performing additional tests in the Appendix. Figures A.1 and A.2 in the Appendix show that the exclusion of WISE data does not change the results of Figure 3.4 and does not have a systematic effect on the derived stellar mass and SFR. This can in part be understood by the fact that in many galaxies, such as the one shown in Figure 3.3, the SED fit is already constrained by the data just below 5 micron and remains unchanged with or without WISE photometry included in the fit.

We include AGN emission templates when we fit the samples (S1-Lum-AGN and S1-Lum-AGN-WISE) of galaxies hosting X-ray luminous AGN. However, we do not include AGN emission templates in the SED fit of the sample (S2-No-Lum-AGN and S2-No-Lum-AGN-WISE) of galaxies without X-ray luminous AGN because (a) it is computationally expensive to fit the AGN emission models to $> 100,000$ galaxies and (b) when we do include the AGN emission in the SED fit of a small subsample of galaxies in S2-No-Lum-AGN-WISE we find that $f_{\rm AGN}$ is extremely low (< 0.05) for 90% of the sample, moderately low (< 0.2) for 8% of the sample, and that there is no systematic change in the derived SFRs.

3.4 Derived Stellar Mass and SFR of Sample Galaxies

We discuss in the following subsections the stellar mass completeness, stellar mass function (SMF) (Section 3.4.1) and SFR distributions (Section 3.4.2) of our sample of galaxies with (S1-Lum-AGN) and without (S2-No-Lum-AGN) X-ray luminous AGN.

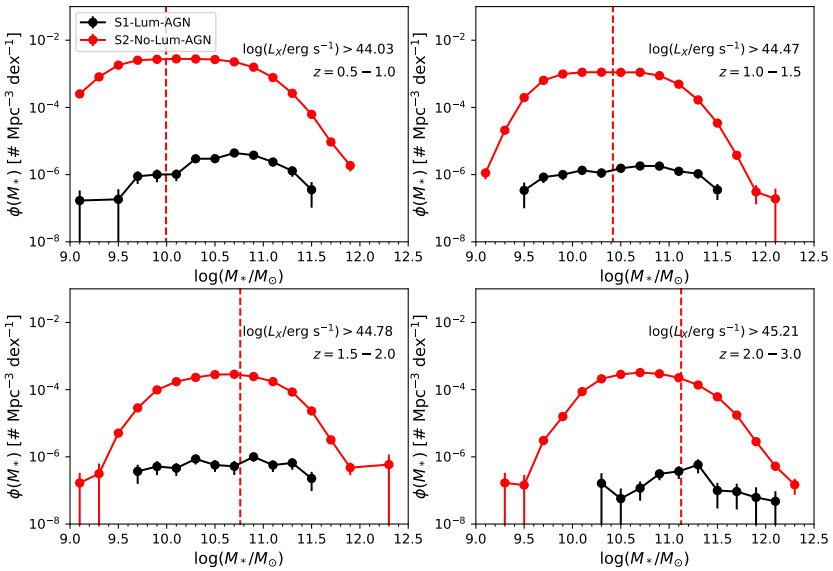

Figure 3.5: Galaxy stellar mass function (SMF) for our samples of galaxies with (S1-Lum-AGN, black) and without (S2-No-Lum-AGN, red) X-ray luminous AGN at four different redshift ranges. All galaxies with X-ray luminous AGN (S1-Lum-AGN) are complete in X-ray luminosity at their respective redshift bin; we show the X-ray completeness limit in each panel. The dashed vertical line indicates the stellar mass completeness of the sample of galaxies without X-ray luminous AGN (S2-No-Lum-AGN) at each bin. The error bars at each stellar mass bin are Poisson errors. The SMF is calculated using the $1/V_{\rm max}$ correction described in Section 3.2.4 for the X-ray luminosity function. We find that the SMF of galaxies with X-ray luminous AGN is much lower than the SMF of galaxies without X-ray luminous AGN by ~ 2 orders of magnitude at $M_* > 10^{11}\ M_\odot$ and by ~ 3 orders of magnitude at $M_* < 10^{11}\ M_\odot$.

3.4.1 Distribution of Stellar Masses

To estimate stellar mass completeness for each sample, we follow the procedure described in Pozzetti et al. (2010) and Davidzon et al. (2013). As per this method, we assume that the mass completeness limit of a survey can be estimated from the mass of the least massive galaxy that can be detected in a given bandpass with a magnitude equal to the magnitude limit of the survey in that bandpass. At each redshift, we select a representative sample from the faintest 20% of galaxies and scale their stellar mass, $\log(M_*)$, using the following equation:

$$\log(M_{*,m=m_{\rm lim}}) = \log(M_*) + 0.4(m - m_{\rm lim}) \tag{3.2}$$

Here, m is the measured AB magnitude, and $m_{\rm lim}$ is the AB magnitude limit of the survey in a given bandpass. After scaling the stellar masses of the faintest 20% of objects, we take the 95th percentile of the scaled mass distribution to be the mass completeness limit at each redshift bin. For our K_S-band selected sample, the K_S-band limiting magnitude is the 5σ depth magnitude (22.4) measured in NEWFIRM. If we use this as $m_{\rm lim}$ in equation (2) to estimate the stellar mass completeness for sample S2-No-Lum-AGN, we find $\log(M_{*,95\%\rm lim}/M_\odot) = 9.99,\ 10.42,\ 10.76,\ 11.12$ at $z = 0.5 - 1.0,\ z = 1.0 - 1.5,\ z = 1.5 - 2.0,\ z = 2.0 - 3.0$, respectively, for the mass completeness limit.

Although different bandpasses, such as the IRAC 3.6 & 4.5 μm bandpasses, are better suited to tracing the stellar mass buildup of galaxies at $z \sim 2$, the Pozzetti et al. (2010) method for estimating stellar mass completeness takes into account the range in mass-to-light (M/L) ratios at different redshifts using a bandpass that is not close to rest-frame K. We find that the stellar mass completeness limits do not change by more than ~ 0.1 dex at all redshifts if we use IRAC 3.6 μm-band photometry instead of K_S-band photometry to estimate stellar mass completeness. We also find similar stellar mass completeness limits when using 4.5 μm-band pho-

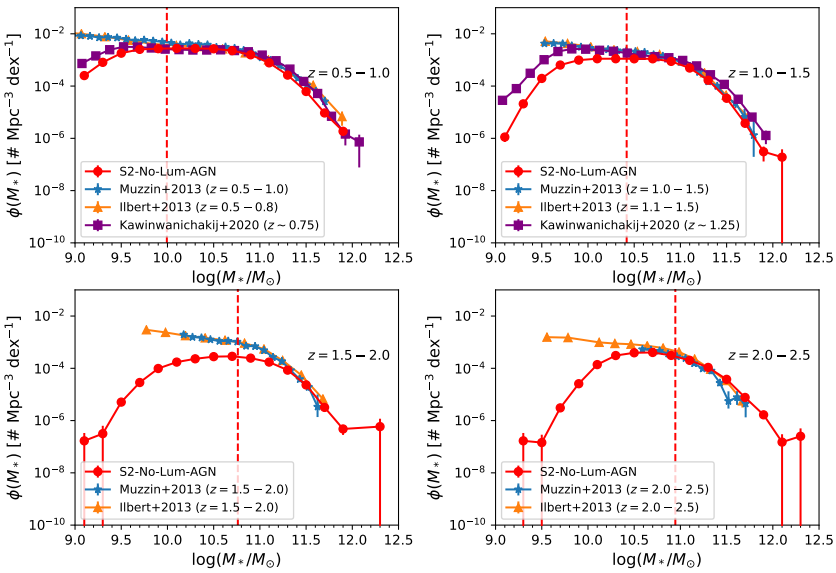

Figure 3.6: The observed galaxy SMF of our sample of galaxies without X-ray luminous AGN (S2-No-Lum-AGN, red) in four redshift bins with observed literature values at the corresponding redshifts plotted from Muzzin et al. (2013) at $z = 0.5 - 2.5$ (blue, stars), Ilbert et al. (2013) at $z = 0.5 - 2.5$ (orange, triangles), and Kawinwanichakij et al. (2020) at $z \sim 0.75$ and $z \sim 1.25$ (purple, squares). As in Figure 3.5 for our sample, the red dashed line represents the stellar completeness limit of our sample, error bars represent Poisson errors, and the SMF is calculated using the $1/V_{\rm max}$ method. We end the last redshift bin here at $z = 2.5$, instead of $z = 3.0$, for comparison purposes. We find good agreement with other observed SMFs at all redshifts for galaxies with $\log(M_*/M_\odot) > 11$ and at all stellar masses above our completeness limit for all redshift ranges except $z = 1.5 - 2.0$ (see text).

tometry to those estimated from K_S-band photometry (i.e., do not vary by more than ~ 0.1 dex) at $z < 2$. At $z = 2.0 - 3.0$, the stellar mass completeness limits estimated from IRAC 4.5 μm-band photometry is 0.3 dex lower than when estimated from K_S band photometry. Because our sample is a K_S-band selected sample, and stellar mass completeness limits do not vary much when using K_S, 3.6, or 4.5 μm-band photometry, we decide to use the K_S limiting magnitude and photometry to estimate stellar mass completeness.

Lastly, we apply this method to our sample of galaxies with X-ray luminous AGN (S1-Lum-AGN) to estimate stellar mass completeness limits for that sample and find that the stellar mass completeness limits of S1-Lum-AGN are lower by 0.1-0.2 dex at $z < 1.5$, and by 0.3-0.5 dex at $z > 1.5$, when compared to those of our sample of galaxies without X-ray luminous AGN (S2-No-Lum-AGN). We use the more stringent completeness limit found from S2-No-Lum-AGN as the stellar mass completeness limits for both samples in this analysis.

In Figure 3.5, we plot the observed SMF of galaxies with (S1-Lum-AGN) and without (S2-No-Lum-AGN) X-ray luminous AGN in four different bins of redshift across $z = 0.5 - 3$. The SMF is estimated using the $1/V_{\rm max}$ method described in Section 3.2.4 for the X-ray luminosity function. The dashed line in each panel indicates the completeness limit of the sample S2-No-Lum-AGN. *The SMF for the sample (S1-Lum-AGN) of galaxies with X-ray luminous AGN shows that the number density of such systems is about three orders of magnitude lower than galaxies without X-ray luminous AGN at* $\log(M_*/M_\odot) < 11$ *and about two orders of magnitude lower at* $\log(M_*/M_\odot) > 11$*, at all redshifts.* All galaxies in S1-Lum-AGN are complete in X-ray luminosity at each given redshift range, and AGN-host galaxies with $L_X > 10^{43}$ erg s^{-1} have been shown to exhibit a turnover with decreasing number densities towards lower masses at $\log(M_*/M_\odot) < 11$ (Bongiorno et al., 2016), which is consistent with what we observe in our SMF of galaxies with X-ray luminous

AGN.

We compare the observed SMF of our sample of galaxies without X-ray luminous AGN (S2-No-Lum-AGN) to the observed SMF from other studies in Figure 3.6. We plot the observed values of Muzzin et al. (2013) and Ilbert et al. (2013) at $z = 0.5 - 2.5$ and the observed values of Kawinwanichakij et al. (2020) at $z \sim 0.75$ and $z \sim 1.25$. Our observed SMF for S2-No-Lum-AGN agrees well with those from other studies at all redshifts for galaxies with $\log(M_*/M_\odot) > 11$ and at all redshifts, except $z = 1.5 - 2.0$, at stellar masses above the 95% completeness limit. The discrepancy between our SMF values and those of Muzzin et al. (2013) and Ilbert et al. (2013) at $z = 1.5 - 2.0$ could arise from a number of factors, such as cosmic variance, since both Muzzin et al. (2013) and Ilbert et al. (2013) probe the same small area (< 1.6 deg^2) on the sky, and/or a lack of photometric filters in our data that allow us to probe certain features in model spectra during SED fitting that can break degeneracies between different redshifts and cause us to miss certain galaxies at $z = 1.5 - 2.0$. Although we do not believe the latter to be the full cause of this discrepancy, we do not have other SMFs to compare to at this redshift range and our SMF agrees with that of Sherman et al. (2020b) at $z = 1.5 - 2.0$.

3.4.2 Distribution of Star Formation Rates

In Figure 3.7, we show the normalized SFR distribution for galaxies with (S1-Lum-AGN) and without (S2-No-Lum-AGN) X-ray luminous AGN. The SFR histograms are normalized by dividing the number of galaxies in each bin by the total number of objects in the redshift bin, such that the sum of all the histogram bins is equal to 1. We remind the reader that the SFRs reported here are the instantaneous SFRs given by equation (1) in Section 3.3 from the SFH of the SED fit. The SFR from an SED fit refers to the intrinsic extinction-corrected SFR and is typically constrained by fitting observed photometry ranging from the UV to the IRAC 4.5 μm band.

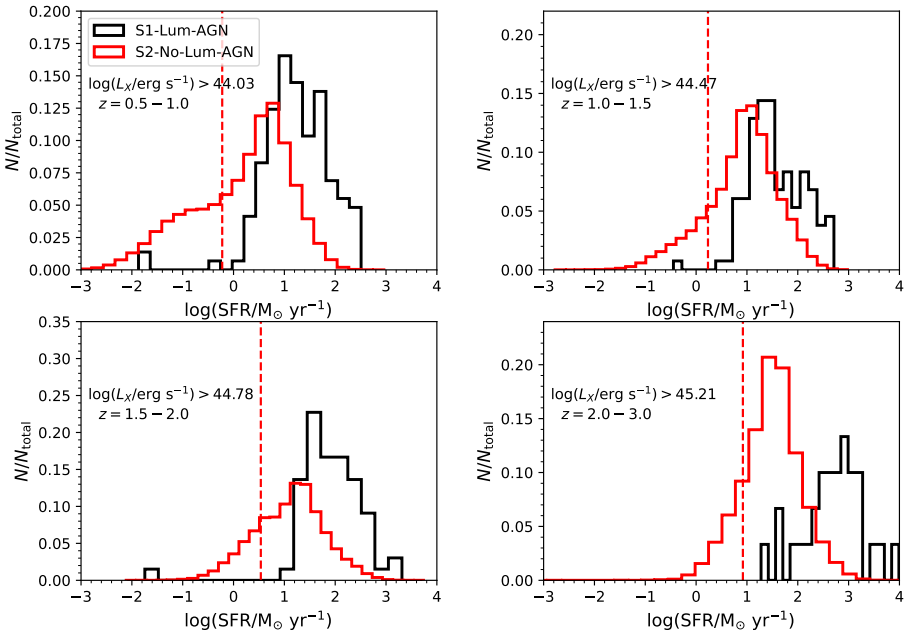

Figure 3.7: We plot the normalized histograms of the log of the measured SFR for our sample of galaxies with (S1-Lum-AGN, black) and without (S2-No-Lum-AGN, red) X-ray luminous AGN across four different redshift bins. The measured SFR refers to the intrinsic dust-corrected SFR derived from the SFH produced by SED fitting with CIGALE of the observed photometry from the UV to the IRAC 4.5 μm band. Note that galaxies with X-ray luminous AGN have a distribution of intrinsic SFRs skewed towards higher values than galaxies without X-ray luminous AGN. We also plot as dotted lines our estimated 5σ completeness limit for the observed dust-extincted FUV-based SFR, which is estimated from the 5σ detection limit in the u-band and g-band filters, which most closely trace the rest-frame 1500 Å luminosity at $z = 0.5 - 1.5$ and $z = 1.5 - 3.0$, respectively. See text in section 4.2 for details.

Figure 3.7 shows that the SFRs for galaxies with X-ray luminous AGN (S1-Lum-AGN) have a distribution skewed towards higher values, and therefore, have higher SFRs than galaxies without X-ray luminous AGN (S2-No-Lum-AGN). The median SFR values for both samples at each redshift range is $\log(\mathrm{SFR}/\mathrm{M}_{\odot}\mathrm{yr}^{-1}) = 1.18,\ 1.41,\ 1.77,\ 2.68$ for S1-Lum-AGN at $z = 0.5 - 1,\ z = 1 - 1.5,\ z = 1.5 - 2$, and $z = 2 - 3$, respectively, and $\log(\mathrm{SFR}/\mathrm{M}_{\odot}\mathrm{yr}^{-1}) = 0.41,\ 0.96,\ 1.15,\ 1.49$ for S2-No-Lum-AGN, respectively. The median SFR values are roughly a factor of 5-10 higher for galaxies with X-ray luminous AGN than galaxies without X-ray luminous AGN.

It is often useful in studies of galaxy evolution to estimate the completeness limit down to which one can measure the SFR. This is not so easy to do for our analysis as our measured SFRs refer to the intrinsic extinction-corrected SFR derived by fitting observed photometry over a wide range of wavelengths from the UV to the IRAC 4.5 μm band using a large set of SED templates with many free parameters. Getting a true completeness limit for this measured SFR would be complicated and requires the analysis of many observed bands and SED templates. Instead, we attempt here to make a simpler estimate of the observed dust-extincted FUV-based SFR by using the detection limits in just a few bands (DECam u and g bands) that trace the rest-frame UV luminosity from massive SF across our redshift range of interest.

For this estimate of the detection limit for the observed dust-extincted SFR, we start by converting the observed magnitude closest to the rest-frame FUV wavelength into a luminosity (i.e., DECam u-band at $z < 1.5$, DECam g-band at $z > 1.5$). We then compute the 100 Myr FUV-based dust-extincted SFR for our sample of galaxies without X-ray luminous AGN (S2-No-Lum-AGN), using the SFR calibrator from Hao et al. (2011) and assume a Kroupa IMF (Kroupa, 2001). The fact that SFRs computed in CIGALE assume a Chabrier (2003) IMF is not a problem as the

shifts in SFR calculated from either IMF are essentially negligible (Speagle et al., 2014).

We estimate the 5σ completeness limit for the observed dust-extincted FUV-based SFR similarly to how we estimate stellar mass completeness. That is, we take the 20% faintest galaxies in each redshift bin, using the u-band at $z < 1.5$ and the g-band at $z > 1.5$, and scale their FUV SFRs to the value they would have if their magnitude was equal to the limiting magnitudes of the survey (25.0 AB magnitude for u-band, 24.8 AB magnitude for g-band), which are the 5σ magnitude depths reported in Wold et al. (2019) using the following equation:

$$\log(\mathrm{SFR_{FUV,lim}}) = \log(\mathrm{SFR_{FUV}}) + 0.4(\mathrm{m} - \mathrm{m_{lim}}) \tag{3.3}$$

From the resulting distribution of values, we take the 95th percentile value as a lower limit to the 5σ completeness limit for the observed dust-extincted FUV-based SFR. The values are $\log(\mathrm{SFR}/\mathrm{M_\odot yr^{-1}}) = -0.22$, 0.23, 0.54, and 0.92 at $z = 0.5 - 1.0$, $z = 1.0 - 1.5$, $z = 1.5 - 2.0$, and $z = 2.0 - 3.0$, respectively. We thus expect our survey to detect dust-extincted FUV-based SFR above these values at the 5σ level. In practice, we do not use a S/N cut for the u or g-band fluxes in our analysis, so we should be able to measure dust-extincted FUV-based SFRs below these 5σ limit values.

We plot our estimated 5σ completeness limit for the observed dust-extincted FUV-based SFR as dotted lines on Figure 3.7, which also shows the distribution of measured SFRs for the samples of galaxies with (S1-Lum-AGN) and without (S2-No-Lum-AGN) X-ray luminous AGN. It is important to bear in mind that the measured SFRs from the SED fit and the observed dust-extincted FUV-based SFRs are two very different quantities. The measured SFRs from the SED fit refer to the intrinsic dust-corrected SFR of a galaxy based on the SED fit and observed photometry from the UV to the IRAC 4.5 μm band and are likely higher than the

observed dust-extincted FUV-based SFRs. The fact that we see some measured intrinsic SFR values lower than the 5 σ completeness limit for the observed dust-extincted FUV-based SFR is likely due to the fact that we do not use a S/N cut for the u or g-band fluxes in our analysis.

3.4.3 Testing CIGALE SFRs Against Previously Published Empirical SFRs

In this section and the following section, we explore whether the SFRs derived by CIGALE for galaxies hosting X-ray luminous AGN are reliable by performing two separate tests which are based, respectively, on previously published SFRs of real galaxies with X-ray luminous AGN and a set of synthetic mock galaxy SEDs.

For the first test, we compare SFRs derived from CIGALE with SFRs from the CANDELS catalog (Grogin et al., 2011; Koekemoer et al., 2011), where SFRs are derived from SED fitting using near-UV to near-IR photometry (see Yang et al., 2019, 2017, for description of SFR estimates). The SFRs presented in Yang et al. (2019) are median values of SFRs obtained from separate teams who perform SED fitting of the same sample and take the total SFR values from the SFH of the SED fit. We do not use the FIR-derived SFRs presented in Yang et al. (2019, 2017) as they are not corrected for AGN emission and thus would overestimate the SFR when converting between FIR luminosity and SFR (see Section 3.1 and Fig. 3). We select 38 sources in the CANDELS catalog with a Chandra X-ray detection with $L_X > 10^{43}$ erg s^{-1} in order to obtain SFRs, using CIGALE, for a sample of galaxies with X-ray luminous AGN. For these sources, we select available photometry from the COSMOS and Ultra-deep Survey (UDS) fields in CANDELS (i.e., CFHT MegaCam u, g, r, i, z-bands, NEWFIRM K_S-band (van Dokkum et al., 2009), IRAC 3.6 and 4.5 μm) to perform SED fitting using photometric bands that cover the same wavelength ranges that we use to perform SED fitting of our S1-

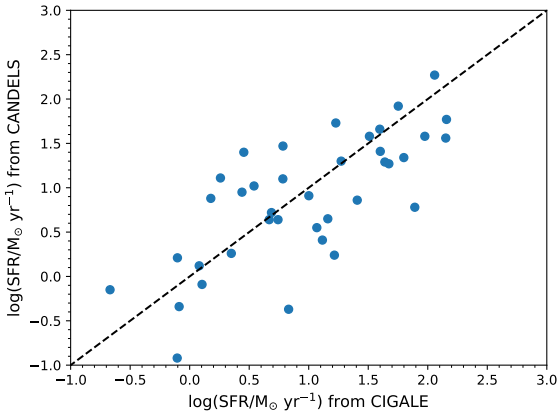

Figure 3.8: SFRs from CANDELS (y-axis) compared to SFRs derived from CIGALE using CFHT (u, g, r, i, z), NEWFIRM (K-band), and IRAC (3.6 and 4.5 μm) photometry for a sample of 38 galaxies with X-ray luminous AGN having $L_X > 10^{43}$ erg s^{-1}. Also shown is the one-to-one line (dashed, black).

Lum-AGN and S2-No-Lum-AGN samples. We also adopt the redshifts from the CANDELS catalog when we perform the SED fit in CIGALE.

In Figure 3.8, we show the SFRs obtained for the CANDELS sample described above using CIGALE to the published SFR values of the CANDELS catalog described in Grogin et al. (2011); Koekemoer et al. (2011). Only at the highest SFRs does the mean CANDELS SFR deviate from the one-to-one line by a factor of ~ 0.5 dex and we note only one source has an SFR that varies by an order of magnitude between the CIGALE SFR and CANDELS reported SFRs.

3.4.4 Testing CIGALE SFRs Against SFRs from Mock SEDs

In this section, we explore whether the SFRs derived by CIGALE for galaxies hosting X-ray luminous AGN are reliable by performing tests on a set of synthetic mock galaxy SEDs. We use CIGALE to generate mock galaxy SEDs with AGN emission and then perform SED fitting on the mock galaxy SED fluxes. We generate two sets of mock galaxy SEDs using the stellar population synthesis models of Bruzual

& Charlot (2003), assume a Chabrier (2003) IMF, and for one set of mocks we employ the Fritz et al. (2006) AGN emission templates with an updated version of the Draine & Li (2007) dust emission models, and for the other set of mocks we employ the Dale et al. (2014) combined dust and AGN emission models. We use varying dust and AGN emission templates when generating mock galaxy SEDs in order to test whether CIGALE can recover the properties of mock galaxies produced with varying models using the same emission templates discussed in Section 3.3.

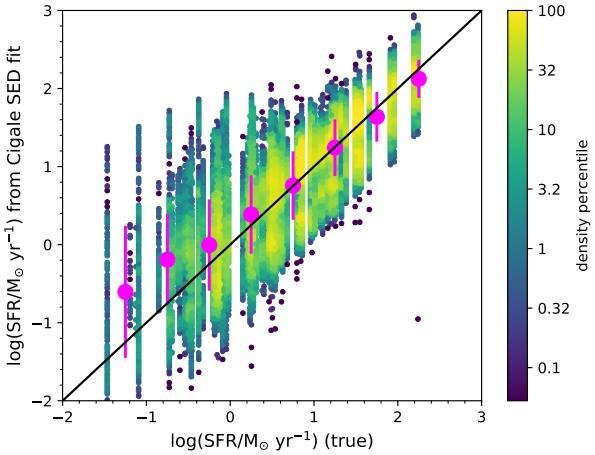

Figure 3.9: Comparison of SFRs from the mock galaxies (x-axis) versus SFRs obtained from the SED fit with CIGALE to the mock galaxy fluxes (y-axis). We do not include WISE photometry in this test in order to resemble the fits we are doing with our S1-Lum-AGN sample. Also shown is the one-to-one line and the mean of the log(SFR) (magenta circles) with the standard deviation represented by the error bars. All points are color-coded by their density on the x (mock SFR) and y (fit SFR) plane, where density is calculated by counting number of neighbors around each data point inside a circular aperture. We find relatively good agreement between the true SFRs of the mock galaxies and the CIGALE-derived SFRs above $\sim$ 1 $M_{\odot}\mathrm{yr}^{-1}$. At the low end of the true SFRs, some mock galaxies have high CIGALE-derived SFRs, however, only 2% of the mock galaxies have true SFRs that differ from their CIGALE-derived SFR by a factor of 10 or more and only 10% of mock galaxies have true SFRs that differ from the CIGALE-derived SFRs by a factor of 4 or more.

When we generate mock galaxy SEDs in CIGALE, we obtain mock observation fluxes in the DECam u, g, r, i, z bands, NEWFIRM K-band, and IRAC 3.6 and 4.5 μm bands. In order to assign flux errors for a given photometric band, we calculate the mean S/N of all sources in our data as a function of magnitude. We then use this mean S/N to assign flux errors to mock sources depending on what their magnitude is. This method produces reasonable flux errors in the mock photometry that match our data. At this stage we perturb the fluxes within the errors by drawing from a normal distribution centered around the mock flux with a standard deviation equal to the photometric error. With the new photometric fluxes and flux errors, we perform the same cuts on the mock objects as the real data to obtain a mock photometric sample that resembles our data in terms of magnitude and S/N ratios. That is, we only perform SED fitting on sources with a S/N greater than 5 in the K_S-band, a S/N greater than 2 in the two IRAC bands, and require a flux detection in the u, g, r, i, z bands.

In Figure 3.9, we compare the SFR derived from SED fitting with CIGALE to the true SFR of the mock galaxy. We only show the results for the mock galaxies generated from the Fritz et al. (2006) and Draine & Li (2007) AGN and dust emission templates. However, our results do not change for the mock galaxies where AGN and dust emission is generated from the Dale et al. (2014) templates, suggesting that the choice of AGN or dust emission templates in CIGALE should not have a large impact on the results.

In Figure 3.9, we see good agreement between the CIGALE-derived SFRs and the true SFRs of mock galaxies above $\sim 1\ M_{\odot}\mathrm{yr}^{-1}$ with a scatter of 0.5 dex. At the low SFR end there are some mock galaxies for which the CIGALE-derived SFRs are significantly higher than the true SFRs. However, only 2% of the mock galaxies have $|\Delta \log(\mathrm{SFR})| > 1$ (where $\Delta \log(\mathrm{SFR}) = \log(\mathrm{SFR_{fit}}) - \log(\mathrm{SFR_{true}})$) and only 10% of mock objects have $|\Delta \log(\mathrm{SFR})| > 0.6$, meaning 90% of our mock sample has

true SFRs that agree with the CIGALE-derived SFRs to within a factor of 3-4. Most of the large scatter between the true and fit SFRs lie at low SFRs ($< 1\ M_{\odot}\mathrm{yr}^{-1}$), however, we note that most ($> 80\%$) of our sample have SFRs above 1 $M_{\odot}\mathrm{yr}^{-1}$. At the low end of the true SFRs, some mock galaxies have high CIGALE-derived SFRs, however, only 2% of the mock galaxies have true SFRs that differ from their CIGALE-derived SFR by a factor of 10 or more and only 10% of mock galaxies have true SFRs that differ from the CIGALE-derived SFRs by a factor of 4 or more. We find that CIGALE does not produce a systematic bias towards higher or lower values of SFRs when recovering SFRs from the true mock galaxy SEDs.

3.5 Results

In the following section we compare the properties of the sample galaxies with (S1-Lum-AGN) and without (S2-No-Lum-AGN) X-ray luminous AGN at fixed redshift and stellar mass. Many studies have looked at the evolution of SFR with stellar mass across redshift (Whitaker et al., 2014; Speagle et al., 2014; Daddi et al., 2007; Elbaz et al., 2007), however, galaxies with X-ray luminous AGN are usually not included in these studies due to AGN emission contaminating the UV and IR wavelengths. Although there have been a few studies that look at the relation between stellar mass and SFR of galaxies with luminous AGN (Shimizu et al., 2015; Masoura et al., 2018; Santini et al., 2012), they do not derive stellar masses and SFRs for their galaxy samples with and without luminous AGN in a self-consistent manner, and their control sample of galaxies without luminous AGN is at least an order of magnitude smaller than the control sample (S2-No-Lum-AGN) in our study.

3.5.1 SFR as a Function of Stellar Mass and Redshift

In Figure 3.10 we show the stellar mass and SFR of our sample of galaxies with (S1-Lum-AGN) and without (S2-No-Lum-AGN) X-ray luminous AGN. The galax-

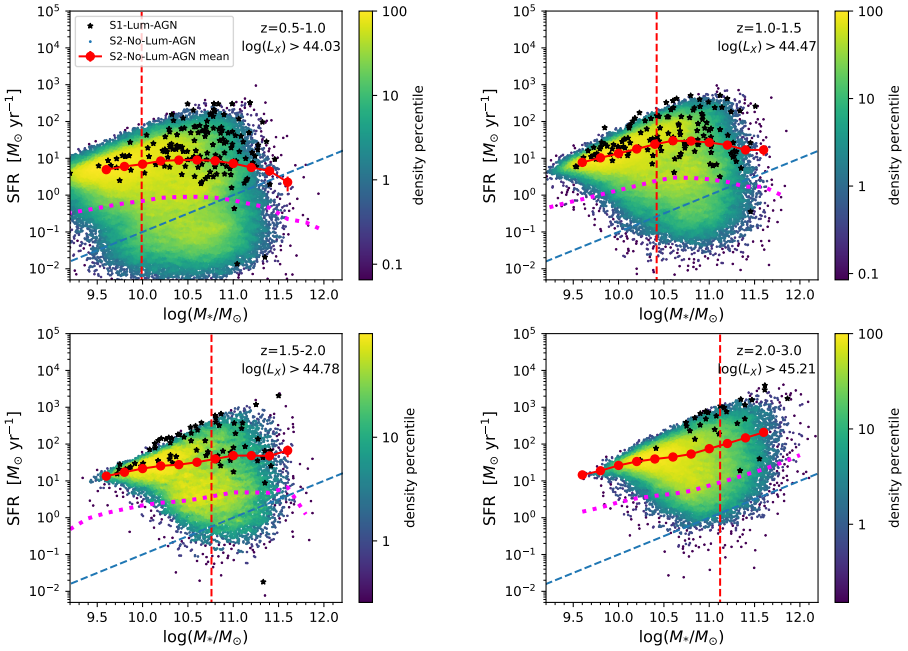

Figure 3.10: SFR vs. stellar mass for our sample of galaxies with (S1-Lum-AGN, black stars) and without (S2-No-Lum-AGN, colored points) X-ray luminous AGN in four different redshift bins. The S2-No-Lum-AGN galaxies are color-coded by their density on the stellar mass-SFR plane (see text). The dashed vertical line on each panel shows the stellar mass completeness limit in that bin (see Section 3.4.1). The X-ray completeness limit for S1-Lum-AGN is shown in each redshift bin in log units of ergs per second. Also shown are the mean SFR of S2-No-Lum-AGN as a function of stellar mass (red circles), which we refer to as the main sequence, the line that falls 1 dex below the main sequence (dotted magenta) and the line where the specific SFR is $10^{-11}\mathrm{yr}^{-1}$ (blue dashed). It is striking that galaxies with X-ray luminous AGN have higher mean SFRs than galaxies without X-ray luminous AGN at a given stellar mass (see also Figure 3.11). Note also that very few galaxies with X-ray luminous AGN have quenched SF if we use the common definition of quenched galaxies as having a specific SFR $< 10^{-11}\mathrm{yr}^{-1}$.

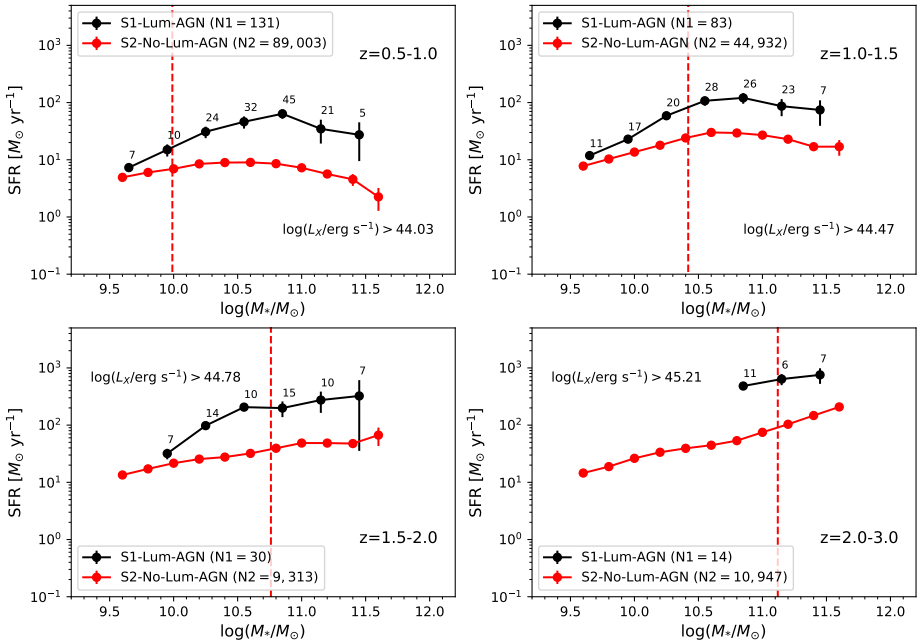

Figure 3.11: The mean SFRs for our sample of galaxies with (S1-Lum-AGN, black circles) and without (S2-No-Lum-AGN, red circles, same as those shown in Figure 3.10) X-ray luminous AGN as a function of stellar mass across four redshift bins. We show the total number (N1 and N2) of galaxies in each sample above the stellar mass completeness limit (shown here as vertical dashed lines), as well as the number of galaxies with X-ray luminous AGN in each stellar mass bin above the X-ray luminosity completeness limit. Error bars are 1σ values from a bootstrap analysis. The mean SFRs of galaxies with X-ray luminous AGN are higher by a factor of 3 to 10 than those of galaxies without X-ray luminous AGN at a given stellar mass.

ies in S2-No-Lum-AGN are color-coded by their density on the stellar mass-SFR plane, where density is calculated by counting number of neighbors around each data point inside a circular aperture with a radius equal to 0.05. The color bar shows the percentile value of the data point's density, where the 100th percentile value corresponds to the highest density and the 0.1 percentile value corresponds to the data points whose density is 1/10th the maximum density. Also shown in Figure 3.10 is the mean SFR in different bins of stellar mass for S2-No-Lum-AGN, which we refer to as the main sequence, with 1σ errors calculated through a bootstrap method. We calculate errors in the mean SFR by resampling (i.e., drawing randomly from) the SFR distribution inside a bin of stellar mass x times, where x is the number of objects inside the bin, build a sample from the random draws and calculate the mean for that sample. We draw objects with replacement so the same object in a given bin can be sampled more than once. We do this 1,000 times and make a distribution of mean SFR values from each resampling and take the 16th and 84th percentile of this distribution to calculate the error on the mean of the SFR.

We make note of the four galaxies with X-ray luminous AGN (S1-Lum-AGN) in Figure 3.10 that have SFRs low enough to be considered outliers with respect to the rest of the galaxies in S1-Lum-AGN on the mass-SFR plane. Two of these objects exist at $z = 0.5 - 1.0$, one object exists at $z = 1.0 - 1.5$, and one object exists at $z = 1.5 - 2.0$. We have inspected the DECam and IRAC images, the flags in the source extractor catalogs, as well as the quality of the SED fits of the two outliers at $z = 0.5 - 1$ and the two outliers at $z = 1 - 1.5$ and $z = 1.5 - 2$. The inspection revealed nothing out of the ordinary or anything that could impair the photometry for these objects. Furthermore, the reduced χ^2 of the SED fit to the photometry is less than 5 in all cases, indicating a good fit. As a result, we have no reason to believe that the measured SFRs are erroneous.

In Figure 3.11, we show the mean SFRs of our sample of galaxies with (S1-Lum-AGN) and without (S2-No-Lum-AGN) X-ray luminous AGN as a function of stellar mass across four redshift bins. Error bars are determined from the bootstrap method described above. In all redshift bins we find that the mean SFRs of galaxies with X-ray luminous AGN are higher by a factor of 3 to 10 than those of galaxies without X-ray luminous AGN at a given stellar mass. This suggests that X-ray luminous AGN tend to coexist in galaxies with enhanced SFRs. In Section 3.6, we discuss how these results fits into possible evolutionary scenarios connecting AGN and SF activity.

Our results are consistent with those of Santini et al. (2012) who find that the SF activity of galaxies with luminous AGN is enhanced with respect to a mass-matched sample of inactive galaxies (i.e., galaxies without AGN activity) at $z = 0.5-2.5$. Furthermore, they find that the level of enhancement in SF activity amongst galaxies with luminous AGN is higher for galaxies with high X-ray luminosities ($L_X > 10^{43.5}\text{ergs}^{-1}$). Our results are also consistent with those of Masoura et al. (2018) who compare the mean SFRs of their sample of galaxies with X-ray luminous AGN to the SFR values of star forming galaxies from Schreiber et al. (2015) at fixed stellar mass and find that the mean SFRs at fixed mass of galaxies with X-ray luminous AGN are higher than those of galaxies without X-ray luminous AGN. We also find that our results are consistent with those of Kirkpatrick et al. (2019). In Kirkpatrick et al. (2019), they find that AGN from $z = 1 - 4$ have high SFRs and star formation efficiencies and show no signs of quenching.

The results in Shimizu et al. (2015) may appear to contradict the results we find here, as they claim their sample of AGN-host galaxies appear to have SFRs that fall off the main sequence of star forming galaxies. However, a subsequent paper Shimizu et al. (2017) claims that when they mass-match their sample of AGN-host galaxies to a control sample, the AGN-host galaxies have higher SFR on average.

The erroneous result in Shimizu et al. (2015) is explained by a mismatch between their sample of AGN-host galaxies and their comparative control sample: the mass distribution of their AGN-host galaxies is shifted towards higher values than the mass distribution of their sample of star forming galaxies, and thus, their AGN-host galaxies have lower specific SFR values typical of higher mass ($M_* > 10^{10.5}\ M_\odot$) galaxies.

In summary, we find that the mean SFR in galaxies with X-ray luminous AGN is significantly larger than in galaxies without X-ray luminous AGN at a given stellar mass. Our results are consistent with those from several earlier studies described above, but they are significantly more robust because our sample of galaxies without X-ray luminous AGN is 10 to 100 times larger than those of earlier studies, and we analyze both our AGN sample (S1-Lum-AGN) and our mass-matched non-AGN sample (S2-No-Lum-AGN) using the same SED fitting code and methodology. Our results are consistent with a scenario where the high SFR and AGN luminosity are triggered by processes that produce large gas inflow rates into the regions (on scales of a few hundreds to few kpc) typically associated with high SFRs, as well as the sub-pc region associated with the AGN accretion disk. We refer the reader to Section 3.6 for a more detailed discussion of potential evolutionary sequences between AGN and SF activity.

3.5.2 Properties and Fraction of Galaxies with Quenched Star Formation

In this section, we explore the quenched fraction of our sample of galaxies with (S1-Lum-AGN) and without (S2-No-Lum-AGN) X-ray luminous AGN at fixed stellar mass. The processes that quench SF (i.e., significantly suppress SF) are important for our understanding of galaxy evolution as they intimately regulate the growth of the stellar mass in galaxies. Theorists often invoke AGN feedback in simulations

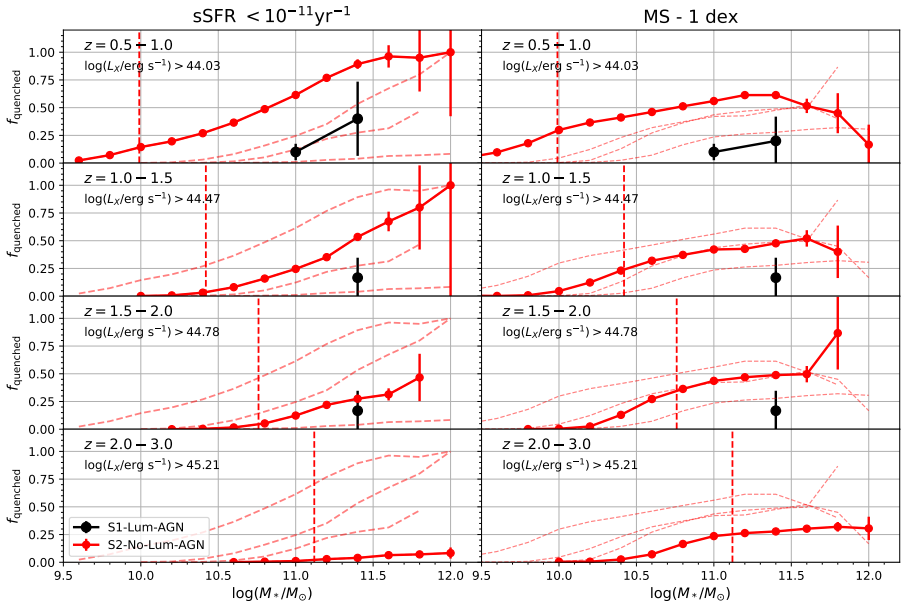

Figure 3.12: This figure shows the quenched fraction as a function of stellar mass in four different bins of redshift spanning $z = 0.5-3$ using two definitions of quiescence, whereby quenched galaxies are defined as having a sSFR $< 10^{-11}\mathrm{yr}^{-1}$ (left panels) or as having a SFR at least 1 dex below the main sequence at a given stellar mass (right panels). In all panels, we plot the fraction of galaxies that are quenched among the sample of galaxies with (S1-Lum-AGN; black circles) and without (S2-No-Lum-AGN; red circles) X-ray luminous AGN. The small dashed red lines in each panel represent the quenched fraction of S2-No-Lum-AGN in all the redshift ranges for easy visualization of the evolution of the quenched fraction with redshift. Poison errors are shown on this plot as error bars. The quenched fractions based on the two definitions of quiescence are roughly consistent at $z < 1.5$, but differ significantly at higher redshifts ($z = 1.5-3$) where the quenched fraction based on sSFR is lower by a factor of $\sim 2-3$ at $z = 1.5-2$ and by a factor of $\sim 5-10$ at $z = 2-3$ for galaxies with $M_* > 10^{11}$ $M_\odot$. The quenched fractions are a strong function of stellar mass in each redshift bin and generally increase with stellar mass, except possibly at the very highest stellar masses.

as a way to quench SF (Hambrick et al., 2011; Fabian, 2012; Vogelsberger et al., 2013; Choi et al., 2015; Roos et al., 2015; Hopkins et al., 2016; Bieri et al., 2017) in massive galaxies and prevent the overproduction of massive galaxies relative to the observed mass and luminosity functions. By measuring the quenched fraction of massive galaxies with and without X-ray luminous AGN, we aim to shed light on the role of quenching mechanisms, such as AGN feedback. While most earlier studies estimate the mean quenched fraction (averaged over massive galaxies) in different redshift ranges, the unprecedented size of our sample of massive galaxies (e.g., $\sim 30,000$ galaxies with $M_* > 10^{11}\ M_\odot$) enables us to study how the quenched fraction ($f_{\rm quenched}$) varies with stellar mass at different redshifts (Figure 3.12).

In the literature, multiple methods are used to identify quenched galaxies. Numerous works define quenched galaxies as galaxies having specific SFR (sSFR) less than $10^{-11}{\rm yr}^{-1}$ (Fontanot et al., 2009; Stefanon et al., 2013). Given the bimodality in color and star formation, it is also common to separate quenched galaxies from star-forming galaxies using a selection based on $U-V$ and $V-J$ colors (UVJ diagram, Wuyts et al., 2007; Whitaker et al., 2011; Muzzin et al., 2013; Fang et al., 2018). In Fang et al. (2018) and Donnari et al. (2019), a separate method used to define quiescence based on distance from the main sequence is introduced, where galaxies that fall 1 dex or 2σ below the main sequence are defined as quenched.

For this work, we select quenched galaxies based on a galaxy's sSFR (sSFR $< 10^{-11}{\rm yr}^{-1}$) and based on distance from the main sequence of star formation. In Figure 3.10, the blue dashed line represents sSFR of $10^{-11}{\rm yr}^{-1}$. If we follow the approach of Fontanot et al. (2009), where quenched galaxies are defined as having a sSFR $< 10^{-11}{\rm yr}^{-1}$, then Figure 3.10 shows that very few galaxies with X-ray luminous AGN ($< 5\%$) have quenched SF. For the second definition of quiescence based on distance from the main sequence, we define a quiescent sample using an approach similar to Donnari et al. (2019) and select our quenched sample in four

different redshift ranges spanning $0.5 < z < 3$. The quenched galaxies we select using this method are galaxies whose SFR is at least 1 dex below the main sequence. We rely on this second method of defining quiescence because it allows one to measure the quenched fraction of galaxies in observations without having to worry about the discrepancies that arise in the measured stellar mass and SFR values amongst different SED fitting codes, which could affect the measured quenched fraction if selecting galaxies based on sSFR. In Figure 3.10 the red line represents the main sequence, which is the mean SFR at fixed stellar mass for galaxies without X-ray luminous AGN, and the dotted magenta line represents the region of the mass-SFR plane that falls exactly 1 dex below the main sequence, meaning any sources that exist below this line satisfy the aforementioned definition of quiescence. We do not use the UVJ diagram method to select quenched galaxies as galaxies with X-ray luminous AGN, typically type I AGN-hosts or quasars, may have extremely blue colors due to emission from the accretion disk and thus affect our selection of quenched objects amongst the sample of galaxies with X-ray luminous AGN. For galaxies with X-ray luminous AGN with L_X above the 80% completeness limit ($L_X = 10^{44.03}$, $10^{44.47}$, $10^{44.78}$ and $10^{45.21}$ erg s^{-1}, respectively, at $z = 0.5 - 1.0$, $z = 1.0 - 1.5$, $z = 1.5 - 2.0$, and $z = 2.0 - 3.0$), the vast majority (97%, 98%, 96% and 100%, respectively, at $z = 0.5-1$, $z = 1.0-1.5$, $z = 1.5-2.0$, and $z = 2.0-3.0$) do not show quenched SF.

In Figure 3.12 we show how the quenched fraction ($f_{\rm quenched}$) varies with stellar mass in four different redshift bins for the two definitions of quiescence that we use here. Figure 3.12 has two solid curves that represent the fraction of galaxies that are quenched among our two samples: the sample of galaxies with (S1-Lum-AGN) and without (S2-No-Lum-AGN) X-ray luminous AGN. The three dashed lines in each panel of Figure 3.12 correspond to the quenched fraction of the S2-No-Lum-AGN sample in all redshift ranges for easy visualization of the evolution of

the quenched fraction with redshift. The error bars represent Poisson errors. The sample without (S2-No-Lum-AGN) X-ray luminous AGN is a factor of ~ 100 to $\sim 1,000$ larger than the sample of galaxies with (S1-Lum-AGN) X-ray luminous AGN, so we expect its behavior to be representative of the underlying sample of all galaxies.

We find that the quenched fractions for galaxies without X-ray luminous AGN, based on the two definitions of quenched galaxies (sSFR $< 10^{-11}\mathrm{yr}^{-1}$ versus SFR at least 1 dex below the main sequence) differ at all redshifts, especially at the highest redshift bin ($z = 2-3$) where the quenched fraction based on sSFR is lower by a factor of $\sim 5-10$ at $z = 2-3$ for galaxies with $M_* > 10^{11}\ M_\odot$. These results are not surprising, as one definition of quiescence (sSFR $< 10^{-11}\mathrm{yr}^{-1}$) ignores the evolution with time of the SFR-stellar mass relation (Whitaker et al., 2014; Speagle et al., 2014), while the other definition of quiescence (SFR at least 1 dex below the main sequence) is based on a main sequence which is allowed to evolve as it is empirically determined in each redshift bin.

We also note that the value of the quenched fraction based on selecting quenched galaxies using their distance from the main sequence is more robust across different studies than the quenched fraction based on a specific value of the sSFR. This is because the latter is highly sensitive to systematic effects, such as those introduced by the different fitting assumptions (e.g., different IMF, treatment of attenuation, choice of SPS, etc.) used by different SED fitting codes, impacting the absolute value of SFRs. For example, we find after running multiple tests that CIGALE produces systematically higher SFRs than EAZY-py by a factor of $\sim 2-3$, meaning that the measured quenched fractions (given by sSFR $< 10^{-11}\mathrm{yr}^{-1}$) would be higher for our sample if we use EAZY-py instead of CIGALE to derive SFRs. Figure 3.12 shows that the quenched fractions based on both definitions of quiescence are a strong function of stellar mass in each redshift bin and generally increase with

stellar mass, except possibly at the very highest stellar masses.

While many earlier studies with smaller samples measured the mean quenched fraction, averaged over stellar mass as a function of redshift (Kriek et al., 2006; Muzzin et al., 2013; Brennan et al., 2015; Fang et al., 2018; Stefanon et al., 2013), very few studies (e.g., Muzzin et al., 2013) measure the quenched fraction as a function of stellar mass over different redshift ranges. Our study is the first to reveal, using such a large sample of massive galaxies, how the quenched fraction ($f_{\rm quenched}$) at a given redshift changes as the galaxy stellar mass varies from 10^{10} $M_{\odot}$ to a few times 10^{11} $M_{\odot}$ (Figure 3.12). The fact that $f_{\rm quenched}$ rises with stellar mass provides important clues on the mechanisms that quench SF in massive galaxies.

3.6 Discussion

In Section 3.5.1, we found that the average SFRs of galaxies with X-ray luminous AGN are higher by a factor of $\sim$ 3 to 10 compared to galaxies without X-ray luminous AGN at a given stellar mass and redshift range (see Figure 3.10 and Figure 3.11). These results are consistent with a scenario where the high SFR and high AGN luminosity are produced by processes that produce large gas inflow rates both into the regions (on scales of a few hundred pc to few kpc) typically associated with high SFRs, as well as the sub-pc region associated with the AGN accretion disk. Assuming a radiative efficiency of $\epsilon = 0.1$, and a bolometric to X-ray luminosity ratio of $L_{\rm bol}/L_X \sim 30$ (Lusso et al., 2012), we estimate that the black hole accretion rates of our sample above the 80% X-ray completeness limit exceed values of 0.48 $M_{\odot}{\rm yr}^{-1}$ (for $L_X > 10^{44.03}$ erg s^{-1} at $z = 0.5 - 1.0$), 1.3 $M_{\odot}{\rm yr}^{-1}$ (for $L_X > 10^{44.47}$ erg s^{-1} at $z = 1.0 - 1.5$), 2.7 $M_{\odot}{\rm yr}^{-1}$ (for $L_X > 10^{44.78}$ erg s^{-1} at $z = 1.5 - 2.0$), and 7.3 $M_{\odot}{\rm yr}^{-1}$ (for $L_X > 10^{45.21}$ erg s^{-1} at $z = 2.0 - 3.0$). Given our maximum X-ray luminosity in each redshift bin, we expect the black hole accretion rates to not exceed values of 14, 45, 50, and 100 $M_{\odot}{\rm yr}^{-1}$ at $z = 0.5 - 1.0$, $z = 1.0 - 1.5$, $z = 1.5 - 2.0$,

and $z = 2.0 - 3.0$, respectively.

Examples of processes that drive large gas inflow rates through gravitational torques, tidal torques, and dissipative shocks include gas-rich major mergers, gas-rich minor mergers, and strong tidal interactions in gas-rich systems. It should be noted that in order to drive gas from kpc scales down to the scales of the AGN accretion disk, we need mechanisms that effectively reduce the angular momentum of the gas by several orders of magnitude, such as gravitational torques from a primary bar, secondary bars or/and other non-axisymmetric features, shocks, dynamical friction on gas clumps, feedback processes from local SF, run-away self-gravitational instabilities, tidal disruption of clumps, and hydro-magnetic winds (e.g., Jogee, 2006, and references therein). Another mechanism which can effectively reduce angular momentum has to do with the ram-pressure shocks described in Capelo & Dotti (2017), where large-scale (few kpc) shocks affect the entire galactic disc and decouple the dynamics of the gas from the stars and are a complementary trigger to tidal torques (see Figure 2 of Capelo & Dotti, 2017).

It is instructive to look at numerical high resolution simulations which explore the onset of high SFR and high AGN luminosity (Springel et al., 2005; Di Matteo et al., 2008; Cox et al., 2008; Capelo et al., 2015; Park et al., 2017). In particular, the more recent numerical simulations of merging galaxies (e.g., Park et al., 2017; Capelo et al., 2015) show that large gas inflows during major mergers can simultaneously trigger SF and AGN activity in the merging galaxies. In these simulations, the peak of black hole accretion of SF activity appear to coincide and the decline of black hole accretion rate appears to trace the decline in SF with time. Park et al. (2017) and Capelo et al. (2015) show that AGN and SF activity are also triggered during minor mergers, but to a much lesser extent. In simulations of isolated galaxies, however, black hole accretion does not necessarily trace SF across time in the same way (Negri & Volonteri, 2017). This can be due to the fact that in some isolated

systems, SF can happen on very large scales (e.g., kpc to tens of kpc) without any associated AGN activity. In isolated barred galaxies, the primary stellar bar can efficiently drive gas down to scales of a few hundred pc to fuel circumnuclear SF activity (e.g., Elmegreen, 1994; Knapen et al., 1995; Hunt & Malkan, 1999; Jogee et al., 2005), but in many cases the gas stalls on scales of a few hundred pc as there are no effective mechanisms to further rapidly drain its angular momentum and drive it down to the sub-pc scales of the AGN accretion disk (e.g., see Jogee, 2006, and references therein).

Figure 3.10 shows that galaxies which have moderate to low SFRs with respect to the average SFR (shown as the red curve) are not associated with X-ray luminous AGN. There are several ways to explain these results. In the aforementioned Park et al. (2017); Capelo et al. (2015) simulations of gas-rich major mergers, the contemporaneous phase of high SFR and AGN activity is followed by a phase where the black hole accretion rate and SFR both decline with time. In this scenario, the factors responsible for depressing SF (e.g., a declining gas supply, the heating or redistribution of the gas via stellar or AGN feedback) are also effective at depressing any AGN activity. We note that although the results in these simulations are for lower-mass galaxies than the ones we examine here, these simulation are of isolated systems and the results should be "scalable" and thus should hold to higher masses. In Figure 3.10, one would expect such an evolution in a merging system to cause low-luminosity AGN to lie in the region of low SFRs. Another possibility is that isolated galaxies (which likely make up the bulk of systems shown in Figure 3.10) exhibit low SFRs and no AGN activity or low-luminosity AGN activity simply because they lack the strong gravitational torques and shocks, which so efficiently drive gas inflows and fuel high central SFRs and AGN luminosity in gas-rich mergers. The X-ray data in our study are not sensitive to these low luminosity AGN, so we cannot directly test their location on Figure 3.10.

A more detailed comparison of our quenched fraction results to a wide range of numerical simulations, including hydrodynamical simulations and semi-analytic models is presented in Sherman et al. (2020b) as well as a discussion of the physical mechanisms that contribute to galaxy quenching across different environments, stellar masses, and epochs.

3.7 Summary

We have analyzed the relation between AGN and SF activity at $0.5 < z < 3$ by comparing the stellar masses and SFRs of 898 massive galaxies with X-ray luminous AGN ($L_X > 10^{44}$ erg s^{-1}) and a large comparison sample of $\sim 320,000$ galaxies without X-ray luminous AGN (see Figure 3.1 and Table 3.2.4). Our samples are selected from a large (11.8 deg^2) area in Stripe82 that has multi-wavelength (X-ray to far-IR) data and corresponds to a very large comoving volume (~ 0.3 Gpc^3) at $0.5 < z < 3$, thus minimizing the effects of cosmic variance and captures a large number of rare massive galaxies ($\sim 30,000$ galaxies with $M_* > 10^{11}$ $M_\odot$) and X-ray luminous AGN. While many galaxy evolution studies discard the hosts of X-ray luminous AGN due to the inability of common SED fitting codes to handle such systems, a strength of our study is that we fit the SED of both galaxies with and without X-ray luminous AGN hosts with the CIGALE SED fitting code, which includes AGN emission templates. We summarize our findings below:

1. The stellar mass and SFRs of galaxies with X-ray luminous AGN are likely to be overestimated if AGN emission is not included in the SED fit (Figure 3.3). For galaxies with large AGN fraction contamination ($f_{\rm AGN} > 0.4$), the stellar mass can be overestimated by factor of up to 5, on average, while SFRs can be overestimated by a factor of up to 10, on average, if AGN emission templates are not included in the SED fit (Figure 3.4).

2. The stellar mass function of galaxies with X-ray luminous AGN (Figure 3.5) shows that the number density of galaxies with X-ray luminous AGN is two to three orders of magnitude lower than galaxies without X-ray luminous AGN for stellar masses in the range of 10^{10} to 3×10^{11} $M_{\odot}$ at redshifts of $0.5 < z < 3$. This suggests that X-ray luminous AGN are a rare and rapid phase in galaxy evolution.

3. We find that the average SFR of galaxies with X-ray luminous AGN is higher by a factor of ~ 3 to 10 compared to galaxies without X-ray luminous AGN at a given stellar mass and redshift (Figures 3.10 and 3.11). We remind the reader that these results only hold for X-ray luminous AGN with X-ray luminosities above the 80% completeness limit at each redshift bin ($L_X > 10^{44.03},\ 10^{44.47},\ 10^{44.78}$ and $10^{45.21}$ erg s^{-1}, respectively, at $z = 0.5 - 1.0,\ z = 1.0 - 1.5,\ z = 1.5 - 2.0$ and $z = 2.0 - 3.0$). These results are consistent with a scenario where the high SFR and high AGN luminosity are produced by processes that produce large gas inflow rates both into the regions (on scales of a few hundred pc to few kpc) typically associated with high SFRs, as well as the sub-pc region associated with the AGN accretion disk. Examples of processes that drive large gas inflow rates through gravitational torques, tidal torques, and dissipative shocks include gas-rich major mergers, gas-rich minor mergers, and strong tidal interactions in gas-rich systems. It should be noted that in order to drive gas from kpc scales down to the scales of the AGN accretion disk, we need mechanisms that effectively reduce the angular momentum of the gas by several orders of magnitude.

4. Due to the unprecedented size of our sample of massive galaxies, we are able to perform one of the first robust explorations of how the quenched fraction of galaxies varies with stellar mass in each redshift bin. The quenched fraction, based on both definitions of quiescence (galaxies with sSFR $< 10^{-11}$ yr^{-1} or

galaxies with SFR at least 1 dex below the main sequence) rises with galaxy stellar mass over the range 10^{10} $M_{\odot}$ to about 3×10^{11} $M_{\odot}$ in each of our four redshift bins in the range $0.5 < z < 3$. The vast majority ($> 95\%$) of galaxies with X-ray luminous AGN at $z = 0.5 - 3$ do not show quenched SF: this suggests that if AGN feedback quenches SF, the associated quenching process takes a significant time to act and the quenched phase sets in after the highly luminous phases of AGN activity.

Chapter 4

AGN and Star Formation at Cosmic Noon: Comparison of Data to Theoretical Models

4.1 Introduction

Understanding the connection between galaxy properties and their central massive black holes (BHs) currently remains one of the biggest challenges to formulating theoretical models of galaxy evolution[1]. Observations have shown that the central BH mass of a galaxy correlates with the galaxy bulge mass (Magorrian et al., 1998; McLure & Dunlop, 2002) and galaxy bulge velocity dispersion (Ferrarese & Merritt, 2000; Gebhardt et al., 2000; Kormendy & Ho, 2013), suggesting a clear link between galaxy and BH growth. Furthermore, the cosmic star formation rate (SFR) density and black hole accretion rate (BHAR) density are observed to peak at $z \sim 2$ and

[1]The work presented in this chapter was submitted to the Monthly Notices of the Royal Astronomical Society (MNRAS) journal on July 17, 2021 and is awaiting final approval for publication. As first author, I contributed by writing the paper and performing the full scientific analysis presented therein.

decline in tandem down to $z \sim 0$ (Babić et al., 2007; Wilkins et al., 2008; Jogee et al., 2009; Madau & Dickinson, 2014; Delvecchio et al., 2014). Such trends suggest that galaxy and BH growth are closely intertwined, but whether they coevolve remains a topic of debate (e.g., Kormendy & Ho, 2013; Jahnke & Macciò, 2011).

Active galactic nuclei (AGN) activity in galaxies arises directly from gas accreting onto a galaxy's central massive BH. The resulting feedback from an AGN is thought to suppress or reduce star formation (SF) in the host galaxy via jets, winds, and radiation. In theoretical simulations of galaxy evolution, AGN feedback is often invoked, along with stellar feedback, in order to solve the "overcooling" problem in galaxy formation models whereby galaxies grow too massive and produce stellar mass functions that do not resemble empirical ones unless some form of heating or feedback is applied to the cooling gas inside the dark matter halo (Naab & Ostriker, 2017; Somerville & Davé, 2015). Different forms of AGN feedback are postulated to affect the host galaxy and the gas in the surrounding environment in different ways. Radiation and winds from the accretion disk near the BH can heat and/or expel gas on various galactic scales (Hopkins et al., 2016; Roos et al., 2015; Choi et al., 2015; Vogelsberger et al., 2013; Fabian, 2012; Hambrick et al., 2011) whereas the jets from an AGN can heat the gas in the intracluster medium (ICM) of clusters of galaxies, therefore preventing the gas from cooling and ultimately preventing future episodes of star formation (Davé et al., 2019; Heckman & Best, 2014; Fabian, 2012; Peterson & Fabian, 2006). Cosmological simulations often try to model these two forms of AGN feedback (i.e., quasar mode and radio/jet mode), however, lack of high spatial and spectral resolution observations of AGN along with poor simulation resolution has made it difficult to constrain the physical mechanisms driving AGN feedback, BH growth, and the extent to which AGN feedback can heat and/or expel gas. It should be noted, however, that some numerical simulations do model AGN feedback parameters based on observations of outflows of molecular and ionised gas

(e.g., Perna et al., 2017; Liu et al., 2013; Sturm et al., 2011) as well as observations of radio-loud jets (Fabian, 2012) in galaxies with luminous AGN (Davé et al., 2019).

While it has been postulated that some stages of AGN activity might suppress SF as outlined above, there is evidence of AGN and enhanced SF activity coexisting in galaxies. Many studies have found, at low and high redshift, luminous AGN residing in galaxies with enhanced episodes of SF (Florez et al., 2020; Masoura et al., 2018; Mahoro et al., 2017; Rosario et al., 2013; Santini et al., 2012; Sanders et al., 1988). Other studies, however, have claimed that galaxies with luminous AGN have decreased SFRs relative to the non-AGN population (Leslie et al., 2016; Shimizu et al., 2015). An enhancement of SF activity in AGN host galaxies could at least be, in part, due to processes that are capable of igniting and fueling circumnuclear SF and BH accretion when the angular momentum problem can be overcome (e.g., Jogee, 2006, and references therein). Examples of such processes include gas-rich major and minor mergers (Hopkins et al., 2008), gravitational torques from bars and/or non-axisymmetric features in the disc, stellar feedback, and hydromagnetic winds (see Jogee, 2006, and references therein). It is critical for models of galaxy evolution to constrain how AGN feedback impacts galaxy formation, especially since AGN and SF are always assumed to be closely linked in such models and AGN feedback is routinely invoked to regulate galaxy growth.

Until recently, studying the SF activity of galaxies with luminous AGN proved rather difficult as AGN emission is capable of dominating the galaxy spectral energy distribution (SED) at UV to mid-IR wavelengths, thus making it difficult to distinguish between AGN activity and star forming processes in the SED fitting. For this reason, many studies of galaxy evolution remove galaxies with luminous AGN from their samples (Stevans et al., 2021; Sherman et al., 2021; Kawinwanichakij et al., 2020; Sherman et al., 2020b,a; Ilbert et al., 2013) or fail to analyze galaxies with and without luminous AGN using a consistent methodology or a statistically

large enough sample (Whitaker et al., 2014; Muzzin et al., 2013; Whitaker et al., 2012; Elbaz et al., 2011; Williams et al., 2009; Elbaz et al., 2007; Salim et al., 2007; Brinchmann et al., 2004). In recent years, however, numerous SED fitting codes have been developed that are capable of disentangling the emission from AGN and SF in the SED and producing more reliable estimates of stellar mass and SFR (e.g., CIGALE (Boquien et al., 2019), AGNfitter (Calistro Rivera et al., 2016), SED3FIT (Berta et al., 2013)). In Florez et al. (2020), we used CIGALE to perform SED fitting on a large sample of massive galaxies with and without high X-ray luminosity AGN at $z = 0.5 - 3$. By using CIGALE we were able to derive galaxy properties, such as stellar mass and SFR, for galaxies with and without high X-ray luminosity AGN in a self-consistent manner.

The goal of this project is to follow up on the work done in Florez et al. (2020) (hereafter Paper 1), which reports two key results: (i.) At fixed stellar mass, galaxies with high X-ray luminosity AGN ($L_X > 10^{44}$ erg s^{-1}) have a mean SFR that is a factor of $\sim 3 - 10$ times higher than galaxies without such AGN; (ii.) The majority ($> 95\%$) of AGN with high X-ray luminosity do not reside in galaxies with quenched star formation. These results suggest that high SFRs and high AGN luminosities are fueled by mechanisms that lead to large gas inflow rates on kpc to sub-pc scales (e.g., mergers), growing both the supermassive BHs (SMBHs) and the stellar masses of the host galaxies. These results also suggest that if AGN feedback quenches SF, the associated quenching process takes a significant time to act and the quenched phase sets in after the highly luminous phases of AGN activity. In this paper, we will expand on these results by analyzing the cosmological hydrodynamical simulations IllustrisTNG (Nelson et al., 2018; Springel et al., 2018; Naiman et al., 2018; Pillepich et al., 2018; Marinacci et al., 2018; Nelson et al., 2019a,b; Pillepich et al., 2019) and SIMBA (Davé et al., 2019), as well as the semi-analytical model of galaxy formation and evolution SAG (Cora et al., 2018). We explore the following questions: (i) How

does the number density of high X-ray luminosity AGN in theoretical models and numerical simulations compare to the empirical number density of observed AGN (Section 4.6.1)? (ii) Do theoretical models reproduce the observed distribution of galaxies with and without high X-ray luminosity AGN in the stellar mass–SFR plane as well as the empirical result that galaxies with high X-ray luminosity AGN have a higher mean SFR at fixed stellar mass than galaxies without such AGN (Section 4.6.2)?

This paper is organized as follows: In Section 4.2, we summarize the results of Paper 1 and briefly outline the data, sample selection, SED fitting procedure, and stellar mass and SFR completeness limit estimates used in that paper. In Section 4.3, we discuss the updates to the sample selection in Paper 1 and in Section 4.4 we discuss the observed demographics of the high X-ray luminosity AGN population. In Section 4.5 we discuss the three theoretical models, their implementation of AGN and SF feedback, and how we obtain the X-ray luminosity from the black hole accretion rate. In Section 4.6 we present our results, and in Sections 4.7 and 4.8 we discuss and summarize our results, respectively. In this paper we assume $H_0 = 70$ km s^{-1} Mpc^{-1}, $\Omega_{\rm M} = 0.3$, and $\Omega_\Lambda = 0.7$ for the observed data (as in Paper 1).

4.2 Overview of Empirical Results and Data Analysis in Paper 1

The goal of the present paper is to evaluate the extent to which three state-of-the-art theoretical models can reproduce the empirical results presented in Paper 1 (Florez et al., 2020). In this section, we summarize the empirical results of Paper 1 and outline the associated data, sample selection, and methodology we follow for the analysis. In Paper 1, we compared the stellar masses and SFRs of a large mass-complete sample of galaxies with and without high X-ray luminosity AGN at

$0.5 < z < 3$ (258 galaxies complete in X-ray luminosity with $L_X \gtrsim 10^{44}$ erg s^{-1}, 153,765 galaxies without). Our data were selected from a large ~ 11.8 deg^2 area in Stripe 82 that has multiwavelength data (X-ray to far-IR) and corresponds to a large comoving volume of ~ 0.3 Gpc^3 at $0.5 < z < 3$. A large strength of this study was that we self consistently fit the SEDs of galaxies with and without high X-ray luminosity AGN using the CIGALE SED fitting code. As mentioned in the introduction, two of the key results we reported in Paper 1 are: (i.) The mean SFR, at fixed stellar mass, of galaxies with high X-ray luminosity AGN is higher by a factor of $\sim 3-10$ than the mean SFR of galaxies without such AGN; (ii.) The vast majority ($> 95\%$) of galaxies with high X-ray luminosity AGN do not have quenched SF.

The data, sample selection, SED fitting, and stellar mass and SFR completeness limit estimates used in the present paper are essentially the same as those used in Paper 1. We give a brief overview of these topics in the following subsections. Before comparing the empirical results of Paper 1 to the theoretical models, we make some small adjustments to the sample selection in order to improve the robustness of these comparisons. These adjustments will be discussed in Section 4.3.

4.2.1 Photometric Catalogs

Our photometric data are primarily obtained from a NEWFIRM K_S-selected catalog (5σ depth of 22.4 AB mag; see Stevans et al., 2021) that covers 17.5 deg^2 of the Sloan Digital Sky Survey (SDSS) Stripe 82 equatorial field. The NEWFIRM K_S-selected catalog includes u, g, r, i, z photometry from DECam as well as 3.6 and 4.5 μm photometry from IRAC. We supplement this photometry with J and K_S data from VICS82 in order to obtain a total of ten photometric filters spanning near-UV to mid-IR wavelengths. In Paper 1 we ran the EAZY-py SED fitting code (Brammer et al., 2008) on this data to obtain photometric redshifts for galaxies without a high

X-ray luminosity AGN. The photometric redshifts have an accuracy of $\sigma_z = 0.037$ at $z < 1$ (Paper 1), and a photometric redshift accuracy of $\sigma_z = 0.102$ at $1.9 < z < 3.5$ (Sherman et al., 2021).

We utilize data from the Stripe 82X X-ray survey (LaMassa et al., 2016) in order to identify and analyze galaxies with high X-ray luminosity AGN. Stripe 82X is an X-ray survey that covers 31.3 deg^2 of the SDSS Stripe 82 equatorial field and includes archival *Chandra* and XMM-*Newton* X-ray data. For this project, we use photometry from the XMM-*Newton* Announcement Opportunity 13 (AO13) that was introduced in LaMassa et al. (2016). We crossmatch the Stripe 82X AO13 data to the NEWFIRM K_S-selected catalog as described in Paper 1 using the maximum likelihood estimator (MLE) method of Sutherland & Saunders (1992). Spectroscopic redshifts for this sample are obtained from LaMassa et al. (2019) with $\sim 70\%$ completeness. The remaining $\sim 30\%$ of sources without a spectroscopic redshift have a photometric redshift obtained from Ananna et al. (2017). The photometric redshifts presented in Ananna et al. (2017), when compared to available spectroscopic redshifts, have a normalized median absolute deviation of $\sigma_{\rm NMAD} \sim 0.06$ at $0 < z < 3$.

4.2.2 Sample Selection

For the analysis in Paper 1 we produced two final samples of galaxies: a sample of galaxies with high X-ray luminosity AGN, and a control sample of galaxies without such AGN. Both samples were chosen from the region of the sky where the *Spitzer*-HETDEX Exploratory Large Area (SHELA, Papovich et al., 2016) and the Stripe 82X footprints overlap, spanning an area of 11.8 deg^2, corresponding to a comoving volume ~ 0.3 Gpc^3 at our redshift range of interest $0.5 < z < 3$. In Paper 1 we did not correct our sample of galaxies with high X-ray luminosity AGN for dust obscuration. We cited Powell et al. (2020) who estimate how many luminous AGN

Sample	All z bins	$0.75 < z < 1.25$	$1.25 < z < 1.75$	$1.75 < z < 2.25$
(a)	(b)	(c)	(d)	(e)
(1) S0-DECam-NEWFIRM-IRAC	209,721	130,650	53,074	25,997
(2) S1-Lum-AGN				
i.) Total Number $N_{\rm tot}$	667	321	228	118
ii.) $L_X > L_{X,\rm lim}$	321	151	117	54
iii.) $L_X > L_{X,\rm lim}$ & $M_* > M_{*,95\%\rm lim}$	203	119	66	18
(4) S2-No-Lum-AGN				
i.) Total Number $N_{\rm tot}$	209,054	130,329	52,846	25,879
ii.) $M_* > M_{*,95\%\rm lim}$	93,104	67,015	21,330	4,759

Table 4.1: (1) The sample S0-DECam-NEWFIRM-IRAC contains galaxies which have a detection in the u, g, r, i, z bands, S/N > 5 in the K-band, and S/N > 2 in the two IRAC bands, and overlap with the Stripe 82X survey. (2) The sample S1-Lum-AGN contains a subset of galaxies in S0-DECam-NEWFIRM-IRAC that have a high X-ray luminosity AGN. The total number of galaxies in the sample, as well as the number of galaxies with X-ray luminosities above the completeness limit ($L_X > L_{X,\rm lim}$) and stellar masses above the 95% stellar mass completeness limit ($M_* > M_{*,95\%\rm lim}$) are shown. (3) The sample S2-No-Lum-AGN contains the subset of galaxies in S0-DECam-NEWFIRM-IRAC that do not contain an high X-ray luminosity AGN.

would be added to their high luminosity ($L_X > 10^{44.5}$ erg s^{-1}) sample at $z > 1$ if they corrected for dust obscuration and found that their sample would only increase by $\lesssim 4\%$. We therefore believe our sample of high X-ray luminosity AGN would similarly not increase by much if we corrected for dust obscuration.

For the final samples we used in our analysis in Paper 1, we required a K_S flux with a signal-to-noise ratio (S/N) detection greater than 5, an IRAC 3.6 and 4.5 μm flux with a S/N detection greater than 2, and a detection in the DECam u, g, r, i, z filters. We required this for both samples of galaxies with and without high X-ray luminosity AGN. These sample cuts gave us a total of 932 galaxies with high X-ray luminosity AGN at $z = 0.5 - 3$ and a total of 318,904 galaxies without high X-ray luminosity AGN at the same redshift range. We clarify here that the sample of galaxies without high X-ray luminosity AGN that we analyze in Paper 1 does not include any galaxies with X-ray emission detected in XMM AO13 (see Figure 1 in Paper 1). This sample, however, may include galaxies hosting AGN

whose X-ray luminosity are lower and lie below the X-ray detection limit of XMM AO13.

4.2.3 SED Fitting

One of the large advantages of Paper 1 is that we fit the SEDs of galaxies with and without high X-ray luminosity AGN using the exact same SED fitting code. This allowed us to self-consistently derive and obtain stellar masses and star formation rates for both samples of galaxies with and without high X-ray luminosity AGN. In our SED fitting of galaxies with high X-ray luminosity AGN, we implemented the Fritz et al. (2006) AGN emission templates to model the AGN emission at UV to mid-IR wavelengths. We did not include AGN emission templates in the SED fitting of galaxies without high X-ray luminosity AGN, however. For all galaxies, we included models of dust emission due to star formation from Dale et al. (2014) and the stellar populations of Bruzual & Charlot (2003). We assumed dust attenuation to the SED as described by Calzetti et al. (2000), a Chabrier initial mass function (IMF; Chabrier, 2003), and a delayed exponential SFH (Ciesla et al., 2018, 2016).

In Paper 1, we performed a number of tests to determine if our CIGALE-derived SFRs were reliable. First, we ran CIGALE on a sample of 38 galaxies with high X-ray luminosity AGN from the CANDELS survey (Grogin et al., 2011; Koekemoer et al., 2011), using photometric bandpasses that span the same wavelength range as our own sample, and compared the CIGALE-derived SFRs to the SFRs presented in Yang et al. (2019, 2017) for the same group of galaxies. We find relatively good agreement between our CIGALE-derived SFRs and those presented in Yang et al. (2019, 2017), who obtain SFRs by taking the median value of the SFR measured by numerous teams for the same object (see Section 4.3 of Paper 1). Second, we created a synthetic mock sample of galaxy SEDs with AGN emission included and then ran CIGALE on the mock galaxy SED fluxes. We then compared

the CIGALE-derived SFRs to the true mock galaxy SFRs and found that $\sim 90\%$ of the CIGALE-derived SFRs agree with the true mock galaxy SFRs to within a factor of 3-4 and only 2% of the CIGALE-derived SFRs differ from the true SFRs by a factor 10 or more (see Section 4.4 of Paper 1). Lastly, we ran EAZY-py on our sample of galaxies without high X-ray luminosity AGN and compared the EAZY-py SFRs to the CIGALE-derived SFRs. We found that EAZY-py SFRs are consistent with CIGALE SFRs, on average, to within a factor $\sim 2-3$ (see Section 5.2 of Paper 1). These tests demonstrated that our SED fitting procedure in Paper 1 is robust and produces reliable SFRs.

4.2.4 Estimate of Stellar Mass and SFR Completeness Limits

In Paper 1, we estimated the stellar mass completeness limits for our sample of galaxies with and without high X-ray luminosity AGN following the procedures described in Davidzon et al. (2013); Pozzetti et al. (2010). This method assumes that the stellar mass completeness limit of a survey can be determined from the least massive galaxy that can be detected in a given filter with a magnitude equal to the magnitude limit of the survey in that filter. Because our samples were constructed from a K_S-selected catalog, we determined the stellar mass completeness limit at each redshift using the K_S-band magnitudes of our sources. We refer the reader to Paper 1 for a full description of our stellar mass completeness limit estimate. The 95% stellar mass completeness limits for the sample used in this work are $\log(M_*/M_\odot) = 10.27$, 10.58, and 11.03 in our $0.75 < z < 1.25$, $1.25 < z < 1.75$, and $1.75 < z < 2.25$ bins, respectively.

For every galaxy in our sample, we derived a dust-corrected SFR from our SED fitting procedure using all available band-passes. Unlike stellar mass, where there is a fairly direct connection between a galaxy's stellar mass and its K_S-band magnitude, it is not so easy to obtain a survey completeness limit for a dust-corrected

SFR as this would require the analysis of many observed bands and SED templates. To overcome this, in Paper 1 we used the DECam u-band and g-band as a proxy for FUV flux and obtained a dust extincted SFR completeness limit based on the u-band and g-band 5σ limiting magnitudes ($m_{u,\rm lim} = 25.0$ AB mag and $m_{g,\rm lim} = 24.8$ AB mag, see Wold et al. (2019)) by applying the $\rm SFR_{FUV}$ conversion factor from Hao et al. (2011). This conversion factor assumes a Kroupa (2001) IMF, so we reduce the estimated $\rm SFR_{FUV}$ by 0.046 dex to make the results consistent with the Chabrier (2003) IMF used throughout this work. For our analysis we used the u-band flux at $z < 1.25$ and the g-band flux at $z > 1.25$ to estimate the FUV flux. The estimated u-band and g-band based dust extincted FUV SFR completeness limits are $\log(\rm SFR_{FUV,lim}/M_{\odot}\ yr^{-1})$ = -0.02, 0.33, and 0.62 at $z = 0.75 - 1.25$, $z = 1.25 - 1.75$ and $z = 1.75 - 2.25$, respectively. We emphasize here that the measured SFRs from the SED fit and the observed dust-extincted FUV-based SFRs are very different quantities. The measured SFRs from the SED fit are likely higher than the dust-extincted FUV-based SFRs as those from the SED have been corrected for dust extinction. If we apply a dust correction based on the median attenuation measured from CIGALE for galaxies within 0.1 mag of the 5σ u and g-band completeness limits, which is $\sim 2 - 2.5$ for all three redshift ranges, we find dust-corrected FUV completeness limits of $\log(\rm SFR_{FUV,lim}/M_{\odot}\ yr^{-1}) = 1.02$, 1.23, and 1.40 at $z = 0.75 - 1.25$, $z = 1.25 - 1.75$ and $z = 1.75 - 2.25$, respectively. We note that we do not use a S/N cut for the u or g-band in our analysis, meaning it would not be unusual to measure intrinsic SFRs from the SED fitting well below the FUV-based SFR completeness limits listed here.

4.3 Updates to the Sample Selection

As mentioned in Section 4.1, the goal of the present paper is to evaluate the extent to which three state-of-the-art theoretical models can reproduce the empirical results

presented in Paper 1. In order to increase the robustness of the comparison between our empirical results and the theoretical models, we make some small updates to the sample selection which we discuss here.

First, we use a narrower redshift range here than the redshift range used in Paper 1, which corresponds to $0.5 < z < 3$. This is because we only have simulation snapshots available at $z = 1.0,\ 1.5$, and 2.0 for the three theoretical models we use in this work, meaning that a more direct comparison of the empirical results to the simulated data can be made at $0.75 < z < 2.25$. Second, the recent availability of spectroscopy by the Hobby Eberly Telescope Dark Energy Experiment (HETDEX, Hill et al., 2008) has allowed us to replace the photometric redshifts of three galaxies from the Stripe 82X sample with spectroscopic redshifts. Lastly, because black hole accretion is intimately connected with the emission produced in the "hard" X-ray spectral range of the galaxy SED (Haardt & Maraschi, 1991), we select our sample of galaxies with high X-ray luminosity AGN based on their rest-frame hard-band (2-10 keV) X-ray luminosities, instead of the observed full-band (0.5-10 keV) X-ray luminosity as is done in Paper 1.

We calculate the rest-frame hard-band (2-10 keV) X-ray luminosity for our sample of sources crossmatched to the AO13 X-ray data following the methodology in LaMassa et al. (2019). We use the `detml` parameter from the Stripe 82X catalog to determine if a source is significantly detected in a given band-pass. A source is considered significantly detected in the hard or full X-ray band-passes if it has `detml` > 15 in the XMM AO13 catalog (LaMassa et al., 2016). If a source is significantly detected in the hard-band, we compute the rest-frame hard-band X-ray flux by multiplying the observed hard-band flux by the k-correction factor $(1+z)^{\Gamma-2}$ and assume $\Gamma = 1.7$. If a source is not detected significantly in the hard-band but is detected with a significance above `detml` $= 15$ in the full-band, we multiply the observed full-band flux by a factor of 0.665 (see LaMassa et al., 2019) and the same

k-correction factor as the hard-band, again assuming $\Gamma = 1.7$, to obtain a rest-frame hard-band X-ray flux. If a source is not detected significantly in either the hard or full X-ray band-passes, then we calculate the rest-frame hard-band X-ray flux from the observed soft-band flux by multiplying the soft-band flux by a factor of 1.27. We assume $\Gamma = 2$ for the soft-band, so no k-correction is needed when calculating the rest-frame hard-band X-ray flux from the observed soft-band flux. Of the 667 sources we use to perform our analysis, 170 are detected significantly in the hard-band, 466 are detected significantly in the full-band but not the hard-band, and 31 are not detected significantly in either the full or hard band-passes.

We compute the 95% completeness limit of the rest-frame hard-band X-ray luminosity in each of our redshift ranges of interest using the XMM AO13 flux area curves presented in LaMassa et al. (2016). Because the majority ($\sim$ 70%) of our sample actually have rest-frame hard-band X-ray luminosities computed from the observed full-band flux, we use the observed full X-ray band-pass flux area curves from LaMassa et al. (2016) to determine a completeness limit for our X-ray sample. We multiply the full band X-ray flux limit by the same conversion factor (0.665) and k-correction factor as mentioned above to obtain a rest-frame hard-band X-ray luminosity completeness limit at each redshift range. The 95% full-band X-ray flux limit of XMM AO13 is $F_X = 2.09 \times 10^{-14}$ erg s^{-1} cm^{-2}. This translates to a 95% rest-frame hard-band X-ray luminosity of $L_X = 10^{44.08}$ erg s^{-1} at $z = 0.75 - 1.25$, $L_X = 10^{44.41}$ erg s^{-1} at $z = 1.25 - 1.75$, and $L_X = 10^{44.66}$ erg s^{-1} at $z = 1.75 - 2.25$. For the analysis of our sample of galaxies with high X-ray luminosity AGN on the mass-SFR plane, we select only objects having rest-frame hard-band X-ray luminosities above the 95% X-ray luminosity completeness limit at each corresponding redshift range.

In Table 4.2.2 we list how many objects are detected in our sample of galaxies with high X-ray luminosity AGN, how many are above the 95% X-ray luminosity

completeness limit, and how many are above both the 95% X-ray luminosity and stellar mass completeness limits. We note that our X-ray sample selection for the present paper produces a slightly larger sample at our redshift range of interest than the X-ray sample selection used in Paper 1. Using the updated X-ray selection method described above, we find 321 galaxies above the X-ray luminosity completeness limit and 203 galaxies above both the X-ray luminosity and stellar mass completeness limits at $0.75 < z < 2.25$. By contrast, using the X-ray selection method of Paper 1, yields 300 galaxies above the X-ray luminosity completeness limit and 181 galaxies above both the X-ray luminosity and stellar mass completeness limits at $0.75 < z < 2.25$. This means our final mass-complete and X-ray luminosity-complete sample of galaxies with high X-ray luminosity AGN is $\sim 12\%$ larger when we use the X-ray sample selection detailed in this paper as opposed to that of Paper 1. We note that this updated sample selection process does not require us to rerun the CIGALE SED fitting code on the sample of galaxies with high X-ray luminosity AGN, meaning that the derived stellar masses and SFRs used here are the same as those used in Paper 1.

4.4 Demographics of high X-ray luminosity AGN

The goal of this work is to compare the empirical results of Paper 1 to three theoretical simulations. As described in Section 4.3, in order make more direct comparisons to the simulations, we improved upon the sample section of AGN of high X-ray luminosity in Paper 1 such that we now select galaxies with high X-ray luminosity AGN based on their hard-band (2-10 keV) X-ray luminosity, rather than their full-band (0.5-10 keV) X-ray luminosity. Before we compare our empirical results to theoretical models, we first perform a consistency check on the distribution and demographics of high X-ray luminosity AGN by measuring the X-ray luminosity function (XLF) of our sample and comparing it to the XLF measured by other

studies. We emphasize that the goal of this test is not to focus on the details and implications of the empirical hard-band XLF, but rather to ensure that our sample selection process is sampling the XLF with relative uniformity. We refer the reader to Ananna et al. (2019) for the most up-to-date observational constraints of the XLF computed from the cosmic X-ray background (CXB).

In Figure 4.1, we plot the observed rest-frame hard-band XLF at three different redshift ranges using our sample of cross-matched galaxies and all galaxies from XMM AO13 that fall in our survey footprint, where SHELA and Stripe 82X overlap, and include the observed XLFs from three other studies (Buchner et al., 2015; Miyaji et al., 2015; Hopkins et al., 2007) for comparison. The Miyaji et al. (2015) XLF is based on the *Swift* Burst Alert Telescope (BAT) survey, the Buchner et al. (2015) XLF is based on a multi-tiered survey consisting of data from the COSMOS (Scoville et al., 2007), CDFS (Xue et al., 2011), AEGIS-XD (Davis et al., 2007), and XMM-XXL (Pierre et al., 2016) surveys, while the Hopkins et al. (2007) XLF is obtained by applying a bolometric correction to the best-fit of the bolometric luminosity function. We include the XLF of the matched and unmatched XMM AO13 sources since the cross-matching can only be done reliably for a subset of the sample (see Paper 1). Our XLF is calculated using the $1/V_{\rm max}$ method described in Schmidt (1968) whereby the luminosity (or mass) function of a sample of galaxies is calculated by dividing the number of galaxies in given bin of luminosity (or mass) by the bin width and the differential comoving volume ΔV_C, where ΔV_C is the difference between the comoving volume ($V_{\rm max}$) at a maximum redshift that a source of a given luminosity (or mass) can probe and the comoving volume at the lower edge of the redshift bin. In all three panels, we show the 95% completeness limit for the corresponding redshift range as the vertical dashed line.

As shown in Figure 4.1, above the 95% completeness limit (especially at $L_X \gtrsim 10^{44.5}$ erg s^{-1}), our XLF agrees relatively well with the XLF from other

studies. For instance, at $z = 0.75 - 1.25$, our XLF agrees well with the XLF from other studies at $L_X > 10^{44.3}$ erg s^{-1} but at lower X-ray luminosities ($L_X < 10^{44.3}$ erg s^{-1}) there is a small dip that is factor of ~ 2 lower for cross-matched sources and a factor of $\sim 1.2 - 1.5$ lower for the full XMM AO13 XLF. This could be due to uncertainties in our XLF introduced by dust obscuration, causing us to miss AGN at lower L_X. At all redshifts, our XLF appears to agree most with the XLF from Miyaji et al. (2015), however, they find brighter objects more frequently than we do with X-ray luminosities exceeding $10^{45.5}$ erg s^{-1}, which could be due to a number of reasons. Their sample size is much larger than ours, as they use data from the *Swift* BAT survey which spans an area on-sky of 3.9×10^4 deg^2 and thus they are able to capture much more extreme and rare systems than we can. The *Swift* BAT survey detects X-rays at energies of $14 - 195$ keV, however, so Miyaji et al. (2015) apply a correction to convert X-ray luminosities from *Swift* BAT to the hard band. This could introduce some source of uncertainty to the measured XLF of Miyaji et al. (2015) and produce inconsistencies with other studies. We note that other discrepancies between the different empirical XLFs can arise from uncertainties due to corrections for Compton-thick sources, as well as photometric redshift estimates. The latter could especially affect the XLF of Buchner et al. (2015) as their sample only has spectroscopic redshifts for $\sim 50\%$ of sources.

4.5 Theoretical Models and Numerical Simulations

In numerical simulations and theoretical models of galaxy evolution, AGN and SF activity are closely linked and AGN feedback is invoked to regulate galaxy growth. In order to constrain such models, we will explore in Section 4.6 how three different simulations (i.e., the hydrodynamical simulations IllustrisTNG and SIMBA, and the semi-analytic model SAG) compare to our empirical results on AGN and SF at cosmic noon (Paper 1). In this section, we describe the three theoretical models,

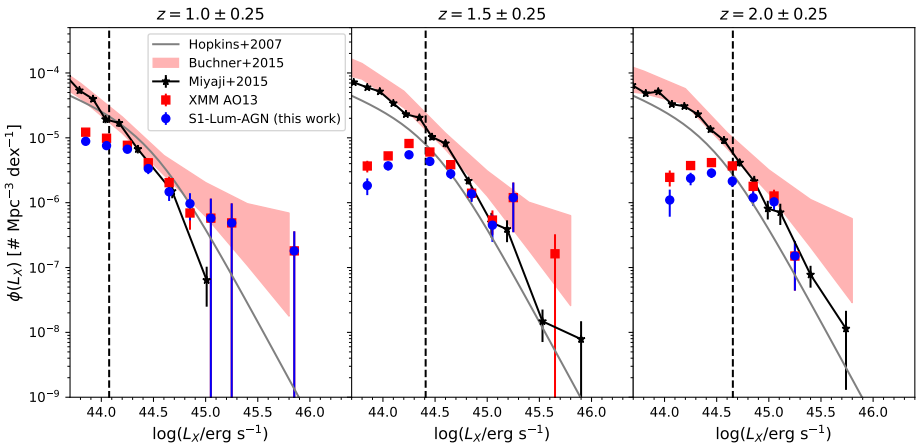

Figure 4.1: We compare the hard (2-10 keV) XLF of our sample of high X-ray luminosity AGN (S1-Lum-AGN, blue), which is based on XMM AO13 sources that have a reliable counterpart in our NEWFIRM K_S-selected catalog, to the XLF from all sources in XMM AO13 (red), and to the XLF from published studies Miyaji et al. (2015) (black, solid), Buchner et al. (2015) (red, shaded), and Hopkins et al. (2007) (gray, solid). The vertical dashed line in each panel indicates the 95% X-ray luminosity completeness limit, computed from the 95% flux limit at the upper edge of each redshift bin. The error bars computed for our sample are Poisson errors, and we calculate the XLF using the $1/V_{\rm max}$ method. We find relatively good agreement between our XLF values and those from the literature, especially at luminosities greater than $L_X = 10^{44.5}$ erg s^{-1}.

their implementation of AGN, stellar, and other feedback, and how we obtain a hard X-ray luminosity from the BHAR in each model. For a recent, comprehensive review of cosmological simulations, we refer the reader to Vogelsberger et al. (2020).

4.5.1 IllustrisTNG

IllustrisTNG is the successor to the Illustris hydrodynamical simulation (Vogelsberger et al., 2014a,b; Genel et al., 2014) and is modeled in varying box sizes and implements improved galaxy physics relative to the original Illustris simulation. The updates to the galaxy physics of Illustris focus on the growth and feedback of massive BHs, galactic winds, and chemical enrichment of gas and stellar evolution (Pillepich et al., 2018). For this project, we utilize the largest box size available, TNG300, which has a volume of $\sim 300^3$ Mpc^3 and a mass resolution of $m_{\rm baryon} = 1.1 \times 10^7$ $M_{\odot}$. Following Sherman et al. (2020b), we utilize the masses and SFRs measured within twice the stellar half mass radius (the $2 \times R_{1/2}$ aperture). The full description of the AGN and stellar feedback implementations in IllustrisTNG, as well as updates to the original Illustris model, can be found in Weinberger et al. (2017) and Pillepich et al. (2018), respectively. Here, we only give a brief overview.

One of the ways in which IllustrisTNG improves upon the Illustris model is by replacing the radio-mode AGN feedback in the low-accretion state with a new kinetic AGN feedback model that produces black hole-driven winds. The radio-mode AGN feedback model of Illustris injected thermal bubbles into the ICM, whereas the new kinetic AGN feedback model produces randomly oriented injections of momentum into the surrounding gas. The choice to replace the radio-mode feedback of Illustris is motivated by recent theoretical work that advocates for the inflow/outflow solutions of advection dominated accretion flows (ADAFs) (Yuan & Narayan, 2014). The new kinetic AGN feedback model is responsible for the quenching of galaxies in massive dark matter halos ($\sim 10^{12} - 10^{14} M_{\odot}$) and for producing 'red and dead' pop-

ulations of galaxies at late times in IllustrisTNG (Weinberger et al., 2017). This in turn produces more realistic SFRs in massive galaxies and estimates of the quenched fraction (Sherman et al., 2020b; Donnari et al., 2019) in IllustrisTNG. In the high-accretion state, both Illustris and IllustrisTNG invoke quasar-mode thermal feedback that heats the gas surrounding the BH. The transition between the low and high-accretion state AGN feedback modes in IllustrisTNG has a dependence on BH mass and Eddington ratio. This choice was made to ensure that BHs can transition to self-regulated states at lower accretion rates, and to ensure that newly seeded BHs do not remain in the low-accretion state.

In addition to AGN feedback, IllustrisTNG also invokes supernova (SN) feedback in order to regulate SF and prevent the over-production of galaxies. The SNe feedback is implemented through wind particles which are injected in random directions, with the strength of the feedback based on the energy released by the SN. In contrast to the original Illustris model, IllustrisTNG injects galactic winds isotropically and modifies the velocity of wind particles by introducing a redshift dependence factor in the calculation of the wind velocity. This choice of adding a redshift-dependent wind velocity is motivated by work done in semi-analytic models that find it necessary to implement a similar approach in order to reproduce the evolution of observed luminosity and stellar mass functions (Henriques et al., 2013). Additional mechanisms capable of heating and/or removing gas from galaxies, such as tidal stripping, ram-pressure stripping, and dynamical friction all occur naturally in IllustrisTNG. Such mechanisms follow the solutions of the equations of gravity and hydrodynamics in an expanding universe with gravitationally-collapsing structures (see Yun et al., 2019, for review of how these processes affect satellite galaxies in IllustrisTNG).

4.5.2 SIMBA

The SIMBA simulation is a hydrodynamical simulation that is run on a box with a side length of 100 Mpc/h and a mass resolution of $m_{\rm gas} = 1.82 \times 10^7\ M_\odot$. SIMBA builds on the MUFASA model (Davé et al., 2016) by introducing a new black hole growth model based on "torque-limited" accretion (Hopkins & Quataert, 2011; Anglés-Alcázar et al., 2013, 2015) as well as a new novel sub-grid prescription for AGN feedback. Further details about the SIMBA model can be found in Davé et al. (2019), we briefly summarize some key aspects below.

The AGN feedback model in SIMBA transfers energy from small to large scales through kinetic outflows with outflow parameters based on observations of AGN feedback. At Eddington ratios greater than 0.02, SIMBA implements a "radiative" feedback mode, modeled after observations of ionised and molecular gas outflows, where the AGN drives multi-phase winds with velocities of $\sim$ 1000 km s^{-1}. At Eddington ratios lower than 0.2, SIMBA transitions to a "jet" feedback mode where the AGN drives hot gas in collimated jets with velocities on the order of $\sim 10^4$ km s^{-1}. Such jets are capable of heating gas on scales up to ~ 8 Mpc away from the source. At late times ($z = 0$), the jet feedback from numerous AGN is shown to impact the inter-galactic medium (IGM) on large scales in SIMBA (Christiansen et al., 2020). We note that both radiative and jet feedback in SIMBA can simultaneously act on the surrounding gas in systems with Eddington ratios between 0.02 to 0.2. All outflows driven by AGN feedback are purely bipolar, meaning that gas elements are ejected in a direction parallel to the angular momentum vector of the accretion disk. We note that both the radiative and jet feedback modes in SIMBA employ kinetic feedback rather than thermal feedback. In addition to the radiative and jet AGN feedback, SIMBA adds an X-ray heating component to AGN with full velocity jets which heats the gas in galaxies. The X-ray feedback mode is motivated by work done in Choi et al. (2012), who show that this feedback is

capable of quenching massive galaxies in high-resolution zoom simulations.

The stellar feedback model implemented in SIMBA is the same feedback model that is implemented in MUFASA. In MUFASA, stellar feedback is attributed to winds from massive stars as well as long-lived stars (e.g., Type Ia supernovae, asymptotic giant branch stars). The stellar feedback model assumes massive stars drive material out through a combination of Type II supernovae winds, radiation pressure, and stellar winds. This type of kinetic feedback from massive stars is described in detail by Springel & Hernquist (2003) and Oppenheimer & Davé (2006). Meanwhile, feedback from long-lived stars is delayed relative to the time of star formation and so is not represented by the same outflows prescribed to massive stars. The prescriptions for Type Ia supernovae feedback and feedback from asymptotic giant branch stars are described in Scannapieco & Bildsten (2005) and Conroy et al. (2015), respectively.

4.5.3 SAG

The semi-analytical model SAG is implemented on the MultiDark Planck 2 (MDPL2) dark-matter only simulation with a volume of $1/h^3$ Gpc^3. The version of SAG we use in the present paper was also used by Sherman et al. (2020b). It is run on 9.4% of the full MDPL2 volume and was provided by the simulation leads (S. Cora, private communication). A full description of the SAG model can be found in Cora et al. (2018), here we briefly describe it.

In SAG, the AGN feedback model is implemented through a radio mode prescription that injects energy into the region surrounding the black hole, thereby reducing hot gas cooling. The accretion of hot gas is assumed to deposit energy into relativistic jets and this energy then gets deposited as heat in the hot gas atmosphere. Black holes in SAG can grow via both radio and quasar mode accretion, however, quasar mode feedback is not implemented in the model. Quasar growth in SAG

occurs during mergers and disc instabilities, whereas radio mode accretion arises from the accretion of hot gas onto the BH. Accretion of hot gas onto a BH occurs once a static hot halo has formed around the galaxy hosting the BH and is assumed to accrete continuously with a dependence on BH mass and hot gas mass (Henriques et al., 2015). For a more detailed description of the AGN feedback model in SAG, we refer the reader to Section 2.2 of Cora et al. (2019). SAG also includes redshift-dependent and virial velocity-dependent stellar feedback that heats gas within the galaxy. The parameter that controls the redshift dependent stellar feedback has been modified to better produce the evolution of the SFR density at high redshifts ($z > 1.5$) (Cora et al., 2018). In addition, the redshift-dependent stellar feedback implemented here has been shown to produce a quiescent fraction in local galaxies that is in better agreement with observations than other SAMs have been able to achieve (Xie et al., 2020; Cora et al., 2018). We note that Sherman et al. (2020b) compare the empirical quiescent fraction at $1.5 < z < 3$ to SAG and two other semi-analytical models and found that SAG best reproduces the observed trend that quenched fraction increases with stellar mass. This could be attributed to the explicit modeling in SAG of ram-pressure stripping and tidal stripping for satellite galaxies falling into a group or cluster. These processes are not instantaneous, meaning they gradually remove gas from the infalling satellite galaxy.

4.5.4 Obtaining an X-ray Luminosity from the BHAR

In this section, we describe how we obtain a hard-band (2-10 keV) X-ray luminosity from the BHAR in the numerical simulations. By obtaining X-ray luminosities from the predicted BHARs, we can select and analyze samples of highly luminous AGN in the simulations and compare to our observational results of galaxies with high X-ray luminosity AGN. In each simulation, we calculate bolometric luminosities for all objects with BHARs > 0 using the following equation:

$$L_{\rm bol} = \epsilon \dot{M} c^2 \tag{4.1}$$

Here, ϵ is the radiative efficiency, $\dot{M}$ is the BHAR, and c is the speed of light. The radiative efficiency ϵ is set internally by each simulation and is set to 0.1 in SAG and SIMBA, and is set to 0.2 in IllustrisTNG. The radiative efficiency of $\epsilon = 0.2$ in IllustrisTNG was chosen from a range of plausible values, however, lower values would have produced a stronger discrepancy between the measured and fiducial BH accretion rate at high redshift in IllustrisTNG (Weinberger et al., 2017). Once we get a bolometric luminosity we apply two different bolometric corrections (BCs) from Hopkins et al. (2007) and Lusso et al. (2012) to get hard-band X-ray luminosities.

One of the BCs we apply to $L_{\rm bol}$ to get L_X is that from Lusso et al. (2012) (hereafter L12), who use observed BH masses, bolometric luminosities, and X-ray luminosities to derive a relation between the BC and the Eddington ratio $f_{\rm Edd}$ of their AGN samples. In L12, they plot $L_{\rm bol}/L_X$ versus $f_{\rm Edd}$ for Type I and Type II AGN and fit a linear relation to the trend. Their Type I sample has higher bolometric luminosities, on average, than their Type II sample. Given that our sample is primarily made up of AGN with high X-ray luminosity, and assuming high X-ray luminosity corresponds to high bolometric luminosity (Duras et al., 2020; Lusso et al., 2012; Hopkins et al., 2007), we use the best-fit BC given in L12 for Type I AGN. The BC is obtained using the following equation:

$$\log(L_{\rm bol}/L_X) = 0.752 \times \log(\max[{\rm f_{Edd}}, 0.0015]) + 2.134 \tag{4.2}$$

We note that we use $\max[{\rm f_{Edd}}, 0.0015]$ in this equation because values of $f_{\rm Edd}$ lower than 0.0015 can result in an X-ray luminosity that exceeds the bolometric luminosity. The other BC we apply to the simulated galaxies to get $L_{\rm bol}$ is from Hopkins et al. (2007) (hereafter H07). In H07, the authors use fully integrated SEDs of quasars

from hard X-rays to radio wavelengths, column densities for a given spectral shape, and X-ray luminosities to derive a relation between X-ray luminosity and bolometric luminosity. The advantage of this method is that the BC only depends on the bolometric luminosity and so it can be applied in reverse to obtain $L_{\rm bol}$ for observed galaxies with high X-ray luminosity AGN. We clarify, however, that we only apply the H07 BC to the simulated galaxies to obtain the predicted X-ray luminosity. The BC for H07 is given by the following equation:

$$L_{\rm bol}/L_X = 10.83 \left(\frac{L_{\rm bol,\odot}}{10^{10} L_\odot} \right)^{0.26} + 6.08 \left(\frac{L_{\rm bol,\odot}}{10^{10} L_\odot} \right)^{-0.02} \tag{4.3}$$

Using these equations (Eqs. 4.2 & 4.3), along with Eq. 4.1, we convert the BHARs of all sources in the simulations with $\dot{M} > 0$ to X-ray luminosities in the hard (2-10 keV) band. This allows us to select and analyze samples of galaxies with high X-ray luminosity AGN in the simulations and make direct comparisons to the observed data.

4.6 Comparison of Empirical Results to Theoretical Models

In Paper 1, we explored the distribution of high X-ray luminosity AGN in the SFR-stellar mass plane and found that galaxies with high X-ray luminosity AGN have higher SFR, on average, than galaxies without such AGN at a given stellar mass. In this paper, we added some refinements to the selection of high X-ray luminosity AGN that increase the fidelity of comparisons to theoretical models and numerical simulations. We now compare our results to the hydrodynamical simulations IllustrisTNG and SIMBA, and the semi-analytic model SAG to explore the following questions: (i) How does the number density of high X-ray luminosity AGN in theoretical models and numerical simulations compare to the observed distribution

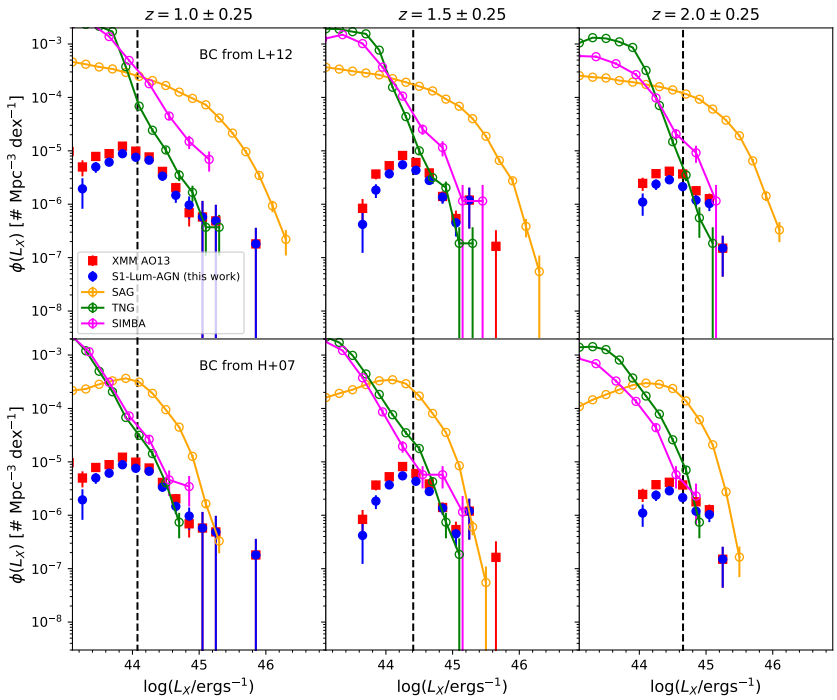

Figure 4.2: The hard (2-10 keV) X-ray luminosity function of our crossmatched sample (blue, same from Figure 4.1) and the full matched and unmatched XMM AO13 sample that falls in our survey footprint (red, same from Figure 4.1) compared to the XLF measured for SAG (orange), IllustrisTNG (green) and SIMBA (magenta) in three different redshift bins. All error bars shown are Poisson errors. Each row corresponds to a different bolometric correction that was used to obtain the X-ray luminosity from the bolometric luminosity in the simulations. Row 1 uses the bolometric correction from L12, and row 2 uses the bolometric correction from H07. Regardless of the bolometric correction used, SAG appears to over-predict the number density of galaxies with high X-ray luminosity AGN, relative to the observed sample, at all redshifts and X-ray luminosities. The XLF of IllustrisTNG appears to agree relatively well with the observed XLF, especially when assuming the bolometric correction from H07. The XLF for SIMBA appears to show that SIMBA over-predicts the number density of galaxies, regardless of bolometric correction used, though not to the extent that SAG does.

(Section 4.6.1)? (ii) Do theoretical models reproduce the observed distribution of galaxies with and without high X-ray luminosity AGN in the SFR-stellar mass plane (Section 4.6.2)? (iii) Do they reproduce the empirical result that galaxies with high X-ray luminosity AGN have a higher mean SFR at fixed stellar mass that galaxies without such AGN (Section 4.6.2)?

4.6.1 The X-ray Luminosity Function

Comparison of our observed XLF (see Figure 4.1) to the predicted XLF from the simulations can provide important insight to the physical processes directly related to AGN feedback and BH growth in the simulations. In Figure 4.2, we plot our XLF from the matched and unmatched XMM AO13 source list and the cross-matched sample (same data points from Figure 4.1) alongside the predicted XLFs from the three different simulations used in this work and the two different BCs, each corresponding to a different row, and at three different redshifts, each corresponding to a different column. The XLF for the simulations is calculated similarly to how it was calculated for the observed sample, but without the $1/V_{\rm max}$ method, which is not necessary for theoretical models.

Regardless of whether one uses the BC of L12 or H07, *SAG appears to over-predict the number density of galaxies with high X-ray luminosity AGN at all redshifts and at almost all but the very highest X-ray luminosities*, in a few instances, by factors ranging from ~ 10 to ~ 100. We note that the bright end of the SAG XLF only appears to agree with the data when applying the BC of H07. When applying the BC of L12, SAG appears to produce objects of impossibly high X-ray luminosities ($L_X > 10^{46}$ erg s^{-1} at $z \sim 1.5$ and at $z \sim 2$), which are not seen in our observations and the other observational studies whose XLF we plot in Figure 4.1. This striking overabundance of high X-ray luminosity AGN in SAG is also evident on the SFR-stellar mass plane (Figure 4.3). The discrepancy between the data and

SAG is large enough that it cannot be accounted for by the inherent uncertainties associated with computing the XLF for a theoretical simulation using a different BC.

In the case of IllustrisTNG and SIMBA, any disagreement with the data is less pronounced and has a larger dependence on which BC is used to obtain X-ray luminosities in the simulations. For both IllustrisTNG and SIMBA, the best agreement between the empirical and observed XLF is given by the BC of H07. However, in the highest redshift bin ($z \sim 2$), this BC produces very few objects above the 95% X-ray luminosity completeness limit and there are no objects above $L_X \sim 10^{45}$ erg s^{-1}. By contrast, the BC given by L12 leads to overproduction of X-ray luminous AGN at $L_X \lesssim 10^{45}$ erg s^{-1} at $z \sim 1$ in SIMBA by a factor of ~ 10 relative to the empirical XLF.

It is important to emphasize here the large uncertainties inherent in computing the XLF for simulations of galaxy evolution. One source of uncertainty we have discussed comes from the different BCs that exist in the literature, which all yield different populations of high X-ray luminosity AGN. Another source of uncertainty arises from the calculation of the bolometric luminosity. In this work, we only use a single expression to calculate bolometric luminosity. Some studies, however, suggest that it is necessary to make a distinction between radiatively efficient and inefficient AGN when computing bolometric luminosity (Giustini & Proga, 2019; Fanidakis et al., 2012; Churazov et al., 2005). Radiatively inefficient AGN are typically associated with low accretion rates, relative to the Eddington limit, and low gas densities. For such AGN, the gas flows do not cool efficiently as the radiative cooling is not capable of counteracting the viscosity-generated energy (Yuan & Narayan, 2014). We consider the effect of using a different expression to calculate bolometric luminosity in the Appendix for the SAG model, as it explicitly separates the radio mode accretion of hot gas from quasar mode accretion, and discuss whether doing so mitigates

the overproduction of high X-ray luminosity AGN by SAG (see Figure B.3). We find that calculating the bolometric luminosity differently for the radio mode accretion hardly affects the XLF predicted by SAG, especially at X-ray luminosities above the observed completeness limits. We note that Habouzit et al. (2019) does this for IllustrisTNG and finds that making a distinction between radiatively efficient and inefficient AGN when computing bolometric luminosity results in an XLF that is largely the same as the XLF that does not make a distinction between radiatively efficient and inefficient AGN, especially at high X-ray luminosities ($L_X > 10^{44}$ erg s^{-1}) (see their Figure A1). Lastly, we note that the fraction of Compton-thick AGN is not accounted for in the simulations, making it yet another source of uncertainty.

4.6.2 High X-ray Luminosity AGN on the SFR-Stellar Mass Plane

In Figures 4.3 and 4.4, we show the stellar mass-SFR relation of galaxies with and without high X-ray luminosity AGN for our observed sample and for the three simulations at three different redshift ranges. Figure 4.3 shows a scatter plot of SFR versus stellar mass, whereas Figure 4.4 shows the mean SFR as a function of stellar mass. Although some refinements were made to the AGN sample selection here based on the hard X-ray luminosity (see Section 4.3), we note that the top rows of Figures 4.3 and 4.4 essentially represent the empirical results from Paper 1 and are similar to Figures 10 and 11 in that paper. We also remind the reader that we use slightly different redshift ranges here so that we can more easily compare the empirical results to the theoretical models.

In Figure 4.3, the sample of galaxies without high X-ray luminosity AGN are color-coded by their density on the stellar mass-SFR plane, where density is calculated by counting number of neighbors around each data point inside an aperture with diameter equal to 0.1 dex. We also plot the mean SFR in different bins of stellar mass for the sample of galaxies without high X-ray luminosity AGN, which we refer

to as the main sequence. We calculate 1σ errors for the main sequence through a bootstrap method described in Paper 1. This bootstrap method re-samples galaxies x times within a given mass bin, where x is the sample size within that bin, with replacement. For each resampling, we calculate the average SFR and do this 1000 times. By taking the average SFR of all 1000 draws, we generate a distribution of average SFR values and take the 16th and 84th percentile of this distribution to calculate the error of the mean SFR. Also shown in each panel of Figure 4.3 is the line that falls 1 dex below the main sequence (magenta, dotted). As is done in Paper 1, we consider any sources that fall below this line to have quenched SFR. In Figure 4.4 we show the mean SFR as a function stellar mass for galaxies with and without high X-ray luminosity AGN separately. Error bars for all samples are calculated using the aforementioned bootstrap method.

As reported in Paper 1, the top row of Figures 4.3 and 4.4 show that galaxies with high X-ray luminosity AGN have a higher mean SFR by a factor of $\sim 3-10$ than galaxies without such AGN at a given stellar mass. We suggested in Paper 1 that this connection between high SFR and high AGN activity could be partly due to processes where large gas inflows fuel both circumnuclear SF and BH growth when the angular momentum problem in fueling BHs can be overcome (e.g., Jogee, 2006, and references therein). It is also clear from Figure 4.3 that the vast majority ($>$ 95%) of galaxies with high X-ray luminosity AGN do not have quenched SF. These results suggest that if AGN feedback quenches SF, then the associated quenching process takes a significant time to act and the quenched phase sets in after the highly luminous phases of AGN activity.

In Figures 4.3 and 4.4, the second, third, and fourth rows from the top show the corresponding distributions of galaxies with and without high X-ray luminosity AGN in the SFR-stellar mass plane in the semi-analytical model SAG (row 2), and the hydrodynamical simulations IllustrisTNG (row 3) and SIMBA (row 4).

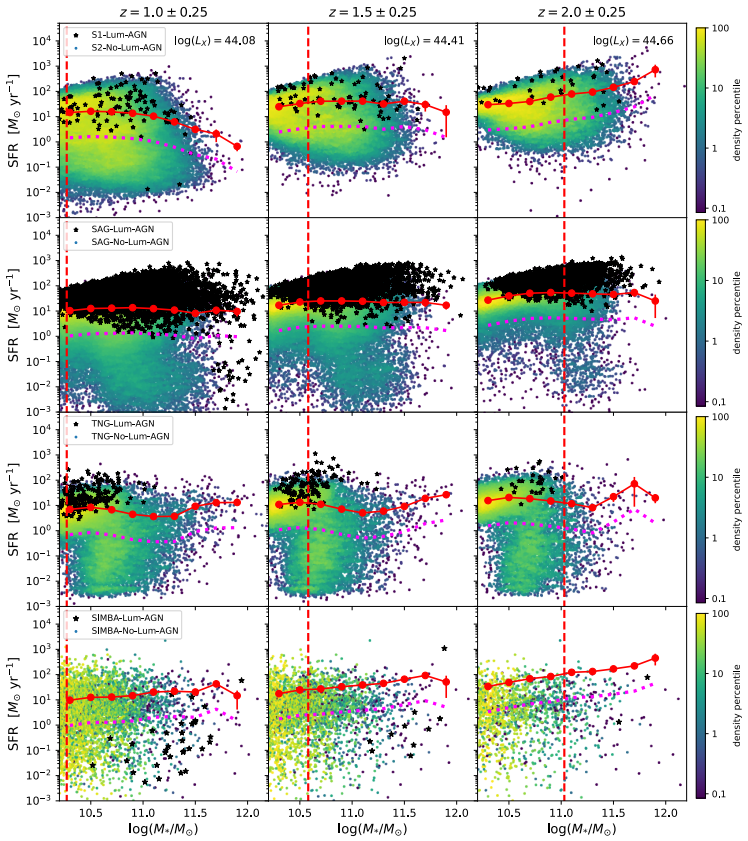

Figure 4.3: The stellar mass-SFR relation for galaxies with (black, stars) and without (colored) high X-ray luminosity AGN for our observed sample (first row), for SAG (second row), for IllustrisTNG (third row), and for SIMBA (fourth row) in three different redshift bins. The galaxies without high X-ray luminosity AGN are color-coded by their density on the mass-SFR plane. The dashed vertical line shows the observed stellar mass completeness limit at each redshift range. Also shown in each panel is the mean SFR, at fixed stellar mass, for the sample of galaxies without high X-ray luminosity AGN (red circles), which we refer to as the main sequence, and the line that falls 1 dex below the main sequence (dotted magenta). We used the H07 bolometric correction to obtain X-ray luminosities in the models for this figure. Compared to the data, SAG strongly over-produces the number density of AGN of high X-ray luminosity in all three redshift bins, as is seen in Figure 4.2, while IllustrisTNG shows a lack of high X-ray luminosity AGN at high stellar masses ($M_* > 10^{11}\ M_\odot$) at $z \sim 2$. However, both SAG and IllustrisTNG qualitatively reproduce the empirical results that galaxies with high X-ray luminosity AGN have higher mean SFR than galaxies without such AGN at a given stellar mass (see Figure 4.4). Contrary to the data, in SIMBA the majority of galaxies with high X-ray luminosity AGN appear to have quenched SF.

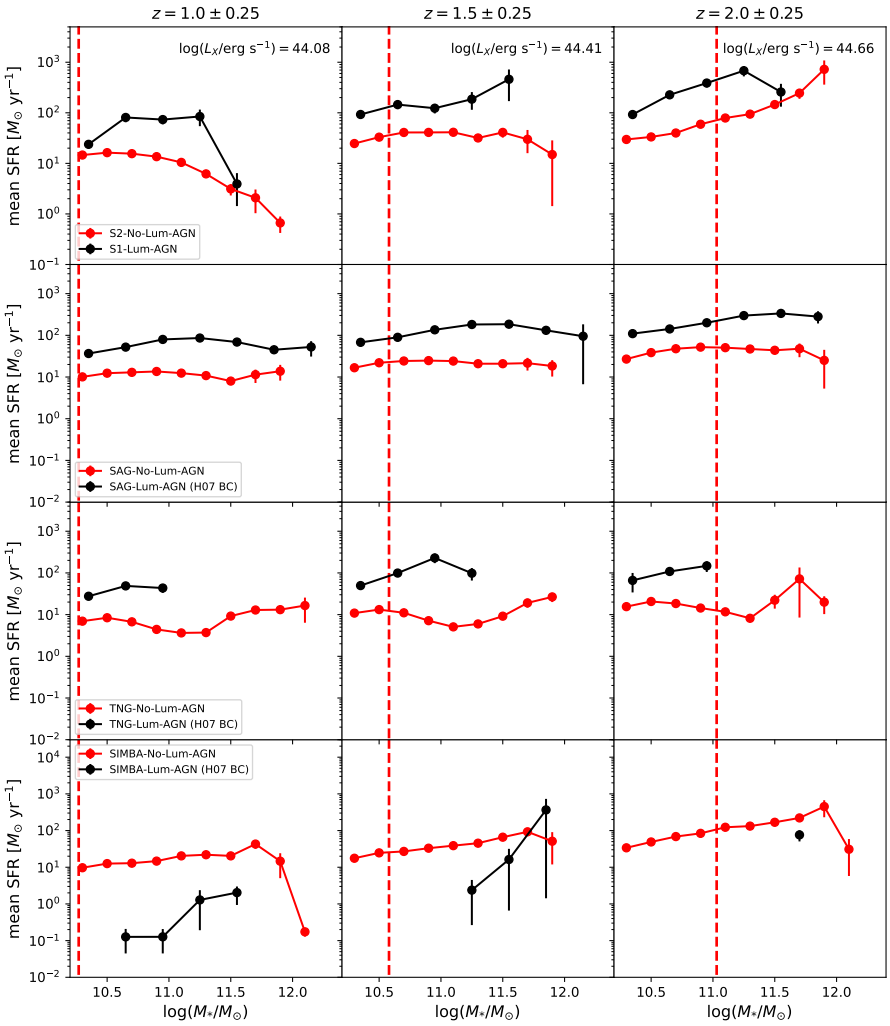

Figure 4.4: Row 1: The mean SFR as a function of stellar mass for the sample of galaxies with (black circles) and without (red circles, same as Figure 4.3) high X-ray luminosity AGN. Rows 2-4: Similar to first row, but for SAG (row 2), IllustrisTNG (row 3), and SIMBA (row 4). As in Figure 4.3, the BC of H07 was used to obtain hard X-ray luminosities in the models shown here. In qualitative agreement with the data, SAG and IllustrisTNG show enhanced SFR in galaxies with high X-ray luminosity AGN compared to galaxies without such AGN, except at the highest stellar masses in IllustrisTNG. Contrary to the data, galaxies with high X-ray luminosity AGN in SIMBA have a mean SFR, at a given stellar mass, that is lower than the mean SFR of galaxies without such AGN.

The results shown in these Figures are based on the BC of H07. We use the BC prescription of H07 here as it seems to provide the best match between the models and the data (Section 4.6.1). These theoretically predicted distributions of galaxies with and without high X-ray luminosity AGN in the SFR-stellar mass plane can be directly compared to the empirical results shown in the top rows of Figures 4.3 and 4.4.

We find that SAG strongly over-produces the number density of high X-ray luminosity AGN by factors of $\sim 10 - 100$. This can be seen in the second row of Figure 4.3, as well as in the Figure 4.2 discussed in Section 4.6.1. However, SAG does qualitatively reproduce the empirical results showing that galaxies with high X-ray luminosity AGN have higher mean SFR than galaxies without such AGN at a given stellar mass (second row from the top in Figures 4.3 and 4.4). As can be seen in Figure 4.3, galaxies in SAG with high X-ray luminosity AGN tend to reside in galaxies with enhanced SFR relative to the main sequence and only a very small fraction ($< 1\%$) of galaxies with high X-ray luminosity AGN in SAG have quenched SFR, consistent with the empirical results.

IllustrisTNG qualitatively reproduce the empirical result that galaxies with high X-ray luminosity AGN have higher mean SFR than galaxies without such AGN activity at a given stellar mass (third row in Figures 4.3 and 4.4). As illustrated in Figure 4.3, in IllustrisTNG, most galaxies with high X-ray luminosity AGN lie above the main sequence. However, IllustrisTNG shows a lack of high X-ray luminosity AGN at high stellar masses ($M_* > 10^{11}\ M_\odot$) at $z \sim 2$ and very few objects with X-ray luminosities above the observed 95% X-ray luminosity completeness limit at the same redshift.

In the SIMBA simulation, we find at $z < 2$ that galaxies with high X-ray luminosity AGN with $M_* < 10^{11.5}\ M_\odot$ have mean SFRs that are 1 to 2 orders of magnitude lower than the main sequence (bottom row of Figure 4.4). As a result,

the mean SFR of galaxies with high X-ray luminosity AGN is lower than the SFR of those without such AGN. This trend is opposite to the empirical results (top row of Figures 4.3 and 4.4). Contrary to the data, many high X-ray luminosity AGN in SIMBA have quenched SF, suggesting that AGN feedback or other feedback modes in galaxies with such AGN might be too efficient in SIMBA. We discuss this further in Section 4.7. In the highest redshift bin, there are very few AGN with L_X above the observational 95% completeness limit.

We note that the number of galaxies with high X-ray luminosity AGN in the models having quenched SF depends on which BC prescription we use to go from bolometric luminosity to X-ray luminosity (see Section 4.5.4). Figures 4.3 and 4.4 currently use the BC from H07. Figures B.1 and B.2 in the Appendix, show the results with the BC in L12. These figures show that the main results remain largely unchanged for all three simulations at $M_* < 10^{11.5}\ M_\odot$. We discuss this further in the Appendix.

4.7 Discussion

In Sections 4.6.1 and 4.6.2, we compare the empirical and predicted XLF and stellar mass-SFR relation of galaxies with and without high X-ray luminosity AGN. These comparisons are critical for guiding how AGN feedback is implemented in theoretical models of galaxy evolution. We discuss the possible sources of discrepancy between the theoretical models and the empirical results, as well as the implications for each theoretical model below.

SAG: We find that SAG over-produces the number density of high X-ray luminosity AGN at all redshifts and almost all X-ray luminosities by two orders of magnitude. Only at the every highest X-ray luminosities obtained from the H07 BC ($L_X \gtrsim 10^{45}$ erg s^{-1}; see Figure 4.2) does the predicted XLF from SAG appear to match that of

data. The overproduction of high X-ray luminosity AGN in galaxies could be due to the lack of quasar mode feedback and/or inefficient stellar feedback allowing high BHARs to go unchecked in such a large fraction of the population. In SAG, the growth of BHs via quasar mode is only triggered by mergers or disc instabilities, meaning such processes would produce high SFRs and AGN activity but may lack the feedback channels to suppress BH growth enough to prevent the overproduction of high X-ray luminosity AGN. The radio mode AGN feedback is only activated through the accretion of hot gas during the cooling process (Cora et al., 2018), meaning there is no AGN feedback present when BHs grow in the quasar mode (i.e., via mergers or disc instabilities). Observations of quasars have shown that AGN with typically higher accretion rates (> few percent of $f_{\rm Edd}$) are capable of driving molecular and ionised gas outflows with velocities of up to ~ 1000 km s^{-1} or more (Perna et al., 2017; Liu et al., 2013; Sturm et al., 2011). Therefore, it is not unreasonable to speculate that SAG needs to implement some form of quasar feedback in order to regulate the overproduction of high X-ray luminosity AGN.

In Figures 4.3 and 4.4, we find that an excessive number of high mass galaxies ($M_* > 10^{11.5}$ $M_\odot$) in SAG have high X-ray luminosity AGN, but the most massive galaxies in our sample do not. This is consistent with the fact that SAG overproduces the number of high X-ray luminosity AGN at all redshifts. The average SFR of galaxies with and without high X-ray luminosity AGN in SAG follows a trend similar to what is seen in the observations. The mean SFR of galaxies with high X-ray luminosity AGN is higher, by a factor of $\sim 2-10$, than the mean SFR of galaxies without high X-ray luminosity AGN at the same stellar mass. We also find that very few galaxies with high X-ray luminosity AGN have quenched SF, consistent with what we find in the observations. Starbursts in SAG are triggered via mergers and disc instabilities, as is the accretion of cold gas onto the BH in quasar mode. It is therefore no surprise that objects growing their BHs through

these mechanisms experience large amounts of SF.

IllustrisTNG: The XLF of IllustrisTNG agrees with the empirical XLF more than the XLF of the other two simulations, especially when considering the BC of H07 and the BC of L12 at $z > 1$. We find, however, that even when applying the H07 or L12 BC to obtain X-ray luminosities, the XLF of IllustrisTNG does not reproduce the bright end of the empirical XLF at $z = 1$ or $z = 2$. This is in agreement with what is found in Habouzit et al. (2019), who compare the XLF of IllustrisTNG to observations and find that IllustrisTNG cannot produce galaxies with X-ray luminosities at the bright end of the empirical XLF. They suggest that this could be due to the high efficiency of the kinetic mode AGN feedback which suppresses the BH accretion and AGN luminosity. In IllustrisTNG, the kinetic mode AGN feedback is activated at low accretion rates relative to the Eddington limit and has a dependence on BH mass. More specifically, the transition between feedback modes in IllustrisTNG occurs when the Eddington ratio exceeds or drops below a BH mass dependent threshold of $\min[f(M_{\rm BH}), 0.1]$, where $f(M_{\rm BH})$ is a quantity proportional to $M_{\rm BH}^2$. As shown in Weinberger et al. (2017), galaxies with BHs more massive than $\sim 10^8$ $M_\odot$ tend to have lower Eddington ratios than galaxies with less massive BHs. The dependence of the kinetic feedback mode on BH mass in IllustrisTNG could mean that galaxies with more massive BHs ($M_{\rm BH} \gtrsim 10^8$ $M_\odot$) will always be prevented from producing X-ray luminosities seen at the bright end of the XLF. Galaxies with lower mass BHs ($M_{\rm BH} \leq 10^7$ $M_\odot$) cannot produce such luminous AGN either as the bolometric luminosity required to produce X-ray luminosities at the bright end of the observed XLF would exceed the Eddington limit by an order of magnitude or more (e.g., $L_{\rm Edd} = 1.2 \times 10^{45}$ erg s^{-1} for $M_{\rm BH} = 10^7$ $M_\odot$). We note that IllustrisTNG explicitly limits BH growth by the Eddington limit by estimating the accretion rate as $\dot{M}_{\rm BH} = \min(\dot{M}_{\rm Bondi}, \dot{M}_{\rm Edd})$, where $\dot{M}_{\rm Bondi}$ is the

Bondi accretion rate and $\dot{M}_{\rm Edd}$ is the Eddington limit (Weinberger et al., 2017).

In the highest redshift bin of Figures 4.3 and 4.4, we do not find any high X-ray luminosity AGN in IllustrisTNG residing in galaxies above our observed stellar mass completeness limit. As discussed above, feedback from AGN with BHs more massive than 10^8 $M_\odot$ is more likely to be kinetic mode feedback. Therefore, if one were to reasonably expect that more massive ($M_* > 10^{11}$ $M_\odot$) galaxies, with accreting BHs, in IllustrisTNG host more massive BHs ($M_{\rm BH} > 10^8$ $M_\odot$), then there is a high probability that the kinetic feedback mode is activated in those galaxies and the feedback, in turn, prevents the accretion rate and the resulting X-ray luminosity from reaching the observed values We note that Figure 6 of Weinberger et al. (2017) explicitly shows how the BHAR drastically drops once the kinetic mode feedback is triggered, which typically occurs at $M_{\rm BH} \gtrsim 10^8$ $M_\odot$. At $z < 2$ we find that the mean SFR, at a given stellar mass, of galaxies with high X-ray luminosity AGN is higher than the mean SFR of galaxies without such AGN in IllustrisTNG (Figures 4.3 and 4.4).

SIMBA: The XLF produced by SIMBA agrees with the empirical XLF to within a factor of $\sim 2-3$ at all redshifts when using the H07 BC to derive X-ray luminosities. However, SIMBA does not seem to be able to produce AGN with X-ray luminosities seen at the bright end of the empirical XLF (with $L_X \gtrsim 10^{45}$ erg s^{-1}). A likely reason for this could simply be due to the limited volume of SIMBA ($\sim 3 \times 10^6$ Mpc^3), as AGN with such high X-ray luminosities are extremely rare and have low number densities ($\lesssim 10^{-7}$ Mpc^{-3}). It has been shown in Thomas et al. (2021) that the radio luminosity function of AGN in SIMBA extends up to the highest observed luminosities, without any evidence for truncation, lending credit to the idea that the lack of AGN with $L_X \gtrsim 10^{45}$ erg s^{-1} in SIMBA is due to limited volume rather than the implementation of BH accretion in the model. We remind the reader that, unlike

IllustrisTNG, whose AGN kinetic feedback is injected in randomized directions and is capable of clearing all the gas near the BH, the AGN kinetic feedback in SIMBA is purely bipolar and decoupled from the gas, meaning it explicitly avoids clearing gas in the vicinity of the BH.

In SIMBA, the mean SFR of galaxies with high X-ray luminosity AGN is lower than the mean SFR of galaxies without high X-ray luminosity AGN. For SIMBA, it is clear that the quenching mechanisms are far too efficient in galaxies with high X-ray luminosity AGN as the SFRs of these objects are far lower than the empirical SFRs of galaxies with high X-ray luminosity AGN. Not only does SIMBA implement jet and radiative mode feedback, it also implements X-ray heating in AGN with full velocity jets. This form of feedback is invoked in gas-poor (i.e., having $M_{\rm gas}/M_* < 0.2$) galaxies when the AGN jet mode feedback is active, meaning two forms of AGN feedback can rapidly heat and eject the gas in galaxies. X-ray feedback is not applied to more gas-rich galaxies under the assumption that such galaxies would be able to absorb and radiate away the X-ray energy (Davé et al., 2019). Another possible reason that SF is much lower in galaxies with high X-ray luminosity AGN in SIMBA is because the radiative mode feedback injects momentum, rather than thermal energy (as is done in IllustrisTNG for quasar-mode feedback), into the surrounding gas. Such injections of momentum are more effective at quenching SF than injections of thermal energy as the resulting winds from the kinetic feedback are capable of ejecting gas from the galaxy. It is important to note that due to the small volume of SIMBA, the results we are seeing could also be in part due to environment. The jet mode feedback in SIMBA is shown to have a widespread effect on the IGM (Christiansen et al., 2020), meaning that jet mode feedback could effectively quench the SF of many galaxies existing in large groups or clusters. This would make it such that quasars in groups or clusters have quenched SF, even if the quasar-mode (i.e., radiative) feedback itself is not the

primary driver of SF quenching. It is therefore possible that a larger volume could weaken the discrepancy between the empirical results and SIMBA. Future work that explores the characterization of environment in both observations and larger volume simulations will shed light on this issue.

We note that part of the discrepancy we find between SIMBA and the empirical results could be also due to the stochastic accretion of hot gas. The Bondi accretion for a BH could essentially be nonexistent until the BH accretes a single hot gas particle, and then the accretion rate is high for that time step. If this happens to occur during the time step of the output, one gets a very high accretion rate. This was dealt with in Thomas et al. (2021) by smoothing the accretion rate over a 50 Myr window, which ultimately resulted in lower Bondi accretion rates more consistent with observations. The smoothing of the accretion rate in SIMBA has the potential to prevent quenched galaxies from achieving such high X-ray luminosities and therefore move the mean SFR of galaxies with high X-ray luminosity AGN to higher values and result in slightly better agreement with the empirical results. We note that yet another part of the discrepancy between SIMBA and the empirical results could be due to the fact that the kinetic feedback in SIMBA is bipolar and decoupled from the gas. Since the AGN kinetic feedback avoids clearing gas in the vicinity of the BH, it is possible that the feedback modes cannot prevent BHs in massive quiescent galaxies from accreting too much hot gas and becoming luminous AGN.

4.8 Summary

In Paper 1 we explored the relation between AGN and SF activity at cosmic noon. We found that galaxies with high X-ray luminosity AGN have higher mean SFR by a factor of $\sim 3-10$, at a given stellar mass, than galaxies without such AGN. We also found that the vast majority ($> 95\%$) of galaxies with high X-ray luminosity AGN

do not have quenched SF. Our empirical results from Paper 1 are consistent with a scenario where high SFRs and high AGN luminosities are triggered by mechanisms capable of producing large gas inflow rates into the sub-pc region associated with the AGN accretion disk. These results also suggest that if AGN feedback quenches SF, the associated quenching process takes a significant time to act and the quenched phase sets in after the highly luminous phases of AGN activity.

In numerical simulations and theoretical models of galaxy evolution, AGN and SF activity are closely intertwined and AGN feedback is routinely invoked to regulate galaxy growth. In this paper, we explored such models by comparing three different simulations (i.e., the hydrodynamical simulations IllustrisTNG and SIMBA, and the semi-analytical model SAG) to our empirical results (Paper 1) and provide guidance and constraints for future developments and improvement of these models. We made some small refinements to the sample selection in order to increase the fidelity of comparisons to theoretical models. We explored the following questions: (i) How does the number density of high X-ray luminosity AGN in theoretical models and numerical simulations compare to the observed distribution (Section 4.6.1)? (ii) Do theoretical models reproduce the observed distribution of galaxies with and without high X-ray luminosity AGN in the SFR-stellar mass plane (Section 4.6.2)? (iii) Do theoretical models reproduce the empirical result that galaxies with high X-ray luminosity AGN have a higher mean SFR at fixed stellar mass than galaxies without such AGN (Section 4.6.2)? We summarize our findings below.

(1) **SAG:** We find that SAG over-produces the number density of high X-ray luminosity AGN at all redshifts and almost all X-ray luminosities by factors of $\sim 10-100$. This is evident in the XLF produced by SAG (Figure 4.2) and in the distribution of high X-ray luminosity AGN on the SFR-stellar mass plane (Figure 4.3). This could be due to a lack of quasar mode feedback and/or

inefficient stellar feedback which is allowing high BHARs to go unchecked in a large fraction of the population. Observations of quasars have shown that such AGN are capable of driving outflows with velocities of up to ~ 1000 km s^{-1} or more. It is therefore not unreasonable to speculate that SAG may need to implement some form of quasar mode feedback in order to regulate the overproduction of high X-ray luminosity AGN.

In Figure 4.3, we find an excessive number of high mass galaxies ($M_* > 10^{11.5} M_\odot$) in SAG have high X-ray luminosity AGN, consistent with the fact that SAG over-produces the number density of high X-ray luminosity AGN at all redshifts. SAG qualitatively reproduces the empirical result that galaxies with high X-ray luminosity AGN have higher mean SFR, at fixed stellar mass, than galaxies without such AGN by a factor of $\sim 2 - 10$. SAG also produces very few quenched galaxies with high X-ray luminosity AGN, consistent with what we find in the observations. Starbursts in SAG are triggered via mergers and disc instabilities, so it is no surprise that objects growing their BHs through these mechanisms also experience large amounts of SF.

(2) **IllustrisTNG:** The XLF produced by IllustrisTNG shows relatively good agreement with the empirical XLF, especially when considering the BC of H07. IllustrisTNG, however, cannot seem to produce AGN observed at the bright end of the empirical XLF. This could be due to the high efficiency of the kinetic mode AGN feedback which suppresses BH accretion and therefore AGN luminosity. Because the feedback mode has a dependence on BH mass, it is possible that galaxies with BHs more massive than $\sim 10^8 M_\odot$ will always be prevented from producing X-ray luminosities seen at the bright end of the XLF.

When examining the highest redshift bin in Figures 4.3 and 4.4, we do not find any high X-ray luminosity AGN residing in galaxies above our observed

stellar mass completeness limit in IllustrisTNG. As discussed above and in Section 4.7, this is likely due to the dependence of the feedback mode on BH mass in IllustrisTNG. The kinetic mode feedback is more likely to be activated in higher stellar mass galaxies ($M_* > 10^{11}\ M_\odot$), simply due to higher mass galaxies hosting higher mass BHs, and the feedback in turn prevents the AGN X-ray luminosity from reaching observed values. At $z < 2$, we find the mean SFR, at fixed stellar mass, of galaxies with high X-ray luminosity AGN is higher than the mean SFR of galaxies without such AGN in IllustrisTNG.

(3) **SIMBA:** Similar to IllustrisTNG, SIMBA does not seem able to produce AGN with X-ray luminosities seen at the bright end of the empirical XLF (with $L_X \gtrsim 10^{45}$ erg s^{-1}). This is could likely be due to the limited volume of SIMBA rather than the BH accretion model itself, as high X-ray luminosity AGN at the bright end of of the XLF are extremely rare and have low number densities. Unlike IllustrisTNG, the bipolar kinetic feedback in SIMBA explicitly avoids clearing out the gas in the vicinity of the BH, meaning that it does not suppress BH growth as effectively as the kinetic AGN feedback model does in IllustrisTNG.

Contrary to the empirical results, the mean SFR of galaxies with high X-ray luminosity AGN is lower than the mean SFR of galaxies without such AGN in SIMBA (Figures 4.3 and 4.4). It is clear that the quenching mechanisms in SIMBA act far too efficiently in galaxies with high X-ray luminosity AGN. We note that both forms of AGN feedback in SIMBA (i.e., jet mode and radiative mode) inject momentum into the surrounding gas, rather than thermal energy. Such injections of momentum are capable of removing gas from a galaxy and quenching SF more effectively than injections of thermal energy. In addition to radiative and jet mode feedback, SIMBA implements X-ray feedback in AGN with full-velocity jets meaning multiple forms of feedback can rapidly heat and

eject the gas in galaxies. Because the jet mode feedback can affect the IGM on scales up to ~ 8 Mpc, we note that the quenching of SF in galaxies with high X-ray luminosity AGN could be partially due to volume and/or environment as a high density environment is much more likely to experience widespread quenching.

We note that part of the discrepancy between SIMBA and the empirical results on the stellar mass-SFR plane could also be due to the stochastic accretion of hot gas onto the BH. If BHARs are smoothed over some range of time, as is done in Thomas et al. (2021), it could potentially prevent quiescent galaxies from achieving such high X-ray luminosities and therefore move the mean SFR of galaxies with high X-ray luminosity AGN towards higher values. It is also possible that the bipolar nature of the kinetic feedback model in SIMBA contributes to the disagreement with the empirical results. Since the kinetic feedback is bipolar and decoupled from the gas, the kinetic AGN feedback model in SIMBA may not prevent BHs in massive quiescent galaxies from accreting too much hot gas and becoming luminous AGN.

Chapter 5

Summary and Future Work

One of the central goals of extragalactic astronomy is to understand how galaxies grow their stellar mass and central black holes, the connection between AGN and star formation, and the impact of environment on galaxy and black hole growth. This thesis has made significant advances on these topics through three papers, corresponding to Chapters 2, 3, and 4. More specifically, this thesis has made advancements in characterizing and analyzing the relation between low-density environments and observed distributions of galaxy properties, as well as comparing statistically robust populations of galaxies with and without high X-ray luminosity AGN. Such advancements are made possible by the large area, multi-wavelength surveys used in this thesis, which probe galaxy evolution over a large volume at low redshift ($z = 0.015 - 0.023$) and at cosmic noon ($z = 0.5 - 3.0$), thereby rendering the effects of cosmic variance negligible. Advancements have also been made in the SED fitting methods used for analyzing populations of galaxies with high X-ray luminosity AGN. In this Chapter, I summarize the key results of this thesis (Section 5.1), and in Section 5.2 I describe the next steps that can be taken with the rich data sets used in this work.

5.1 Key Results

5.1.1 How do Galaxies Evolve in Low Density and Void-like Environments?

In Chapter 2, we find galaxies in voids and low density environments are typically less massive, more star-forming, and more gas-rich than galaxies living in higher density environments (e.g., Figures 2.6 and 2.7). Our study is the first to find that such trends persist at fixed mass and morphology. Although satellite galaxies can contribute to the variations we see in the observed mean quantities of galaxies in low and high density environments, the observed trends persist (albeit more weakly) when satellites are removed from the analysis and only central galaxies are considered (Figure 2.7). This could be explained by a number of reasons. Galaxies that live in low-density and void-like regions grow and evolve in relatively pristine environments. Transformation processes that are common in groups or clusters, such as ram-pressure stripping, tidal stripping, mergers, etc., are absent (in the case of ram-pressure stripping), or less frequent (in the case of mergers), in lower density environments. This, in part, explains why late-type galaxies are more common in voids (Hoyle et al., 2012). It does not explain, however, why late-type and early-type galaxies in voids or low-density environments are bluer, more star-forming, and more gas-rich than late-type or early-type galaxies at fixed mass in higher density environments (see Figure 2.10). The populations of blue and star forming early-types we find in voids do not appear to arise from mergers or other interactive transformation mechanisms, thus challenging assumptions about how early types are formed in the Universe. Further work analyzing the structural properties of early-type galaxies in low-density environments could shed light on this issue.

One possible explanation for our results could be attributed to galaxy assembly bias. This is the observed phenomenon that the properties of galaxies correlate

with galaxy formation time and assembly history. Simply put, galaxies at $z \sim 0$ that formed at earlier epochs will have had more time to quench star formation than galaxies, of the same mass, that formed at later epochs. This is, in part, supported by the comparison of our empirical results to abundance matching models which have built-in assembly bias.

5.1.2 What is the Relation Between AGN Activity and Star Formation in Massive Galaxies at Cosmic Noon?

The epoch of cosmic noon ($z \sim 1 - 3$) is an interesting and important epoch of galaxy evolution. Star formation and AGN activity in galaxies peaked around this time, protoclusters began to collapse, and massive galaxies began to transition from primarily star-forming galaxies to primarily quiescent galaxies. Because the peak of AGN activity and star formation coincide around this epoch, it is imperative to understand the connection between AGN and star formation at cosmic noon and what role AGN feedback plays in the quenching of massive galaxies at cosmic noon. Several studies have explored the relation between high luminosity AGN and star formation (e.g., Kirkpatrick et al., 2019; Masoura et al., 2018; Shimizu et al., 2017, 2015), however, none of these studies obtain stellar masses and star formation rates in a self-consistent manner and none compare their luminous AGN galaxy sample to a statistically significant sample of massive galaxies without luminous AGN. Chapter 3 of this thesis makes significant advances in exploring the AGN and star formation connection at cosmic noon by being the first study of its kind to self-consistently obtain stellar masses and star formation rates for a large, statistically robust, sample of massive galaxies with and without high X-ray luminosity AGN. Such a study allows us to reasonably detail the physical mechanisms driving the observed properties of galaxies with high X-ray luminosity AGN.

Chapter 3 of this thesis reports two key results: (i) At fixed stellar mass,

galaxies with high X-ray luminosity AGN have a mean star formation rate that is a factor of $\sim 3-10$ times higher than galaxies without such AGN; (ii.) The majority ($> 95\%$) of AGN with high X-ray luminosity do not reside in galaxies with quenched star formation. These results are consistent with a scenario where high star formation and high AGN luminosity is produced by processes that drive large gas inflows into the sub-kpc regions typically associated with high star formation rates, as well as the sub-pc regions associated with the AGN accretion disk. Examples of such processes include gas-rich major mergers, gas-rich minor mergers, and strong tidal interactions in gas-rich systems. In order to drive gas from kpc scales down to the scales of the AGN accretion disk, however, we need mechanisms that can effectively reduce the angular momentum of the gas by several orders of magnitude, such as shocks, dynamical friction on gas clumps, feedback processes from local star formation activity, gravitational torques from a primary bar, secondary bars or/and other non-axisymmetric features, tidal disruption of clumps, and hydro-magnetic winds (e.g., Jogee, 2006, and references therein).

It is instructive to look at high resolution zoom simulations which explore the onset of high star formation and high AGN luminosity (Park et al., 2017; Capelo et al., 2015; Cox et al., 2008; Di Matteo et al., 2008; Springel et al., 2005). Such simulations show that large gas inflows during major mergers can simultaneously trigger star formation and AGN activity in the merging of two galaxies. In these simulations, the peak of black hole accretion and star formation activity appear to coincide and then the star formation rate and black hole accretion decline in tandem to the final stages of the merger. Because we see high luminosity AGN exist in galaxies with high star formation rates, it is imperative to ask whether we should look to observations of mergers for signatures of AGN as well as deeper X-ray data to find populations of AGN in different phases of evolution.

5.1.3 What Can We Infer about AGN Feedback?

One of the key questions of extragalactic astronomy that we try to address in this thesis is: what role does AGN feedback play in the quenching of massive galaxies at cosmic noon? This is not such a straightforward question to answer, however, as this work does not necessarily explore outflows and energetics produced by luminous AGN in galaxies. We can infer several things about the nature of AGN feedback from this study, however, that can improve our understanding on the role of AGN feedback in galaxy evolution.

One important result we can infer from the work done in Chapter 3 of this thesis is that if AGN feedback quenches star formation, it does not do so during the highly luminous phases of AGN activity. It is therefore not unreasonable to speculate that AGN feedback might be more efficient in lower-luminosity AGN with lower black hole accretion rates. This is, in part, supported by observations of quasars that show AGN with typically higher accretion rates ($>$ few percent of the Eddington ratio) can drive molecular and ionised gas outflows with velocities of up to ~ 1000 km s^{-1} or more (Perna et al., 2017; Liu et al., 2013; Sturm et al., 2011), whereas AGN with much lower accretion rates, and therefore lower luminosities, can produce jets that eject matter with velocities of up to $\sim 10^4$ km s^{-1}, an order of magnitude higher. We can also infer, from the few but noticeably present quenched galaxies with high X-ray luminosity AGN in Chapter 3, that if star formation in quenched during the luminous AGN phase, the AGN will only remain luminous for an extremely short time thereafter. These results help guide how models of black hole growth and AGN feedback are implemented in theoretical models of galaxy evolution, as will be discussed in the following section.

5.1.4 How Well Do Theoretical Models Reproduce Observed Properties of Galaxies with and without High X-ray Luminosity AGN?

In Chapter 4, I compare the empirical results from Chapter 3 on the AGN and star formation connection to several classes of theoretical models of galaxy evolution (e.g., hydrodynamical simulations and semi-analytical models). None of the models I utilized were able to accurately reproduce the empirical results from Chapter 3. The possible sources of discrepancy between the theoretical models and the empirical results, implications for each theoretical model, and possible improvements are discussed below.

The semi-analytic model SAG (Cora et al., 2018) over-produces the number of high X-ray luminosity AGN at all redshifts and almost all X-ray luminosities by almost two orders of magnitude. The overproduction of high X-ray luminosity AGN in SAG could be due to the lack of quasar mode feedback that allows high black hole accretion rates to go unchecked in a large number of galaxies. In SAG, the growth of black holes via quasar mode is only triggered by mergers or disc instabilities, meaning such processes would produce high star formation rates and AGN activity but may lack the feedback channels to suppress black hole growth enough to prevent the overproduction of high X-ray luminosity AGN. Radio mode AGN feedback is only activated through the accretion of hot gas during the cooling process, meaning there is no AGN feedback present when black holes grow in the quasar mode (i.e., via mergers or disc instabilities). Observations of quasars have shown that AGN with typically higher accretion rates are capable of driving molecular and ionised gas outflows with velocities of up to $\sim$ 1000 km s^{-1} or more (Perna et al., 2017; Liu et al., 2013; Sturm et al., 2011). Therefore, it is not unreasonable to speculate that SAG needs to implement some form of quasar feedback in order to regulate the overproduction of high X-ray luminosity AGN.

In Figures 4.3 and 4.4, I show that an excessive number of high mass galaxies ($M_* > 10^{11.5}\ M_\odot$) in SAG have high X-ray luminosity AGN, but the most massive galaxies in our sample do not. This is consistent with the fact that SAG overproduces the number of high X-ray luminosity AGN at all redshifts. The average SFR of galaxies with and without high X-ray luminosity AGN in SAG follows a trend similar to what is seen in the observations. The mean star formation rate of galaxies with high X-ray luminosity AGN is higher, by a factor of $\sim 2 - 10$, than the mean star formation rate of galaxies without high X-ray luminosity AGN at the same stellar mass. I also find that very few galaxies with high X-ray luminosity AGN have quenched star formation, consistent with what is found in the observations. Starbursts in SAG are triggered via mergers and disc instabilities, as is the accretion of cold gas onto the black hole in quasar mode. It is therefore no surprise that objects growing their black holes through these mechanisms experience large amounts of star formation.

The X-ray luminosity function of IllustrisTNG agrees well with the empirical X-ray luminosity function. It appears, however, that IllustrisTNG does not reproduce the bright end of the empirical X-ray luminosity function at $z = 1$ or $z = 2$. This could be, in part, due to the high efficiency of the kinetic mode AGN feedback which suppresses the black hole accretion and AGN luminosity. In IllustrisTNG, the kinetic mode AGN feedback is activated at low accretion rates relative to the Eddington limit and has a dependence on black hole mass. The dependence of the kinetic feedback mode on black hole mass in IllustrisTNG could mean that galaxies with more massive black holes ($M_{\rm BH} \gtrsim 10^8\ M_\odot$) will always be prevented from producing X-ray luminosities seen at the bright end of the X-ray luminosity function. Galaxies with lower mass black holes ($M_{\rm BH} \leq 10^7\ M_\odot$) cannot produce such luminous AGN either as the bolometric luminosity required to produce X-ray luminosities at the bright end of the observed X-ray luminosity function would exceed

the Eddington limit by an order of magnitude or more (e.g., $L_{\rm Edd} = 1.2 \times 10^{45}$ erg s^{-1} for $M_{\rm BH} = 10^7\ M_\odot$). We note that IllustrisTNG explicitly limits the black hole accretion by the Eddington limit.

In the highest redshift bins, we do not find any high X-ray luminosity AGN in IllustrisTNG residing in galaxies above $M_* > 10^{11}\ M_\odot$. As discussed above, feedback from AGN with black holes more massive than $10^8\ M_\odot$ is more likely to be kinetic mode feedback. Therefore, if one were to reasonably expect that more massive ($M_* > 10^{11}\ M_\odot$) galaxies, with accreting black holes, in IllustrisTNG host more massive black holes ($M_{\rm BH} > 10^8\ M_\odot$), then there is a high probability that the kinetic feedback mode is activated in those galaxies and the feedback, in turn, prevents the accretion rate and the resulting X-ray luminosity from reaching the observed values. At $z < 2$ I find that the mean star formation rate, at a given stellar mass, of galaxies with high X-ray luminosity AGN is higher than the mean star formation rate of galaxies without such AGN in IllustrisTNG (Figures 4.3 and 4.4).

The X-ray luminosity function produced by SIMBA agrees with the empirical X-ray luminosity function to within a factor of $\sim 2-3$ at all redshifts. However, SIMBA does not seem to be able to produce AGN with X-ray luminosities seen at the bright end of the empirical X-ray luminosity function (with $L_X \gtrsim 10^{45}$ erg s^{-1}). A likely reason for this could simply be due to the limited volume of SIMBA ($\sim 3 \times 10^6$ Mpc^3), as AGN with such high X-ray luminosities are extremely rare and have low number densities ($\lesssim 10^{-7}$ Mpc^{-3}). It has been shown in (Thomas et al., 2021) that the radio luminosity function of AGN in SIMBA extends up to the highest observed luminosities, without any evidence for truncation, lending credit to the idea that the lack of AGN with $L_X \gtrsim 10^{45}$ erg s^{-1} in SIMBA is due to limited volume rather than the implementation of black hole growth in the model. Unlike IllustrisTNG, whose AGN kinetic feedback is injected in randomized directions and

is capable of clearing all the gas near the black hole, the AGN kinetic feedback in SIMBA is purely bipolar and decoupled from the gas, meaning it explicitly avoids clearing gas in the vicinity of the black hole.

In SIMBA, the mean star formation rate of galaxies with high X-ray luminosity AGN is lower than the mean star formation rate of galaxies without high X-ray luminosity AGN. For SIMBA, it is clear that the quenching mechanisms are far too efficient in galaxies with high X-ray luminosity AGN as the star formation rates of these objects are far lower than the empirical star formation rates of galaxies with high X-ray luminosity AGN. Not only does SIMBA implement jet and radiative mode feedback, it also implements X-ray heating in AGN with full velocity jets. This form of feedback is invoked in gas-poor (i.e., having $M_{\rm gas}/M_* < 0.2$) galaxies when the AGN jet mode feedback is active, meaning two forms of AGN feedback can rapidly heat and eject the gas in galaxies. X-ray feedback is not applied to more gas-rich galaxies under the assumption that such galaxies would be able to absorb and radiate away the X-ray energy (Davé et al., 2019). Another possible reason that star formation is much lower in galaxies with high X-ray luminosity AGN in SIMBA is because the radiative mode feedback injects momentum, rather than thermal energy (as is done in IllustrisTNG for quasar-mode feedback), into the surrounding gas. Such injections of momentum are more effective at quenching star formation than injections of thermal energy as the resulting winds from the kinetic feedback are capable of ejecting gas from the galaxy. It is important to note that due to the small volume of SIMBA, the results we are seeing could also be in part due to environment. The jet mode feedback in SIMBA is shown to have a widespread effect on the IGM (Christiansen et al., 2020), meaning that jet mode feedback could effectively quench the star formation of many galaxies existing in large groups or clusters. This would make it such that quasars in groups or clusters have quenched star formation, even if the quasar-mode (i.e., radiative) feedback itself is not the

primary driver of star formation quenching. It is therefore possible that a larger volume could weaken the discrepancy between the empirical results and SIMBA. Future work that explores the characterization of environment in both observations and larger volume simulations will shed light on this issue.

5.2 Future Work

5.2.1 Searching for Signatures of Mergers in Massive Galaxies with and without X-ray Luminous AGN

In Chapter 3 of this thesis, it is reported that massive galaxies with high X-ray luminosity AGN have higher star formation rates, on average, than galaxies without such AGN. One of the key implications of this result is that high AGN luminosities and high star formation rates are both fueled by processes that drive large gas inflow rates into the central regions of galaxies. Examples of such processes include gas-rich mergers and strong tidal interactions in gas-rich systems. To gain further insight, it is instructive to look at high resolution numerical simulations that explore the onset of star formation and black hole growth. Numerous studies of such simulations have shown that large gas inflows during major mergers simultaneously trigger star formation and black hole growth in the merging galaxies (Park et al., 2017; Capelo et al., 2015; Cox et al., 2008; Di Matteo et al., 2008; Springel et al., 2005). In these simulations, the peak of black hole accretion and star formation activity appear to coincide and the decline of the black hole accretion rate appears to trace the decline of star formation with time (see Figure 5.1). Given the empirical results of this thesis showing that high X-ray luminosity AGN are frequently found in galaxies with high star formation rates, it is not unreasonable to think that galaxies with high X-ray luminosity AGN are experiencing a merger with another galaxy and are in the phase of the merger where black hole accretion and star formation activity

peak. In order to test the validity of this scenario, one could measure and compare the frequency of major and minor mergers in massive galaxies with and without high X-ray luminosity AGN.

While numerical simulations of mergers show that black hole accretion and star formation peak and decline around the same time, simulations of isolated galaxies show that the black hole accretion rate does not necessarily trace star formation across time in the same way (Negri & Volonteri, 2017). Accurately measuring the merger rates of massive galaxies with and without high X-ray luminosity AGN would either confirm whether the high AGN luminosities and high star formation rates are triggered by physical processes like mergers, or reveal if other mechanisms are at play. I previously attempted to measure the major merger rates from close pairs for massive galaxies with and without high X-ray luminosity AGN with the data set used in Chapters 3 and 4 at $z \sim 1-3$, however, the results were inconclusive, in part due to the poor quality of the photometric redshifts ($\sigma_{\rm NMAD} \sim 0.102$ at $z = 1.9-3.5$, see Chapter 4). For a more conclusive test, one could attempt to measure merger rates following a methodology similar to that of Duncan et al. (2019) who use a probabilistic pair-count procedure that considers the full photometric redshift posteriors as well as stellar mass completeness corrections to the sample. Until further spectroscopic data are available, such an approach would likely provide the best measurements of merger rates at high redshifts for deep large-area surveys that rely heavily on photometric redshifts.

Future spectroscopic data from HETDEX in the SHELA field will allow for far more accurate measurements of merger rates in massive galaxies with and without high X-ray luminosity AGN at $z = 1.9-3.5$. This is extremely beneficial for studies of galaxy mergers as it not only provides actual spectroscopic redshifts, and therefore accurate 3D information, for a large fraction of the galaxy population, but it also allows for the development of more accurate photometric redshifts through

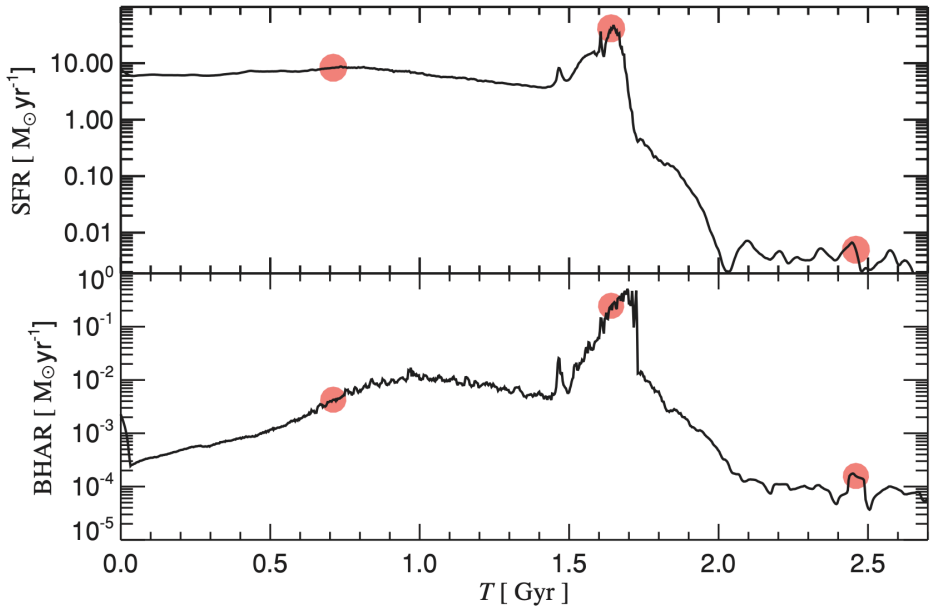

Figure 5.1: From the bottom panels of Figure 14 in Springel et al. (2005), this figure shows the time evolution of the total black hole accretion rate (bottom) and the star formation rate (top) of two galaxies during a merger. The red dots correspond to different phases of the merger. The first red dot corresponds to the phase of the merger just after the first passage of the two discs. The second red dot corresponds to the phase of the merger when the galaxies are coalescing, at which point the star formation and black hole accretion rates peak. Finally, the third red dot corresponds to the phase of the merger just after the galaxies have fully merged. Given the results reported in Chapter 3 showing that high X-ray luminosity AGN are frequently found in galaxies with high star formation rates, it is not unreasonable to think that galaxies with high X-ray luminosity AGN are likely experiencing a merger with another galaxy and are in the phase of the merger represented by the second red dot in this figure, where black hole accretion and star formation activity peak. It would be possible to further test this scenario in observations with deep X-ray data by analyzing if AGN with lower black hole accretion rates, and therefore lower X-ray luminosities, tend to exist in galaxies with low, average, or high star formation rates.

techniques like machine learning. This, in turn, allows one to obtain more accurate measures of merger rates for galaxies at higher redshifts. It should be noted that the major merger rate for the general galaxy population is largely unconstrained at $z \gtrsim 2$ (see Rodriguez-Gomez et al., 2015). Therefore, accurately measuring the merger rates for galaxies with and without high X-ray luminosity AGN at higher redshifts would not only inform how current models of galaxy evolution buildup the mass of all galaxies and black holes at $z \gtrsim 2$, but it would also reveal whether high star formation activity and high AGN luminosity are triggered largely by mergers or by other mechanisms.

In addition to using close pair counts, an alternative way of estimating the merger rates for galaxies with and without high X-ray luminosity AGN is to utilize images of high (sub-kpc) resolution to search for signs of morphological asymmetries indicative of tidal interactions and mergers, such as double nuclei, train-wreck morphologies, ripples, arcs, shells, tails, and other asymmetries. Future high resolution imaging from observatories like the Giant Magellan Telescope (GMT), James Webb Space Telescope (JWST), or the Wide-Field Infrared Survey Telescope (WFIRST), would allow for morphological studies of massive galaxies with and without high X-ray luminosity AGN. Observations at wavelengths of $\sim 1-3$ μm would be particularly useful as this is where the AGN to stellar light ratio appears to be lowest. I determined this by visually inspecting the SEDs of many galaxies with high X-ray luminosity AGN at $z \sim 1.5$ while preparing a JWST proposal (see Figure 5.2). The AGN component can be seen frequently dominating the SED emission at wavelengths outside of $\sim 1-3$ μm, meaning that observations at these observed wavelengths would suffer less light contamination from the AGN component and would reveal more about the stellar structure and component of the galaxy. High resolution imaging at near to mid-infrared wavelengths can therefore significantly aid our search for signatures of mergers in galaxies with high X-ray luminosity AGN

and help reveal the role of mergers in galaxy evolution.

5.2.2 AGN Growth and Feedback

This thesis has made significant advances in understanding the connection between star formation and high X-ray luminosity AGN at $z \sim 1-3$. In Chapter 4, I discuss how implementations of black hole growth and AGN feedback can be improved upon in theoretical models of galaxy evolution based on the empirical results presented in Chapter 3. The analysis of the star formation activity of galaxies with high X-ray luminosity ($L_X > 10^{44}$ erg s^{-1}) AGN at $z \sim 2$ in this thesis has provided important constraints for how theoretical models of galaxy evolution should model feedback from luminous AGN. However, the AGN studied here have high X-ray and bolometric luminosities typical of quasars and are rare objects with low number densities that only represent a small fraction of the total AGN population. In order to fully understand the connection between AGN and star formation, it is necessary to analyze the star formation activity of galaxies with more abundant lower luminosity AGN at $z \sim 2$.

Observations have shown that X-ray emission from star forming processes does not typically exceed X-ray luminosities of $L_X \sim 10^{42}$ erg s^{-1}, and any emission that results in higher X-ray luminosities is thought to be due largely to AGN activity (Lehmer et al., 2012; Brandt & Hasinger, 2005). This means X-ray photometry can be used to select galaxies with luminous and less luminous AGN down to luminosities of $L_X = 10^{42}$ erg s^{-1}. Any X-ray emission resulting in luminosities below this threshold is largely thought to be due to star formation. Deep X-ray observations targeting a large area are required to analyze AGN down to such faint luminosities at $z \sim 1-2$, with flux sensitivities on the order of $\sim 10^{-17}$ erg s^{-1} cm^{-2} to reach $L_X \sim 10^{42}$ erg s^{-1} in the hard-band. Unfortunately, the latest space-based X-ray observatory performing an all-sky survey, *eRosita* (Merloni et al., 2012), will

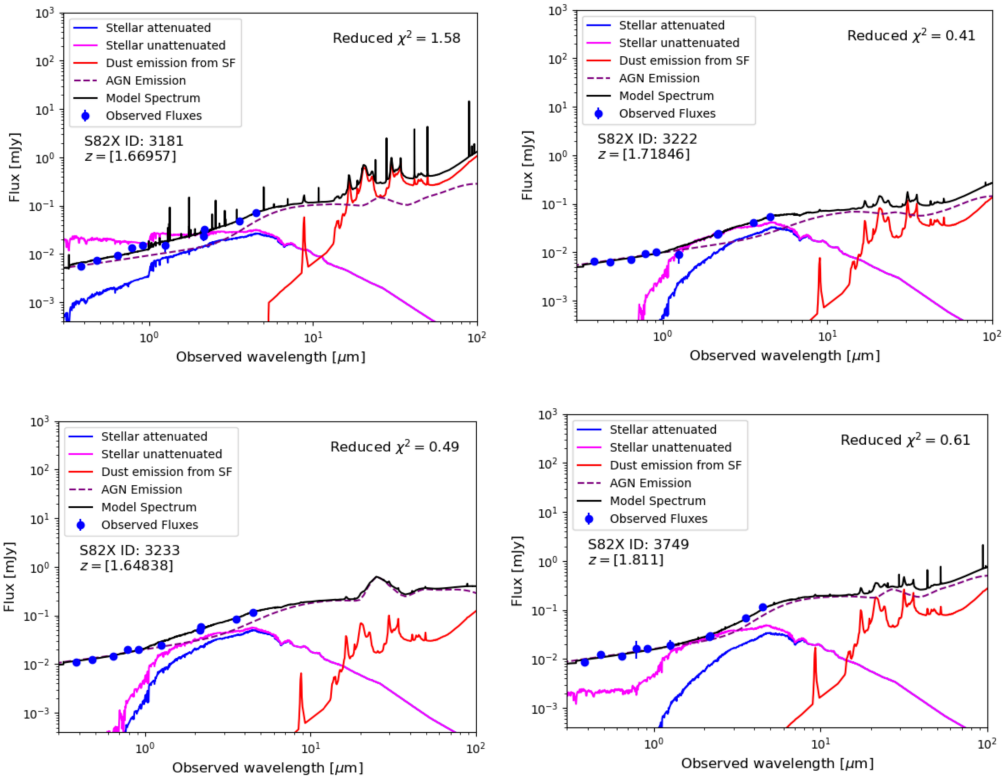

Figure 5.2: Four example SEDs for galaxies with high X-ray luminosity AGN at $z = 1.5 - 2$. These SEDs were generated by CIGALE and visually inspected for a potential JWST proposal. The different components of the SED shown here correspond to the attenuated (blue) and unattenuated (magenta) stellar emission, the dust emission due to star formation (red), the AGN emission (purple, dashed), and the total sum of these different components that produce the model spectrum (black). The blue circles show the photometric fluxes with error bars. The AGN to stellar light ratio appears to be lowest at wavelengths of $\sim 1 - 3$ μm, while AGN emission appears to largely dominate the SED outside of these wavelengths. If one wished to therefore study the stellar components of such galaxies, it would appear particularly useful to focus on obtaining observations of these galaxies at near to mid-infrared wavelengths.

not achieve even the depth of current X-ray surveys (LaMassa et al., 2016, 2013a,b) available in the region studied in Chapters 3 and 4 of this thesis. Targeted observations from observatories such as *Chandra*, however, would allow us to sample AGN with X-ray luminosities down to X-ray luminosities of $L_X \sim 10^{43}$ erg s^{-1} at $z \sim 1-2$, which is $\sim 1-2$ orders of magnitude fainter than what we can sample in Chapters 3 and 4 of this thesis. This would allow us to explore a different and much more representative population of AGN, in addition to the highly luminous and rare AGN we already study in this work. The results of this thesis currently lay the groundwork for future *Chandra* proposals and could play a role in the design of future X-ray observatories. By sampling and analyzing galaxies with luminous and less luminous AGN across a large range of redshifts, X-ray luminosities, and environments, we can begin to understand the full role of AGN in galaxy evolution and to what extent different populations of AGN affect galaxy and black hole growth.

Another one of the central topics we explore in this thesis is how AGN feedback affects galaxy growth. While the results of Chapters 3 and 4 shed some light on this issue (see Section 5.1.3), they are not able to provide any information about specific feedback mechanisms. Work done by Perna et al. (2017) has analyzed the outflow strength of X-ray luminous AGN at $z < 0.8$ and found ionised gas outflows with velocities on the order of $\sim 1,000$ km s^{-1}. More recent work by Leung et al. (2019) using the MOSFIRE Deep Evolution Field (MOSDEF) survey (Kriek et al., 2015) analyze AGN-driven outflows at $z \sim 2$, however, this study samples galaxies over a very small region of the sky and is limited by cosmic variance. Spectroscopic followup on select galaxies with high X-ray luminosity AGN across the SHELA field from observatories like GMT will allow us to zoom in on the central nuclear regions of AGN to study emission-line based outflows stemming from the nucleus. The wide-field spectrographs that will be available on GMT will enable searches for extended line-emitting gas at distances ten times larger than the optical disk of the

host galaxy, thus helping establish physical connections between nuclear activity and gas on large scales.

While observations at rest-frame UV and optical wavelengths can shed light on AGN-driven outflows in luminous quasars, ALMA observations can shed light on the outflows driven by radio-loud jets originating from AGN. Observations with ALMA, for instance, have shown that outflows in galaxies at low redshift can be boosted by the AGN radio jet through entrainment (Audibert et al., 2019). Studying such outflows in radio-loud AGN at higher redshifts can shed light on mass outflow rates and outflow velocities and help us determine to what extent AGN feedback can quench star formation. This is important to analyze at redshifts near cosmic noon, when many star-forming galaxies begin transitioning to a quiescent state. Since simulations of galaxy evolution, such as IllustrisTNG, invoke 'radio-mode' AGN feedback to quench a large fraction of the galaxy population and produce a 'red and dead' population of galaxies at low redshifts (Weinberger et al., 2017), understanding whether AGN outflows are strong enough to heat, destroy, and/or eject large amounts of cold gas and prevent future episodes of star formation is critical for formulating quenching mechanisms in theoretical models of galaxy evolution.

5.2.3 Environmental Studies

The results of Chapter 2 of this thesis provide strong evidence that environment plays a large role in influencing the observed properties of galaxies at low redshifts. Conducting a similar study on galaxies around cosmic noon, the epoch during which protoclusters begin to collapse (Muldrew et al., 2015; Chiang et al., 2014, 2013) and star formation and black hole activity peak (Madau & Dickinson, 2014), would shed light on the role of environment in galaxy and black hole growth and would inform how galaxies in different environments contribute to the cosmic star formation rate density and black hole accretion rate density at $z \sim 1-3$. The SHELA field is cur-

rently being targeted by HETDEX and a significant portion (an expected 23% at the current survey fill factor of 1/4.5 and a larger fraction if targeted pointings are added) of it will have spectroscopic data available in coming years. This is extremely beneficial as it will provide accurate 3D information for a large number of galaxies and will allow for the development of more accurate photometric redshifts through techniques like machine learning. This, in turn, allows us to accurately characterize environment and measure the clustering of different populations of galaxies on varying scales.

The SHELA field is estimated to be large enough to host around a few tens of massive protoclusters at $z = 1.9-3.5$ with a $z = 0$ halo mass of $> 10^{14.5}\ M_{\odot}$ (Chiang et al., 2015). Such protoclusters are estimated to have $\sim 90\%$ of their mass spread across a diameter of ~ 30 arcmin (Muldrew et al., 2015). Analyzing protoclusters at $z \gtrsim 2$ would directly probe the rapid mass assembly and galaxy growth of present-day clusters. The search for protoclusters can be challenging, however, due to lack of highly evolved cluster signatures such as X-ray emission (Fassbender et al., 2011), the Sunyaev-Zel'dovich effect (Bleem et al., 2015), and a prominent galaxy red sequence (Gladders & Yee, 2005). HETDEX will aid the search for protoclusters by providing precise 3D information for Lyman-alpha emitters (LAEs) over a large and homogeneous region of the sky. However, photometric redshifts will still need to be utilized to characterize environment as the fill factor for HETDEX is 1/4.5 and HETDEX only targets LAEs at $z = 1.9 - 3.5$. In order to determine how well the photometric redshifts can accurately recover measures of environment it is necessary to conduct tests on mock catalogs before and after degrading the line-of-sight velocities down to the quality of the observed photometric redshifts. This has been largely difficult to accomplish as many simulations do not have volumes large enough to construct wide-field mock catalogs at $z > 1$. The recent development of the LEGACY simulation (S. Khochfar, private communication) which was run

on a box with a side length of 1600 Mpc/h, will allow for the construction of such mock catalogs due to its enormous volume. Smaller, higher resolution runs on high and low-density regions of the LEGACY box will also provide useful comparisons of environmental trends to observations.

In addition to characterizing environment, accurate redshift data from a combination of spectroscopic redshifts and improved photometric redshifts would allow one to obtain more accurate measurements of galaxy clustering on numerous scales. Measurements of clustering, such as the two-point correlation function or galaxy bias, can inform the characteristic halo masses of different galaxy populations (Zehavi et al., 2011). By measuring the environment and clustering of massive galaxies with and without high X-ray luminosity AGN at the redshifts we probe in this work, we can begin to uncover what sort of environments AGN are preferentially found in, the characteristic halo masses of high mass galaxies with and without high X-ray luminous AGN, and what the interplay between AGN, star formation, and environment is at cosmic noon.

5.2.4 Advancements in SED Fitting

The SED fitting performed in this work was done by running CIGALE on ten photometric filters obtained from the data sets discussed in Chapters 3 and 4. Additional wavelength coverage could help improve the SED fitting and provide more reliable estimates of photometric redshifts, stellar masses, and star formation rates for galaxies with and without high X-ray luminosity AGN. In the case of high X-ray luminosity AGN, further mid-infrared and far-infrared coverage can help disentangle the emission between AGN emission and dust from star-forming processes more accurately and provide improved estimates of star formation. Moreover, observations and photometric coverage at mid-infrared wavelengths could help us further constrain the shape of the SED when a luminous AGN is present, as there is currently

some debate about how AGN emission should be modeled at mid-infrared wavelengths and whether one should assume a smooth or clumpy dust torus geometry (Feltre et al., 2012). Such wavelength coverage can be obtained from instruments such as the GMT or JWST.

The authors of the SED fitting code CIGALE have recently released a new version of the code, X-CIGALE (Yang et al., 2020), that now allows one to include X-ray photometry in the SED fitting of galaxies with X-ray luminous AGN. This new X-ray module includes X-ray emission from the galaxy, the AGN, and hot gas. The purpose of this development is to connect intrinsic X-ray emission to other wavelengths. This, in turn, can provide estimates of dust obscuration at X-ray wavelengths. Utilizing SED fitting codes that can correct X-ray emission for dust obscuration would help us obtain a more complete sample of high X-ray luminosity AGN and would allow for the study of sub-populations of X-ray luminous AGN. Such studies would test the AGN unification model (Urry, 2004) by allowing one to determine if the intrinsic properties of obscured AGN are different from those of unobscured AGN. One could also study whether AGN that are obscured and unobscured tend to occupy different types of environments and learn something about the physical mechanisms that drive different phases of AGN evolution.

Current, state-of-the-art SED fitting algorithms are exploring large regions of parameter space using MCMC methods and non-parametric star formation histories to fit broadband galaxy photometry. At low redshifts, these codes have been shown to accurately recover the redshift and parameters of galaxies. Prospector-α (Leja et al., 2017), is an example of such a code. While Prospector-α provides improved estimates of galaxy properties, it currently cannot run efficiently on large numbers of galaxies. Even while running on a supercomputer, individual galaxies can take several hours to model. It may be possible to followup on certain objects of interest using codes like Prospector-α, but future improvements to the code's speed are

required if it is going to be used to model large samples of galaxies.

5.2.5 Improving Numerical Simulations and Theoretical Models of AGN Growth and Feedback

It was shown in Chapter 4 of this thesis that significant improvements must be made to theoretical models of galaxy evolution in order for them to reproduce observed trends of high X-ray luminosity AGN in massive galaxies. The semi-analytical model SAG, for instance, over-produced the number of high X-ray luminosity AGN by orders of $\sim 10-100$. This could have been likely due to a lack of quasar-mode feedback preventing such high accretion rates in a large fraction of the population. It should be noted that other semi-analytical models, such as Galacticus (Benson, 2012), do not include quasar-mode feedback in their model either. Measuring the XLF for other simulations that do not explicitly model quasar-mode feedback would help elucidate whether the quasar-mode feedback is needed to mitigate the overproduction of high X-ray luminosity AGN in theoretical models of galaxy evolution.

In Chapter 4 it was shown that IllustrisTNG seems to have trouble producing high X-ray luminosity AGN seen at the bright end of the empirical X-ray luminosity function. This was attributed to the dependence of the feedback mode on black hole mass and to the strong AGN kinetic feedback mode which significantly lowers the black hole accretion rate and thus the AGN luminosity. The IllustrisTNG kinetic-mode feedback injects momentum spherically, making it capable of clearing gas out in the vicinity of the black hole rapidly and effectively. Future modeling could try to take into account the strength and orientation of outflows based on observations (e.g., Perna et al., 2017).

It was also shown in Chapter 4 that SIMBA produced galaxies with high X-ray luminosity AGN having low levels of star formation, in contrast with the observations. While SIMBA does try to model AGN feedback based on observations

of outflows and jets (Davé et al., 2019), it is clear that quenching mechanisms might be too efficient in massive galaxies with high X-ray luminosity AGN. As discussed in Chapter 4, however, this could also be attributed to the fact that the AGN feedback is bipolar and decoupled from the gas. This means the AGN feedback explicitly avoids clearing the gas in the vicinity of the black hole. The feedback modes may therefore not be physically capable of stopping massive quiescent galaxies from accreting too much hot gas. One could perform a test like that done in Thomas et al. (2021) which smooths the accretion rate over some period of time to reduce the high accretion rates produced by the stochastic accretion of hot gas. This could potentially mitigate the differences between SIMBA and the empirical results.

It should be noted that hydrodynamical models tend to have small volumes, making it difficult for them to produce large populations of rare massive galaxies and high X-ray luminosity AGN. Additionally, such models are limited by their computational power which in turn limits their resolution. This forces theorists to make certain prescriptions about physical mechanisms driving galaxy evolution on small scales. Semi-analytical models, on the other hand, have large volumes but the models are built on simplified physics. Often times, semi-analytical models are calibrated to small area surveys, which do not provide constraints for rare objects like massive galaxies and high X-ray luminosity AGN.

Moving forward, theoretical models of galaxy evolution can use the results of Chapter 4 of this thesis to guide their implementations of AGN feedback and black hole growth. These results provide benchmarks for theoretical models and can be used to calibrate semi-analytic models due to the large volume the observational data probes. This thesis also details physical mechanisms driving the AGN and star formation connection at cosmic noon that theorists can revisit for future development of theoretical models of galaxy evolution.

Appendices

Appendix A

Appendix to Chapter 3

A.1 Assessing the Impact of WISE Data on the Analysis

Figure 3.1 and Table 3.2.4 show that if we require WISE detection, our sample of galaxies with X-ray luminous AGN would be reduced from 932 sources (in sample S1-Lum-AGN) to 356 sources (in sample S1-Lum-AGN-WISE), while our sample of galaxies without with X-ray luminous AGN be reduced from 318,904 sources (in sample S2-No-Lum-AGN) to 4,695 sources (in sample S2-No-Lum-AGN-WISE). In order to better sample the X-ray luminosity function and prevent a drastic reduction in sample size, we use the samples without WISE data (S1-Lum-AGN and S2-No-Lum-AGN) in our main analysis. However, here in the Appendix, we perform some tests where we compare the SFR and stellar mass derived with and without WISE mid-IR data, and demonstrate that the inclusion of WISE data would not change the results of this work.

In Figure A.1, we show the results of a test similar to that shown in Figure 3.4 for galaxies with X-ray luminous AGN and with a WISE detection. We find that when WISE photometry is included in the SED fitting, our results remain largely

the same for this test. That is, we still find that stellar masses and SFRs can be overestimated, on average, by a factor of up to $\sim$ 5 and $\sim$ 10 for $f_{\rm AGN} > 0.4$, respectively, if AGN emission templates are not included in the SED fit.

The top panels of Figure A.2 show the stellar mass estimate using WISE data in the SED fit versus the stellar mass estimate without using WISE data for galaxies with and without X-ray luminous AGN. The bottom panels of Figure A.2 show the SFR estimate using WISE data in the SED fit versus the SFR estimate without using WISE data for both samples of galaxies with and without X-ray luminous AGN. The stellar mass estimates do not change by much when WISE data is added to the SED fit. The SFR estimates, however, change by quite a bit on a case to case basis and have a large scatter of $\sim$ 0.3 dex. There is no systematic offset, however, in SFRs derived with and without WISE data.

In Figure A.3, we show the mean SFR of galaxies with (S1-Lum-AGN-WISE) and without X-ray luminous AGN (S2-No-Lum-AGN-WISE) and with photometry out to 22 μm. Although we have poor number statistics, we find that the trends are consistent with the trends we see in Figure 3.11 for both samples of galaxies with and without X-ray luminous AGN as the sample of galaxies with X-ray luminous AGN has higher SFRs, on average, at a given stellar mass.

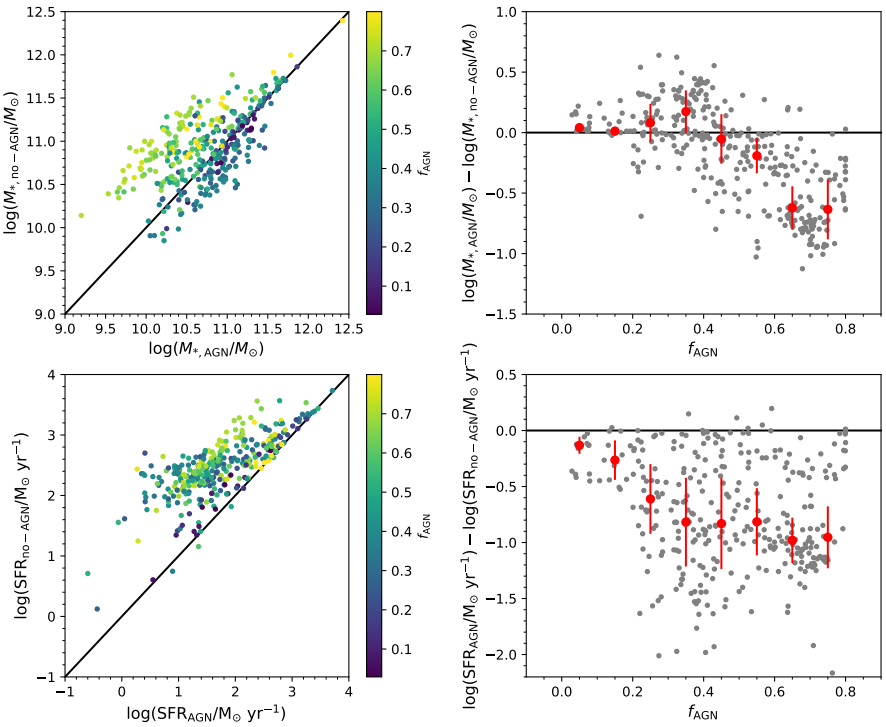

Figure A.1: Similar to Figure 3.4 but for sources in S1-Lum-AGN-WISE, that is, galaxies with X-ray luminous AGN and WISE photometry available. Left: Stellar mass and SFR estimates for our sample of galaxies with X-ray luminous AGN (S1-Lum-AGN-WISE) when AGN emission is included in the SED fit (x-axis) versus when AGN emission is not included (y-axis). Points are colored according to their fractional AGN contamination (f_{AGN}), defined as the fraction of light in the $8-1000$ μm wavelength range that is contributed by the AGN. Right: Difference in log stellar mass and SFR as a function of the fractional AGN contamination. Also shown is the median (red circles) log difference of stellar mass and SFR with and without the AGN emission in the SED fit in four bins of f_{AGN} with the median absolute deviation shown as error bars. We note that the results of this test are qualitatively similar to those shown in Figure 3.4, where WISE photometry is not used in the sample.

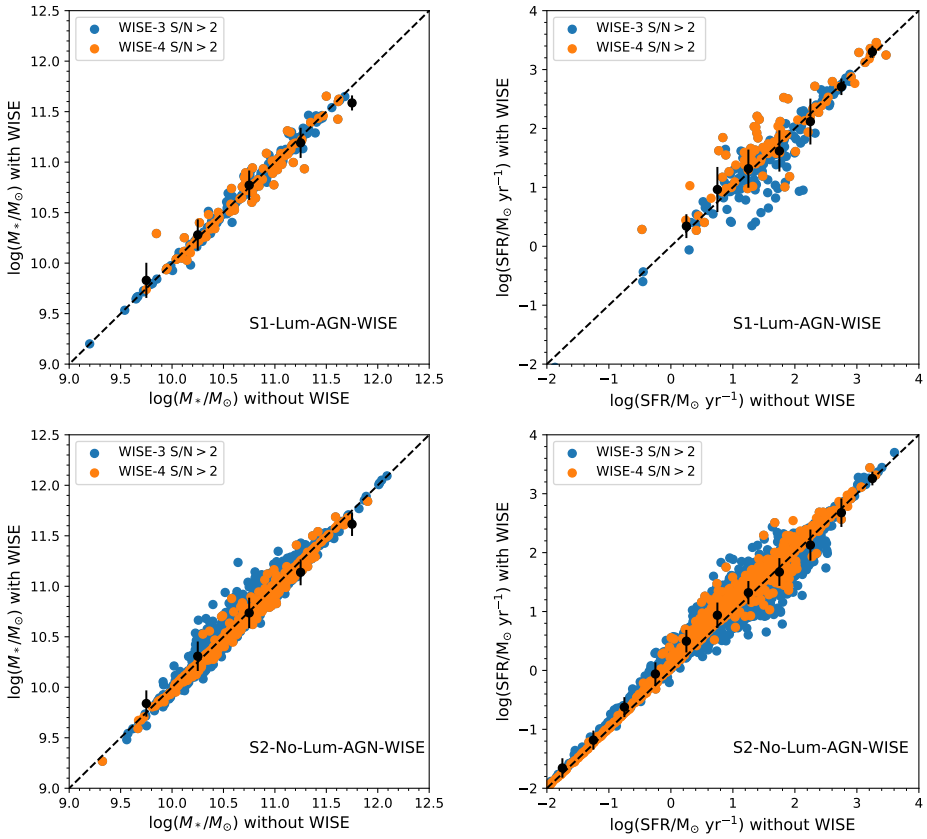

Figure A.2: Left: The stellar mass estimate of galaxies with (S1-Lum-AGN-WISE, top) and without (S2-No-Lum-AGN, bottom) X-ray luminous AGN. Right: The The SFR estimate of galaxies with (S1-Lum-AGN-WISE, top) and without (S2-No-Lum-AGN, bottom) X-ray luminous AGN. The y-axis on all panels shows the stellar mass (or SFR) value obtained when WISE-3 or WISE-4 photometry is included in the SED fit, while the x-axis shows the value that is obtained when WISE photometry is not included in the SED fit. We find that stellar masses do not vary by more than 0.5 dex when WISE data is excluded from the photometry in either sample. SFRs, on the other hand, can vary by a factor of $\sim$ 1 dex when WISE photometry is not included in the SED fit, however, we find no systematic bias.

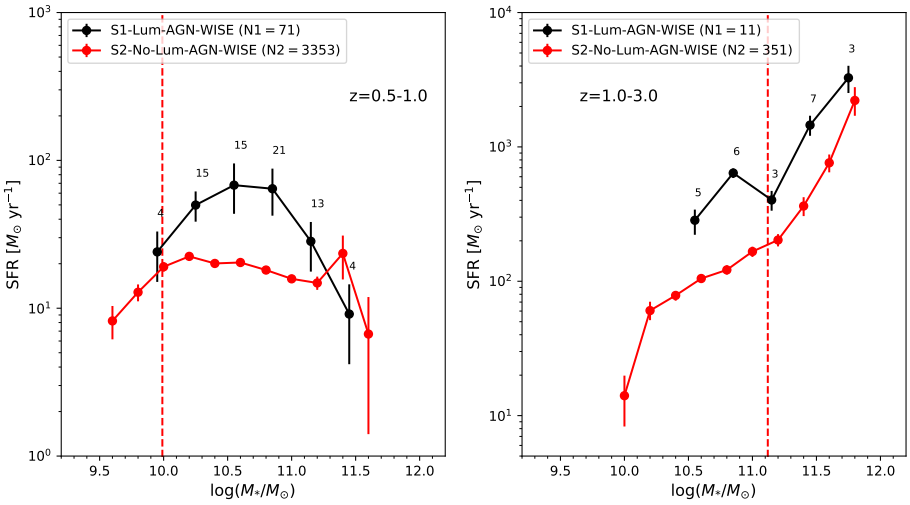

Figure A.3: The mean SFR of galaxies with (S1-Lum-AGN-WISE) and without (S2-No-Lum-AGN-WISE) X-ray luminous AGN as a function of stellar mass in two different bins of redshift. The dashed vertical line shows the mass completeness limit discussed in Section 3.4.1. Our results here for the two samples with WISE photometry do not change qualitatively from those of Figure 3.11.

Appendix B

Appendix to Chapter 4

B.1 Applying the L12 Bolometric Correction to Theoretical Models

In this appendix, we follow up on Section 4.5.4 and discuss whether the results change when we derive X-ray luminosities in the theoretical models using the L12 BC. We plot the same quantities as in Figures 4.3 and 4.4 using the L12 BC and show the new results in Figures B.1 and B.2. The most notable difference in the distributions of high X-ray luminosity AGN we get from the H07 BC to the L12 BC can be seen in SAG where more of these AGN reside in galaxies with quenched SF and in IllustrisTNG where more high X-ray luminosity AGN reside in more massive galaxies with high and low SF. In Figure B.2, we see that galaxies with high X-ray luminosity AGN in SAG have lower SFR than galaxies without such AGN at $M* \gtrsim 10^{11.5}\ M_{\odot}$, contrary to what we see in Figure 4.4. We discuss the changes for each model below when using the L12 BC.

SAG: When we apply the L12 BC to SAG, we find many more galaxies with high X-ray luminosity AGN to have quenched SF, especially in the lowest redshift bin.

This causes a turnover in the mean SFR-stellar mass trend where galaxies with high X-ray luminosity AGN go from having higher mean SFR than galaxies without such AGN to having lower mean SFR than galaxies without such AGN at $M_* \gtrsim 10^{11.5}\ M_\odot$ at $z \sim 1$. This turnover is not seen in Figure 4.4, where we use the BC of H07 to obtain X-ray luminosities. We note, however, that the main discrepancies we found between the empirical results and SAG when using the H07 were: (i) The overproduction of high X-ray luminosity AGN (Figures 4.2 and 4.3) relative the observed distribution of high X-ray luminosity AGN; (ii) The existence of galaxies with high X-ray luminosity AGN in high mass ($M_* > 10^{11.5}\ M_\odot$) galaxies, which is not seen in the observed data. We find that these conclusions remain true even when using the BC of L12 to obtain X-ray luminosities in SAG. The abundance of quenched galaxies with AGN of high X-ray luminosity arises from the fact that the L12 BC assigns higher X-ray luminosities to objects with lower Eddington ratios (Equation 4.2). Therefore, many more objects experiencing quenching through radio mode feedback are going to be assigned X-ray luminosities that are above the observed 95% X-ray luminosity completeness limit when we apply the L12 prescription to obtain X-ray luminosity. Lastly, we note that only $\sim 10\%$ of the high X-ray luminosity AGN actually reside in galaxies with quenched SF when applying the BC of L12 to galaxies in SAG.

IllustrisTNG: It is notable that when using the L12 BC to obtain X-ray luminosities for AGN in IllustrisTNG, there are high X-ray luminosity AGN present in galaxies with $M_* > 10^{11}$, given that many of these objects are missing in row 3 of Figures 4.3 and 4.4. We find that at higher stellar masses, the mean SFR of galaxies with high X-ray luminosity AGN matches the sample of galaxies without high X-ray luminosity AGN in IllustrisTNG (Figure B.2). At higher stellar masses, galaxies with high X-ray luminosity AGN have BHs accreting at lower rates relative to the

Eddington limit, meaning the efficient AGN kinetic feedback mode is activated in these systems. As mentioned in Section 4.5.4, the BC of L12 assigns higher X-ray luminosities to objects with lower Eddington ratios. This is why the BC of L12 picks up more galaxies with high X-ray luminosity AGN above the 95% X-ray luminosity completeness limit at $M_* > 10^{11}\ M_\odot$ in all three simulations than the H07 BC. What the L12 BC is doing is essentially producing higher X-ray luminosities for objects with low Eddington ratios ($f_{\rm Edd} \lesssim 0.1$). Such AGN tend to exist in higher mass galaxies and are accreting in the kinetic mode in the case of IllustrisTNG. Such galaxies will have SF that is quenched by the kinetic mode feedback of IllustrisTNG.

SIMBA: We find very little change, qualitatively, between the results given by the L12 BC and H07 BC for SIMBA. The results given by the L12 BC remain consistent to what we found previously for the H07 BC, with the only real notable difference being seen at the lowest and highest redshift bins where more high X-ray luminosity AGN are produced by the L12 BC.

B.2 Calculating Bolometric Luminosity with a Dependence on Eddington Ratio

In this appendix, we follow up on Section 4.5.4 and discuss the effect of making a distinction between radiatively efficient and inefficient AGN when computing bolometric luminosity. We consider using a different expression that depends on the Eddington ratio to calculate bolometric luminosity for the SAG model, as it explicitly separates the radio mode accretion of hot gas from quasar mode accretion.

For sources accreting in the radio mode in SAG, we compute their bolometric luminosities using Eq. (7) of Fanidakis et al. (2012) and recalculate their X-ray luminosities using the BCs of H07 and L12. We note that all sources accreting in

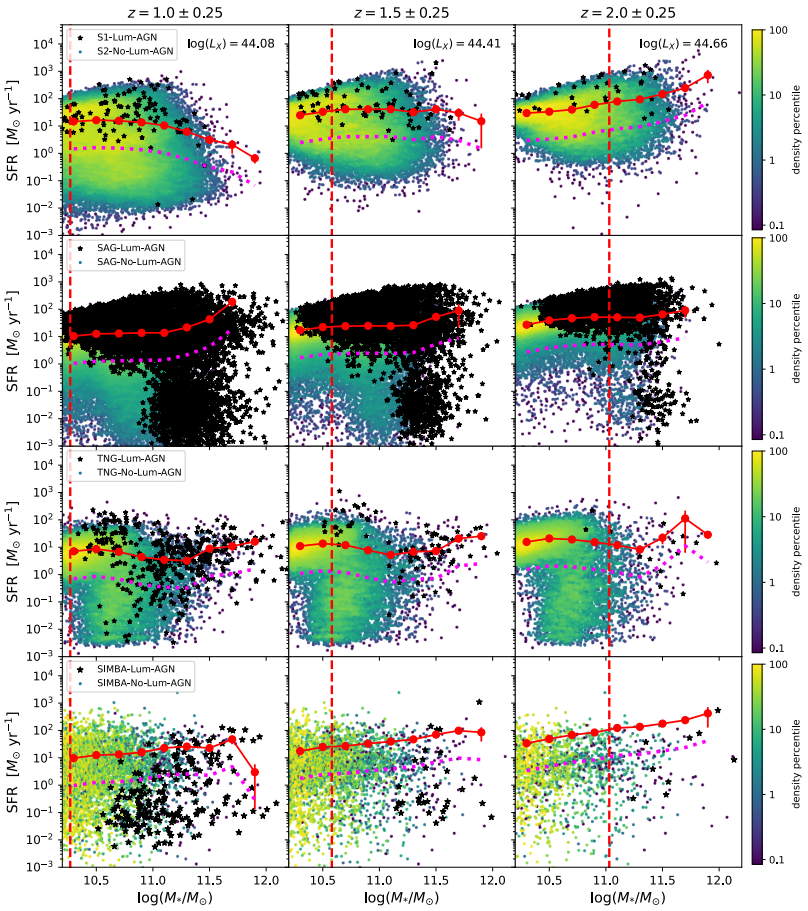

Figure B.1: The stellar mass-SFR relation for galaxies with (black, stars) and without (colored) high X-ray luminosity AGN for our observed sample (first row), for SAG (second row), for IllustrisTNG (third row), and for SIMBA (fourth row) in three different redshift bins. The galaxies without high X-ray luminosity AGN are color-coded by their density on the mass-SFR plane. The dashed vertical line shows the observed stellar mass completeness limit at each redshift range. Also shown in each panel is the mean SFR, at fixed stellar mass, for the sample of galaxies without high X-ray luminosity AGN (red circles), which we refer to as the main sequence, and the line that falls 1 dex below the main sequence (dotted magenta). We used the L12 bolometric correction to obtain X-ray luminosities in the models for this figure. Both SAG and IllustrisTNG appear to predict that the majority of galaxies with high X-ray luminosity AGN have enhanced SFRs, relative to the main sequence, at $M_* \lesssim 10^{11.5}\ M_\odot$. The majority of galaxies with high X-ray luminosity AGN in SIMBA, however, appear to have quenched SF. These results are consistent with what we found in Figure 4.3

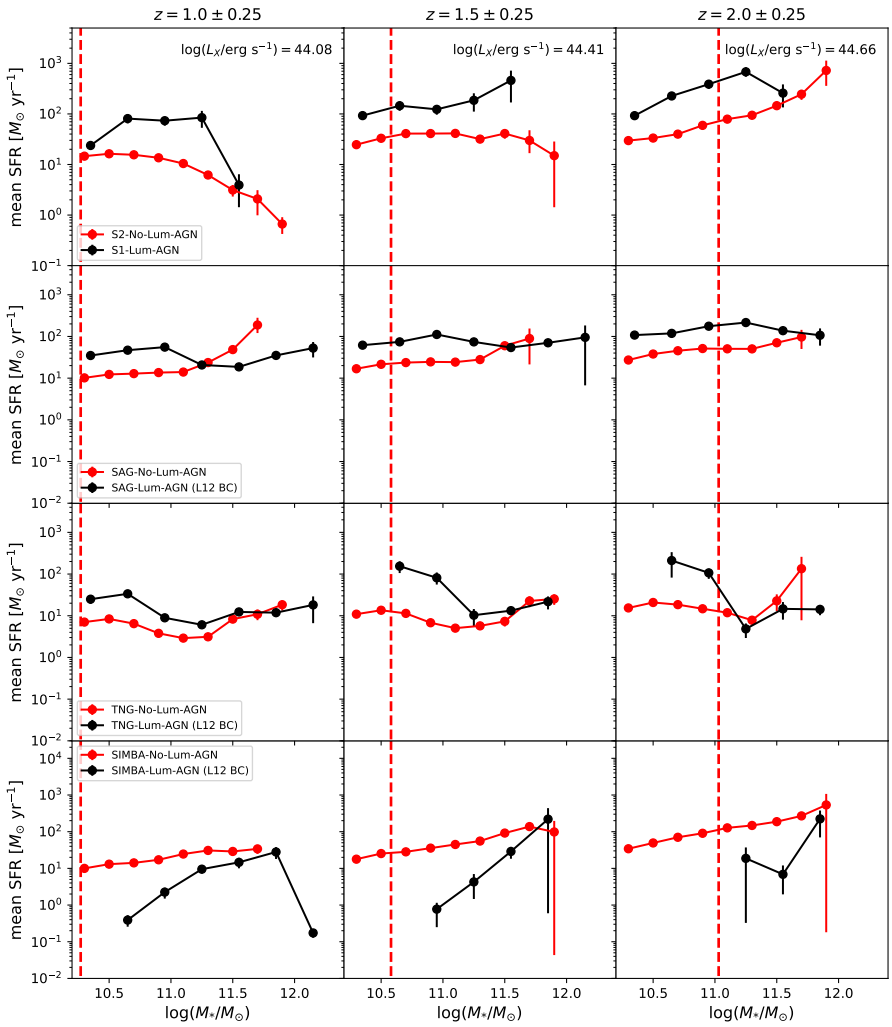

Figure B.2: The mean SFR as a function of stellar mass for the sample of galaxies with (black circles) and without (red circles) high X-ray luminosity AGN. As in Figure B.1, the BC of L12 was used to obtain hard X-ray luminosities in the models shown here. SAG and IllustrisTNG appear to show enhanced SFR in galaxies with high X-ray luminosity AGN compared to galaxies without such luminous AGN, except at the highest stellar mass in IllustrisTNG and SAG ($M_* \gtrsim 10^{11.5}\ M_\odot$). SIMBA appears to show that the mean SFR of galaxies with high X-ray luminosity AGN fall below the main sequence, consistent with what we found in Figure 4.4.

radio mode in SAG have very low Eddington ratios ($f_{\rm Edd} < 0.01$). We show the predicted XLF by SAG in Figure B.3 when assuming a constant radiative efficiency for all sources (orange circles with error bars, same as in Figure 4.2), and when using Eq. (7) of Fanidakis et al. (2012) to calculate bolometric luminosity for AGN accreting in radio mode (orange, dashed line). Again, we show the XLFs when applying the L12 BC to the model (top panels), as well as the H07 BC (bottom panels). The only difference between the predicted XLFs produced by SAG can be seen in the top panels, where the BC of L12 is applied to get X-ray luminosity. The faint end slope of the SAG XLF predicted by the variable radiative efficiency slightly flattens out relative to the SAG XLF predicted by assuming a constant radiative efficiency, however, both XLFs predicted by SAG in the top and bottom panels are largely the same in shape and normalization above the observed X-ray luminosity completeness limit. We find that SAG still overproduces high X-ray luminosity AGN and the XLF remains largely unchanged when assuming a variable radiative efficiency to calculate bolometric luminosity.

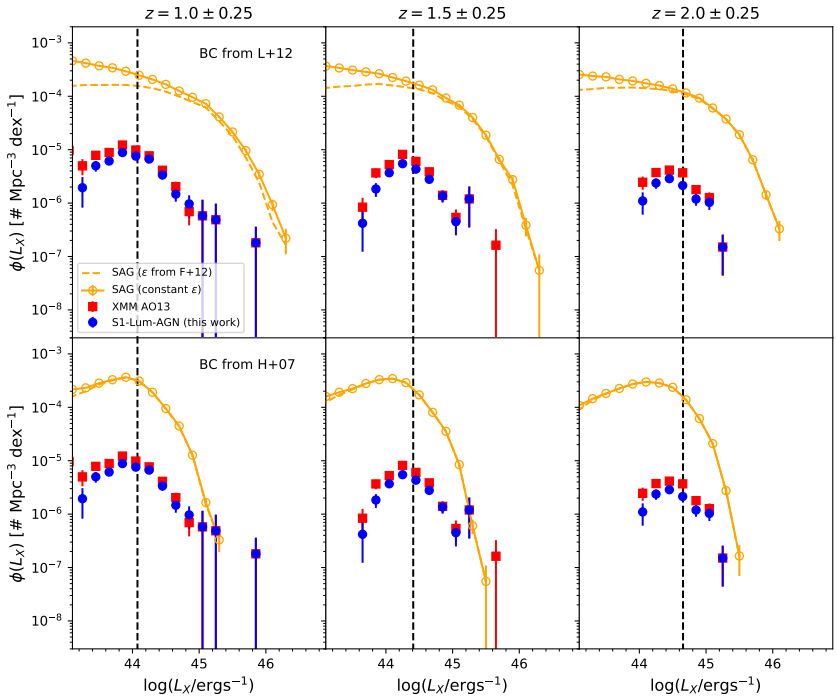

Figure B.3: Similar to Figure 4.2 which shows the XLF of our observed sample (blue), XMM AO13 (red), and the theoretical models using the L12 BC (top row) and H07 (bottom row) BC. We remind the reader that the dashed vertical line represents the X-ray luminosity completeness limit. Here, we only focus on the SAG model (orange) and show the predicted XLF that arises when we apply two different methods to obtain bolometric luminosity. The SAG XLF with the error bars and circles is the same that is shown in Figure 4.2, where the radiative efficiency ϵ is treated as a constant. The SAG XLF shown by the dashed line is computed by treating the radiative efficiency of the radio accretion mode as a variable that depends on the Eddington ratio (from Fanidakis et al., 2012). The only difference between the two predicted XLFs produced by SAG is seen at the faint end of the XLF in the top panels, where the BC of L12 is applied to get X-ray luminosity. The faint end slope of the SAG XLF predicted by the variable radiative efficiency slightly flattens out relative to the SAG XLF predicted by assuming a constant radiative efficiency. We find that SAG still overproduces high X-ray luminosity AGN and the XLF remains largely unchanged when assuming a variable radiative efficiency to calculate bolometric luminosity.

Bibliography

Abbott, R., Abbott, T. D., Abraham, S., et al. 2021, ApJL, 915, L5. doi:10.3847/2041-8213/ac082e

Acquaviva, V., Gawiser, E., & Guaita, L. 2011, ApJ, 737, 47. doi:10.1088/0004-637X/737/2/47

Aird, J., Nandra, K., Laird, E. S., et al. 2010, MNRAS, 401, 2531. doi:10.1111/j.1365-2966.2009.15829.x

Ajello, M., Alexander, D. M., Greiner, J., et al. 2012, ApJ, 749, 21. doi:10.1088/0004-637X/749/1/21

Alpaslan, M., Robotham, A. S. G., Obreschkow, D., et al. 2014, MNRAS, 440, L106. doi:10.1093/mnrasl/slu019

Ananna, T. T., Treister, E., Urry, C. M., et al. 2019, ApJ, 871, 240. doi:10.3847/1538-4357/aafb77

Ananna, T. T., Salvato, M., LaMassa, S., et al. 2017, ApJ, 850, 66. doi:10.3847/1538-4357/aa937d

Anglés-Alcázar, D., Özel, F., & Davé, R. 2013, ApJ, 770, 5. doi:10.1088/0004-637X/770/1/5

Anglés-Alcázar, D., Özel, F., Davé, R., et al. 2015, ApJ, 800, 127. doi:10.1088/0004-637X/800/2/127

Audibert, A., Combes, F., García-Burillo, S., et al. 2019, A&A, 632, A33. doi:10.1051/0004-6361/201935845

Avila-Reese, V., Colín, P., Gottlöber, S., et al. 2005, ApJ, 634, 51. doi:10.1086/491726

Babić, A., Miller, L., Jarvis, M. J., et al. 2007, A&A, 474, 755. doi:10.1051/0004-6361:20078286

Baldry, I. K., Driver, S. P., Loveday, J., et al. 2012, MNRAS, 421, 621. doi:10.1111/j.1365-2966.2012.20340.x

Baldry, I. K., Glazebrook, K., Brinkmann, J., et al. 2004, ApJ, 600, 681. doi:10.1086/380092

Balogh, M. L., Baldry, I. K., Nichol, R., et al. 2004, ApJL, 615, L101. doi:10.1086/426079

Bamford, S. P., Nichol, R. C., Baldry, I. K., et al. 2009, MNRAS, 393, 1324. doi:10.1111/j.1365-2966.2008.14252.x

Bauer, A. E., Drory, N., Hill, G. J., et al. 2005, ApJL, 621, L89. doi:10.1086/429289

Behroozi, P. S., Conroy, C., & Wechsler, R. H. 2010, ApJ, 717, 379. doi:10.1088/0004-637X/717/1/379

Bekki, K. 2008, MNRAS, 388, L10. doi:10.1111/j.1745-3933.2008.00489.x

Benson, A. J. 2012, New Astron., 17, 175. doi:10.1016/j.newast.2011.07.004

Berlind, A. A., Frieman, J., Weinberg, D. H., et al. 2006, ApJS, 167, 1. doi:10.1086/508170

Bernardi, M., Sheth, R. K., Annis, J., et al. 2003, AJ, 125, 1866. doi:10.1086/367794

Berta, S., Lutz, D., Santini, P., et al. 2013, A&A, 551, A100. doi:10.1051/0004-6361/201220859

Bertin, E. & Arnouts, S. 1996, A &AS, 117, 393. doi:10.1051/aas:1996164

Bett, P., Eke, V., Frenk, C. S., et al. 2007, MNRAS, 376, 215. doi:10.1111/j.1365-2966.2007.11432.x

Beygu, B., Kreckel, K., van de Weygaert, R., et al. 2013, AJ, 145, 120. doi:10.1088/0004-6256/145/5/120

Bieri, R., Dubois, Y., Rosdahl, J., et al. 2017, MNRAS, 464, 1854. doi:10.1093/mnras/stw2380

Bleem, L. E., Stalder, B., de Haan, T., et al. 2015, ApJS, 216, 27. doi:10.1088/0067-0049/216/2/27

Blumenthal, G. R., Faber, S. M., Primack, J. R., et al. 1984, Nature, 311, 517. doi:10.1038/311517a0

Bondi, H. & Hoyle, F. 1944, MNRAS, 104, 273. doi:10.1093/mnras/104.5.273

Bongiorno, A., Schulze, A., Merloni, A., et al. 2016, A&A, 588, A78. doi:10.1051/0004-6361/201527436

Boquien, M., Burgarella, D., Roehlly, Y., et al. 2019, A&A, 622, A103. doi:10.1051/0004-6361/201834156

Boselli, A., Boissier, S., Cortese, L., et al. 2006, ApJ, 651, 811. doi:10.1086/507766

Brammer, G. B., van Dokkum, P. G., & Coppi, P. 2008, ApJ, 686, 1503. doi:10.1086/591786

Brandt, W. N. & Alexander, D. M. 2015, A&ARv, 23, 1. doi:10.1007/s00159-014-0081-z

Brandt, W. N. & Hasinger, G. 2005, ARA&A, 43, 827. doi:10.1146/annurev.astro.43.051804.102213

Brennan, R., Pandya, V., Somerville, R. S., et al. 2015, MNRAS, 451, 2933. doi:10.1093/mnras/stv1007

Brinchmann, J., Charlot, S., White, S. D. M., et al. 2004, MNRAS, 351, 1151. doi:10.1111/j.1365-2966.2004.07881.x

Brusa, M., Civano, F., Comastri, A., et al. 2010, ApJ, 716, 348. doi:10.1088/0004-637X/716/1/348

Bruzual, G. & Charlot, S. 2003, MNRAS, 344, 1000. doi:10.1046/j.1365-8711.2003.06897.x

Buat, V., Heinis, S., Boquien, M., et al. 2014, A&A, 561, A39. doi:10.1051/0004-6361/201322081

Buchner, J., Georgakakis, A., Nandra, K., et al. 2015, ApJ, 802, 89. doi:10.1088/0004-637X/802/2/89

Burlon, D., Ajello, M., Greiner, J., et al. 2011, ApJ, 728, 58. doi:10.1088/0004-637X/728/1/58

Calistro Rivera, G., Lusso, E., Hennawi, J. F., et al. 2016, ApJ, 833, 98. doi:10.3847/1538-4357/833/1/98

Calzetti, D., Armus, L., Bohlin, R. C., et al. 2000, ApJ, 533, 682. doi:10.1086/308692

Campbell, D., van den Bosch, F. C., Padmanabhan, N., et al. 2018, MNRAS, 477, 359. doi:10.1093/mnras/sty495

Capelo, P. R., Volonteri, M., Dotti, M., et al. 2015, MNRAS, 447, 2123. doi:10.1093/mnras/stu2500

Capelo, P. R. & Dotti, M. 2017, MNRAS, 465, 2643. doi:10.1093/mnras/stw2872

Cattaneo, A., Faber, S. M., Binney, J., et al. 2009, Nature, 460, 213. doi:10.1038/nature08135

Chabrier, G. 2003, PASP, 115, 763. doi:10.1086/376392

Chiang, Y.-K., Overzier, R., & Gebhardt, K. 2014, ApJL, 782, L3. doi:10.1088/2041-8205/782/1/L3

Chiang, Y.-K., Overzier, R., & Gebhardt, K. 2013, ApJ, 779, 127. doi:10.1088/0004-637X/779/2/127

Chiang, Y.-K., Overzier, R. A., Gebhardt, K., et al. 2015, ApJ, 808, 37. doi:10.1088/0004-637X/808/1/37

Choi, E., Ostriker, J. P., Naab, T., et al. 2012, ApJ, 754, 125. doi:10.1088/0004-637X/754/2/125

Choi, E., Ostriker, J. P., Naab, T., et al. 2015, MNRAS, 449, 4105. doi:10.1093/mnras/stv575

Christiansen, J. F., Davé, R., Sorini, D., et al. 2020, MNRAS, 499, 2617. doi:10.1093/mnras/staa3007

Churazov, E., Sazonov, S., Sunyaev, R., et al. 2005, MNRAS, 363, L91. doi:10.1111/j.1745-3933.2005.00093.x

Ciesla, L., Boselli, A., Elbaz, D., et al. 2016, A&A, 585, A43. doi:10.1051/0004-6361/201527107

Ciesla, L., Elbaz, D., Schreiber, C., et al. 2018, A&A, 615, A61. doi:10.1051/0004-6361/201832715

Ciesla, L., Elbaz, D., & Fensch, J. 2017, A&A, 608, A41. doi:10.1051/0004-6361/201731036

Ciesla, L., Charmandaris, V., Georgakakis, A., et al. 2015, A&A, 576, A10. doi:10.1051/0004-6361/201425252

Cole, S., Lacey, C. G., Baugh, C. M., et al. 2000, MNRAS, 319, 168. doi:10.1046/j.1365-8711.2000.03879.x

Colless, M., Dalton, G., Maddox, S., et al. 2001, MNRAS, 328, 1039. doi:10.1046/j.1365-8711.2001.04902.x

Conroy, C. & Wechsler, R. H. 2009, ApJ, 696, 620. doi:10.1088/0004-637X/696/1/620

Conroy, C., Gunn, J. E., & White, M. 2009, ApJ, 699, 486. doi:10.1088/0004-637X/699/1/486

Conroy, C., van Dokkum, P. G., & Kravtsov, A. 2015, ApJ, 803, 77. doi:10.1088/0004-637X/803/2/77

Conroy, C., Wechsler, R. H., & Kravtsov, A. V. 2006, ApJ, 647, 201. doi:10.1086/503602

Conselice, C. J., Bluck, A. F. L., Buitrago, F., et al. 2011, MNRAS, 413, 80. doi:10.1111/j.1365-2966.2010.18113.x

Conselice, C. J. 2006, MNRAS, 373, 1389. doi:10.1111/j.1365-2966.2006.11114.x

Cora, S. A., Hough, T., Vega-Martínez, C. A., et al. 2019, MNRAS, 483, 1686. doi:10.1093/mnras/sty3214

Cora, S. A., Vega-Martínez, C. A., Hough, T., et al. 2018, MNRAS, 479, 2. doi:10.1093/mnras/sty1131

Cox, T. J., Jonsson, P., Somerville, R. S., et al. 2008, MNRAS, 384, 386. doi:10.1111/j.1365-2966.2007.12730.x

Croton, D. J., Springel, V., White, S. D. M., et al. 2006, MNRAS, 365, 11. doi:10.1111/j.1365-2966.2005.09675.x

Croton, D. J., Stevens, A. R. H., Tonini, C., et al. 2016, ApJS, 222, 22. doi:10.3847/0067-0049/222/2/22

Croton, D. J., Gao, L., & White, S. D. M. 2007, MNRAS, 374, 1303. doi:10.1111/j.1365-2966.2006.11230.x

Cutri, R. M., Wright, E. L., Conrow, T., et al. 2013, Explanatory Supplement to the AllWISE Data Release Products, by R. M. Cutri et al.

da Cunha, E., Charlot, S., & Elbaz, D. 2008, MNRAS, 388, 1595. doi:10.1111/j.1365-2966.2008.13535.x

Daddi, E., Dickinson, M., Morrison, G., et al. 2007, ApJ, 670, 156. doi:10.1086/521818

Dale, D. A., Helou, G., Magdis, G. E., et al. 2014, ApJ, 784, 83. doi:10.1088/0004-637X/784/1/83

Darvish, B., Mobasher, B., Sobral, D., et al. 2015, ApJ, 805, 121. doi:10.1088/0004-637X/805/2/121

Davidzon, I., Bolzonella, M., Coupon, J., et al. 2013, A&A, 558, A23. doi:10.1051/0004-6361/201321511

Davies, R. L., Förster Schreiber, N. M., Lutz, D., et al. 2020, ApJ, 894, 28. doi:10.3847/1538-4357/ab86ad

Davis, M., Guhathakurta, P., Konidaris, N. P., et al. 2007, ApJL, 660, L1. doi:10.1086/517931

Davé, R., Anglés-Alcázar, D., Narayanan, D., et al. 2019, MNRAS, 486, 2827. doi:10.1093/mnras/stz937

Davé, R., Thompson, R., & Hopkins, P. F. 2016, MNRAS, 462, 3265. doi:10.1093/mnras/stw1862

Delvecchio, I., Gruppioni, C., Pozzi, F., et al. 2014, MNRAS, 439, 2736. doi:10.1093/mnras/stu130

Di Matteo, T., Colberg, J., Springel, V., et al. 2008, ApJ, 676, 33. doi:10.1086/524921

Di Matteo, T., Springel, V., & Hernquist, L. 2005, Nature, 433, 604. doi:10.1038/nature03335

Dickinson, M., Papovich, C., Ferguson, H. C., et al. 2003, ApJ, 587, 25. doi:10.1086/368111

Donnari, M., Pillepich, A., Nelson, D., et al. 2019, MNRAS, 485, 4817. doi:10.1093/mnras/stz712

Draine, B. T. & Li, A. 2007, ApJ, 657, 810. doi:10.1086/511055

Dressler, A. 1980, ApJ, 236, 351. doi:10.1086/157753

Driver, S. P., Hill, D. T., Kelvin, L. S., et al. 2011, MNRAS, 413, 971. doi:10.1111/j.1365-2966.2010.18188.x

Duarte, M. & Mamon, G. A. 2014, MNRAS, 440, 1763. doi:10.1093/mnras/stu378

Duivenvoorden, S., Oliver, S., Buat, V., et al. 2016, MNRAS, 462, 277. doi:10.1093/mnras/stw1466

Duncan, K., Conselice, C. J., Mundy, C., et al. 2019, ApJ, 876, 110. doi:10.3847/1538-4357/ab148a

Duras, F., Bongiorno, A., Ricci, F., et al. 2020, A&A, 636, A73. doi:10.1051/0004-6361/201936817

Eckart, A. & Genzel, R. 1997, MNRAS, 284, 576. doi:10.1093/mnras/284.3.576

Eckert, K. D., Kannappan, S. J., Stark, D. V., et al. 2016, ApJ, 824, 124. doi:10.3847/0004-637X/824/2/124

Eckert, K. D., Kannappan, S. J., Stark, D. V., et al. 2015, ApJ, 810, 166. doi:10.1088/0004-637X/810/2/166

Elbaz, D., Daddi, E., Le Borgne, D., et al. 2007, A&A, 468, 33. doi:10.1051/0004-6361:20077525

Elbaz, D., Dickinson, M., Hwang, H. S., et al. 2011, A&A, 533, A119. doi:10.1051/0004-6361/201117239

Elmegreen, B. G. 1994, ApJL, 425, L73. doi:10.1086/187313

Etherington, J., Thomas, D., Maraston, C., et al. 2017, MNRAS, 466, 228. doi:10.1093/mnras/stw3069

Event Horizon Telescope Collaboration, Akiyama, K., Alberdi, A., et al. 2019, ApJL, 875, L1. doi:10.3847/2041-8213/ab0ec7

Fabian, A. C. 2012, ARA&A, 50, 455. doi:10.1146/annurev-astro-081811-125521

Fakhouri, O. & Ma, C.-P. 2009, MNRAS, 394, 1825. doi:10.1111/j.1365-2966.2009.14480.x

Fakhouri, O. & Ma, C.-P. 2010, MNRAS, 401, 2245. doi:10.1111/j.1365-2966.2009.15844.x

Falco, E. E., Kurtz, M. J., Geller, M. J., et al. 1999, PASP, 111, 438. doi:10.1086/316343

Fang, J. J., Faber, S. M., Koo, D. C., et al. 2018, ApJ, 858, 100. doi:10.3847/1538-4357/aabcba

Fanidakis, N., Baugh, C. M., Benson, A. J., et al. 2012, MNRAS, 419, 2797. doi:10.1111/j.1365-2966.2011.19931.x

Fassbender, R., Böhringer, H., Nastasi, A., et al. 2011, New Journal of Physics, 13, 125014. doi:10.1088/1367-2630/13/12/125014

Feltre, A., Hatziminaoglou, E., Fritz, J., et al. 2012, MNRAS, 426, 120. doi:10.1111/j.1365-2966.2012.21695.x

Ferrarese, L. & Merritt, D. 2000, ApJL, 539, L9. doi:10.1086/312838

Fiore, F., Feruglio, C., Shankar, F., et al. 2017, A&A, 601, A143. doi:10.1051/0004-6361/201629478

Fliri, J. & Trujillo, I. 2016, MNRAS, 456, 1359. doi:10.1093/mnras/stv2686

Florez, J., Jogee, S., Sherman, S., et al. 2020, MNRAS, 497, 3273. doi:10.1093/mnras/staa2200

Fontanot, F., De Lucia, G., Monaco, P., et al. 2009, MNRAS, 397, 1776. doi:10.1111/j.1365-2966.2009.15058.x

Fritz, J., Franceschini, A., & Hatziminaoglou, E. 2006, MNRAS, 366, 767. doi:10.1111/j.1365-2966.2006.09866.x

Fumagalli, M., Gavazzi, G., Scaramella, R., et al. 2011, A&A, 528, A46. doi:10.1051/0004-6361/201015463

Gao, L., Springel, V., & White, S. D. M. 2005, MNRAS, 363, L66. doi:10.1111/j.1745-3933.2005.00084.x

Gao, L. & White, S. D. M. 2007, MNRAS, 377, L5. doi:10.1111/j.1745-3933.2007.00292.x

Geach, J. E., Lin, Y.-T., Makler, M., et al. 2017, ApJS, 231, 7. doi:10.3847/1538-4365/aa74b6

Gebhardt, K., Bender, R., Bower, G., et al. 2000, ApJL, 539, L13. doi:10.1086/312840

Genel, S., Vogelsberger, M., Springel, V., et al. 2014, MNRAS, 445, 175. doi:10.1093/mnras/stu1654

Ghez, A. M., Klein, B. L., Morris, M., et al. 1998, ApJ, 509, 678. doi:10.1086/306528

Ghez, A. M., Duchêne, G., Matthews, K., et al. 2003, ApJL, 586, L127. doi:10.1086/374804

Giustini, M. & Proga, D. 2019, A&A, 630, A94. doi:10.1051/0004-6361/201833810

Gladders, M. D. & Yee, H. K. C. 2005, ApJS, 157, 1. doi:10.1086/427327

Glazebrook, K., Schreiber, C., Labbé, I., et al. 2017, Nature, 544, 71. doi:10.1038/nature21680

Grogin, N. A. & Geller, M. J. 2000, AJ, 119, 32. doi:10.1086/301179

Grogin, N. A. & Geller, M. J. 1999, AJ, 118, 2561. doi:10.1086/301126

Grogin, N. A., Kocevski, D. D., Faber, S. M., et al. 2011, ApJS, 197, 35. doi:10.1088/0067-0049/197/2/35

Guzzo, L., Scodeggio, M., Garilli, B., et al. 2014, A&A, 566, A108. doi:10.1051/0004-6361/201321489

Haardt, F. & Maraschi, L. 1991, ApJL, 380, L51. doi:10.1086/186171

Habouzit, M., Genel, S., Somerville, R. S., et al. 2019, MNRAS, 484, 4413. doi:10.1093/mnras/stz102

Habouzit, M., Li, Y., Somerville, R. S., et al. 2021, MNRAS, 503, 1940. doi:10.1093/mnras/stab496

Hambrick, D. C., Ostriker, J. P., Naab, T., et al. 2011, ApJ, 738, 16. doi:10.1088/0004-637X/738/1/16

Hao, C.-N., Kennicutt, R. C., Johnson, B. D., et al. 2011, ApJ, 741, 124. doi:10.1088/0004-637X/741/2/124

Haynes, M. P., Giovanelli, R., Martin, A. M., et al. 2011, AJ, 142, 170. doi:10.1088/0004-6256/142/5/170

Hearin, A. P., Watson, D. F., Becker, M. R., et al. 2014, MNRAS, 444, 729. doi:10.1093/mnras/stu1443

Hearin, A. P. & Watson, D. F. 2013, MNRAS, 435, 1313. doi:10.1093/mnras/stt1374

Hearin, A. P., Campbell, D., Tollerud, E., et al. 2017, AJ, 154, 190. doi:10.3847/1538-3881/aa859f

Heckman, T. M. & Best, P. N. 2014, ARA&A, 52, 589. doi:10.1146/annurev-astro-081913-035722

Henriques, B. M. B., White, S. D. M., Thomas, P. A., et al. 2013, MNRAS, 431, 3373. doi:10.1093/mnras/stt415

Henriques, B. M. B., White, S. D. M., Thomas, P. A., et al. 2015, MNRAS, 451, 2663. doi:10.1093/mnras/stv705

Hill, G. J., Gebhardt, K., Komatsu, E., et al. 2008, Panoramic Views of Galaxy Formation and Evolution, 399, 115

Hogg, D. W., Blanton, M. R., Brinchmann, J., et al. 2004, ApJL, 601, L29. doi:10.1086/381749

Hopkins, P. F., Torrey, P., Faucher-Giguère, C.-A., et al. 2016, MNRAS, 458, 816. doi:10.1093/mnras/stw289

Hopkins, P. F., Hernquist, L., Cox, T. J., et al. 2006, ApJS, 163, 50. doi:10.1086/499493

Hopkins, P. F., Richards, G. T., & Hernquist, L. 2007, ApJ, 654, 731. doi:10.1086/509629

Hopkins, P. F., Hernquist, L., Cox, T. J., et al. 2008, ApJS, 175, 356. doi:10.1086/524362

Hopkins, P. F. & Quataert, E. 2011, MNRAS, 415, 1027. doi:10.1111/j.1365-2966.2011.18542.x

Hoyle, F., Vogeley, M. S., & Pan, D. 2012, MNRAS, 426, 3041. doi:10.1111/j.1365-2966.2012.21943.x

Hunt, L. K. & Malkan, M. A. 1999, ApJ, 516, 660. doi:10.1086/307150

Ibar, E. & Lira, P. 2007, A&A, 466, 531. doi:10.1051/0004-6361:20065350

Ilbert, O., McCracken, H. J., Le Fèvre, O., et al. 2013, A&A, 556, A55. doi:10.1051/0004-6361/201321100

Ishibashi, W., Fabian, A. C., & Maiolino, R. 2018, MNRAS, 476, 512. doi:10.1093/mnras/sty236

Jahnke, K. & Macciò, A. V. 2011, ApJ, 734, 92. doi:10.1088/0004-637X/734/2/92

Jing, Y. P., Suto, Y., & Mo, H. J. 2007, ApJ, 657, 664. doi:10.1086/511130

Jogee, S. 2006, Physics of Active Galactic Nuclei at all Scales, 143. doi:10.1007/3-540-34621-X_6

Jogee, S., Miller, S. H., Penner, K., et al. 2009, ApJ, 697, 1971. doi:10.1088/0004-637X/697/2/1971

Jogee, S., Scoville, N., & Kenney, J. D. P. 2005, ApJ, 630, 837. doi:10.1086/432106

Johnson, J. W., Maller, A. H., Berlind, A. A., et al. 2019, MNRAS, 486, 1156. doi:10.1093/mnras/stz942

Jones, D. H., Read, M. A., Saunders, W., et al. 2009, MNRAS, 399, 683. doi:10.1111/j.1365-2966.2009.15338.x

Kakkad, D., Mainieri, V., Vietri, G., et al. 2020, A&A, 642, A147. doi:10.1051/0004-6361/202038551

Kannappan, S. J. 2004, ApJL, 611, L89. doi:10.1086/423785

Kannappan, S. J., Guie, J. M., & Baker, A. J. 2009, AJ, 138, 579. doi:10.1088/0004-6256/138/2/579

Kannappan, S. J., Stark, D. V., Eckert, K. D., et al. 2013, ApJ, 777, 42. doi:10.1088/0004-637X/777/1/42

Kawinwanichakij, L., Papovich, C., Ciardullo, R., et al. 2020, ApJ, 892, 7. doi:10.3847/1538-4357/ab75c4

Kirkpatrick, A., Sharon, C., Keller, E., et al. 2019, ApJ, 879, 41. doi:10.3847/1538-4357/ab223a

Kirkpatrick, A., Urry, C. M., Brewster, J., et al. 2020, ApJ, 900, 5. doi:10.3847/1538-4357/aba358

Knapen, J. H., Beckman, J. E., Heller, C. H., et al. 1995, ApJ, 454, 623. doi:10.1086/176516

Knebe, A., Stoppacher, D., Prada, F., et al. 2018, MNRAS, 474, 5206. doi:10.1093/mnras/stx2662

Koekemoer, A. M., Faber, S. M., Ferguson, H. C., et al. 2011, ApJS, 197, 36. doi:10.1088/0067-0049/197/2/36

Kormendy, J. & Richstone, D. 1995, ARA&A, 33, 581. doi:10.1146/annurev.aa.33.090195.003053

Kormendy, J. & Ho, L. C. 2013, ARA&A, 51, 511. doi:10.1146/annurev-astro-082708-101811

Kravtsov, A. V., Berlind, A. A., Wechsler, R. H., et al. 2004, ApJ, 609, 35. doi:10.1086/420959

Kreckel, K., Joung, M. R., & Cen, R. 2011, ApJ, 735, 132. doi:10.1088/0004-637X/735/2/132

Kriek, M., van Dokkum, P. G., Labbé, I., et al. 2009, ApJ, 700, 221. doi:10.1088/0004-637X/700/1/221

Kriek, M., van Dokkum, P. G., Franx, M., et al. 2006, ApJL, 649, L71. doi:10.1086/508371

Kriek, M., Shapley, A. E., Reddy, N. A., et al. 2015, ApJS, 218, 15. doi:10.1088/0067-0049/218/2/15

Kroupa, P. 2001, MNRAS, 322, 231. doi:10.1046/j.1365-8711.2001.04022.x

Kulier, A., Ostriker, J. P., Natarajan, P., et al. 2015, ApJ, 799, 178. doi:10.1088/0004-637X/799/2/178

Lagos, C. D. P., Cora, S. A., & Padilla, N. D. 2008, MNRAS, 388, 587. doi:10.1111/j.1365-2966.2008.13456.x

Laigle, C., McCracken, H. J., Ilbert, O., et al. 2016, ApJS, 224, 24. doi:10.3847/0067-0049/224/2/24

LaMassa, S. M., Georgakakis, A., Vivek, M., et al. 2019, ApJ, 876, 50. doi:10.3847/1538-4357/ab108b

LaMassa, S. M., Urry, C. M., Cappelluti, N., et al. 2013, MNRAS, 436, 3581. doi:10.1093/mnras/stt1837

LaMassa, S. M., Urry, C. M., Glikman, E., et al. 2013, MNRAS, 432, 1351. doi:10.1093/mnras/stt553

LaMassa, S. M., Urry, C. M., Cappelluti, N., et al. 2016, ApJ, 817, 172. doi:10.3847/0004-637X/817/2/172

Lang, D., Hogg, D. W., & Mykytyn, D. 2016, Astrophysics Source Code Library. ascl:1604.008

Lehmann, B. V., Mao, Y.-Y., Becker, M. R., et al. 2017, ApJ, 834, 37. doi:10.3847/1538-4357/834/1/37

Lehmer, B. D., Brandt, W. N., Alexander, D. M., et al. 2008, ApJ, 681, 1163. doi:10.1086/588459

Lehmer, B. D., Xue, Y. Q., Brandt, W. N., et al. 2012, ApJ, 752, 46. doi:10.1088/0004-637X/752/1/46

Leja, J., Johnson, B. D., Conroy, C., et al. 2017, ApJ, 837, 170. doi:10.3847/1538-4357/aa5ffe

Leslie, S. K., Kewley, L. J., Sanders, D. B., et al. 2016, MNRAS, 455, L82. doi:10.1093/mnrasl/slv135

Leung, G. C. K., Coil, A. L., Aird, J., et al. 2019, ApJ, 886, 11. doi:10.3847/1538-4357/ab4a7c

Liu, G., Zakamska, N. L., Greene, J. E., et al. 2013, MNRAS, 436, 2576. doi:10.1093/mnras/stt1755

Liu, Z., Merloni, A., Georgakakis, A., et al. 2016, MNRAS, 459, 1602. doi:10.1093/mnras/stw753

Lopes, P. A. A., Rembold, S. B., Ribeiro, A. L. B., et al. 2016, MNRAS, 461, 2559. doi:10.1093/mnras/stw1497

Lusso, E., Comastri, A., Simmons, B. D., et al. 2012, MNRAS, 425, 623. doi:10.1111/j.1365-2966.2012.21513.x

Madau, P. & Dickinson, M. 2014, ARA&A, 52, 415. doi:10.1146/annurev-astro-081811-125615

Magorrian, J., Tremaine, S., Richstone, D., et al. 1998, AJ, 115, 2285. doi:10.1086/300353

Mahoro, A., Pović, M., & Nkundabakura, P. 2017, MNRAS, 471, 3226. doi:10.1093/mnras/stx1762

Mao, Y.-Y., Zentner, A. R., & Wechsler, R. H. 2018, MNRAS, 474, 5143. doi:10.1093/mnras/stx3111

Marinacci, F., Vogelsberger, M., Pakmor, R., et al. 2018, MNRAS, 480, 5113. doi:10.1093/mnras/sty2206

Masoura, V. A., Mountrichas, G., Georgantopoulos, I., et al. 2018, A&A, 618, A31. doi:10.1051/0004-6361/201833397

McLure, R. J. & Dunlop, J. S. 2002, MNRAS, 331, 795. doi:10.1046/j.1365-8711.2002.05236.x

McNamara, B. R. & Nulsen, P. E. J. 2007, ARA&A, 45, 117. doi:10.1146/annurev.astro.45.051806.110625

Meléndez, M., Mushotzky, R. F., Shimizu, T. T., et al. 2014, ApJ, 794, 152. doi:10.1088/0004-637X/794/2/152

Mendez, A. J., Coil, A. L., Aird, J., et al. 2016, ApJ, 821, 55. doi:10.3847/0004-637X/821/1/55

Merloni, A., Predehl, P., Becker, W., et al. 2012, arXiv:1209.3114

Meyer, M. J., Zwaan, M. A., Webster, R. L., et al. 2007, ApJ, 654, 702. doi:10.1086/508799

Miyaji, T., Hasinger, G., Salvato, M., et al. 2015, ApJ, 804, 104. doi:10.1088/0004-637X/804/2/104

Mo, H. J. & White, S. D. M. 1996, MNRAS, 282, 347. doi:10.1093/mnras/282.2.347

Moffett, A. J., Kannappan, S. J., Berlind, A. A., et al. 2015, ApJ, 812, 89. doi:10.1088/0004-637X/812/2/89

More, S., van den Bosch, F. C., Cacciato, M., et al. 2009, MNRAS, 392, 801. doi:10.1111/j.1365-2966.2008.14095.x

Moster, B. P., Somerville, R. S., Newman, J. A., et al. 2011, ApJ, 731, 113. doi:10.1088/0004-637X/731/2/113

Moustakas, J., Coil, A. L., Aird, J., et al. 2013, ApJ, 767, 50. doi:10.1088/0004-637X/767/1/50

Muldrew, S. I., Hatch, N. A., & Cooke, E. A. 2018, MNRAS, 473, 2335. doi:10.1093/mnras/stx2454

Muldrew, S. I., Hatch, N. A., & Cooke, E. A. 2015, MNRAS, 452, 2528. doi:10.1093/mnras/stv1449

Mullaney, J. R., Alexander, D. M., Goulding, A. D., et al. 2011, MNRAS, 414, 1082. doi:10.1111/j.1365-2966.2011.18448.x

Muzzin, A., Marchesini, D., Stefanon, M., et al. 2013, ApJ, 777, 18. doi:10.1088/0004-637X/777/1/18

Naab, T. & Ostriker, J. P. 2017, ARA&A, 55, 59. doi:10.1146/annurev-astro-081913-040019

Nadathur, S., Hotchkiss, S., & Crittenden, R. 2017, MNRAS, 467, 4067. doi:10.1093/mnras/stx336

Naiman, J. P., Pillepich, A., Springel, V., et al. 2018, MNRAS, 477, 1206. doi:10.1093/mnras/sty618

Negri, A. & Volonteri, M. 2017, MNRAS, 467, 3475. doi:10.1093/mnras/stx362

Nelson, D., Springel, V., Pillepich, A., et al. 2019, Computational Astrophysics and Cosmology, 6, 2. doi:10.1186/s40668-019-0028-x

Nelson, D., Pillepich, A., Springel, V., et al. 2018, MNRAS, 475, 624. doi:10.1093/mnras/stx3040

Nelson, D., Pillepich, A., Springel, V., et al. 2019, MNRAS, 490, 3234. doi:10.1093/mnras/stz2306

Nenkova, M., Sirocky, M. M., Ivezić, Ž., et al. 2008, ApJ, 685, 147. doi:10.1086/590482

Neyrinck, M. C. 2008, MNRAS, 386, 2101. doi:10.1111/j.1365-2966.2008.13180.x

Noll, S., Burgarella, D., Giovannoli, E., et al. 2009, A&A, 507, 1793. doi:10.1051/0004-6361/200912497

Norberg, P., Baugh, C. M., Hawkins, E., et al. 2002, MNRAS, 332, 827. doi:10.1046/j.1365-8711.2002.05348.x

Oemler, A. 1974, ApJ, 194, 1. doi:10.1086/153216

Oppenheimer, B. D. & Davé, R. 2006, MNRAS, 373, 1265. doi:10.1111/j.1365-2966.2006.10989.x

Pacucci, F. & Loeb, A. 2020, ApJ, 895, 95. doi:10.3847/1538-4357/ab886e

Papovich, C., Shipley, H. V., Mehrtens, N., et al. 2016, ApJS, 224, 28. doi:10.3847/0067-0049/224/2/28

Paranjape, A., Kovač, K., Hartley, W. G., et al. 2015, MNRAS, 454, 3030. doi:10.1093/mnras/stv2137

Park, C., Choi, Y.-Y., Vogeley, M. S., et al. 2007, ApJ, 658, 898. doi:10.1086/511059

Park, J., Smith, R., & Yi, S. K. 2017, ApJ, 845, 128. doi:10.3847/1538-4357/aa81c6

Patiri, S. G., Prada, F., Holtzman, J., et al. 2006, MNRAS, 372, 1710. doi:10.1111/j.1365-2966.2006.10975.x

Paturel, G., Petit, C., Prugniel, P., et al. 2003, A&A, 412, 45. doi:10.1051/0004-6361:20031411

Peebles, P. J. E. 2001, ApJ, 557, 495. doi:10.1086/322254

Penrose, R. 1969, Nuovo Cimento Rivista Serie, 1, 252

Penrose, R. 1963, Phys. Rev. Lett., 10, 66. doi:10.1103/PhysRevLett.10.66

Perna, M., Lanzuisi, G., Brusa, M., et al. 2017, A&A, 603, A99. doi:10.1051/0004-6361/201630369

Peterson, J. R. & Fabian, A. C. 2006, Phys. Rep., 427, 1. doi:10.1016/j.physrep.2005.12.007

Pierre, M., Pacaud, F., Adami, C., et al. 2016, A&A, 592, A1. doi:10.1051/0004-6361/201526766

Pillepich, A., Nelson, D., Springel, V., et al. 2019, MNRAS, 490, 3196. doi:10.1093/mnras/stz2338

Pillepich, A., Nelson, D., Hernquist, L., et al. 2018, MNRAS, 475, 648. doi:10.1093/mnras/stx3112

Pillepich, A., Springel, V., Nelson, D., et al. 2018, MNRAS, 473, 4077. doi:10.1093/mnras/stx2656

Powell, M. C., Urry, C. M., Cappelluti, N., et al. 2020, ApJ, 891, 41. doi:10.3847/1538-4357/ab6e65

Pozzetti, L., Bolzonella, M., Zucca, E., et al. 2010, A&A, 523, A13. doi:10.1051/0004-6361/200913020

Reddick, R. M., Wechsler, R. H., Tinker, J. L., et al. 2013, ApJ, 771, 30. doi:10.1088/0004-637X/771/1/30

Ricciardelli, E., Cava, A., Varela, J., et al. 2014, MNRAS, 445, 4045. doi:10.1093/mnras/stu2061

Rigby, E. E., Best, P. N., Brookes, M. H., et al. 2011, MNRAS, 416, 1900. doi:10.1111/j.1365-2966.2011.19167.x

Rodriguez-Gomez, V., Genel, S., Vogelsberger, M., et al. 2015, MNRAS, 449, 49. doi:10.1093/mnras/stv264

Rojas, R. R., Vogeley, M. S., Hoyle, F., et al. 2004, ApJ, 617, 50. doi:10.1086/425225

Rojas, R. R., Vogeley, M. S., Hoyle, F., et al. 2005, ApJ, 624, 571. doi:10.1086/428476

Roos, O., Juneau, S., Bournaud, F., et al. 2015, ApJ, 800, 19. doi:10.1088/0004-637X/800/1/19

Rosario, D. J., Santini, P., Lutz, D., et al. 2013, ApJ, 771, 63. doi:10.1088/0004-637X/771/1/63

Rupke, D. S., Veilleux, S., & Sanders, D. B. 2005, ApJ, 632, 751. doi:10.1086/444451

Saito, S., Leauthaud, A., Hearin, A. P., et al. 2016, MNRAS, 460, 1457. doi:10.1093/mnras/stw1080

Salim, S., Rich, R. M., Charlot, S., et al. 2007, ApJS, 173, 267. doi:10.1086/519218

Sanders, D. B., Salvato, M., Aussel, H., et al. 2007, ApJS, 172, 86. doi:10.1086/517885

Sanders, D. B., Soifer, B. T., Elias, J. H., et al. 1988, ApJ, 325, 74. doi:10.1086/165983

Santini, P., Rosario, D. J., Shao, L., et al. 2012, A&A, 540, A109. doi:10.1051/0004-6361/201118266

Scannapieco, E. & Bildsten, L. 2005, ApJL, 629, L85. doi:10.1086/452632

Schmidt, M. 1963, Nature, 197, 1040. doi:10.1038/1971040a0

Schmidt, M. 1968, ApJ, 151, 393. doi:10.1086/149446

Schreiber, C., Pannella, M., Elbaz, D., et al. 2015, A&A, 575, A74. doi:10.1051/0004-6361/201425017

Scoville, N., Aussel, H., Brusa, M., et al. 2007, ApJS, 172, 1. doi:10.1086/516585

Seyfert, C. K. 1943, ApJ, 97, 28. doi:10.1086/144488

Sherman, S., Jogee, S., Florez, J., et al. 2020, MNRAS, 491, 3318. doi:10.1093/mnras/stz3229

Sherman, S., Jogee, S., Florez, J., et al. 2021, MNRAS, 505, 947. doi:10.1093/mnras/stab1350

Sherman, S., Jogee, S., Florez, J., et al. 2020, MNRAS, 499, 4239. doi:10.1093/mnras/staa3167

Shimizu, T. T., Mushotzky, R. F., Meléndez, M., et al. 2017, MNRAS, 466, 3161. doi:10.1093/mnras/stw3268

Shimizu, T. T., Mushotzky, R. F., Meléndez, M., et al. 2015, MNRAS, 452, 1841. doi:10.1093/mnras/stv1407

Sijacki, D., Springel, V., Di Matteo, T., et al. 2007, MNRAS, 380, 877. doi:10.1111/j.1365-2966.2007.12153.x

Silk, J. 2013, ApJ, 772, 112. doi:10.1088/0004-637X/772/2/112

Somerville, R. S., Hopkins, P. F., Cox, T. J., et al. 2008, MNRAS, 391, 481. doi:10.1111/j.1365-2966.2008.13805.x

Somerville, R. S. & Davé, R. 2015, ARA&A, 53, 51. doi:10.1146/annurev-astro-082812-140951

Speagle, J. S., Steinhardt, C. L., Capak, P. L., et al. 2014, ApJS, 214, 15. doi:10.1088/0067-0049/214/2/15

Springel, V., Pakmor, R., Pillepich, A., et al. 2018, MNRAS, 475, 676. doi:10.1093/mnras/stx3304

Springel, V. & Hernquist, L. 2003, MNRAS, 339, 289. doi:10.1046/j.1365-8711.2003.06206.x

Springel, V., Di Matteo, T., & Hernquist, L. 2005, MNRAS, 361, 776. doi:10.1111/j.1365-2966.2005.09238.x

Stark, D. V., Kannappan, S. J., Wei, L. H., et al. 2013, ApJ, 769, 82. doi:10.1088/0004-637X/769/1/82

Stark, D. V., Kannappan, S. J., Eckert, K. D., et al. 2016, ApJ, 832, 126. doi:10.3847/0004-637X/832/2/126

Stefanon, M., Marchesini, D., Rudnick, G. H., et al. 2013, ApJ, 768, 92. doi:10.1088/0004-637X/768/1/92

Steinmetz, M. & Navarro, J. F. 2002, New Astron., 7, 155. doi:10.1016/S1384-1076(02)00102-1

Stevans, M. L., Finkelstein, S. L., Kawinwanichakij, L., et al. 2021, arXiv:2103.14690

Strüder, L., Briel, U., Dennerl, K., et al. 2001, A&A, 365, L18. doi:10.1051/0004-6361:20000066

Sturm, E., González-Alfonso, E., Veilleux, S., et al. 2011, ApJL, 733, L16. doi:10.1088/2041-8205/733/1/L16

Sutherland, W. & Saunders, W. 1992, MNRAS, 259, 413. doi:10.1093/mnras/259.3.413

Thomas, N., Davé, R., Anglés-Alcázar, D., et al. 2019, MNRAS, 487, 5764. doi:10.1093/mnras/stz1703

Thomas, N., Davé, R., Jarvis, M. J., et al. 2021, MNRAS, 503, 3492. doi:10.1093/mnras/stab654

Timlin, J. D., Ross, N. P., Richards, G. T., et al. 2016, ApJS, 225, 1. doi:10.3847/0067-0049/225/1/1

Tinker, J. L. & Conroy, C. 2009, ApJ, 691, 633. doi:10.1088/0004-637X/691/1/633

Tonnesen, S. & Cen, R. 2015, ApJ, 812, 104. doi:10.1088/0004-637X/812/2/104

Tristram, K. R. W., Meisenheimer, K., Jaffe, W., et al. 2007, A&A, 474, 837. doi:10.1051/0004-6361:20078369

Ueda, Y., Akiyama, M., Hasinger, G., et al. 2014, ApJ, 786, 104. doi:10.1088/0004-637X/786/2/104

Urry, C. 2004, AGN Physics with the Sloan Digital Sky Survey, 311, 49

Vale, A. & Ostriker, J. P. 2004, MNRAS, 353, 189. doi:10.1111/j.1365-2966.2004.08059.x

van de Voort, F., Bahé, Y. M., Bower, R. G., et al. 2017, MNRAS, 466, 3460. doi:10.1093/mnras/stw3356

van der Burg, R. F. J., Muzzin, A., Hoekstra, H., et al. 2013, A&A, 557, A15. doi:10.1051/0004-6361/201321237

van Dokkum, P. G., Labbé, I., Marchesini, D., et al. 2009, PASP, 121, 2. doi:10.1086/597138

Veilleux, S., Maiolino, R., Bolatto, A. D., et al. 2020, A&ARv, 28, 2. doi:10.1007/s00159-019-0121-9

Verbeke, R., De Rijcke, S., Koleva, M., et al. 2014, MNRAS, 442, 1830. doi:10.1093/mnras/stu947

Viero, M. P., Asboth, V., Roseboom, I. G., et al. 2014, ApJS, 210, 22. doi:10.1088/0067-0049/210/2/22

Virtanen, P., Gommers, R., Oliphant, T. E., et al. 2020, Nature Methods, 17, 261. doi:10.1038/s41592-019-0686-2

Vogelsberger, M., Genel, S., Springel, V., et al. 2014, Nature, 509, 177. doi:10.1038/nature13316

Vogelsberger, M., Marinacci, F., Torrey, P., et al. 2020, Nature Reviews Physics, 2, 42. doi:10.1038/s42254-019-0127-2

Vogelsberger, M., Genel, S., Springel, V., et al. 2014, MNRAS, 444, 1518. doi:10.1093/mnras/stu1536

Vogelsberger, M., Genel, S., Sijacki, D., et al. 2013, MNRAS, 436, 3031. doi:10.1093/mnras/stt1789

Wagner, C. R., Courteau, S., Brodwin, M., et al. 2017, ApJ, 834, 53. doi:10.3847/1538-4357/834/1/53

Watson, D. F., Hearin, A. P., Berlind, A. A., et al. 2015, MNRAS, 446, 651. doi:10.1093/mnras/stu2065

Wechsler, R. H., Zentner, A. R., Bullock, J. S., et al. 2006, ApJ, 652, 71. doi:10.1086/507120

Weigel, A. K., Schawinski, K., & Bruderer, C. 2016, MNRAS, 459, 2150. doi:10.1093/mnras/stw756

Weinberger, R., Springel, V., Hernquist, L., et al. 2017, MNRAS, 465, 3291. doi:10.1093/mnras/stw2944

Wellons, S., Torrey, P., Ma, C.-P., et al. 2015, MNRAS, 449, 361. doi:10.1093/mnras/stv303

Whitaker, K. E., Labbé, I., van Dokkum, P. G., et al. 2011, ApJ, 735, 86. doi:10.1088/0004-637X/735/2/86

Whitaker, K. E., Franx, M., Leja, J., et al. 2014, ApJ, 795, 104. doi:10.1088/0004-637X/795/2/104

Whitaker, K. E., van Dokkum, P. G., Brammer, G., et al. 2012, ApJL, 754, L29. doi:10.1088/2041-8205/754/2/L29

White, S. D. M. & Rees, M. J. 1978, MNRAS, 183, 341. doi:10.1093/mnras/183.3.341

Wilkins, S. M., Trentham, N., & Hopkins, A. M. 2008, MNRAS, 385, 687. doi:10.1111/j.1365-2966.2008.12885.x

Williams, R. J., Quadri, R. F., Franx, M., et al. 2009, ApJ, 691, 1879. doi:10.1088/0004-637X/691/2/1879

Wold, I. G. B., Kawinwanichakij, L., Stevans, M. L., et al. 2019, ApJS, 240, 5. doi:10.3847/1538-4365/aaee85

Wright, E. L., Eisenhardt, P. R. M., Mainzer, A. K., et al. 2010, AJ, 140, 1868. doi:10.1088/0004-6256/140/6/1868

Wuyts, S., Labbé, I., Franx, M., et al. 2007, ApJ, 655, 51. doi:10.1086/509708

Xie, L., De Lucia, G., Hirschmann, M., et al. 2020, MNRAS, 498, 4327. doi:10.1093/mnras/staa2370

Xue, Y. Q., Luo, B., Brandt, W. N., et al. 2011, ApJS, 195, 10. doi:10.1088/0067-0049/195/1/10

Yang, G., Brandt, W. N., Alexander, D. M., et al. 2019, MNRAS, 485, 3721. doi:10.1093/mnras/stz611

Yang, G., Chen, C.-T. J., Vito, F., et al. 2017, ApJ, 842, 72. doi:10.3847/1538-4357/aa7564

Yang, X., Mo, H. J., & van den Bosch, F. C. 2009, ApJ, 693, 830. doi:10.1088/0004-637X/693/1/830

Yang, G., Boquien, M., Buat, V., et al. 2020, MNRAS, 491, 740. doi:10.1093/mnras/stz3001

York, D. G., Adelman, J., Anderson, J. E., et al. 2000, AJ, 120, 1579. doi:10.1086/301513

Yuan, F. & Narayan, R. 2014, ARA&A, 52, 529. doi:10.1146/annurev-astro-082812-141003

Yun, K., Pillepich, A., Zinger, E., et al. 2019, MNRAS, 483, 1042. doi:10.1093/mnras/sty3156

Zehavi, I., Zheng, Z., Weinberg, D. H., et al. 2011, ApJ, 736, 59. doi:10.1088/0004-637X/736/1/59

Zentner, A. R., Hearin, A. P., & van den Bosch, F. C. 2014, MNRAS, 443, 3044. doi:10.1093/mnras/stu1383

Zu, Y. & Mandelbaum, R. 2018, MNRAS, 476, 1637. doi:10.1093/mnras/sty279